CELLULOSIC NANOCOMPOSITES

WITH UNIQUE MORPHOLOGY AND PROPERTIES

A Dissertation
Presented to
The Academic Faculty

by

JIHOON LEE

In Partial Fulfillment
of the Requirements for the Degree
Doctor of Philosophy in the
School of Chemical & Biomolecular Engineering

Georgia Institute of Technology
December 2010

CELLULOSIC NANOCOMPOSITES

WITH UNIQUE MORPHOLOGY AND PROPERTIES

Approved by:

Dr. Yulin Deng, Advisor
School of Chemical & Biomolecular Engineering
Georgia Institute of Technology

Dr. Peter Ludovice
School of Chemical & Biomolecular Engineering
Georgia Institute of Technology

Dr. John Muzzy
School of Chemical & Biomolecular Engineering
Georgia Institute of Technology

Dr. Art Ragauskas
School of Chemistry & Biochemistry
Georgia Institute of Technology

Dr. Jeff Hsieh
School of Chemical & Biomolecular Engineering
Georgia Institute of Technology

Date Approved: September 22, 2010

To my family.

Dongyoon Lee, Yangsoon Kim,

Sun Lee and Boram Lee

ACKNOWLEDGEMENTS

My life at Georgia Tech has been very successful because of a lot of helps and supports by faculty members, colleagues and friends. First of all, I would like to thank my advisor, Dr. Yulin Deng. Whenever I have met obstacles, he helped me to solve the problems. He also motivated and encouraged me to be an innovative and successful researcher. I also would like thank Dr. Art Ragauskas for allowing me to use his excellent facilities at anytime as well as helpful comments and recommendation. I also thank to other committee members, Dr. Jeff Hsieh, Dr. John Muzzy and Dr. Peter Ludovice for all the thoughtful comments and suggestions. I also thank Dr. Ken Gall, Dr. Sujit Banerjee, and Dr. Yonathan Thio for allowing me to share the equipments. Also thanks to my lab colleagues, Dr. Seyoung Yoon, Dr. Myoungchul Park, Dr. Yulin Zhao, Dr. Brett Brotherson, Dr. Zhengzhi Zhou, Dr. Zeshan Hu, Dr. Jian Gong, Delong Song, Mallarie Mccune, Also thanks to Dr. Ragauskas group members, Goetz, Hu and Dr. Shaobo.

I also would like thank to my Korean friends in ChBE and GaTech tennis club. They gave me thoughtful advices and refreshed me whenever I was depressed. Especially thanks to Dr. Jay Lee, Dr. Sungho Park, Dr. Yeuchun Kim, Dr. Wonjong Rhee, Dr. Jungwoo Lee, Dr. Jaekyu Cho, Taehyun, Junghyun, Doyoung, Jongsuk, Kwanghun, Jinwoo. Also thanks to Sungsoo at Boulder, Junwon at UIUC, Sungwoo at UMass, Jaewook at Houston, Sanghyun at Hillsboro and Youngeun at Minessota. Also thanks to my old friends in Korea, Hungoo, Hyungro, Joongwon, Sangon, Wonrock, Wangyoun and Changtae.

Last, I would like to express my special thanks to my parents, Dongyoon Lee and Yangsoon Kim for their endless care and love. I also thanks to my older sister, Sun Lee and my lovely younger sister, Boram Lee. I cannot express with any words how much I love my family.

TABLE OF CONTENTS

LIST OF TABLES

Page

LIST OF FIGURES

LIST OF SYMBOLS

A	Area
a_0	Average intermolecular distance
B_E	Fiber - fiber bonding character
b_1	Fiber alignment degree
b_2	Fiber connectivity
b_3	Bonding area between fibers
C	Concentration
D	Overall thickness
D_c	Diffusion coefficient
D_f	Fractal dimension
d	Diameter of filler
h_c	Contact depth of the tip
h_{max}	Maximum contact depth of the tip
h_r	Contact depth of the tip after tip removal
I	Second moment area of the beam

E	Modulus
E_C	Elastic modulus
E_f	Modulus of filler
E_i	Modulus of the indenter tip
E_L	Longitudinal modulus
E_m	Modulus of matrix
E_R	Modulus of rigid phase
E_r	Relative modulus
E_S	Modulus of soft phase
E_T	Transverse modulus
F_C	Maximum compression load
$F_{C\text{-}S1}$	Hydrophobic interaction force between cellulose microfibril and substrate 1
$F_{C\text{-}S2}$	Hydrophobic interaction force between cellulose microfibril and substrate 2
$F_{C\text{-}W}$	Hydrophobic interaction force between cellulose microfibril and water
$F_{W\text{-}S1}$	Hydrophobic interaction force between water and substrate 1
$F_{W\text{-}S2}$	Hydrophobic interaction force between water and substrate 2
f_V	Surface fraction of vapor phase

f_S	Surface fraction of solid phase
G	Growth speed of the ice crystal
$G_{a\text{-}axis}$	Growth speed of the ice crystal along a-axis
$G_{b\text{-}axis}$	Growth speed of the ice crystal along b-axis
$G_{c\text{-}axis}$	Growth speed of the ice crystal along c-axis
L	Length of filler
L_f	Upper limit of the fractal structure
l	Suspended length
l_f	Lower limit of the fractal structure
M	Mechanical properties of electrospun fiber webs
$M_{aligned}$	Mechanical properties of aligned electrospun fiber webs
$M_{isotropic}$	Mechanical properties of isotropic electrospun fiber webs
M_w	Molecular weight
m_L	Slope of the liquid line
P	Load on the tip
P_{max}	Maximum force
R	Radius of particle

S	Initial slope
S_C	Compressive stress
S_E	Electrospun fiber properties
s_1	Cellulose nanowhiskers loading ratio
s_2	Crystallinity of electrospun fibers
s_3	Average diameter of electrospun fibers
T	Temperature
T_g	Glass transition temperature
v	Deflection of the beam
$v_{a\text{-}axis}$	Ice-front velocity along a-axis
$v_{b\text{-}axis}$	Ice-front velocity along b-axis
v_c	Critical velocity
$v_{c\text{-}axis}$	Ice-front velocity along c-axis
v_{front}	Cell-front velocity
$v_{ice\text{-}front}$	Ice-front velocity
β	Tip geometry factor
γ	Surface tension

γ_{LV}	Liquid phase - vapor phase interfacial surface tension
γ_{SL}	Solid phase - liquid phase interfacial surface tension
γ_{SV}	Solid phase – vapor phase interfacial surface tension
ε	Degree of compression
ζ	Shape factor
η	Solution viscosity
θ	Scattering angle of the X-ray beam
θ_c	Cassie-Baxter model apparent contact angle
θ_e	Equilibrium contact angle
θ_f	Wenzel and Cassie-Baxter combination model apparent contact angle
$\theta_{S,e}$	Equilibrium contact angle of liquid droplet at solid phase
$\theta_{V,e}$	Equilibrium contact angle of liquid droplet at vapor phase
θ_w	Wenzel model apparent contact angle
$\theta_{\parallel}$	Contact angle parallel to the groove
$\theta_{\perp}$	Contact angle vertical to the groove
λ	Channel wavelength
λ_B	Wavelength of the X-ray beam

ν_i	Poisson's ratio of the sample
ν_m	Poisson's ratio of the tip
ν_R	Volume fraction of rigid phase
ν_{Rc}	Percolation threshold
ρ	Density
ρ_F	Density of the foam
ρ_P	Density of the foam materials
Φ	Volume fraction
φ_F	Porosity of the foam

LIST OF ABBREVIATIONS

2D	2-Dimension
3D	3-Dimension
AFM	Atomic force microscopy
CBD	Chemical bath deposition
CEC	Cation exchange capacity
CNT	Carbon nanotube
CVD	Chemical vapor deposition
DI	Deionized
FFT	Fast fourier transform
HDPE	High density polyethlyene
H-T	Halpin-Tsai
IT	Ice-templated
LbL	Layer-by-layer
LDPE	Low density polyethylene
MMT	Montmorillonite

MWCNT	Multi-walled carbon nanotube
NIH	National Institute of Health
NMMO	N-methylmorpholine-N-oxide
OMLS	Organically modified layered silicate
OTS	Octadecyltrichlorosilane
PAA	Poly(acryl acid)
PAH	Polyallyamine hydrochloride
PCL	Poly(caprolectone)
PDMS	Polydimethylsiolxane
PE	Polyethylene
PEO	Poly(ethylene oxide)
PLS	Polymer/layered silicate
PP	Polypropylene
PPFEMA	Polymerized perfluoroalkyl ethyl methacrylate
PS	Polystyrene
PTFE	Poly(tetrafluoroethylene)
PVA	Poly(vinyl alcohol)

SEM	Scanning electron microscopy
SWNT	Single-walled nanotube
TEM	Transmission electron microscopy
UTHSCSA	University of Texas Health Science Center at San Antonio
WXRD	Wide angle X-ray diffraction
XRD	X-ray diffraction
ZnO	Zinc oxide

SUMMARY

A new and environmental benign method for preparing regenerated cellulose and montmorillonite (MMT) biodegradable nanocomposites is developed using 4-methyl morpholine N-oxide (NMMO) as the solvent. Results showed that the modulus of the nanocomposites increases linearly at the MMT loading range of 1–10%. Using Wide Angle X-ray Diffraction (WXRD) analysis, scanning electron microscopy (SEM) and transmission electron microscopy (TEM) observation, it was found for the first time that the MMT was intercalated and exfoliated in the pure cellulose matrix.

Cellulose nanowhiskers reinforced poly(vinyl alcohol) (PVA) nanofiber web was successfully fabricated using electrospinning technique. The morphology and mechanical properties of highly aligned electrospun fiber webs were investigated. The relative alignment degree of electrospun fiber webs was analyzed using a fast Fourier transform (FFT) method. It was found that the modulus and tensile strength of aligned webs are higher than those of isotropic electrospun fiber webs. The relations of reinforcement effects, fiber alignment and cellulose nanowhiskers alignment have been investigated.

The mechanical properties of cellulose nanowhiskers reinforced poly(vinyl alcohol) (PVA) electrospun fiber rather than fiber webs have been measured using nanoindentation method. The modulus of PVA/cellulose nanowhiskers electrospun fiber increases linearly with increasing loading ratio of cellulose nanowhiskers up to 20.0wt%. Experimental results were compared with a longitudinal Halpin-Tsai model. The nanoindentation results are 20~30% smaller than the longitudinal model predictions.

Ice-templated (IT) cellulose microfibril porous foams are successfully fabricated via unidirectional freezing methods. IT cellulose microfibrils foam prepared from 1.0wt% suspension shows a cross-linked network structure. As increasing the concentrations of cellulose microfibrils suspension from 1.0wt% up to 2.75wt%, a transition from a

network structure to a lamellar channel structure happens gradually. As increasing the concentration of suspensions from 3.0wt% up to 8.0wt%, highly aligned channel structures parallel to the freezing direction were obtained. It was found that cellulose microfibrils are partially aligned along the freezing direction. It was found that the compressive stresses of IT cellulose microfibril foams increase linearly as increasing concentrations of suspension.

The morphology and growth mechanism of IT surfaces were investigated successfully using cellulose microfibrils and hydrophilic substrates. When the height of IT cellulose microfibril surface is 50 μm, the surface shows honey-comb like structures. When the height of IT surfaces is between 100 μm and 200 μm, a transition from honey-comb like structures to multilayer structures happens. In these cases, ellipse-shape channels are observed. If the height of IT surfaces is larger than 300 μm, fully developed multichannel surfaces are obtained. By controlling the temperature gradient between cellulose microfibril suspensions and secondary freezing mediums, various surface structures including honey-comb like structures, ellipse-shape channel structures, fully developed multichannel structures are obtained successfully. For the honey-comb like patterned surface, high contact angles are observed. On the other hand, for the layered patterned surface, anisotropic wetting properties were observed.

CHAPTER 1

INTRODUCTION

Cellulose is the most abundant natural polymer. It is environmentally friendly, biocompatible and renewable. Due to the hydroxyl groups on cellulose, there are strong hydrogen bonds between cellulose molecules. Especially, cellulose nanowhiskers and cellulose microfibrils which are high aspect ratio belt-type particles show good mechanical properties. Moreover, they have a low density compared with inorganic filler materials. Therefore, cellulose based materials including cellulose nanowhiskers and cellulose microfibrils are excellent candidates for biocompatible nanocomposites with good mechanical properties.

For the fabrication of a new type of functional products, there are 3 important factors to consider. Which materials is the most appropriate? Which design is the best to get the required properties? Which fabrication method is the most effective? Any of them cannot be neglected and three of the factors affect each other. Recently, interests on the control of the 2D/3D architectures of nanostructures and their properties have been increased due to the fast development of fabrication techniques. Especially, alignment, anisotropy and orientation control of the nanostructures are critical issues.

In this study, new types of cellulose based nanocomposites and their fabrication methods are introduced. Especially, the relationships between 2D/3D architectures of the nanocomposites and their properties are investigated. At the following chapter, literatures including the background of my researches and relevant topics are reviewed. At Chapter 3, nanocomposites from regenerated cellulose and montmollironite (MMT) nanoclays are introduced. The effects of MMT structures and surface properties on the mechanical performance of nanocomposites are investigated. At Chapter 4, cellulose nanowhiskers

reinforced PVA electrospun fiber webs are fabricated. The relationships among the alignment of fibers, the orientation of cellulose nanowhiskers and physical properties of fiber webs are investigated. At Chapter 5, individual fiber properties of cellulose nanowhiskers reinforced electrospun fibers are measured using nanoindentation method. The effects of alignment of cellulose nanowhiskers on the electrospun fibers are studied. At Chapter 6, cellulose microfibril porous foams are made using Ice-templated (IT) method. The morphology, growth mechanism and mechanical properties of IT cellulose microfibril foams are investigated. At Chapter 7, cellulose microfibril pattern surfaces are fabricated using IT method. The morphology, growth mechanism and wetting properties of IT cellulose microfibril patterned surfaces are studied. The relationship between surface structures and wetting properties are also investigated.

CHAPTER 2

LITERATURE REVIEW

2.1 Cellulose

2.1.1 Structure and Polymorphism of Cellulose

Cellulose is the most abundant natural polymer. It is the very commonly found in a wide variety of living species such as plants, animals, bacteria and some amoebas. It has been estimated that globally between 10^{10} and 10^{11} tons of cellulose are synthesized [1]. Cellulose whose formula is $(C_6H_{10}O_5)_n$ is the natural polymeric polysaccharide carbohydrate. Cellulose is derived from (β-glucose), which condense through β(1→4)-glycosidic bonds. Structure of cellulose is shown in Fig. 2-1. The cellulose monomers are linked together by condensation and the sugar rings are joined by glycosidic oxygen bridges. The average degree of polymerization in native cellulose is reported as around 13,000.

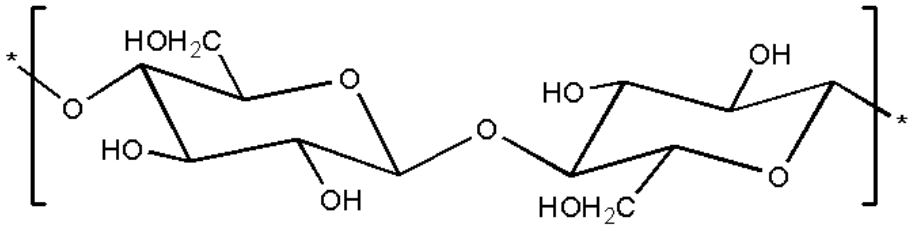

Figure 2-1. Structure of cellulose through β(1→4) glycosidic bonds.

Cellulose exists as six different polymorphs, cellulose I, II, III_I, III_{II}, IV_I, and IV_{II} [2]. The interconversion between the polymorphs of cellulose is summarized at Fig 2-2.

Cellulose I is found in nature. Cellulose II can be obtained from cellulose I by regeneration process. Interconversion between cellulose I and II is the irreversible reaction. Cellulose III_I and cellulose III_{II} are formed from cellulose I and II, respectively, by the amine treatment. Interconversion between cellulose I and III_I or cellulose II and III_{II} is reversible. Cellulose IV_I and IV_{II} may be prepared by heating cellulose III_I and III_{II} to 206°C in glycerol, respectively.

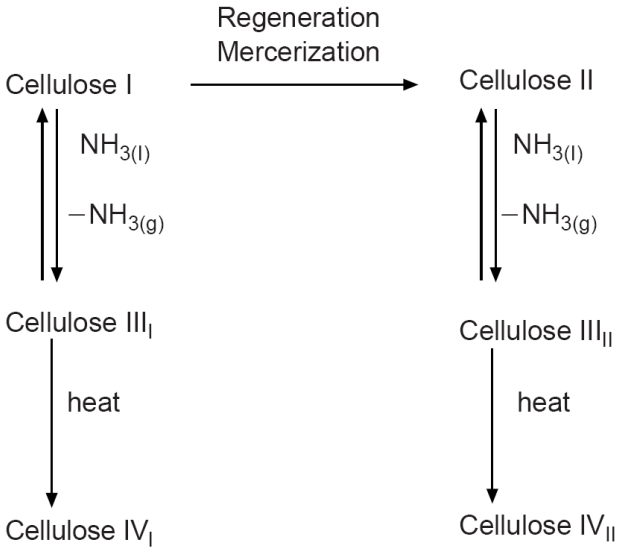

Figure 2-2. Interconversion of the polymorphs of cellulose [2].

It was also found that Cellulose I has two polymorphs, cellulose Iα and cellulose Iβ. The fractions of cellulose Iα and cellulose Iβ in native cellulose depend on the origin of the cellulose. Iα phase is a meta stable and can be converted to the more stable Iβ form by annealing.

2.1.2 Cellulose ultrastructure

The extended cellulose chain forms a flat ribbon-like structure. Cellulose chains are stiffened by Van der Waals forces, as well as intra and intermolecular hydrogen bonds, resulting in a regular crystalline arrangement of cellulose chains. In nature, it is hard to find a single cellulose chain. Most of cellulose exists as the forms of crystalline array of cellulose chains.

Elementary fibrils are the basic unit of cellulose morphology. Their lateral dimension is about 30 x 30 Angstrom^2 and their average length is 300 Angstroms. Elementary fibrils are connected by amorphous cellulose region. Microfibrils are composed of a bundle of elementary fibrils. Their size is approximately 120 x 120 Angstroms and infinite length. Fibrils are composed of bundles of microfibrils. It is approximately 2000 Angstroms in length. When viewed in cross-section, fibril structures are blocked within a matrix of hemicellulose and lignin as shown in Fig 2-3 [2].

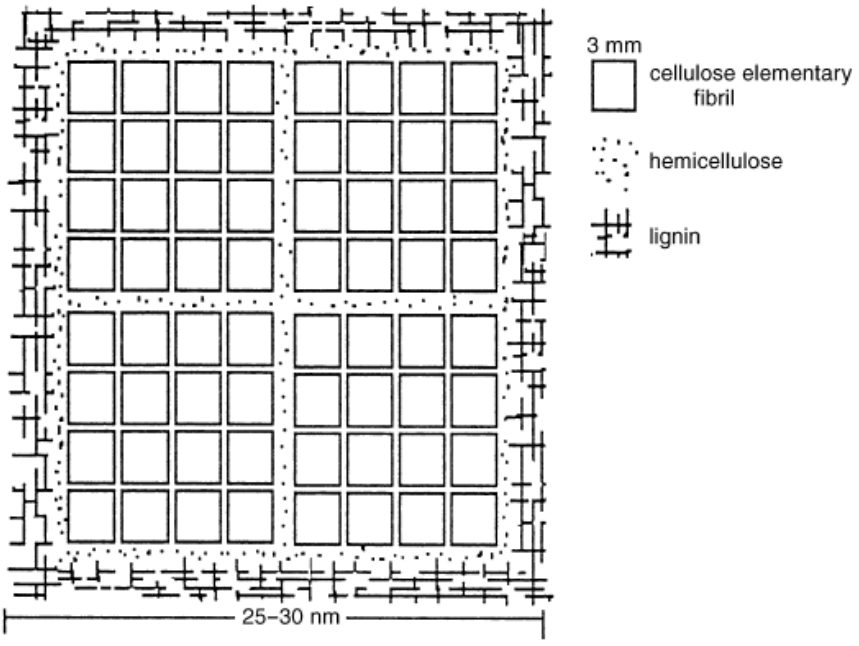

Figure 2-3. Schematic of cross-sectional view of the ultrastructural organization of the cell wall components in wood [2].

Each microfibril can be considered as a string of cellulose crystals, linked along the microfibril by amorphous domains and having a modulus close to that of the perfect crystal of native cellulose (estimated to be around 150GPa) and a strength that should be in the order of 10GPa.

2.1.3 Amorphous cellulose

Cellulose that lacks a degree of order is considered amorphous cellulose. Elementary fibrils are connected by amorphous cellulose. Amorphous cellulose are also located between cellulose microfibrils. The amount of amorphous cellulose depends on the species of cellulose source. For example, cellulose from cotton has high crystalline cellulose ratio and a small amount of amorphous cellulose. On the other hand, regenerated cellulose has higher amorphous cellulose ratio. High amorphous ratio in cellulose means high accessibility of chemicals to cellulose structure. The schematic of amorphous cellulose and crystalline cellulose is shown in Fig 2-4. Disordered red region represents amorphous cellulose and ordered blue region is crystalline cellulose.

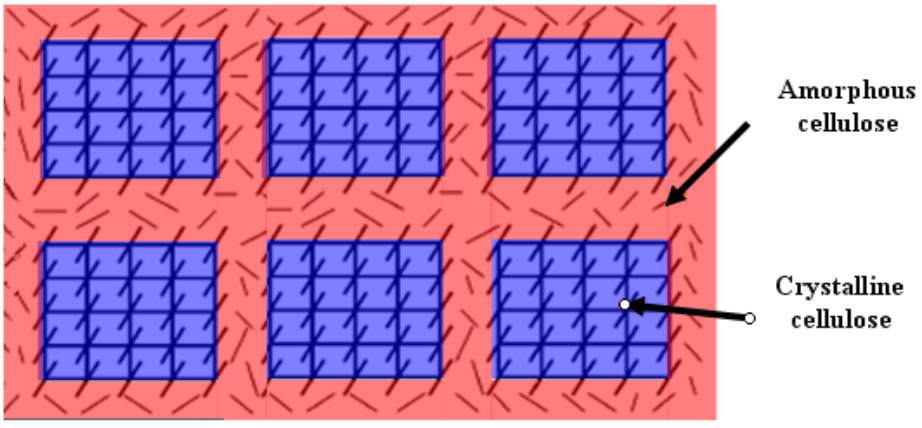

Figure 2-4. Schematic of amorphous cellulose and crystalline cellulose.

Compared to starch, cellulose is also much more crystalline. Whereas starch undergoes a crystalline to amorphous transition when heated beyond 60-70 °C in water (as in cooking), cellulose requires a temperature of 320 °C and pressure of 25 MPa to become amorphous in water

2.1.4 N-methylmorpholine-N-oxide (NMMO)

Cellulose is the most abundant natural polymer with outstanding properties. However, chemical processing of cellulose is difficult because cellulose is not meltable and not soluble in usual solvents due to its strong hydrogen bonds and partially crystalline structure. Therefore, more than 100 years, processing and manufacturing process of cellulose largely depends on the hazardous viscose technology. Viscose process is accompanied by serious environmental byproducts such as CS_2, H_2S and several heavy metals. After the first patent of N-methylmorpholine-N-oxide (NMMO) method at 1969 [3], lots of researches on N-methylmorpholine-N-oxide (NMMO) and cellulose system have been done [4-6]. Nowadays, NMMO process is popularly used to produce regenerated cellulose products such as Lyocell

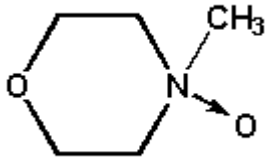

Figure 2-5. Formation and molecular structure of N-methylmorpholine-N-oxide [5].

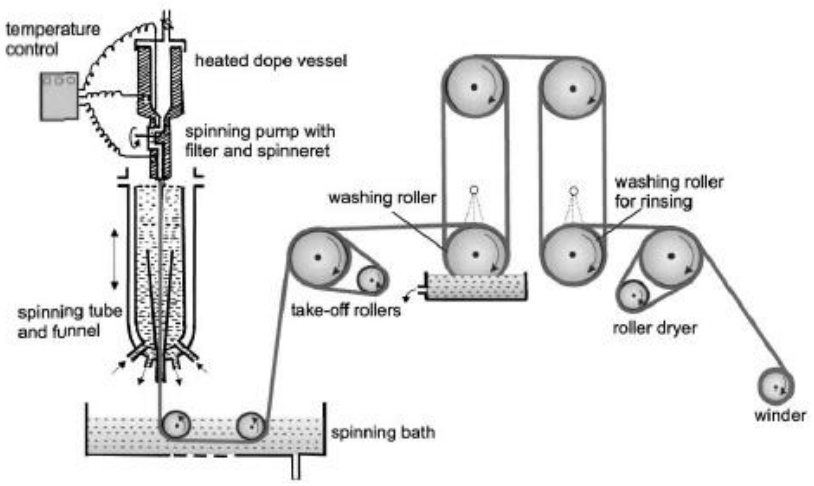

Figure 2-6. Scheme of Lyocell spinning process based on cellulose-NMMO method [5].

N-methylmorpholine-N-oxide (NMMO) has strong N-O dipoles which can substitute the hydrogen bonds between cellulose molecules during dissolving process. NMMO is produced by the oxidation of the ternary amine N-methylmorpholine with hydrogen peroxide. A molecular structure of NMMO is shown in Fig 2-5. The most outstanding advantage of NMMO as solvent is that it is environmentally friendly and 100% recyclable in comparison to the hazardous viscose techniques. Fig 2-6 is the scheme of the Lyocell spinning process based on cellulose-NMMO method [5].

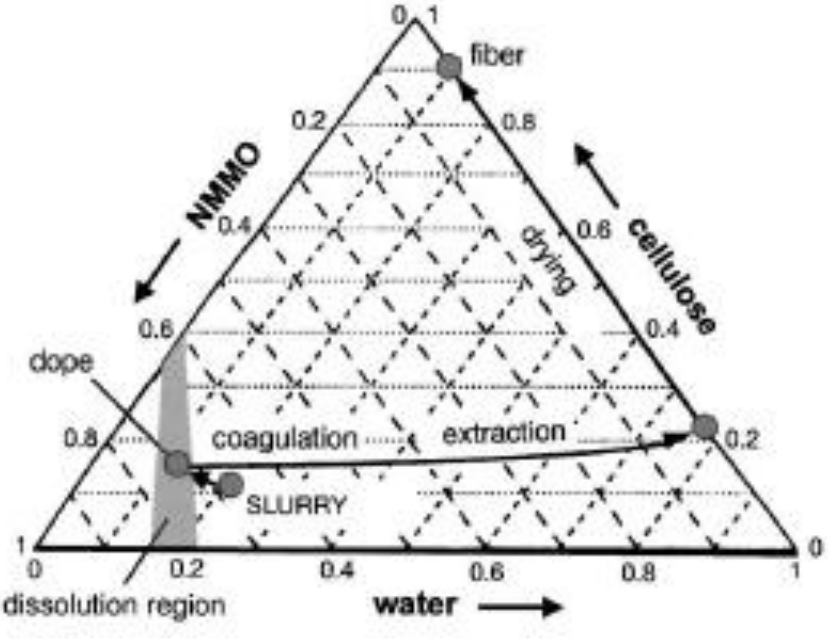

Figure 2-7. Phase diagram of cellulose-NMMO-water system [5].

2.1.5 Cellulose and N-methylmorpholine-N-oxide (NMMO) system

The melting point of the pure NMMO is at 170°C and hydration with one water molecule per NMMO molecule leads to the NMMO monohydrate with a melting point of 74°C which improve dissolution strength for cellulose. The solubility of cellulose in the binary NMMO/water system is shown in Fig 2-7. The phase diagram indicates that complete dissolving of cellulose happens only in the small region, highly concentrated NMMO. Dissolving process of cellulose in NMMO/water system starts after the water content is reduced to 13~15wt% through evaporation. If regenerated cellulose dissolution with NMMO/water is put in the large amount of water, a competing reaction happens between water molecules and NMMO molecules for cellulose molecules which prefer water. Therefore, NMMO is removed entirely and homogeneous regenerated cellulose which contains small amount of water can be obtained.

2.2 Cellulose nanowhiskers

2.2.1 Preparation of cellulose nanowhiskers

Cellulose nanowhiskers can be obtained by a careful acid hydrolysis with sulfuric acid [7]. The amorphous regions are the weaker part in cellulose microfibrils so sulfuric acid breaks the amorphous parts first. As shown in Fig 2-4, crystalline cellulose structures are surrounded by the amorphous cellulose. Therefore, cellulose nanowhiskers consist of high contents of cellulose crystalline domain and small amount of amorphous domain. The exact ratio of cellulose crystals and amorphous parts depends on the hydrolysis condition and the source of cellulose. Transmission electron microscope photos of cellulose nanowhiskers from different cellulose sources such as cotton, sugar-beet pulp and tunicin were shown in Fig 2-8.

Cellulose nanowhiskers are generally stiff rod-like particles. Their average diameter of cellulose nanowhiskers is between 5nm and 20nm and their length ranges from 150nm to 400nm. Geometrical characteristics of cellulose whiskers depend on the origin of cellulose microfibrils and acid hydrolysis process conditions such as time, temperature, and purity of materials. The effects of hydrolysis condition on the characteristics of cellulose nanowhiskers are summarized at Table 2-1 [7].

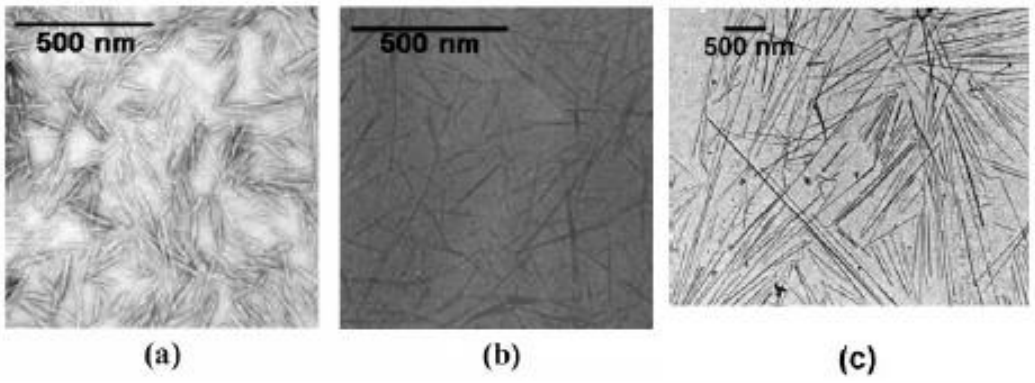

Figure 2-8. Transmission electron microscope photos of cellulose nanowhiskers from (a) cotton (b) sugar-beet pulp and (c) tunicin [8].

Table 2-1. Effect of hydrolysis time on the properties of cellulose nanowhiskers [7].

Sample	*Hydrolysis time* (min)	*Total sulfur content* (%)[a]	*Surface charge* (OSO_3^-)(S%)[b]	*Particle length* (nm)[c]	*Ordered phase*
6	10	0.53	0.30	390	–
7	20	0.50	0.33	332	+
8	30	0.58	0.50	276	+
9	45	0.62	0.64	226	+
10	60	0.69	0.68	197	+
11	120	0.74	0.68	179	+
12	240	0.75	0.62	177	+

As the hydrolysis time increased from 10 to 240mins, the total sulfur content and the surface charge of the cellulose nanowhiskers generally increased. The particle size of cellulose microcrystallites decreased from 390nm to 177nm. The relationship between hydrolysis time and average length of cellulose nanowhiskers was shown in Fig 2-9 [7].

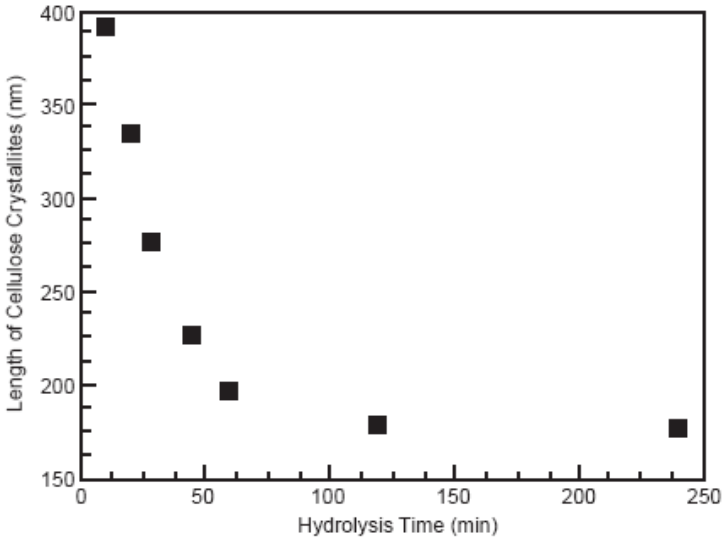

Figure 2-9. The relationship between hydrolysis time and the average length of cellulose nanowhiskers [7].

2.2.2. Orientation of cellulose nanowhiskers in aqueous solution

Cellulose crystalline has highly oriented structure. Even though the surface of cellulose nanowhiskers is slightly occupied by amorphous cellulose, the alignment and arrangement of amorphous cellulose are affected by the orientation of cellulose crystals inside of the cellulose nanowhiskers. Besides, the hydroxyl groups on cellulose surface enhance the interaction between cellulose nanowhiskers. In conclusion, due to the highly oriented cellulose crystalline structure and strong hydrogen bonds, cellulose nanowhiskers have a strong tendency to align side by side. As a result, the cellulose nanowhiskers aqueous suspension has a strong birefringence [9]. Fig 2-10 (a) shows a nematic phase of cellulose nanowhiskers in aqueous suspension [8].

In a dilute regime, the average distance between cellulose nanowhiskers and interaction force are not enough, therefore cellulose nanowhiskers suspension forms isotropic phase. However, above the critical concentration (4.9wt%), cellulose nanowhiskers suspension starts to form anisotropic phase and show birefringence [8]. Fig 2-11 shows the relationship between suspension concentration and the volume fraction of anisotropic phase. If the concentration of suspension is 5wt%, 50% of the cellulose nanowhisker particles exist as a nematic phase. Above 10wt%, 100% of cellulose nanowhiskers is the anisotropic condition [8]. Cellulose nanowhiskers thin film still maintains the chiral nematic order after evaporation of solvent such as water. Fig 2-10 (b) shows the image of cellulose nanowhiskers thin film through cross-polarizers.

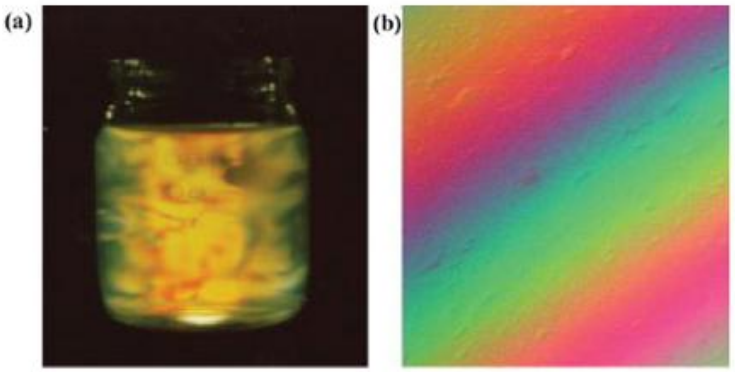

Figure 2-10. (a) A birefringence of cellulose nanowhiskers in aqueous suspension (b) an image of cellulose nanowhiskers thin film through a cross-polarizer [8].

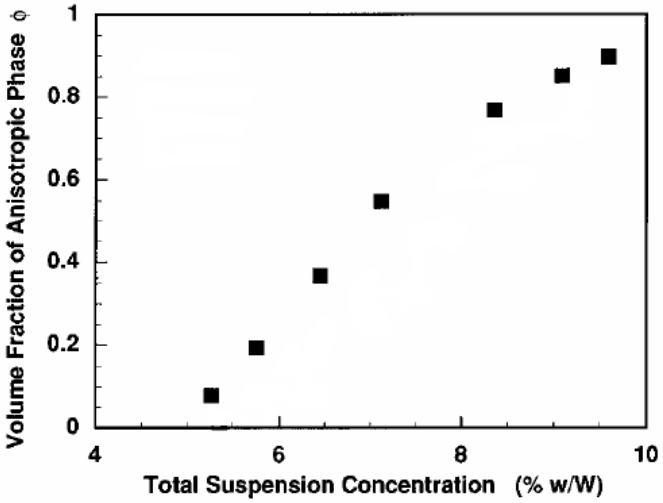

Figure 2-11. A relationship between suspension concentration and the volume fraction of anisotropic phase [8].

2.3 Cellulose microfibrils

Cellulose microfibrils are called as several different names such as cellulose nanofibrils, microfibrillated cellulose nanofibers and cellulose nanofibers. Cellulose microfibrils are the main components of plants and wood pulps. To obtain the cellulose

microfibrils, lignins and hemicelluloses should be removed. Several preparation methods have been reported using a mechanical processing [10-11], an enzyme treatment [12] and a grinder treatment [13]. The diameter and length of cellulose microfibrils are different according to the source materials. The diameter of microfibrils usually ranges from 10nm to 30nm and their length is between 1 μm and 30 μm [10-13]. Fig 2-12 is the AFM image of cellulose microfibrils prepared using an enzyme treatment and the SEM image of cellulose microfibrils obtained by a grinder treatment.

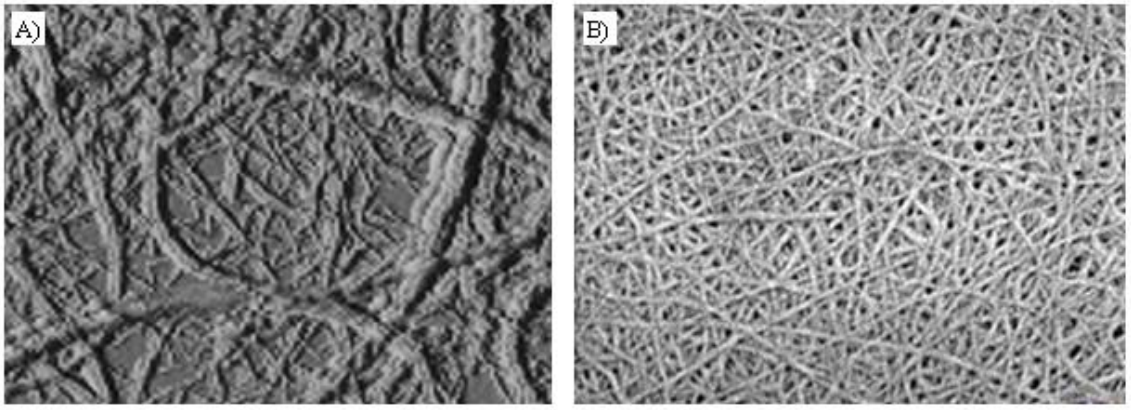

Figure 2-12 (a) AFM image of cellulose microfibrils prepared using an enzyme treatment [12] (b) SEM image of cellulose microfibrils obtained by a grinder treatment [13].

Cellulose microfibrils have been widely used as reinforcement materials in polymeric nanocomposites and porous foams. Cellulose microfibrils show environmental friendly characters and good mechanical properties. So far it was reported that cellulose microfibrils were used as reinforcement materials for the nanocomposites with various matrix materials such as polyurethane [14] and poly(lactic acid) [15]. Porous foams were prepared from cellulose microfibrils and amylopectin [16]. Recently, optically transparent paper [11] and highly touch nanopapers [17] prepared from pure cellulose microfibrils were reported. Cellulose microfibrils are also widely used for biomedical

applications such as wound coverage materials [18] and a scaffold for tissue engineering [19].

2.4 Cellulose nanowhisker reinforced nanocomposites

Cellulose nanowhiskers have been widely used as reinforcing materials for cellulosic nanocomposites after the first synthesis by Favier et al. [20]. It was reported that cellulose nanowhisker reinforced nanocomposites showed significantly improved mechanical properties for both of the natural and synthetic polymer matrix such as starch [21], cellulose acetate butyrate [22], poly(vinyl chloride) (PVC) [23] and poly(vinyl alcohol) (PVA) [24].

Cellulose nanowhiskers are stable in aqueous solution and dispersed well with most of the hydrosoluble polymers. It was also reported that surface modified cellulose nanowhiskers are mixed well with organic solvents. Due to the highly reactive hydroxyl groups on cellulose nanowhiskers, their surfaces can be easily modified with a surfactant [25], chemicals [26-27] and cross-linking agent [28].

2.4.1. Mechanical properties of cellulose nanowhiskers reinforced nanocomposites

In the past 10 years, a great interest was focused on the improvement of mechanical properties of cellulose nanowhisker reinforced nanocomposites. The reinforcement effect attributes to several factors such as a modulus of cellulose nanowhiskers, an aspect ratio of cellulose nanowhiskers and a whisker/whisker interaction**.** It was reported that the modulus of the crystalline region of cellulose is 137GPa measured by X-ray diffraction [29], 143GPa measured by Raman spectroscopic technique [30], 149GPa ~ 155GPa calculated by computational simulation [31]. The modulus of a single cellulose microfibril was measured directly using atomic force microscope (AFM) 3-point bend test and was evaluated to be 93GPa [32]. It is very

difficult to measure the mechanical properties of cellulose nanowhiskers directly. The diameter and the length of cellulose nanowhiskers are nano-size and much smaller than those of cellulose microfibrils, therefore isolating, gripping and holding a single cellulose nanowhisker is not technically feasible. Therefore the modulus of a single cellulose nanowhisker should be assumed based on the modulus of the crystalline cellulose and cellulose microfibrils. It looks reasonable the modulus of cellulose nanowhiskers is between that of crystalline cellulose (137GPa ~ 155GPa) and that of cellulose microfibrils (~93GPa) because the ratio of crystalline domain in cellulose nanowhiskers is between crystalline cellulose and cellulose microfibrils. The density of crystalline cellulose is relatively low compared with other inorganic materials. The modulus of engineering materials and cellulose crystalline is summarized at Table 2-2.

Table 2-2. Modulus of engineering materials and crystalline cellulose [37].

Materials	Modulus (GPa)	Density (Mg/m3)	Spedific modulus (Gpa.m3/Mg)
Aluminium	69	2.7	26
Steel	200	7.8	26
Glass	69	2.5	28
Crystalline cellulose	138	1.5	92

It is well known that fillers with a high aspect ratio can enhance the mechanical properties of nanocomposites. The aspect ratio of cellulose nanowhiskers is varied according to the source of cellulose and preparation conditions [33]. The average aspect ratios of cellulose nanowhiskers prepared from tunicin, bacterial and Avicel are 67, 60 and 10, respectively [34]. Celluloses nanowhiskers show a strong whisker/whisker

interaction due to the strong hydrogen bonds. The network structure of cellulose nanowhiskers increases the elastic modulus of nanocomposites, especially above the T_g [35-36].

2.4.2. Model studies

Halpin-Tsai model

Halpin-Tsai equation is the most widely used model for the analysis of mechanical properties of nanocomposites [38-40]. Model equation is given by,

$$\frac{E}{E_m} = \frac{1+\zeta\eta\phi_f}{1-\eta\phi_f} \tag{2.1}$$

Where E is modulus of composite, E_m is modulus of matrix, E_f is modulus of filler, ζ is shape factor and Φ is volume fraction and η is given by,

$$\eta = \frac{E_f / E_m - 1}{E_f / E_m + \zeta} \tag{2.2}$$

Shape factor ζ is defined as the geometry of filler materials. Various geometries of fillers and their shape factors are summarized at Table 2-3.

Table 2-3. Various geometries of fillers and their shape factors.

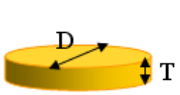


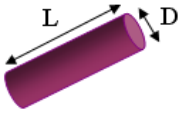

Geometry of fillers	Disk	Sphere	Tube	
			longitudinal	transverse
Shape factor	$2\frac{diameter\,(D)}{thickness\,(T)}$	2	$2\frac{length\,(L)}{diameter\,(D)}$	2

The modulus of cellulose nanowhiskers reinforced nanocomposites can be expressed using tube geometry shape factor. When cellulose nanowhiskers are aligned parallel to tensile test direction, longitudinal shape factor can be applied to the model. On the other hand, transverse shape factor can be used if cellulose nanowhiskers are aligned vertical to the tensile test direction. If the alignment of cellulose nanowhiskers in matrix is isotropic, the modulus of nanocomposites is expressed as the fractional summation of E_L and E_T.

$$E = \frac{3}{8}E_L + \frac{5}{8}E_T \tag{2.3}$$

where E_L is the longitudinal modulus and E_T is the transverse modulus.

Percolation model

When the loading ratio of fillers increases, the interaction between fillers should be considered in mechanical properties of nanocomposites. Cellulose nanowhiskers show relatively large interactions between particles because of the high aspect ratio of the

particles and strong hydrogen bonds. Percolation theory considers various parameters such as particle-particle interactions, orientation of particles and aspect ratio. In percolation approach, the elastic modulus E_C of the composites is given by

$$E_C = \frac{(1-2\varphi+\varphi v_R)E_S E_R + (1-v_R)\varphi E_R^{\,2}}{(1-v_R)E_R + (v_R-\varphi)E_S} \tag{2.4}$$

where subscripts S and R refer to the soft phase (polymeric matrix) and rigid phase (cellulose nanowhiskers). v and E are the volume ratio and elastic modulus of given phases. φ and v_{Rc} defined as

$$\begin{aligned} &\varphi = 0 && for\ v_R < v_{Rc} \\ &\varphi = v_R\left(\frac{v_R - v_{Rc}}{1-v_{Rc}}\right)^b && for\ v_R > v_{Rc} \\ &v_{Rc} = \frac{0.7}{L/d} \end{aligned} \tag{2.5}$$

where b = 0.4 for a 3D network. v_{Rc} is the percolation threshold which means the lowest volume ratio of cellulose nanowhiskers that can be considered as a percolating phase. It was found that percolation theory agrees well with experimental data above $T_g + 50^\circ C$ [41-42]. Fig 2-13 is the logarithm plot of the relative tensile modulus of various cellulose nanowhiskers nanocomposites measured at $T_g + 50^\circ C$. Black and white circles are experimental data. A dotted line is the percolation model value and a solid line is Halpin-Tsai model prediction [34].

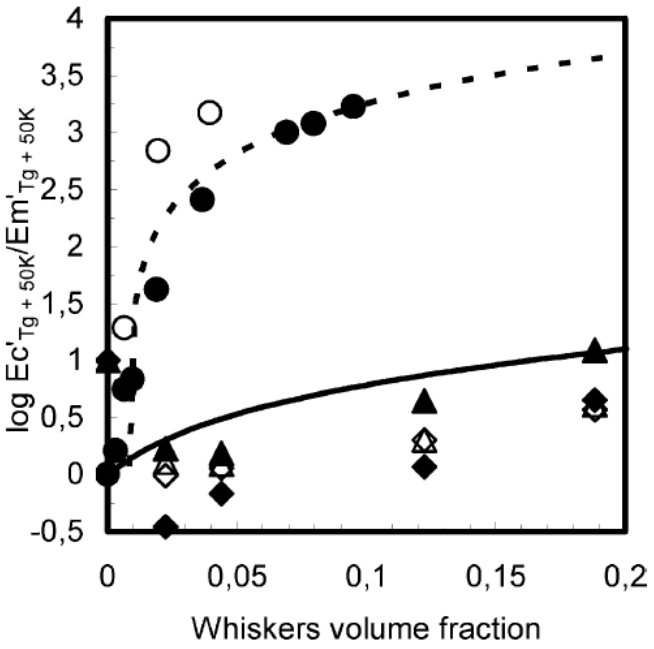

Figure 2-13. Logarithm of the relative tensile modulus of various cellulose nanowhiskers nanocomposites measured at $T_g + 50^{\circ}C$ [34].

2.5 Polymer/layered silicate (PLS) nanocomposites

At chapter 3, one of the layered silicates (montmorillonite) is used as filler materials for regenerated cellulose nanocomposites. Therefore, the background about layered silicates and polymer/layered silicate (PLS) nanocomposites is reviewed in this section.

Nanocomposites refer to polymers mixture filled with small inorganic particles. Polymer/layered silicate (PLS) nanocomposites have attracted great interest both in industry and in academia because they showed remarkable improvement in their properties due to the high aspect ratio of layered silicate. The improvements of modulus [43], heat resistance [44], flammability [45], biodegradability [46] and decreased gas permeability [47] have been reported. The commonly used layered silicates for the PLS nanocomposites were made up of two tetrahedrally coordinated silicon atoms fused to an edge-shared octahedral sheet of either aluminum or magnesium hydroxide.

2.5.1 Structure and properties of layered silicates

The commonly used layered silicates for the preparation of PLS nanocomposites is the groups of 2:1 layered or phyllosilicates. Their basic structure consists of two layers of tetrahedral structure coordinated with silicon atoms and octahedral sheet between them. Either aluminum or magnesium hydroxide is located inside the structure The layer thickness is around 1 nm, and the lateral dimensions of these layers may vary from 30 nm to several microns or larger, depending on the particular layered silicate. Typical particle length of commonly used layered silicate is 50~60nm (Saponite), 100~200nm (Montmorillonite) or 200~300nm (Hectorite). The structure of these layered silicates is shown in the Fig 2-14.

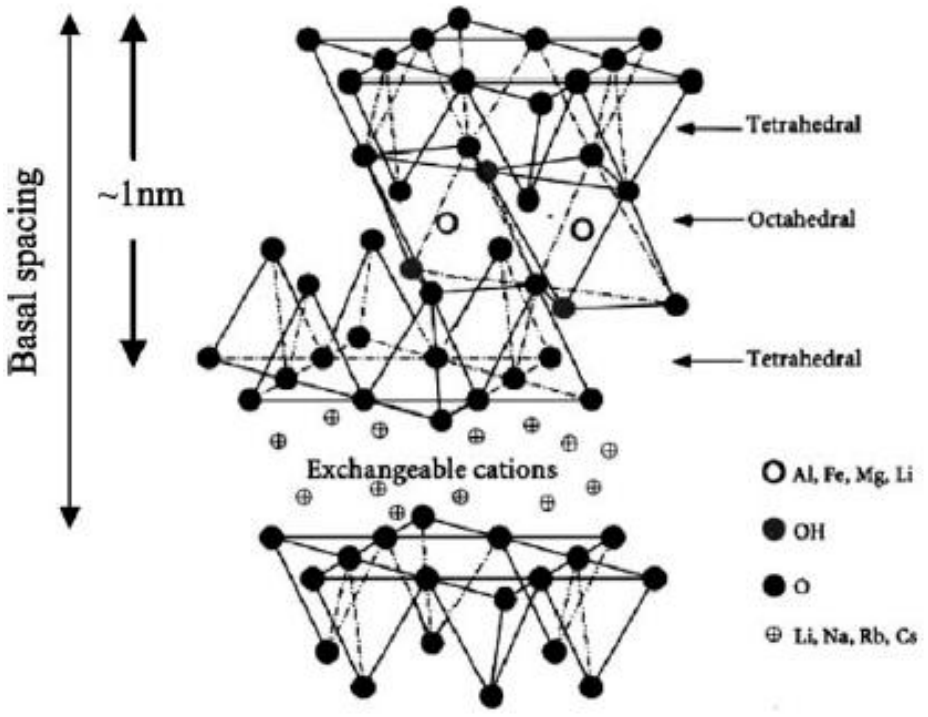

Figure 2-14. General structure of layered silicate [48].

Between the layers, Exchangeable cations exist. The cation exchange capacity (CEC) is the unique and important characteristic of layered silicates. When ion exchange happens, the cations exchange their sites with another organic or inorganic cations. In the pristine state, layered silicate is only miscible with hydrophilic polymers such as poly(ethylene oxide)(PEO) or poly(vinyl alcohol)(PVA). Organically modified layered silicate (OMLS) can be obtained through ion-exchange reactions with cationic surfactants. OMLS is miscible with many organophilic engineering polymers. The chemical formula and characteristics of commonly used layered silicates are summarized in Table 2-4.

Table 2-4. The chemical formula and characteristics of commonly used layered silicates [49].

2:1 phyllosilicates	Chemical formula	CEC (mequiv/100 g)	Particle length (nm)
Montmorillonite	$Mx(Al_{4-x}Mg_x)Si_8O_{20}(OH)_4$	110	100–150
Hectorite	$Mx(Mg_{6-x}Li_x)Si_8O_{20}(OH)_4$	120	200–300
Saponite	$MxMg_6(Si_{8-x}Al_x)Si_8O_{20}(OH)_4$	86.6	50–60

2.5.2 Organically modified layered silicate (OMLS)

To prevent the phase separation between pristine layered silicate and organophilic polymers and promote the good dispersion of layered silicates in polymer matrix, originally hydrophilic silicate surfaces must be converted to organophilic surfaces.

Normally, pristine cations (Na^+ or K^+) were exchanged with cationic surfactants including primary, secondary, tertiary, and quaternary alkylammonium or alkylphosphonium cations by ion-exchange reactions. The size of cationic surfactants is larger than Na^+ or K^+ ions, resulting in a larger interlayer spacing. Sometimes, several cationic surfactants have the functional groups which make or initiate the reactions with the polymer matrix.

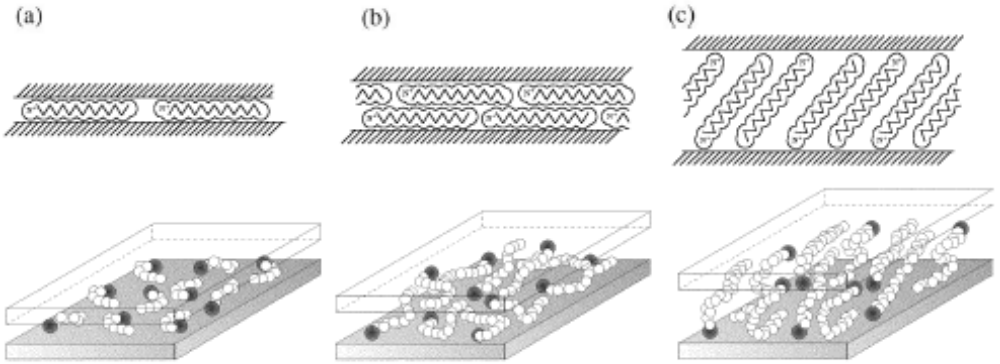

Figure 2-15 (a) schematic of pristine layered silicate (b) schematic of OMLS and primary alkylammonium cationic surfactant at low temperature (c) schematic of OMLS and tertiary alkylammonium cationic surfactant at high temperature [48].

Table 2-5. Properties of commercial MMT products [38].

Sample	2θ (°)	*d*-spacing (Å)	Organic modifier	Modifier concentration meq/100g clay
MMT Na^+	7.66	11.5	N/A	N/A
MMT 10A	4.58	19.2	Dimethyl benzyl dehydrogenated tallow quaternary ammonium	125
MMT 30B	4.77	18.5	Methyl tallow bis-2-hydroxyethyl quaternary ammonium	90
MMT 25A	4.75	18.6	Dimethyl dehydrogenated tallow 2-ethylhexyl quaternary ammonium	95
MMT 93A	3.74	23.6	Methyl dehydrogenated tallow ammonium	90
MMT 20A	3.67	24.2	Dimethyl dehydrogenated tallow quaternary ammonium	95
MMT 15A	2.80	31.5	Dimethyl dehydrogenated tallow quaternary ammonium	125

Usually, the characterization of interlayer distance change is done using wide angle X-ray diffraction (WXRD). The schematics of pristine layered silicate and organically modified layered silicate (OMLS) were shown in Fig 2-15. The detailed structure of layered silicates and interlayer distance are affected by several factors such as the species of cationic surfactants, packing density of surfactants between layers, the length of alkyl

chain of surfactants and temperature.

Montmorillonite (MMT) is one of the most widely used layered silicates. According to the species of organic surfactants, MMT can be classified with MMT Na+, MMT 10A, MMT 30B and so on. Wide angle X-ray diffraction (WXRD) results (2θ), interlayer distance (d-spacing), the species of organic modifiers and modifier concentration of commercial MMT products were summarized in Table 2-5.

2.5.3 Structure of Polymer/layered silicate (PLS) nanocomposites

When the layered silicate are mixed and dispersed in polymer matrix, the insertion of polymer matrix into the layers happens. Depending on the degree of polymer insertion, the strength of interfacial interactions between the polymer matrix and layered silicate and the change of the interlayer distance, three different types of PLS nanocomposites are obtained. When the insertion of a polymer matrix into the layered silicate structure occurs, it is called as intercalated structure. In this case, the interlayer distance changes but maintained regular after intercalation. The exfoliated nanocomposite is one that the individual clay layers are separated in a continuous polymer matrix. The average distance between each clay layer depends on clay loading. The clay content of an exfoliated nanocomposite is usually lower than that of an intercalated nanocomposite. If the insertion of polymer matrix doesn't happen and layered silicates forms aggregates, it is called as phase separation. Schematic illustration and their TEM images are shown in Fig 2-16 and Fig 2-17. The structure change of layered silicate after forming nanocomposites can be confirmed using wide angle X-ray diffraction (WXRD). For intercalated nanocomposites, d-spacing peak shifts to smaller angle. On the other hand, d-spacing peak in WXRD disappears after exfoliation.

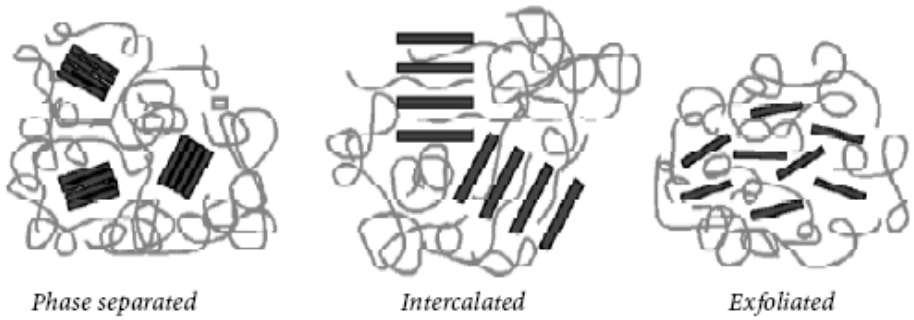

Figure 2-16. Schematic illustration of three different types of PLS nanocomposites [48].

2.5.4 Preparation methods of Polymer/layered silicate (PLS) nanocomposites

The preparation methods of PLS nanocomposites are classified into three main groups. The first method is intercalation of polymer or pre-polymer from solution, based on a solvent system where polymer is soluble and the layered silicates are swellable. During the dissolving process, dissolved polymer chains intercalate into the layers and exchange the location with the solvent within the interlayer. After removing the solvent, PLS nanocomposites can be obtained. In situ intercalative polymerization is the second method. In this method, monomer penetrates between the layers and then polymerization occurs by heat or radiation. Sometimes, a catalyst fixed on the surface of each layer can be used for the initiator of the polymerization reaction. In melt intercalation method, layered silicates and polymer are mixed above the softening point of the polymer without solvent. Third method is environmentally benign due to the absence of organic solvents and it is applicable to the current industrial process such as extrusion and injection molding. However, uniform dispersing of nanoclay in the polymer matrix is a common problem in melting method.

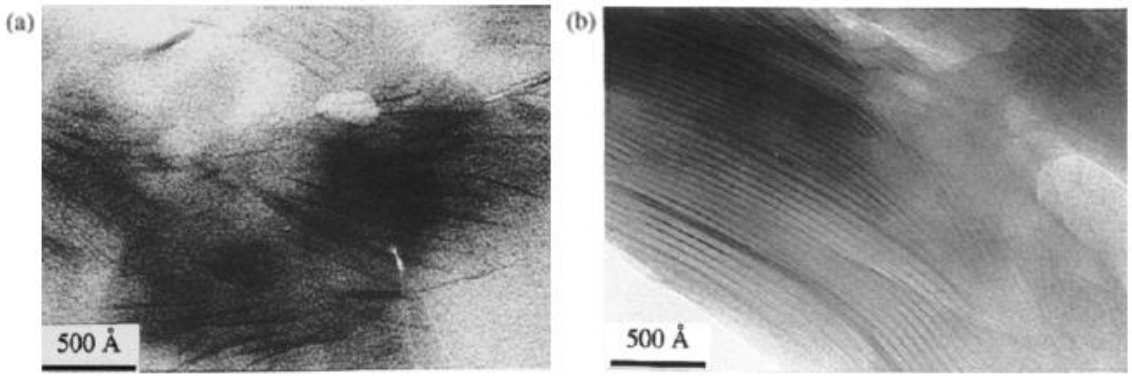

Figure 2-17. (a) TEM image of intercalated nanocomposites (b) TEM image of exfoliated TEM image [49].

2.6 Electrospinning

Electrospinning is the most efficient technique for the fabrication of polymer nanofibers. Various polymers have been successfully used to fabricate nanofiber via electrospinning method in recent years. Electrospinning is a very versatile method. Most of polymers can be electrospun in solvent solution or in melt form. Potential applications of electrospun fibers are also various. Application fields targeted by US patents on electrospun fibers were summarized at Fig 2-18 [50].

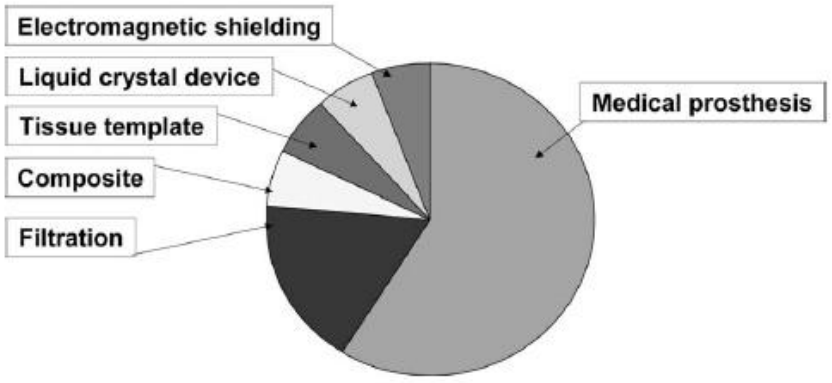

Figure 2-18. The number of US patents related to electrospun nanofibers [50].

Electrospun fibers or electrospun fiber membrane have unique properties. First of all, the size of electrospun fiber is very small. They show a high modulus and tensile strength compared to the light weight. Electrospun fiber membranes also have a very large surface area. Electrospun fibers membrane can be used as skin therapy materials. They can be also fabricated as liquid or gas filters. Tissue engineering scaffolds are possible applications of electrospun fibers. They can be fabricated as porous membranes, blood vessels and cell culture scaffolds. Nano-sensor is the possible application of electrospun fibers due to the large surface area. The potential applications of electrospun fibers were summarized at Fig 2-19 [50].

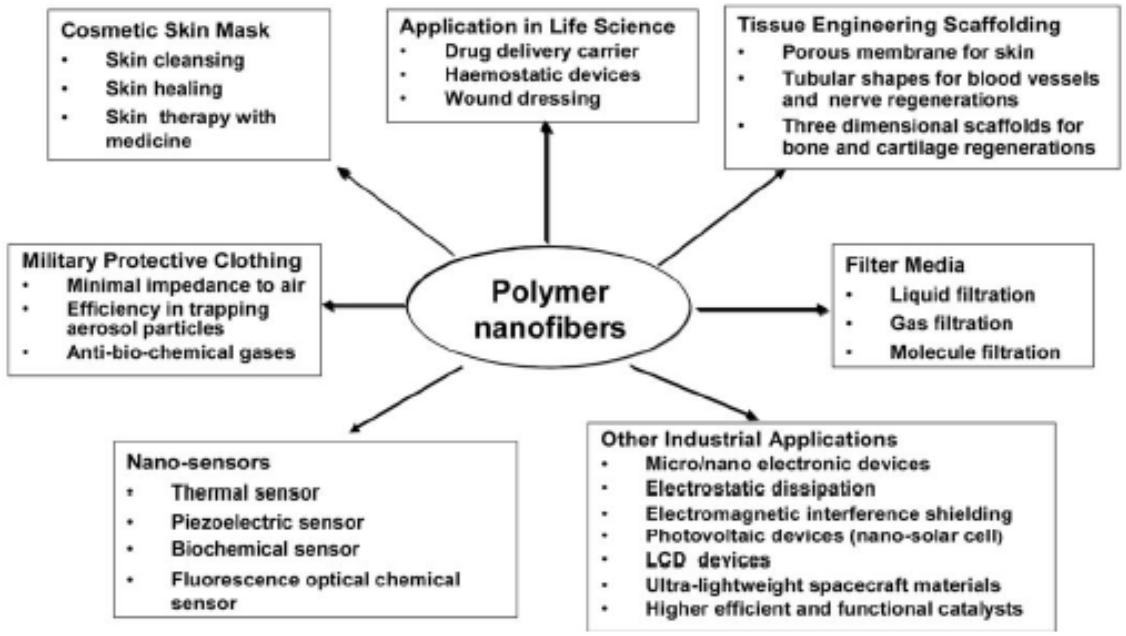

Figure 2-19. Potential applications of electrospun fibers [50].

2.6.1 Process of electrospinning

The schematic of a typical electrospinning apparatus is shown in Fig 2-20. The basic units are a high voltage supply, a syringe filled with polymer solution and a metal

collector. One electrode (positive or negative) is immersed into the polymer solution. The metal collector is normally grounded. When High voltage is applied to the polymer solution, a charge is induced on the surface of liquid solution. As the intensity of collected charge increases, elongated polymer surface forms hemispherical shape which is known as Taylor cone (Fig 2-20 (b))[51]. Further increasing of the electric field makes repulsive electrostatic force of charged surface overcome the surface tension. Therefore, charged polymer jet is ejected from the end of the Taylor cone and flies to the metal collector. During the flight, the solvent evaporates and solidified electrospun fibers are collected. The discharged polymer jet undergoes high shear force, therefore the polymer jet and electrospun fiber become very long and thin.

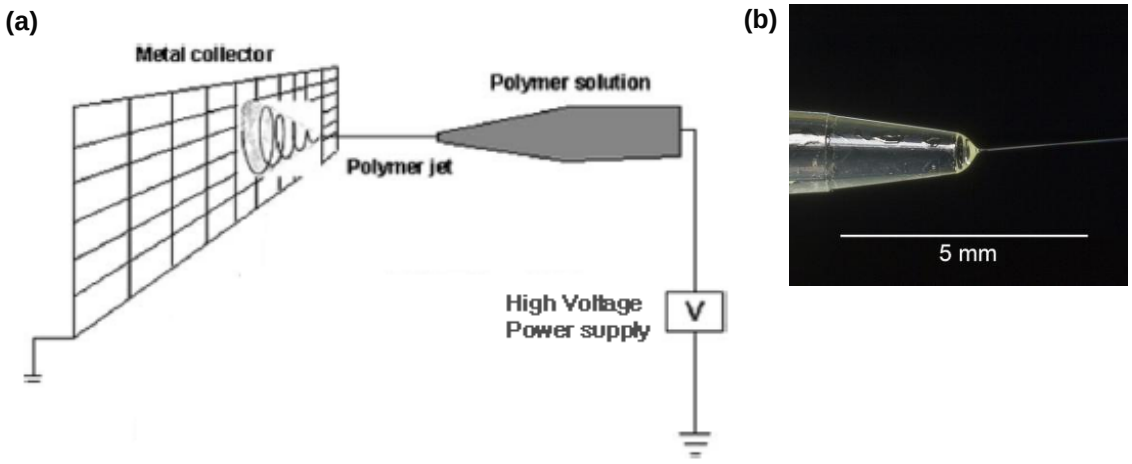

Figure 2-20. (a) The schematic of a typical electrospinning apparatus (b) Photograph of electrospun jet from Taylor cone [51].

2.6.2 Parameters in electrospinning

Electrospinning is affected by several factors such as (a) the solution properties (viscosity, elasticity, conductivity, and surface tension), (b) apparatus parameters (applied

voltage, the distance between the tip and the metal collector, and the size of the capillary tip), and (c) ambient parameters (solution temperature and humidity)

The fiber diameter is affected by the viscosity of polymer solution. It was reported that a higher viscosity results in a larger fiber diameter [52]. The viscosity of polymer solution is proportional to the polymer concentration. Therefore the higher concentration of polymer solution makes the fiber diameter larger. Applied voltage is also important parameter to the morphology of electrospun fibers. In general, a higher voltage induces larger amount of polymer eject from Taylor cone resulting in the larger diameter of electrospun fibers [53]. Polymer beads are easily observed in electrospun fibers. Higher polymer concentration solution and higher viscosity of polymer solution makes fewer beads. On the other hand, for the lower concentration polymer solution, lots of polymer beads are found as shown in Fig 2-21 [54]. It is also reported that salt added polymer solution results in bead-free electrospun fibers due to higher electric charge on polymer jet [55].

Figure 2-21. SEM images of electrospun fibers from different concentration polymer solution [54].

2.6.3 Alignment of electrospun fibers

Basically, most of electrospun fibers are obtained as isotropic non-woven from. If it is possible to control the arrangement and alignment of electrospun fibers, their possible applications can be expanded. However, it is very difficult to control the fabrication of electrospun fibers because the size of fibers is very small and polymer jet trajectory is very complicated. So far, a few techniques have been developed to get the aligned electrospun fibers.

A rotating cylinder collector

It was reported that highly aligned electrospun fibers can be fabricated using a rotating cylinder collector at a very high speed [56]. A schematic of the apparatus and SEM images are shown in Fig 2-22.

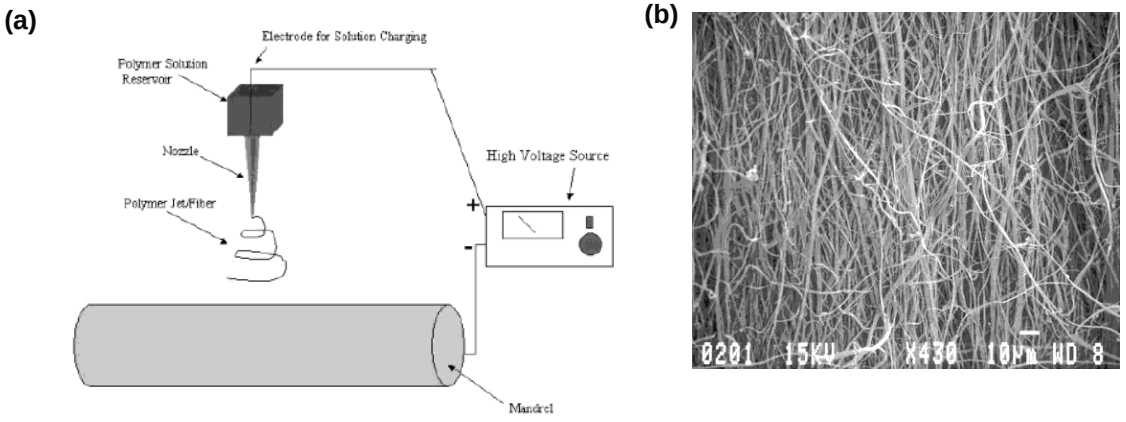

Figure 2-22 (a) A scheme of the rotating cylinder collector and electrospinning apparatus (b) SEM image of aligned electrospun collagen fibers [56].

The mechanism of electrospun fiber alignment via rotating cylinder has not been

very clear yet. A reasonable explanation is given as follows. When the end of fiber is attached on the cylinder surface and a linear speed of the rotating cylinder surface is same with the flying speed of polymer jet, the fibers are taken up on the rotating surface of the cylinder tightly resulting in the alignment of electrospun fibers. Such a speed can be called as an alignment speed. If the surface speed of the cylinder is slower than the alignment speed, randomly deposited fibers will be collected. On the other hand, too high rotating speed will break the fiber jet resulting in no fiber collection [50]. Therefore, the rotating speed of metal cylinder should be selected very carefully.

A thin wheel with sharp edge

A highly aligned electrospun fiber has been obtained using a thin wheel collector with sharp edge as shown in Fig 2-23 [57].

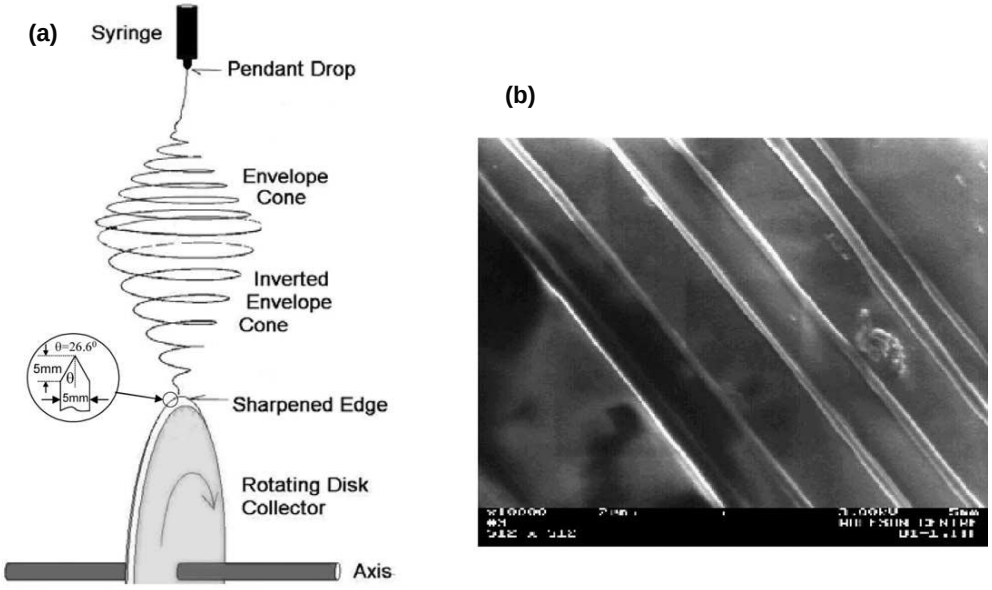

Figure 2-23 (a) A scheme of thin wheel electrospinning equipment (b) SEM image of aligned PEO electrospun fibers [57].

Before reaching the electrically grounded target, electrospun fibers retain sufficient residual charges to repel each other. As a result, once a nanofiber is attached to the wheel tip, it will exert a repulsive force on the next fiber attracted to the tip. This repulsion from one another results in a separation between the deposited nanofibers [50]. This technique is very sensitive to the rotating speed. Therefore, it is not possible to retain high alignment of fibers when the deposited fibers are thicker. It is also difficult to fabricate large area aligned membrane using this apparatus.

A parallel electrodes collector

A new collector consisting of two pieces of parallel electrodes separated by a gap whose width could be varied from hundreds micrometers to several centimeters (Fig 2-24) was introduced [58].

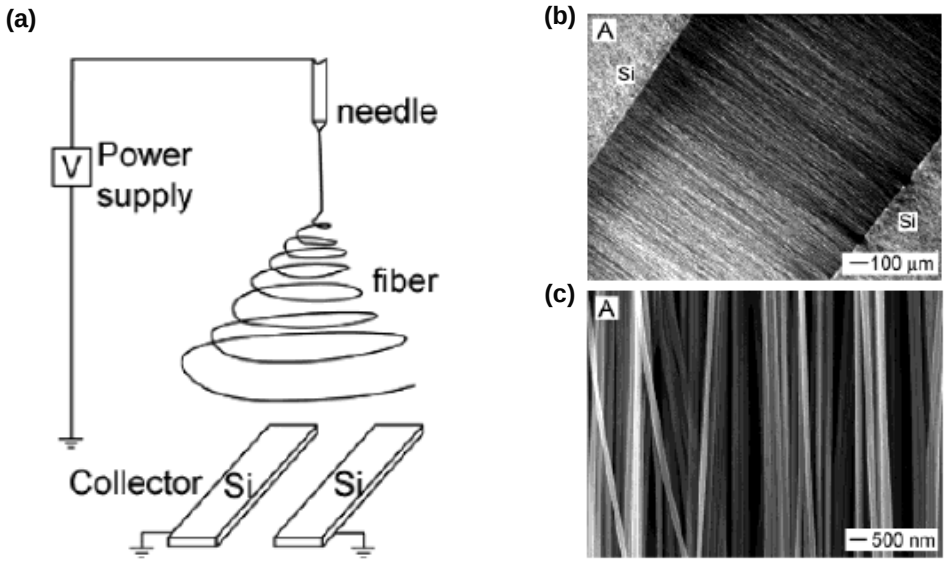

Figure 2-24 (a) A scheme of parallel electrode electrospinning equipment (b) SEM image of aligned PVP electrospun fibers (c) Higher resolution SEM image of aligned carbon electrospun fibers [58].

Using this technique, highly aligned fibers are easily obtained compared to other methods. Moreover aligned fibers are located between electrodes, not on the substrate, therefore it is easy to separate and transfer the aligned fibers. However the gap between two electrodes should be smaller than few centimeters and there is a limitation in the length of aligned fibers.

A rotating wire drum collector

A rotating wire drum collector combined the advantages of a rotating cylinder collector and a parallel electrode collector. The basic concept is similar with a rotating cylinder collector but separated wires enhance the alignment of electrospun fibers. Collected electrospun fibers are highly aligned and relatively long compared with a parallel electrodes collector. A scheme of the apparatus and SEM images are shown in Fig 2-25 [59].

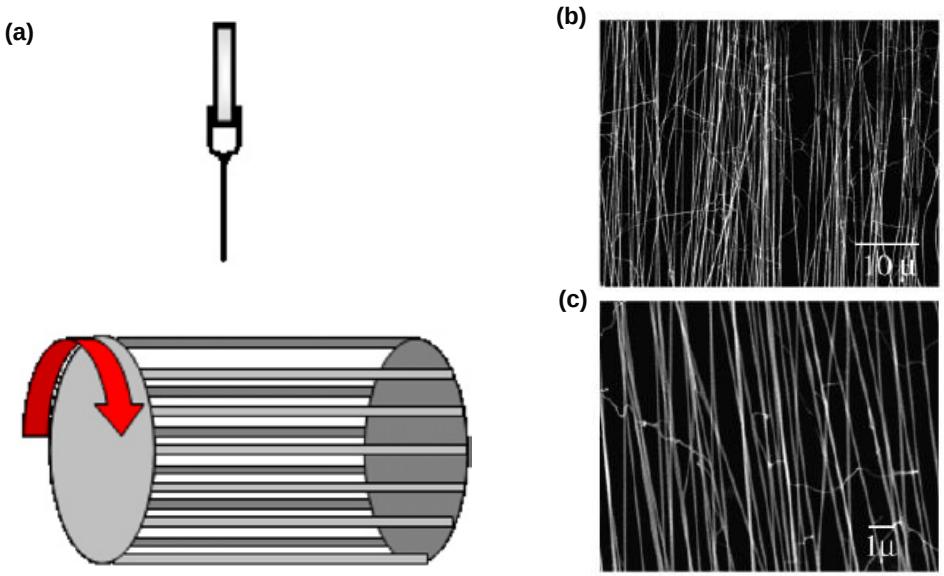

Figure 2-25 (a) A scheme of the rotating wire drum collector electrospinning equipment (b) SEM image of aligned nylon-6 electrospun fibers (c) Higher resolution SEM image of aligned nylon-6 electrospun fibers [59].

2.7 Nanoindentation

2.7.1 Nano tensile test

Atomic force microscope (AFM) cantilevers have been used for tensile tests of electrospun polyethylene oxide (PEO) nanofibers. Aligned electrospun fibers were deposited on two parallel electrodes. The nanofiber was stretched by AFM tip and the force was measured via the deflection of the cantilever. A schematic of the tensile test using AFM tip was shown in Fig 2-26 [60].

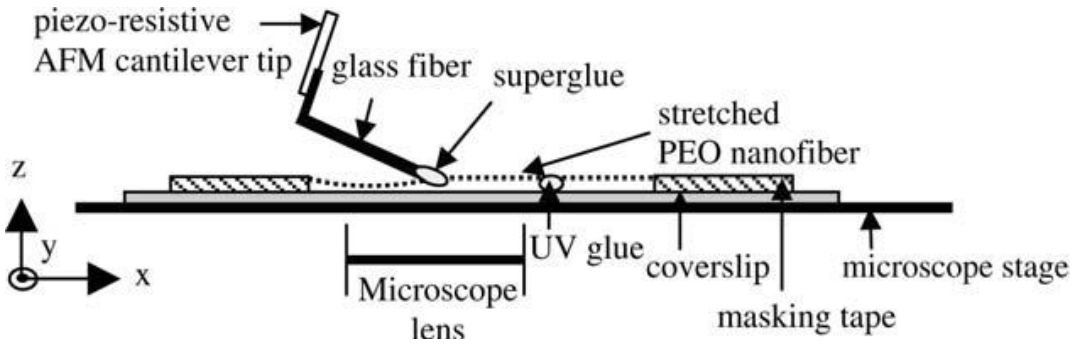

Figure 2-26. Schematic of the nano tensile test of PEO electrospun fiber using a piezo-resistive AFM tip [60].

Nano tensile test method also has been used to measure the mechanical properties of CNT [61]. Both ends of CNT were attached to the AFM cantilevers using electron beam. A soft cantilever was used as the force transducer and a stiff cantilever was used as the rigid link from the nanotube to the actuator. This attachment technique cannot be used for polymer fibers because of the damage by the electron beam. The schematic and SEM images of AFM cantilevers with CNT are shown in Fig 2-27.

The AFM cantilever methods for tensile test are useful to measuring the

mechanical properties of nanofibers ranging from tens of nanometers to several hundred nanometers in diameter. However, this method is very time consuming and it is difficult to manipulate, control and test the single nanofiber.

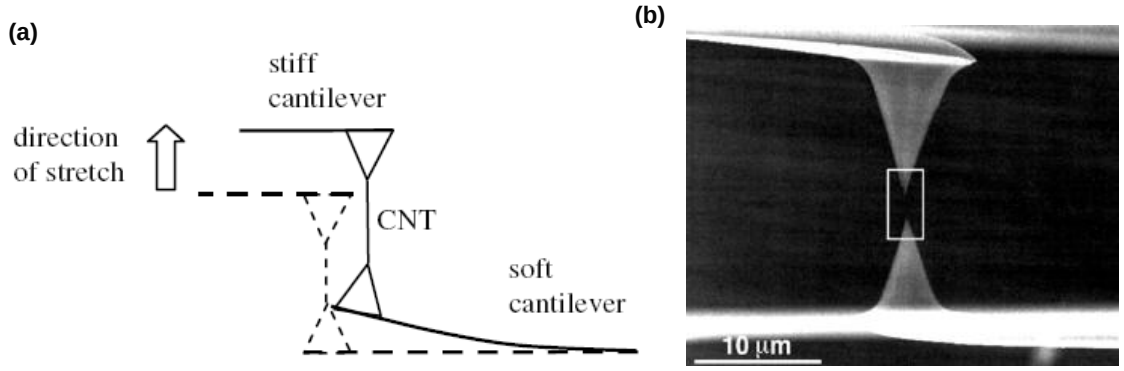

Figure 2-27 (a) The schematic of CNT attached AFM cantilevers (b) SEM image of CNT attached AFM cantilevers [61].

2.7.2 Nanoscale three-point bend test

The nanofiber is deposited on the substrate with holes or grooves. Silicon and silicon dioxide nanobeams have been fabricated using AFM anodization to carry out three-point

bend test with both ends fixed [62]. This method is only limited to samples that can be fabricated using AFM anodization. AFM image of the sample and schematic of nanoscale three-point bend test were shown in Fig 2-28 [63].

The modulus can be found from beam bending theory [64]. The modulus for the beam with two ends fixed is given by

$$E = \frac{P_{\max} l^3}{192 v I} \tag{2.6}$$

Where P_{max} is the maximum force applied, L is the suspended length, v is the deflection of the beam and I is the second moment of area of the beam.

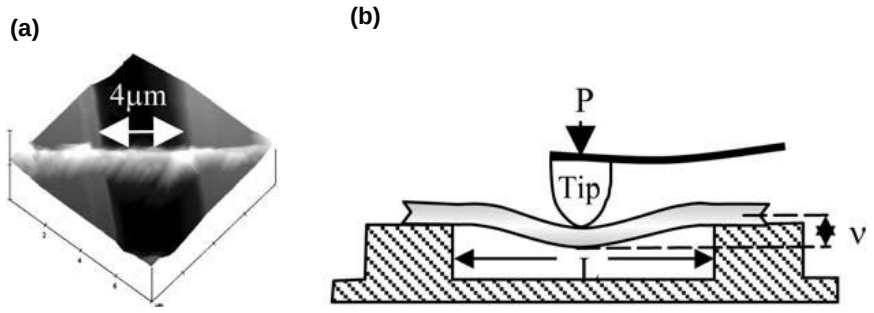

Figure 2-28 (a) AFM contact mode image of a single nanofiber suspended over an etched groove (b) Schematic of nanoscale three-point bend test [63].

2.7.3 Nanoindentation

Of all the nanomechanical characterization techniques mentioned, nanoindentation is perhaps the most convenient to perform as the sample can be prepared for testing by simply depositing the nanorods, nanowires and nanofibers on a hard and flat substrate, with sufficient adhesion between the substrate and the nanomaterials [62]. The schematic of nanoindenter [65] and AFM image of indented sample [66] were shown in Fig 2-29.

The elastic modulus is obtained form the slope of the initial slope of unloading curve (S). The relationship between the initial slope S and modulus of the sample was first formulated by Oliver and Pharr [67]. The unloading stiffness, S is given by

$$S = \frac{dP}{dh} \tag{2.7}$$

where P is the load and h is the contact depth of the tip. The reduced elastic modulus, E_r, is expressed as

$$\frac{1}{E_r} = \frac{(1-v_m^2)}{E_m} + \frac{(1-v_i^2)}{E_i} \tag{2.8}$$

where E_m and E_i are the elastic modulus of the sample and the indenter tip respectively. v_m and v_i is the Poisson's ratio of the sample and the tip. The relationship between S and E_r is represented by

$$S = 2aE_r = 2\beta\sqrt{\frac{A}{\pi}}E_r \tag{2.9}$$

where β is a constant that depends on the geometry of the indenter tip, A is the projected area of the indenter. The key issues and problems of nanoindentation are summarized in Table 2-6.

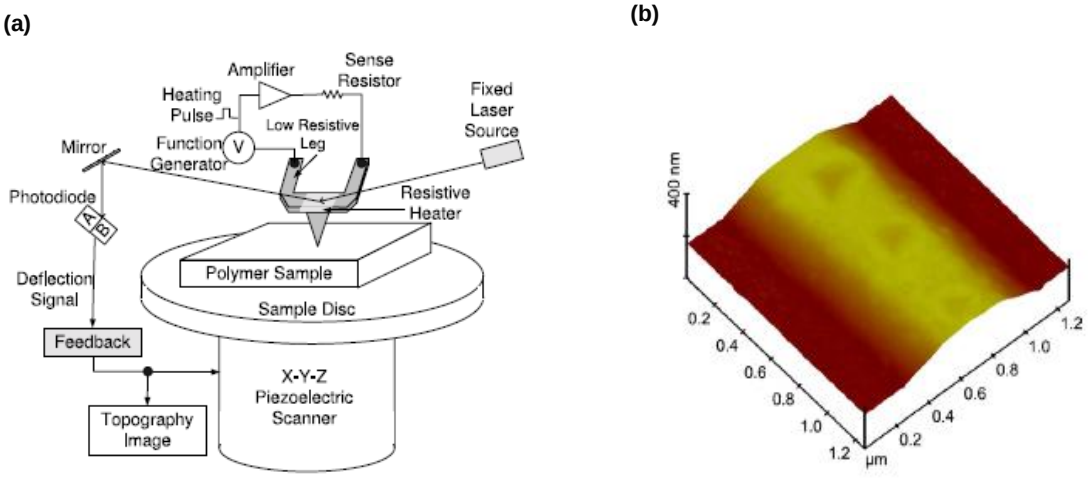

Figure 2-29 (a) A schematic of nanoindentation method based on the atomic force microscopy (AFM) using a heated cantilever [65] (b) AFM image of gold nanowire after nanoindentation [66].

Table 2-6. Key issues and problems of nanoindentation.

Key issues	Problems	Problem solving
Effect of underlying substrate	The modulus can be overestimated due to the hard substrate if the diameter of the nanofiber is too small	The indenting depth is set up as 10% of the sample thickness
Fiber surface roughness	The roughness of the sample surface changes the contact pressrue resulting in the change of laod	Confirm the morphology of sample surface before indentaion
Curvature of fiber surface	Nanoindentiaon method assumes that the sample surface is flat	Confirm that the fiber diameter is much larger than tip diameter
Non-perpendicular loading and slippage of the sample	Non-perpendicular loading of the tip cuases slip and friction between the tip and the sample	Confirm that the sample is tightly attached to the substrate
Adhesion force	In a high humid condition, the adhesion between the tip and the humidity-sensitive sample increases	Maintain the indenter chamber dry

2.8 Ice-templated (IT) structure

Porous foam materials have attracted a great attention in both of the academy and the industry due to a wide range of applications such as artificial bone materials, drug delivery carriers, filter materials and the parts of a motor vehicle. They show a good mechanical performance in spite of light weights and have a large porosity to store or carry other materials. Porous foams show various properties according to their architecture. Therefore, it is very important to control of the architectural structure such

as the size of pores, morphology of the porosity and the arrangement of porous space. The main processing methods are template replica methods [56-60], sacrificial template techniques [61-64] and direct foaming [68] [68-71].

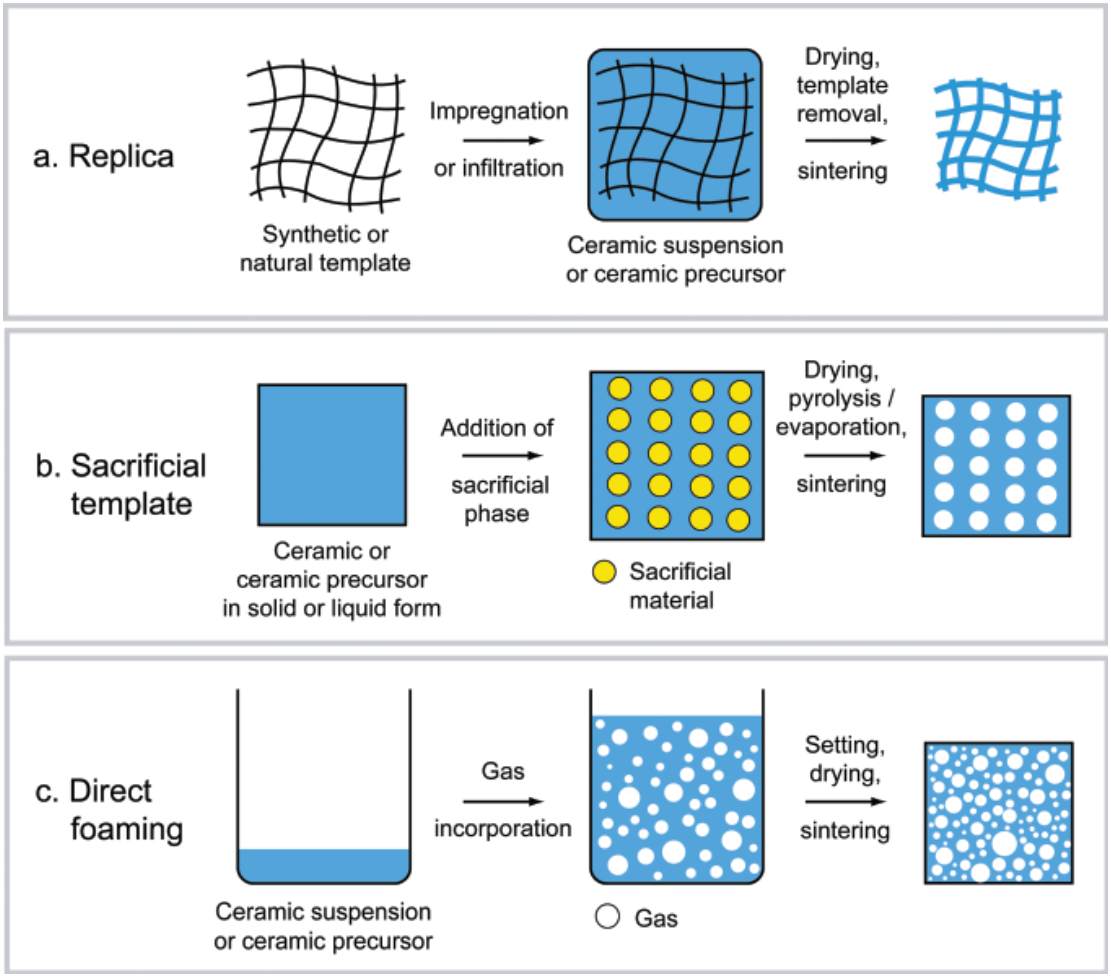

Figure 2-30. Schematic of 3 main processing methods to produce porous foam materials [72].

2.8.1 Replica techniques

The synthetic replica technique is the first method used for the production of porous ceramic foams. In this approach, polymer foams such as a polyurethane sponge

were widely used as templates. The sponge replica method is the most popular technique in industry to produce ceramic foams such as ceramic filters. First, pores of polymer template are filled with ceramic materials. After drying, the polymer template is removed through a pyrolysis ($300^{o}C \sim 800^{o}C$). And then remained ceramic materials are sintered at appropriate temperature ($1100^{o}C \sim 1700^{o}C$). A schematic of replica method is shown in Fig 2-30 (a).

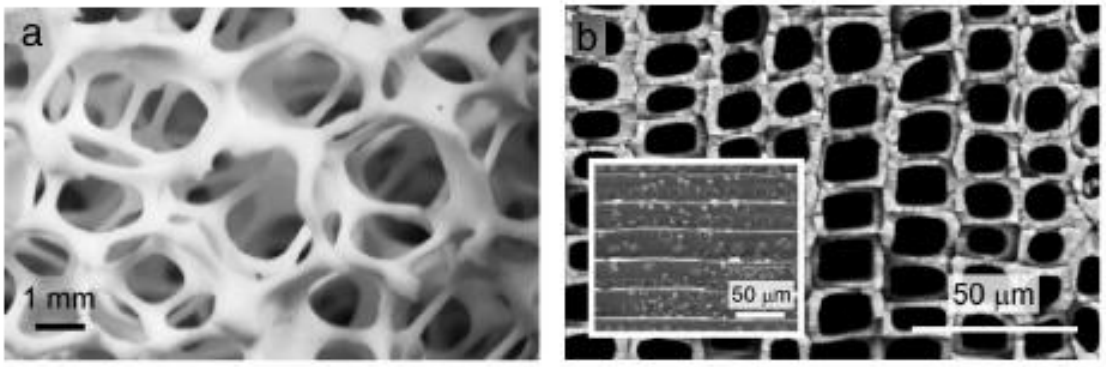

Figure 2-31 (a) SEM image of alumina based open-cell structure obtained using polyurethane sponge template [73] (b) SEM image of a highly oriented SiC porous ceramic obtained by wood replica method [74].

The typical porosity of ceramics foams prepared by a synthetic replica technique ranges from 40% to 95%. Typically, they show open-cell structures and their pore size is between 200 μm and 3 mm (Fig 2-32). If the pore size of polymer template is smaller than 200 μm, it is difficult to fill the pore with ceramic materials [75]. A synthetic replica method sometimes makes some cracks on foam materials during pyrolysis, resulting in the decrease of a mechanical performance of ceramic foams [76]. The SEM image of ceramic foams prepared by polyurethane sponge template is shown in Fig 2-31 (a). Natural templates such as corals [77] and woods [74] give a chance to make unique and highly oriented structures which is difficult to prepare using synthetic templates.

Basic sequences to prepare natural template replica foams are same with a synthetic replica method. The pore size of wood-replica foams ranges from 10 to 300 μm which is the channel size of the microstructure of wood templates and their porosity is between 25% and 95% (Fig 2-32). The SEM image of wood template foams is shown in Fig 2-31 (b).

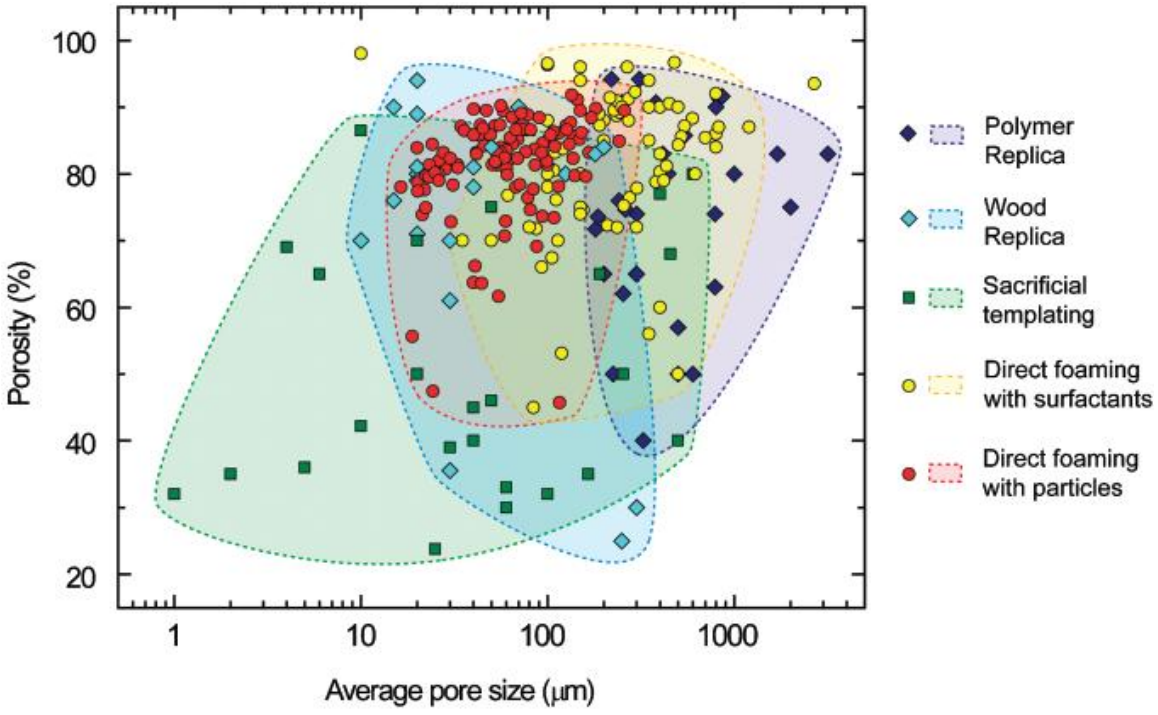

Figure 2-32. Typical porosity and average pore size achieved by the replica, sacrificial templating and direct foaming processing routes [72].

2.8.2 Sacrificial template techniques

In sacrificial template methods, a sacrificial phase is added to ceramic particles or ceramic precursors. Various materials have been used as sacrificial template such as PVA, PEO, PMMA, starch and so on. They are extracted from the mixture through pyrolysis (200^{o}C ~ 600^{o}C) to produce micro-pore foam materials. A sacrificial template method

generates a negative replica as shown in Fig 2-30 (b) and their SEM images are shown in Fig 2-33.

As opposed to the replica methods, it is feasible to control the pore size, pore morphology and porosity of foaming materials prepared by sacrificial template techniques. Through the appropriate choice of the sacrificial materials, the pore size ranges from 1 μm to 700 μm and the porosity changes from 20% to 90% as shown in Fig 2-32. Sacrificial template foams are usually closed-cell structures. Therefore, they show higher mechanical properties, compared with replica foams which have open-cell structures. The relationship between relative density and relative compressive strength of ceramic foam materials prepared by various methods is shown in Fig 2-34. The theoretical expectation of compressive strength for closed-cell and open-cell foams is also indicated.

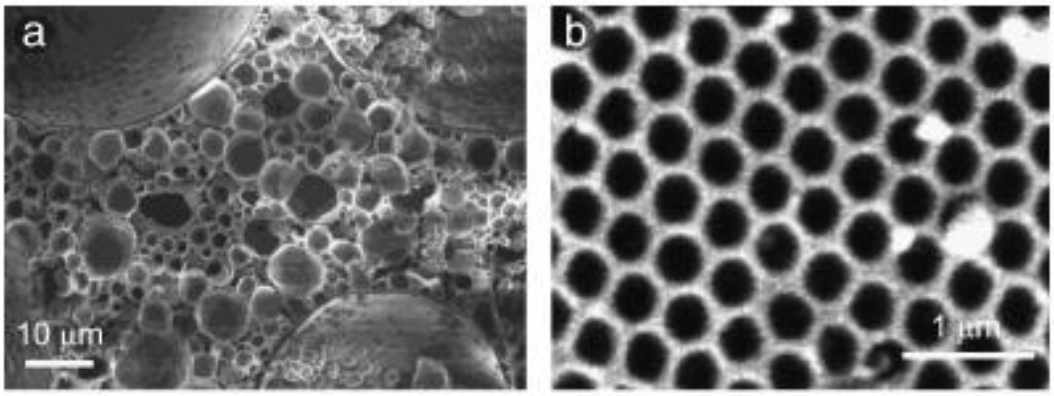

Figure 2-33 (a) SEM image of TiO_2 foam produced via emulsion sacrificial template method [78] (b) SEM image of SiO_2 foam obtained using polystyrene beads sacrificial template method [79].

2.8.3 Direct foaming methods

In direct foaming methods, air is directly incorporated into a ceramic suspension

and porous foams are obtained simply by sintering process (Fig 2-30 (c)). The porosity is proportional to the amount of incorporated air and the pore size is determined by the stability of wet foam. Wet foams are thermodynamically unstable due to their high gas-liquid interfacial energy. They undergo drainage, coalescence and Ostwald ripening to decrease the overall free energy [72]. Usually surfactants are used to stabilize the air bubbles in suspension. The pore size is between 35 μm and 1.2 mm according to the species of surfactants (Fig 2-32). A direct foaming method produces a negative replica as shown in Fig 2-30 (c). The SEM image of foam materials prepared by the direct foaming method is shown in Fig 2-35.

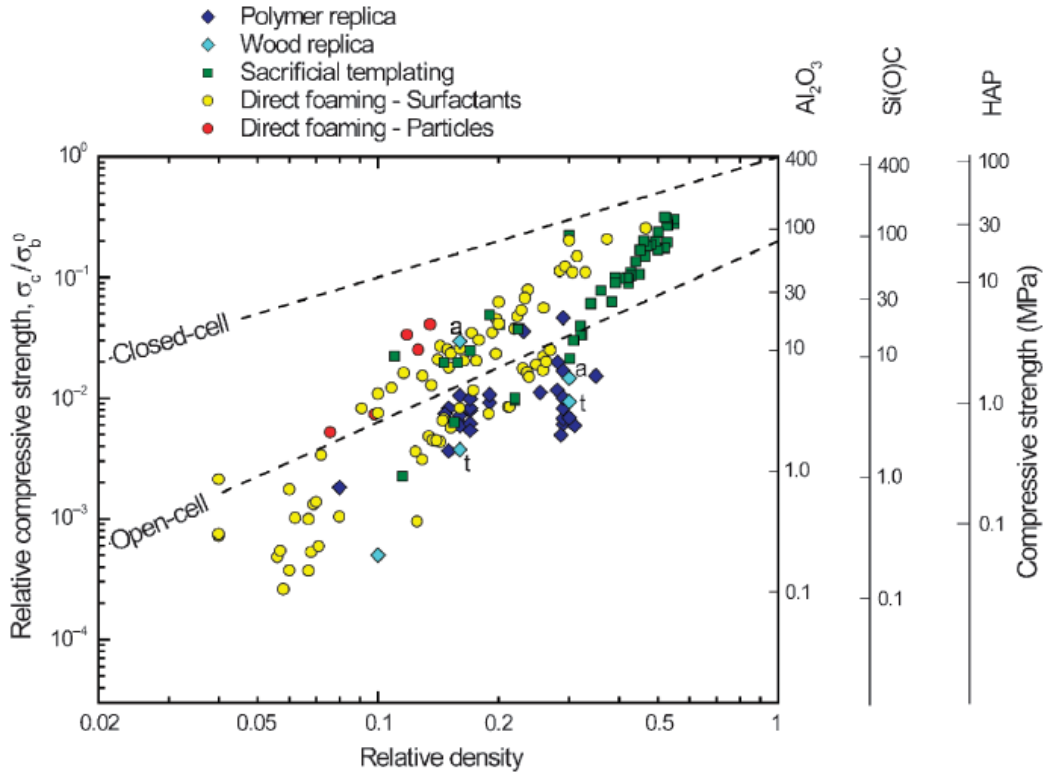

Figure 2-34. The relationship between relative density and relative compressive strength of ceramic foam materials prepared by various methods [72].

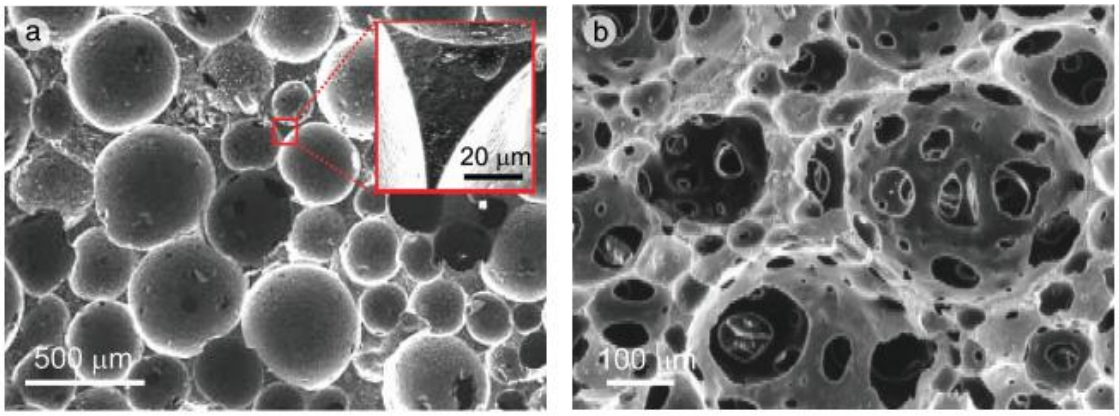

Figure 2-35. SEM images of microstructure of porous foams prepared by direct foaming methods (a) closed-cell structure [80] (b) open-cell structure [76].

2.8.4 Ice-templated (IT) methods

In ice-templated methods, the unidirectional freezing of the aqueous suspension, followed by the unidirectional growth of ice crystals, results in high ordered porous foams with unidirectional channels. Ice crystals grow with the same direction of the temperature gradient. During the growth of ice crystals, particles or polymers are entrapped between ice crystals as shown in Fig 2-36. After removing ice crystal templates by sublimation, the porous structure which is the replica of the original ice-template is obtained. In ice-templated methods, the porosity of the foam is same with the volume ratio of water in suspension. The porosity of IT foams ranges from 99% to 20%. If the particle concentration is too high (>80wt%), the characteristic channel structure of IT foams is lost [81].

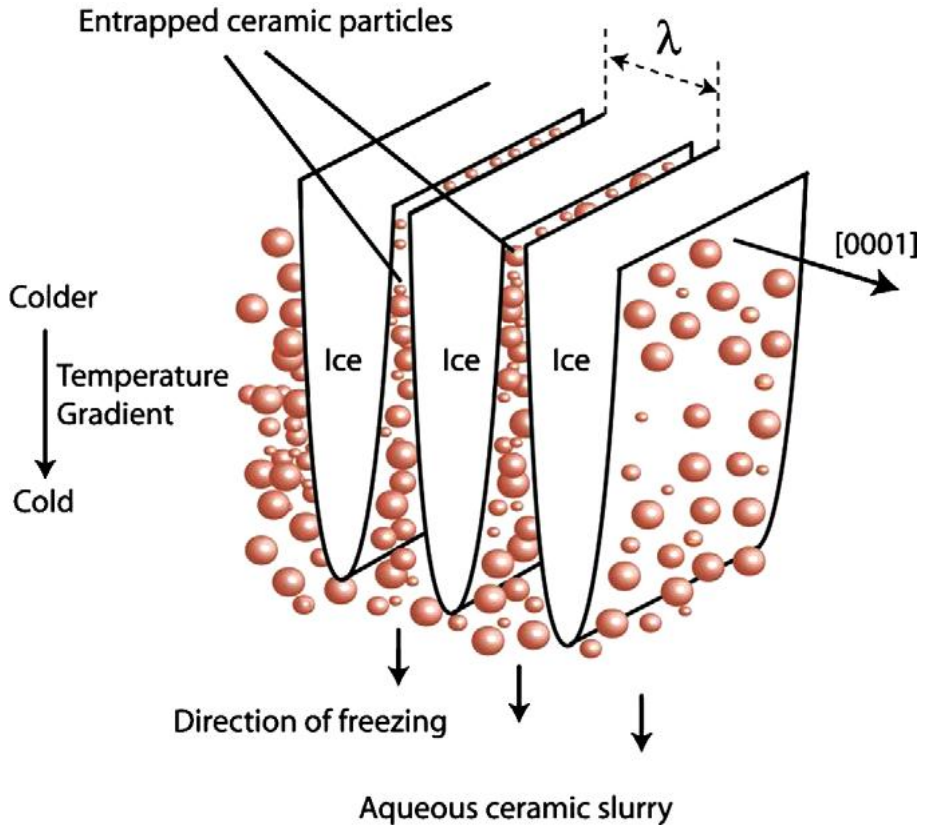

Figure 2-36. Schematic of growth of ice crystals and particle entrapment [81].

The channel size of IT foams is able to be controlled and ranges from 1 to 130 μm. If the freezing rate of ice crystals increases, the width of ice templates decreases, resulting in the decrease of average channel size of IT foams. In this case, the average thickness of lamellae wall decreases together. The relation between the ice crystal freezing rate and the channel wavelength is simply described by the empirical power law, $\lambda \propto v^{-n}$. N is dependent on the particle size ($n \approx 0.66 \sim 1$) [82]. Various SEM images of porous structures made by IT methods are shown in Fig 2-37.

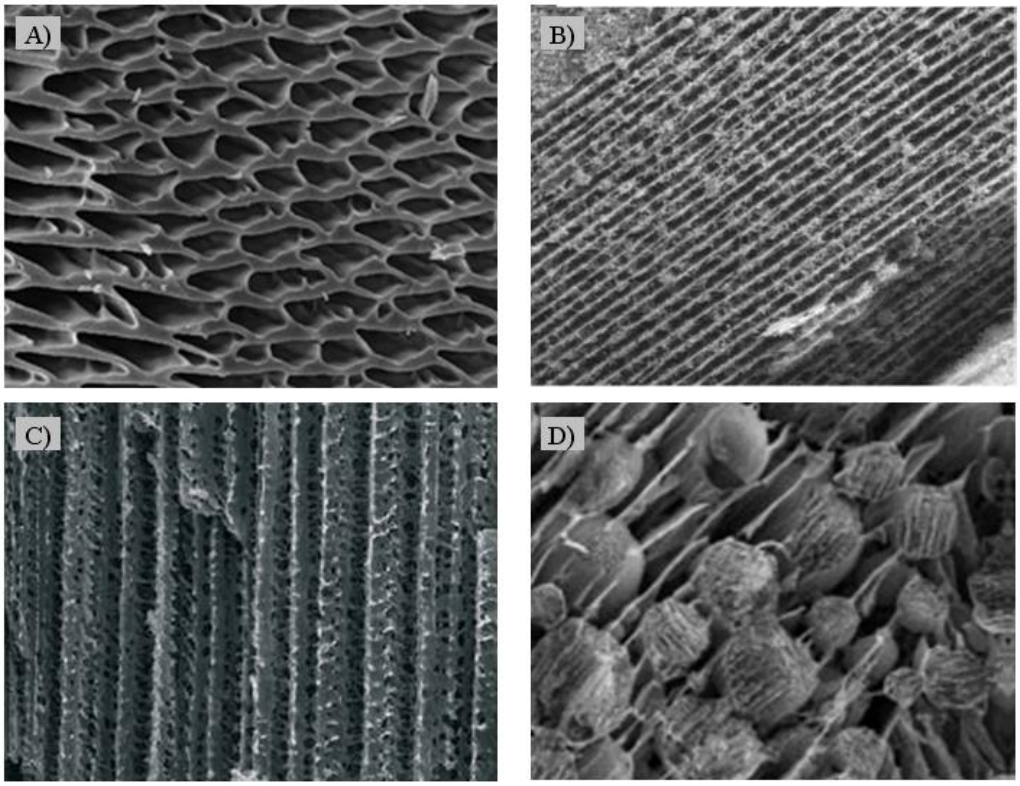

Figure 2-37. Various SEM images of porous foam structures prepared by ice-templated methods. Each sample was prepared from (a) Silica aqueous suspension [83] (b) MWCNT aqueous suspension [84] (c) PVA aqueous suspension [85] (d) PCL emulsion in o-xylene [86].

2.8.5 Physics of ice crystal growth in a suspension

In case that the ice front pushes and transports the particles, a liquid film of sufficient thickness is needed between the ice front and particles. When the velocity of ice front increases, the thickness of the liquid film decreases. If the ice front velocity is too high ($v_{ice-front} > v_c$), the particles are embedded inside the ice crystals instead of being entrapped between ice crystals [87]. The critical velocity, v_c is given by

$$v_c = \frac{\Delta\sigma D}{3\eta R}\left(\frac{a_0}{D}\right)^z \tag{2.10}$$

Where a_0 is an average intermolecular distance in the film, D is the overall thickness, η is the solution viscosity, R is the particles radius and z is an exponent that can vary from 1 to 5 depending on the specific model. For micron size particles, typical critical velocity ranges from 1 to 10 $\mu m\, s^{-1}$ and for nanometer size particles, the typical values is $0.1 \sim 1\, m\, s^{-1}$ which is reversely proportional to the particle radius [88].

Planar structure region

When a suspension is freezed unidirectionally, the ice crystals start to grow at the bottom which is contacted to a freezing source. At that moment, the freezing velocity usually is larger than v_c, therefore the ice front is planar and particles are encapsulated in the ice front. Therefore, the morphology of the bottom of the porous foams is a dense planar layer structure.

Columnar structure region

When the ice crystals grow further, a transition from planar structure to columnar structure happens. This transition phenomenon can be explained by two theories. First one is Mullins-Serkerka instablility [89]. Because the crystal structure of ice has a very low solubility, particles which are initially located at the nucleation center of ice crystals are separated from ice crystals, resulting in a local increase of the particle concentration. A concentration gradient around the ice front leads to a local decrease of the freezing point and the formation of a local supercooling zone. The instability of the supercooling zone breaks the planar interface of initial ice crystals and generates the columnar interface. The transition phenomenon is simply explained by the decrease of freezing velocity [81]. Because this cooling process is unidirectional, a temperature gradient exists. After a formation of planar ice crystals at $v_{ice-front} > v_c$ zone, $v_{ice-front}$ decreases gradually

below v_c and particles starts to be separated from ice-front, resulting in the transition from the planar structure to the columnar structure.

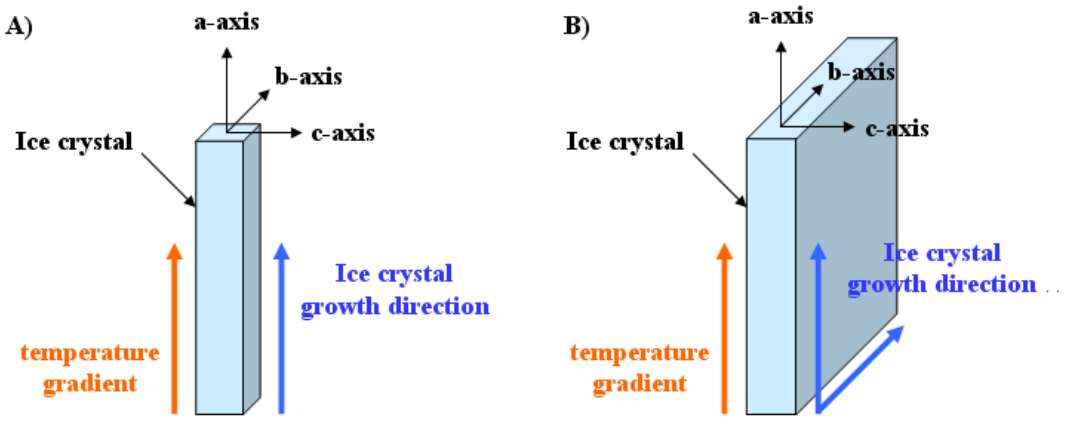

Figure 2-38 (a) Scheme of ice crystal growth at the columnar region (b) scheme of ice crystal growth at the lamellar region.

Lamellar structure region

Ice crystals grow anisotropically. The ice front velocity parallel to the temperature gradient orientation, crystallographic a-axis, is 10^2 ~ 10^3 times faster than that of c-axis which is perpendicular to the temperature gradient. At the columnar ice crystal zone, the ice front grows to a-axis orientation (Fig 2-38 (a)). When the ice crystals keep growing and $v_{ice-front}$ decreases further, columnar to lamellar transition happens. At this region, ice crystals grow to the a-axis and b-axis direction but the growth to c-axis direction is still very slow. Therefore, the thickness of ice crystals along c-axis is very small and ice crystal grows as a flat platelet form as shown in Fig 2-38 (b). At each of the scheme, ice crystals are simplified as a cubic form.

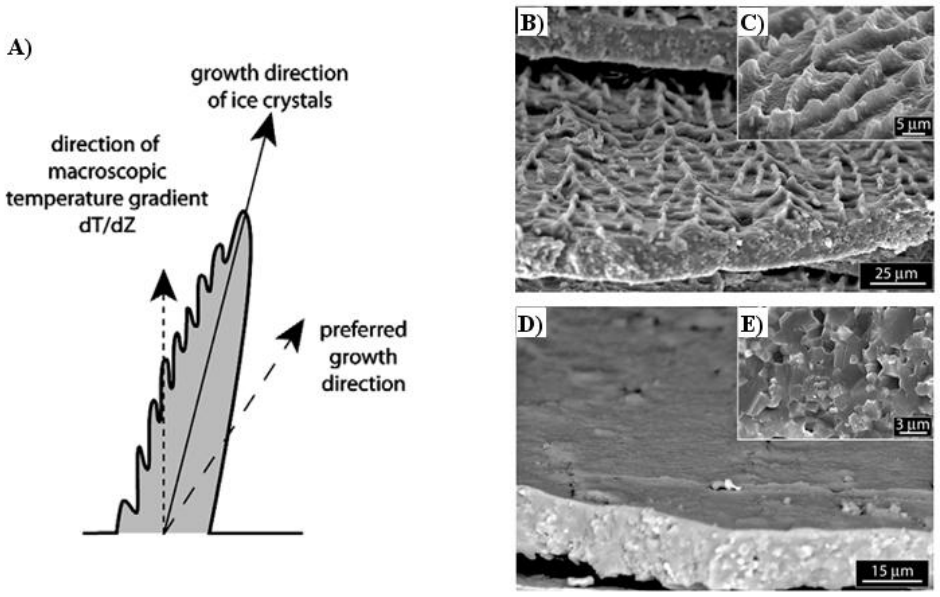

Figure 2-39 (a) Scheme of ice crystal growth at small temperature gradient and formation of ice dendrite (b) and (c) SEM images of dendritic structures on lamellar surface (d) and (e) SEM images of smooth lamellar surface [81].

Lamellar and dendritic structure region

When the temperature gradient becomes small, the growth direction of ice crystals is tilted to the preferred growth direction. Therefore, there is a few degree difference between the ice crystal growth direction and the temperature gradient direction. In this case, small dendrites start to grow on one side of the ice crystals with the direction of the temperature gradient. The other side of ice lamellar structure is flat without dendrites. During freezing, particles are entrapped between dendrites, resulting in the generation of rough structure on one side of lamellar structure after removing ice template. The scheme of a formation of ice dendrite and SEM image of particle dendrites are shown in Fig 2-39. As shown in Fig 2-39 (b), dendritic structures are observed on one side of lamellar surface and the other surface is smooth (Fig 2-39 (c)).

Bridge structures in ice-templated foams

For IT porous structures prepared from highly concentrated suspension, bridge structures are observed. The growth mechanism of a bridge structure is not clear yet. The possible mechanism is ice crystal tip splitting and subsequent tip healing [81]. When high concentration suspension is freezed, particle agglomerates are sometimes repelled from the ice-suspension interface and engulfed in ice crystal tip (tip splitting). After that, subsequent tip healing happens and makes the bridge structure. Bridge structures connect two lamellar structures entirely or partially according to the extent of tip splitting and healing process.

2.9 Wetting properties of patterned surfaces

2.9.1 Superhydrophobicity

Superhydrophobic surfaces display very high contact angles with water (greater than 150° and low contact angle hysteresis. The design of superhydrophobic surfaces have been biologically inspired by the lotus leaf [90], legs of the water strider [91], eyes of mosquito [92], beetles [93] and so on. Superhydrophobic surfaces have attracted great interests because of the potential applications such as antibiofouling boats [94-95], antisticking antennas [96], antisticking windows [97], self-cleaning windshields [98] and stain resistant textiles [99].

The contact angle of a liquid droplet on a flat and smooth surface is given by Young's equation as

$$\cos\theta = \frac{\gamma_{SV} - \gamma_{SL}}{\gamma_{LV}} \tag{2.11}$$

where γ is the interfacial surface tension. Subscripts S, V, L refer to the solid, vapor and liquid phase, respectively. The contact angle in Young's equation is measured when the liquid droplet is at thermodynamic equilibrium of the free energy at the S-V-L phases.

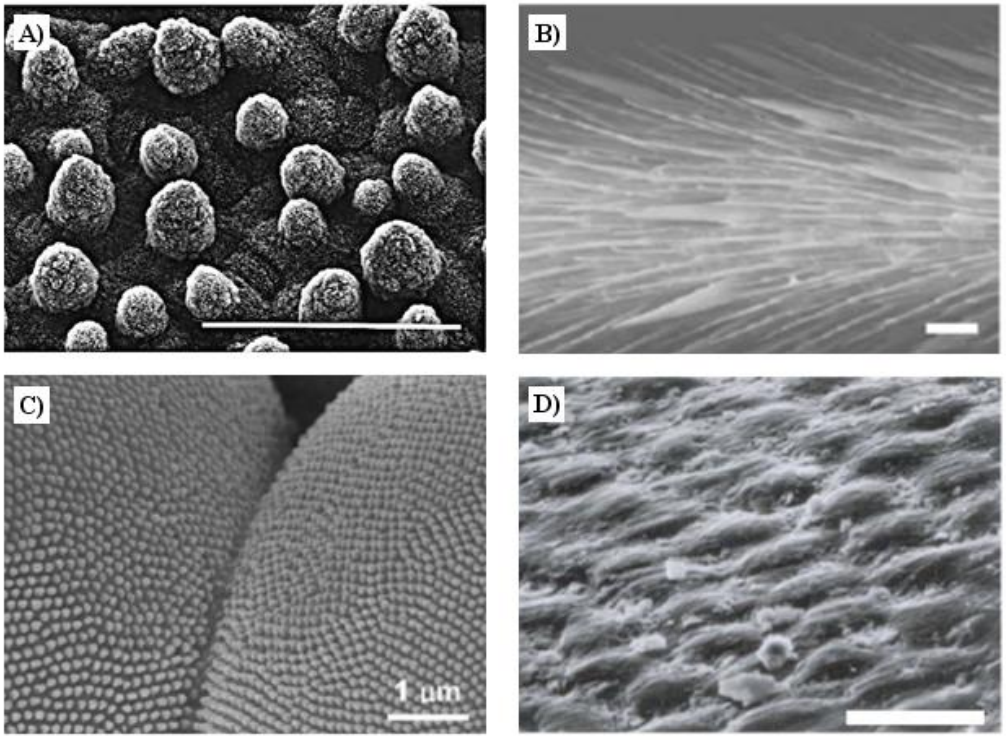

Figure 2-40. SEM images of biological structures in nature. (a) the lotus leaf [90], (b) legs of the water strider [91], (c) eyes of mosquito [92], (d) the shell of beetles [93]. Scale bars represent 20 μm, 20 μm, 1 μm and 10 μm, respectively.

Two models were developed to explain the wettability of the rough surface by Wenzel [100] and Cassie and Baxter [101]. In Wenzel model, it is assumed that the liquid contacts the rough surface directly and there is no air gap between a liquid phase and a surface (Fig 2-41 (a)). Therefore, surface roughness increases the available surface area and the contact angle is given by

$$\cos\theta_w = r\cos\theta_e \tag{2.12}$$

where θ_w is the apparent contact angle on the rough surface, θ_e is the equilibrium contact angle on a smooth flat surface of the same material (Young's contact angle) and r is the roughness factor which is defined by the actual surface area divided by the projected surface area (r > 1). In the Wenzel model, the relationship $\theta_w > \theta_e > 90^\circ$ and $\theta_w < \theta_e < 90^\circ$ are predicted. It suggests that both of the hydrophobicity and hydrophilicity are enhanced at Wenzel regime.

Cassie-Baxter model focused on the air gap between liquid droplet and rough surface (Fig 2-41 (b)). The contact angle on rough surfaces is given by

$$\cos\theta_c = f_V \cos\theta_{V,e} + f_S \cos\theta_{S,e} \tag{2.13}$$

where θ_c is the apparent contact angle. f_V and f_S are surface fraction of vapor phase and solid phase which contact with liquid phase. $\theta_{V,e}$ and $\theta_{S,e}$ are equilibrium contact angle of liquid droplet at vapor phase and solid phase, respectively. For air, $\theta_{V,e} = 180^\circ$, therefore, Cassie-Baxter model is expressed as

$$\cos\theta_c = -1 + f_s(1+\cos\theta_e) \tag{2.14}$$

In Cassie-Baxter model, the fraction of solid phase surface should be as small as possible to get the superhydrophobic surface. Schematics of Wenzel model and Cassie model are shown in Fig 2-41. As shown at both of the models, two key parameters are important to the superhydrophobic surface, surface energy and roughness. However, both theories can predict the contact angle of a rough surface only qualitatively [102].

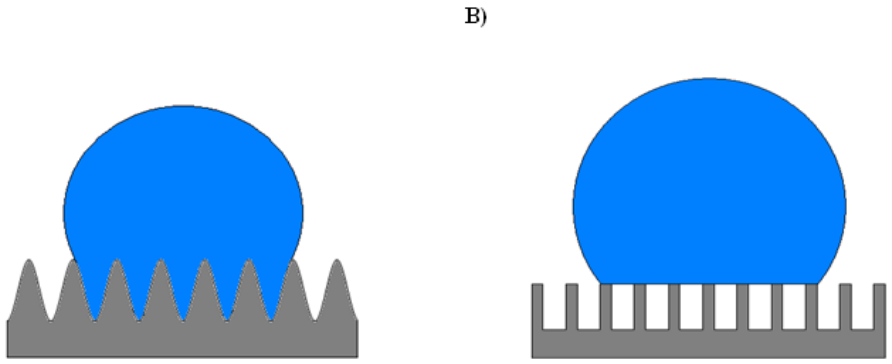

Figure 2-41. Schematics of Wenzel model and Cassie model.

For the rough surfaces which have a fractal geometry, a combined model of Wenzel model and Cassie-Baxter model was suggested [103].

$$\cos\theta_f = f_S (L_f / l_f)^{D_f - 2} \cos\theta_e - f_V \tag{2.15}$$

where $(L_f / l_f)^{D_f - 2}$ is the surface roughness factor, L_f is the upper limit scales of the fractal structures, l_f is the lower limit scales, D_f is the fractal dimension. Calculated contact angles of typical multi-scale fractal geometry surfaces are fitted in Fig 2-42.

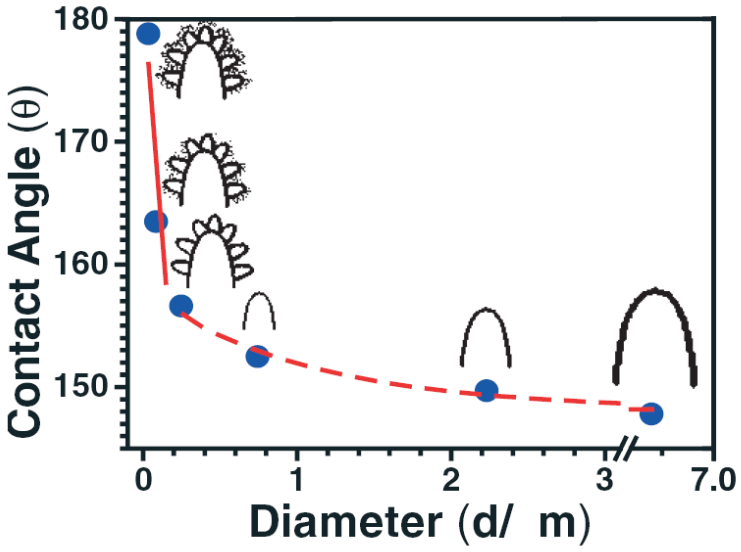

Figure 2-42. The contact angles of multi-scale fractal geometry surfaces [103].

Top-down approaches

The methods for superhydrophobic surface preparation can be categorized into two directions, top-down and bottom-up approaches. Top-down approaches refer to the fabrication methods via carving, molding, machining and so on. So far, templation methods, lithographic approaches, plasma treatment and micromachining have been used for the fabrication of superhydrophobic surfaces [102].

Templation methods include several steps: preparation of a template, replication by molding and removing a template. PDMS has been used as molding materials (Fig 2-43) [104]. Polystyrene substrates and aluminum oxide templates have been used to prepare superhydrophobic surfaces [105]. Templation is a versatile method which can be applicable to many polymeric systems. However, there is a limitation of the feasible geometry using templation approaches.

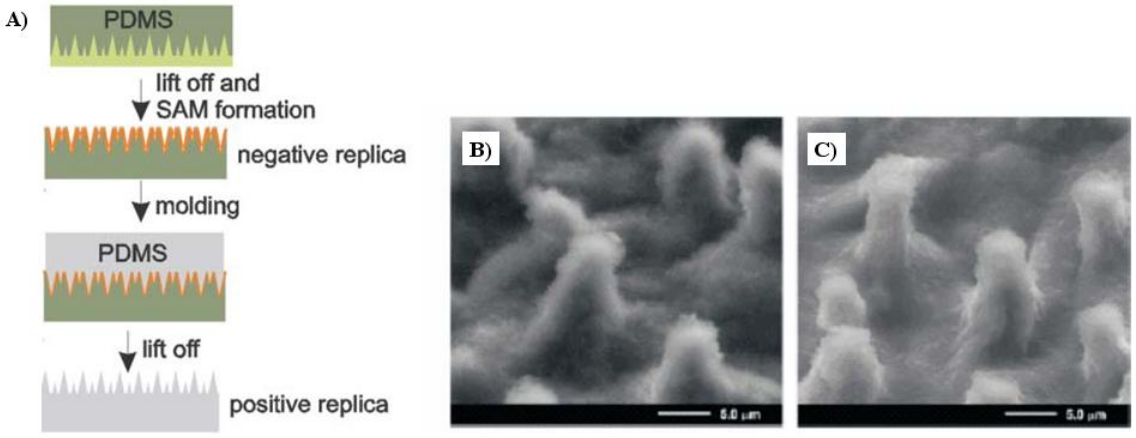

Figure 2-43. (a) Schematic of PDMS templation method (b) SEM image of a natural lotus leaf (c) SEM image of the positive PDMS replica [104].

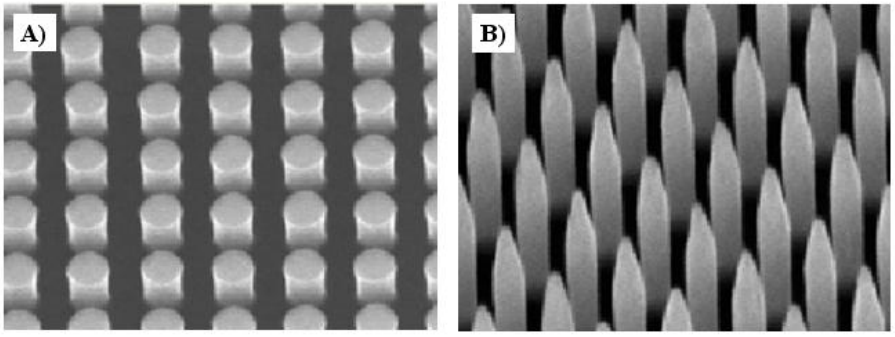

Figure 2-44. SEM images of superhydrophobic surfaces via e-beam lithography and Octadecyltrichlorosilane (OTS) treatment [106].

In photolithographic approaches, light (radiation or electrons) is applied to the substrate through a mask. After developing and etching steps, patterned surface can be obtained. To improve the superhydrophobicity, additional surface treatments with chemicals is sometimes needed. X-ray and silicon wafer substrates were used to prepare patterned surface. Subsequent sputtering of gold particles and hexadecanethiol treatment have been applied to the prepared surface [107]. Patterned surfaces prepared using e-

beam lithography was also reported (Fig 2-44) [106]. Octadecyltrichlorosilane (OTS) was treated on the prepared surface.

Plasma etching is a dry etch technique using reactive atoms or ions such as oxygen, chlorine and fluorine. Accelerated ions between plasma and substrates create deep grooves and steep walls [102]. Superhydrophobic low density polyethylene (LDPE) surfaces using oxygen and CF_4 plasma have been reported [108]. Poly(tetrafluoroethylene) (PTFE) was treated using oxygen and ammonia plasma to obtain superhydrophobic surfaces (Fig 2-45) [109].

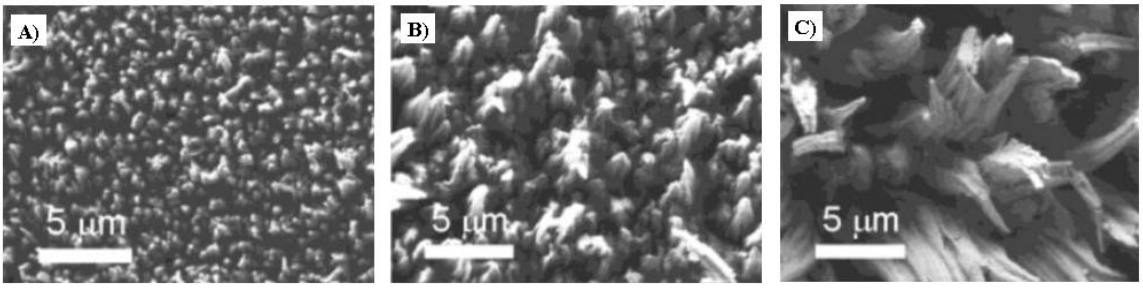

Figure 2-45. SEM images of superhydrophobic Poly(tetrafluoroethylene) (PTFE) surfaces using oxygen and ammonia plasma. Plasma treatment time is (a) 120 sec (b) 5 min (c) 10 min, respectively.

Bottom-up approaches

Bottom-up approaches refer to the fabrication methods from smaller building components to larger objects. Bottom-up approaches for the preparation of superhydrophobic surfaces include chemical bath deposition (CBD), chemical vapor deposition (CVD), electrochemical deposition, layer-by-layer (LbL) deposition, colloidal assembly, sol-gel methods and electrospinning methods [102].

Chemical deposition is crystalline inorganic materials preparation methods on substrates. According to the materials and the reaction conditions, the morphology of inorganic crystals can be controlled. After the deposition, chemical treatments are

sometimes applied to get the superhydrophobic surfaces. Zinc oxide (ZnO) nanorods superhydrophobic surfaces using CBD techniques have been reported [110]. Aligned carbon nanotubes (CNTs) and ZnO coated carbon nanotubes were prepared on Fe-N coated silicon substrate to get the superhydrophobic surfaces (Fig 2-46) [111].

Rough surfaces covered with a single layer of close-packed particles also show superhydrophobicity. Monodispersed close-packed polystyrene (PS) beads were prepared by spin coating [112]. Plasma etching was treated to PS beads surfaces to obtain extra roughness (Fig 2-47).

Polyallyamine hydrochloride (PAH)/poly(acryl acid) (PAA) multilayer thin film were prepared via LbL deposition techniques. After acid treatments, SiO_2 particles deposition and a chemical vapor deposition of semifluorinated silane, (PAH/PAA) films show honey-comb structures which show superhydrophobicity (Fig 2-48) [113]. It was also reported that (PAH/ PAA coated ZrO_2 particles) LbL assemblies prepared on a silicon substrate show superhydrophobicity [114].

Electrospinning techniques are originally the preparation methods of nano-size fibers and their membranes. Recently, electrospinning has been applied for the fabrication of superhydrophobic surfaces [115-116]. The effects of polymer beads during electrospinning process have been investigated (Fig 2-49 (a)) [117]. Sometimes, extra treatments such as CVD or fluorination were applied to the electrospun fiber deposited surfaces. Superhydrophobic poly(caprolectone) (PCL) electrospun fiber mat were prepared after initiated chemical vapor deposition of polymerized perfluoroalkyl ethyl methacrylate (PPFEMA) (Fig 2-49 (b) and (c)) [117].

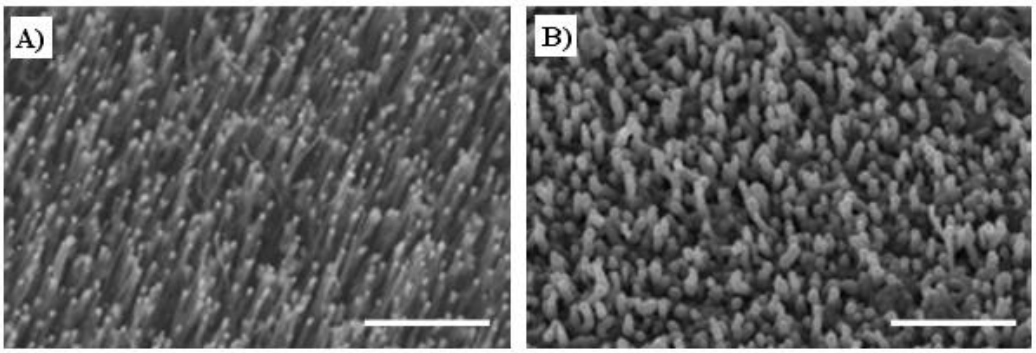

Figure 2-46. SEM images of (a) aligned CNT template (b) ZnO coated CNTs. Scale bars are 5 μm [111].

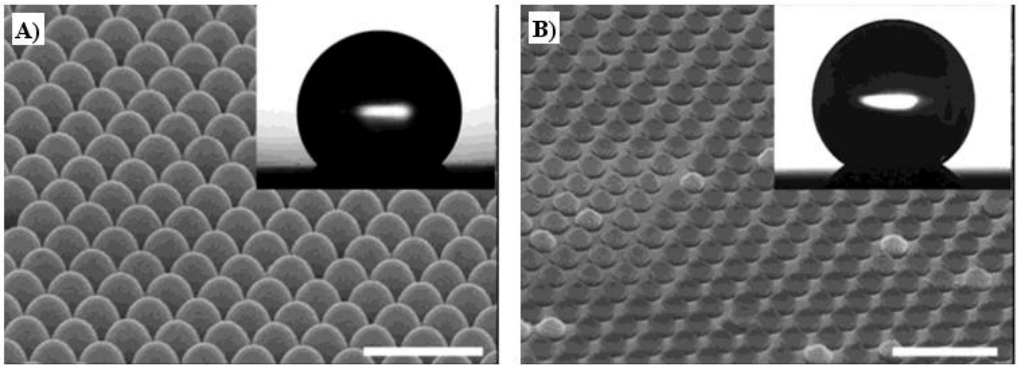

Figure 2-47. SEM images and water contact angles of (a) 400 nm PS beads covered surface (b) 330nm PS beads covered surface. Scare bars are 1 μm, respectively [112].

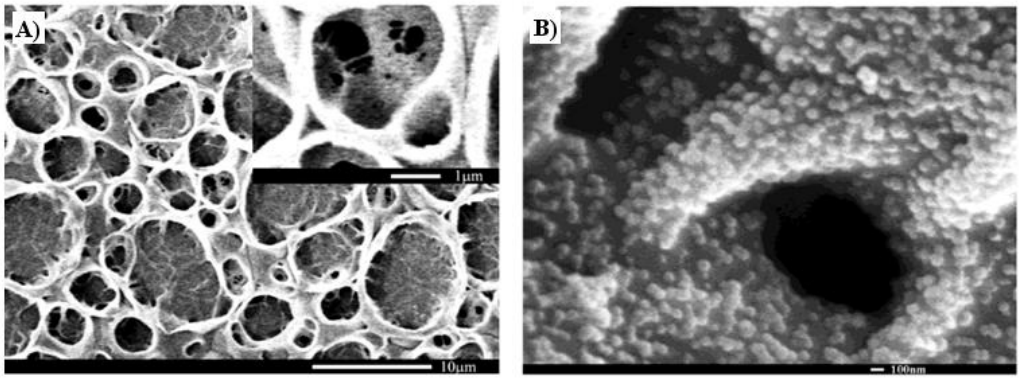

Figure 2-48. SEM images of (a) (PAH/PAA) LbL assembly after acid treatments (b) (PAH/PAA) LbL assembly after acid treatments, SiO_2 particles deposition and a chemical vapor deposition of semifluorinated silane [113].

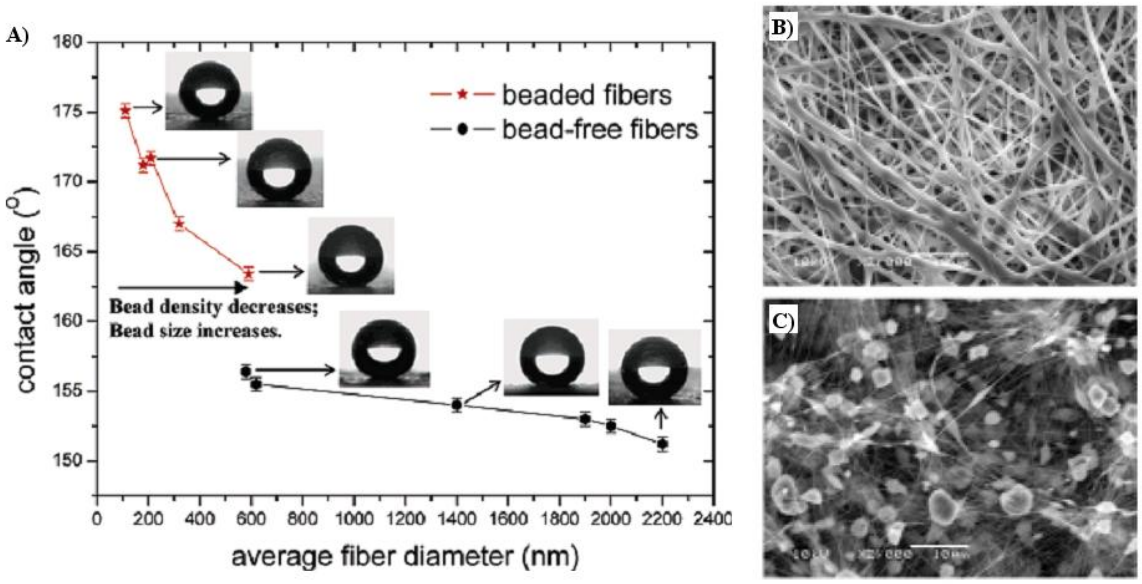

Figure 2-49 (a) Contact angles of bead-free PCL electrospun fiber mats and beaded PCL electrospun fiber mats (b) a SEM image of PCL electrospun fiber mats (c) a SEM image of beaded PCL electrospun fiber mats [117].

2.9.2 Anisotropic wetting properties of one-dimensional patterned surfaces

Recently, interests on the anisotropic wetting properties have been increased. Due to the fast development of the fabrication methods such as photolithography [118], interferometric lithography [119-120] and micro-wrinkling techniques [121], experimental, theoretical [122-124] and simulation studies [125] about the anisotropic wetting phenomenon have been reported. Understanding anisotropic wetting properties is important in that it is possible to control the wettability of the target surface by controlling the architecture of the surface. Potential applications include self-cleaning, biosensing, lab-on-a chip systems, intelligent membranes, microfluid devices and microreactor systems [120]. In spite of several theoretical studies, the quantitative explanation of anisotropic wetting phenomenon is not clear yet.

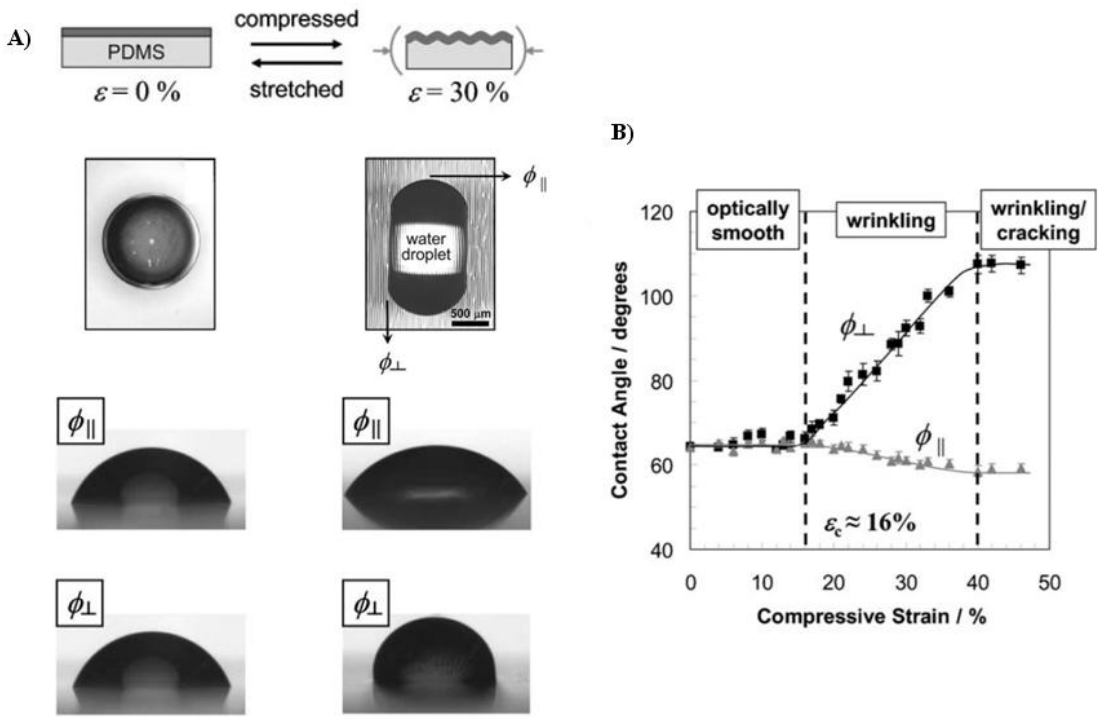

Figure 2-50 (a) Top views and side views of anisotropic wetting phenomenon on the smooth surface and micro-wrinkled surface (b) Dependence of the water contact angles in two directions ($\phi_{\parallel}$ and $\phi_{\perp}$) on sinusoidally patterned surfaces as a function of degree of compression ε (e) [121].

Micro-wrinkled poly(dimethysiloxane) (PDMS) surfaces were fabricated by mechanical compression [121]. The shape of the water droplet on the micro-winkled surfaces is strongly influenced by geometrical anisotropy as shown in Fig 2-50. When PDMS surface is smooth, the contact angle is $\phi_{\parallel} = \phi_{\perp} = 64.3^{\circ} \pm 0.8^{\circ}$. When the wetting direction is perpendicular to the groove direction, the contact line of the droplet looks straight and sticks to the peak of the sinusoidal groove. When the wetting direction is parallel to the groove direction, the droplet is elongated. Maximum $\phi_{\perp}$ value with $\varepsilon = 40\%$ is $92.4^{\circ} \pm 1.0^{\circ}$ and minimum $\phi_{\parallel}$ value with $\varepsilon = 40\%$ is $60.6^{\circ} \pm 1.0^{\circ}$ [121].

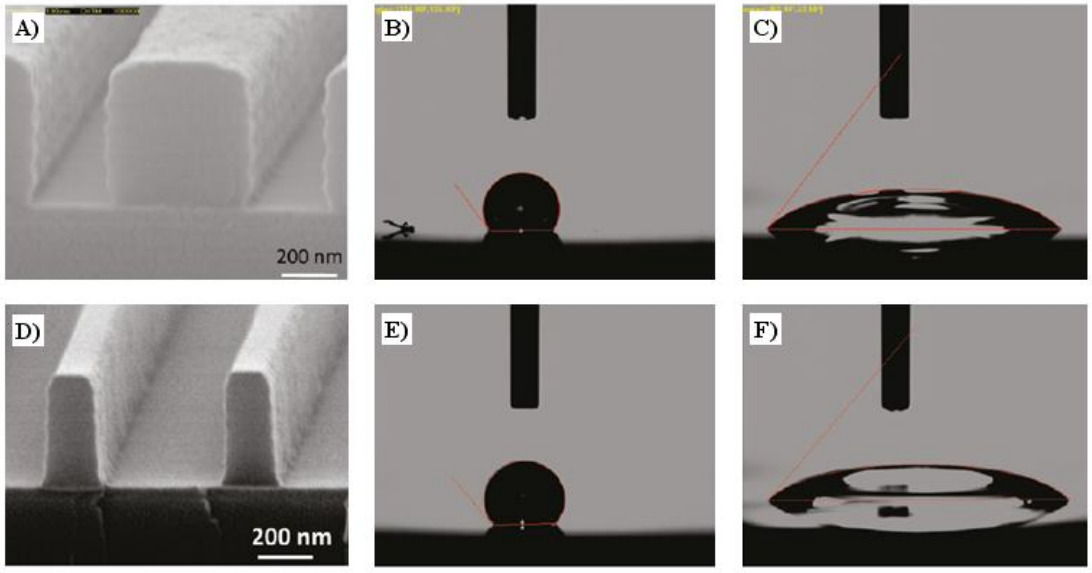

Figure 2-51 (a) Submicron groove surface A (b) $\phi_{\perp}$ on groove surface A (c) $\phi_{\parallel}$ on groove surface A (d) Submicron groove surface B (e) $\phi_{\perp}$ on groove surface B (f) $\phi_{\parallel}$ on groove surface B [120].

Submicron groove surfaces were prepared using interferometric lithography and plasma surface treatment (Fig 2-51) [120]. Grove density of surface A is 800nm, the width of the wall is 500nm and the width of empty channel is 300nm. $\phi_{\perp}$ and $\phi_{\parallel}$ values on groove surface A are 126° and 52°, respectively. Grove density of surface B is also 800nm, however, the width of the wall is 160nm and the width of empty channel is 640nm. $\phi_{\perp}$ and $\phi_{\parallel}$ values on surface B are 130° and 49°, respectively. The additional surface treatments using CHF_3, CF_4 and O_2 plasma were applied to groove surfaces. For all of the cases, the anisotropic wetting properties are clearly observed.

References

1. Hon, D.N.S., *CELLULOSE - A RANDOM-WALK ALONG ITS HISTORICAL PATH.* Cellulose, 1994. **1**(1): p. 1-25.

2. Osullivan, A.C., *Cellulose: the structure slowly unravels.* Cellulose, 1997. **4**(3): p. 173-207.

3. DJ, J., *US Patent 3,447,939.* Assigned to Eastman Kodak.

4. McCorsely CC, V.J., *US Patent 4,142,913.* assigned to Akzona Inc.

5. Fink, H.P., et al., *Structure formation of regenerated cellulose materials from NMMO-solutions.* Progress in Polymer Science, 2001. **26**(9): p. 1473-1524.

6. Chanzy, H., M. Dube, and R.H. Marchessault, *CRYSTALLIZATION OF CELLULOSE WITH N-METHYLMORPHOLINE N-OXIDE - NEW METHOD OF TEXTURING CELLULOSE.* Journal of Polymer Science Part C-Polymer Letters, 1979. **17**(4): p. 219-226.

7. Dong, X.M., J.F. Revol, and D.G. Gray, *Effect of microcrystallite preparation conditions on the formation of colloid crystals of cellulose.* Cellulose, 1998. **5**(1): p. 19-32.

8. Lima, M.M.D. and R. Borsali, *Rodlike cellulose microcrystals: Structure, properties, and applications.* Macromolecular Rapid Communications, 2004. **25**(7): p. 771-787.

9. Marchessault, R.H., F.F. Morehead, and N.M. Walter, *LIQUID CRYSTAL SYSTEMS FROM FIBRILLAR POLYSACCHARIDES.* Nature, 1959. **184**(4686): p. 632-633.

10. Turbak AF, S.F., Sandberg KR, *Microfibrillated cellulose, a new cellulose product: properties, uses, and commercial potential.* J Appl Polym Sci, 1983. **37**(815).

11. Nogi, M., et al., *Optically Transparent Nanofiber Paper.* Advanced Materials, 2009. **21**(16): p. 1595-+.

12. Henriksson, M., et al., *An environmentally friendly method for enzyme-assisted preparation of microfibrillated cellulose (MFC) nanofibers.* European Polymer Journal, 2007. **43**(8): p. 3434-3441.

13. Abe, K., S. Iwamoto, and H. Yano, *Obtaining cellulose nanofibers with a uniform width of 15 nm from wood.* Biomacromolecules, 2007. **8**(10): p. 3276-3278.

14. Wu, Q.J., et al., *A high strength nanocomposite based on microcrystalline cellulose and polyurethane.* Biomacromolecules, 2007. **8**(12): p. 3687-3692.

15. Kim, Y., et al., *Transparent nanocomposites prepared by incorporating microbial nanofibrils into poly(L-lactic acid).* Current Applied Physics, 2009. **9**: p. S69-S71.

16. Svagan, A.J., M. Samir, and L.A. Berglund, *Biomimetic foams of high mechanical performance based on nanostructured cell walls reinforced by native cellulose nanofibrils.* Advanced Materials, 2008. **20**(7): p. 1263-+.

17. Henriksson, M., et al., *Cellulose nanopaper structures of high toughness.* Biomacromolecules, 2008. **9**(6): p. 1579-1585.

18. Fontana, J.D., et al., *ACETOBACTER CELLULOSE PELLICLE AS A TEMPORARY SKIN SUBSTITUTE.* Applied Biochemistry and Biotechnology, 1990. **24-5**: p. 253-264.

19. Backdahl, H., et al., *Mechanical properties of bacterial cellulose and interactions with smooth muscle cells.* Biomaterials, 2006. **27**(9): p. 2141-2149.

20. Favier, V., H. Chanzy, and J.Y. Cavaille, *POLYMER NANOCOMPOSITES REINFORCED BY CELLULOSE WHISKERS.* Macromolecules, 1995. **28**(18): p. 6365-6367.

21. Angles, M.N. and A. Dufresne, *Plasticized starch/tunicin whiskers nanocomposites. 1. Structural analysis.* Macromolecules, 2000. **33**(22): p. 8344-8353.

22. Grunert, M. and W.T. Winter, *Nanocomposites of cellulose acetate butyrate reinforced with cellulose nanocrystals.* Journal of Polymers and the Environment, 2002. **10**(1-2): p. 27-30.

23. Chazeau, L., et al., *Viscoelastic properties of plasticized PVC reinforced with cellulose whiskers.* Journal of Applied Polymer Science, 1999. **71**(11): p. 1797-1808.

24. Lu, J., T. Wang, and L.T. Drzal, *Preparation and properties of microfibrillated cellulose polyvinyl alcohol composite materials.* Composites Part a-Applied Science and Manufacturing, 2008. **39**(5): p. 738-746.

25. Bonini C, H.L., *French patent FR 99.07493.*

26. Gousse, C., et al., *Stable suspensions of partially silylated cellulose whiskers dispersed in organic solvents.* Polymer, 2002. **43**(9): p. 2645-2651.

27. Grunert, M. and W.T. Winter, *Cellulose nanocrystal reinforced cellulose acetate butyrate nanocomposites.* Abstracts of Papers of the American Chemical Society, 2002. **223**: p. 240-PMSE.

28. Samir, M., et al., *Cross-linked nanocomposite polymer electrolytes reinforced with cellulose whiskers.* Macromolecules, 2004. **37**(13): p. 4839-4844.

29. Sakurada, I., Y. Nukushina, and T. Ito, *EXPERIMENTAL DETERMINATION OF ELASTIC MODULUS OF CRYSTALLINE REGIONS IN ORIENTED POLYMERS.* JOURNAL OF POLYMER SCIENCE, 1962. **57**(165): p. 651-&.

30. Sturcova, A., G.R. Davies, and S.J. Eichhorn, *Elastic modulus and stress-transfer properties of tunicate cellulose whiskers.* Biomacromolecules, 2005. **6**(2): p. 1055-1061.

31. Eichhorn, S.J. and G.R. Davies, *Modelling the crystalline deformation of native and regenerated cellulose.* Cellulose, 2006. **13**(3): p. 291-307.

32. Cheng, Q.Z. and S.Q. Wang, *A method for testing the elastic modulus of single cellulose fibrils via atomic force microscopy.* Composites Part a-Applied Science and Manufacturing, 2008. **39**(12): p. 1838-1843.

33. Czaja, W.K., et al., *The future prospects of microbial cellulose in biomedical applications.* Biomacromolecules, 2007. **8**(1): p. 1-12.

34. Samir, M., F. Alloin, and A. Dufresne, *Review of recent research into cellulosic whiskers, their properties and their application in nanocomposite field.* Biomacromolecules, 2005. **6**(2): p. 612-626.

35. Angles, M.N. and A. Dufresne, *Plasticized starch/tunicin whiskers nanocomposite materials. 2. Mechanical behavior.* Macromolecules, 2001. **34**(9): p. 2921-2931.

36. Dubief, D., E. Samain, and A. Dufresne, *Polysaccharide microcrystals reinforced amorphous poly(beta-hydroxyoctanoate) nanocomposite materials.* Macromolecules, 1999. **32**(18): p. 5765-5771.

37. Eichhorn, S.J., et al., *Review: current international research into cellulose nanofibres and nanocomposites.* Journal of Materials Science, 2010. **45**(1): p. 1-33.

38. Lee, J., Q.H. Sun, and Y.L. Deng, *Nanocomposites from regenerated cellulose and nanoclay.* Journal of Biobased Materials and Bioenergy, 2008. **2**(2): p. 162-168.

39. Liu, L.Q., et al., *Mechanical properties of functionalized single-walled carbon-nanotube/poly(vinyl alcohol) nanocomposites.* Advanced Functional Materials, 2005. **15**(6): p. 975-980.

40. Cadek, M., et al., *Morphological and mechanical properties of carbon-nanotube-reinforced semicrystalline and amorphous polymer composites.* Applied Physics Letters, 2002. **81**(27): p. 5123-5125.

41. Hajji, P., et al., *Tensile behavior of nanocomposites from latex and cellulose whiskers.* Polymer Composites, 1996. **17**(4): p. 612-619.

42. Dufresne, A., J.Y. Cavaille, and W. Helbert, *Thermoplastic nanocomposites filled with wheat straw cellulose whiskers .2. Effect of processing and modeling.* Polymer Composites, 1997. **18**(2): p. 198-210.

43. Vaia, R.A., et al., *Polymer/layered silicate nanocomposites as high performance ablative materials.* Applied Clay Science, 1999. **15**(1-2): p. 67-92.

44. Giannelis, E.P., *Polymer-layered silicate nanocomposites: Synthesis, properties and applications.* Applied Organometallic Chemistry, 1998. **12**(10-11): p. 675-680.

45. Bourbigot, S., et al., *PA-6 clay nanocomposite hybrid as char forming agent in intumescent formulations.* Fire and Materials, 2000. **24**(4): p. 201-208.

46. Ray, S.S., et al., *Polylactide-layered silicate nanocomposite: A novel biodegradable material.* Nano Letters, 2002. **2**(10): p. 1093-1096.

47. Xu, R.J., et al., *New biomedical poly(urethane urea) - Layered silicate nanocomposites.* Macromolecules, 2001. **34**(2): p. 337-339.

48. Giannelis, E.P., R. Krishnamoorti, and E. Manias, *Polymer-silicate nanocomposites: Model systems for confined polymers and polymer brushes.* Polymers in Confined Environments, 1999. **138**: p. 107-147.

49. Ray, S.S. and M. Okamoto, *Polymer/layered silicate nanocomposites: a review from preparation to processing.* Progress in Polymer Science, 2003. **28**(11): p. 1539-1641.

50. Huang, Z.M., et al., *A review on polymer nanofibers by electrospinning and their applications in nanocomposites.* Composites Science and Technology, 2003. **63**(15): p. 2223-2253.

51. Taylor, G., *ELECTRICALLY DRIVEN JETS.* Proceedings of the Royal Society of London Series a-Mathematical and Physical Sciences, 1969. **313**(1515): p. 453-&.

52. Fong, H., I. Chun, and D.H. Reneker, *Beaded nanofibers formed during electrospinning.* Polymer, 1999. **40**(16): p. 4585-4592.

53. Demir, M.M., et al., *Electrospinning of polyurethane fibers.* Polymer, 2002. **43**(11): p. 3303-3309.

54. Fong, H. and D.H. Reneker, *Elastomeric nanofibers of styrene-butadiene-styrene triblock copolymer.* Journal of Polymer Science Part B-Polymer Physics, 1999. **37**(24): p. 3488-3493.

55. Zussman, E., A.L. Yarin, and D. Weihs, *A micro-aerodynamic decelerator based on permeable surfaces of nanofiber mats.* Experiments in Fluids, 2002. **33**(2): p. 315-320.

56. Matthews, J.A., et al., *Electrospinning of collagen nanofibers.* Biomacromolecules, 2002. **3**(2): p. 232-238.

57. Theron, A., E. Zussman, and A.L. Yarin, *Electrostatic field-assisted alignment of electrospun nanofibres.* Nanotechnology, 2001. **12**(3): p. 384-390.

58. Li, D., Y.L. Wang, and Y.N. Xia, *Electrospinning of polymeric and ceramic nanofibers as uniaxially aligned arrays.* Nano Letters, 2003. **3**(8): p. 1167-1171.

59. Katta, P., et al., *Continuous electrospinning of aligned polymer nanofibers onto a wire drum collector.* Nano Letters, 2004. **4**(11): p. 2215-2218.

60. Tan, E.P.S., et al., *Tensile test of a single nanofiber using an atomic force microscope tip.* Applied Physics Letters, 2005. **86**(7).

61. Yu, M.F., et al., *Strength and breaking mechanism of multiwalled carbon nanotubes under tensile load.* Science, 2000. **287**(5453): p. 637-640.

62. Tan, E.P.S. and C.T. Lim, *Mechanical characterization of nanofibers - A review.* Composites Science and Technology, 2006. **66**(9): p. 1102-1111.

63. Tan, E.P.S., S.Y. Ng, and C.T. Lim, *Tensile testing of a single ultrafine polymeric fiber.* Biomaterials, 2005. **26**(13): p. 1453-1456.

64. AC, U., *Stresses in beams, in mechanics of materials.* McGraw-Hill, 1993: p. p. 152–213.

65. Yang, F., et al., *Nanoscale indent formation in shape memory polymers using a heated probe tip.* Nanotechnology, 2007. **18**(28).

66. Li, X.D., et al., *Direct nanomechanical machining of gold nanowires using a nanoindenter and an atomic force microscope.* Journal of Micromechanics and Microengineering, 2005. **15**(3): p. 551-556.

67. Oliver, W.C. and G.M. Pharr, *AN IMPROVED TECHNIQUE FOR DETERMINING HARDNESS AND ELASTIC-MODULUS USING LOAD AND DISPLACEMENT SENSING INDENTATION EXPERIMENTS.* Journal of Materials Research, 1992. **7**(6): p. 1564-1583.

68. Bao, X., M.R. Nangrejo, and M.J. Edirisinghe, *Synthesis of silicon carbide foams from polymeric precursors and their blends.* Journal of Materials Science, 1999. **34**(11): p. 2495-2505.

69. Colombo, P. and M. Modesti, *Silicon oxycarbide ceramic foams from a preceramic polymer.* Journal of the American Ceramic Society, 1999. **82**(3): p. 573-578.

70. Kim, Y.W., et al., *Fabrication of porous preceramic polymers using carbon dioxide.* Journal of Materials Science Letters, 2002. **21**(21): p. 1667-1669.

71. Grader, G.S., G.E. Shter, and Y. de Hazan, *Novel ceramic foams from crystals of AlCl3((Pr2O)-O-i) complex.* Journal of Materials Research, 1999. **14**(4): p. 1485-1494.

72. Studart, A.R., et al., *Processing routes to macroporous ceramics: A review.* Journal of the American Ceramic Society, 2006. **89**(6): p. 1771-1789.

73. Innocentini, M.D.M., et al., *Permeability and structure of cellular ceramics: A comparison between two preparation techniques.* Journal of the American Ceramic Society, 1998. **81**(12): p. 3349-3352.

74. Vogli, E., H. Sieber, and P. Greil, *Biomorphic SiC-ceramic prepared by Si-vapor phase infiltration of wood.* Journal of the European Ceramic Society, 2002. **22**(14-15): p. 2663-2668.

75. Lange, F.F. and K.T. Miller, *OPEN-CELL, LOW-DENSITY CERAMICS FABRICATED FROM RETICULATED POLYMER SUBSTRATES.* Advanced Ceramic Materials, 1987. **2**(4): p. 827-831.

76. Sepulveda, P., *Gelcasting foams for porous ceramics.* American Ceramic Society Bulletin, 1997. **76**(10): p. 61-65.

77. Roy, D.M. and S.K. Linnehan, *HYDROXYAPATITE FORMED FROM CORAL SKELETAL CARBONATE BY HYDROTHERMAL EXCHANGE.* Nature, 1974. **247**(5438): p. 220-222.

78. Koch, D., et al., *Evolution of porosity by freeze casting and sintering of sol-gel derived ceramics.* Journal of Sol-Gel Science and Technology, 2003. **26**(1-3): p. 149-152.

79. Hotta, Y., P.C.A. Alberius, and L. Bergstrom, *Coated polystyrene particles as templates for ordered macroporous silica structures with controlled wall thickness.* Journal of Materials Chemistry, 2003. **13**(3): p. 496-501.

80. Colombo, P. and J.R. Hellmann, *Ceramic foams from preceramic polymers.* Materials Research Innovations, 2002. **6**(5-6): p. 260-272.

81. Deville, S., E. Saiz, and A.P. Tomsia, *Ice-templated porous alumina structures.* Acta Materialia, 2007. **55**(6): p. 1965-1974.

82. Zhang, H.F., et al., *Aligned two- and three-dimensional structures by directional freezing of polymers and nanoparticles.* Nature Materials, 2005. **4**(10): p. 787-793.

83. Nishihara, H., S. Iwamura, and T. Kyotani, *Synthesis of silica-based porous monoliths with straight nanochannels using an ice-rod nanoarray as a template.* Journal of Materials Chemistry, 2008. **18**(31): p. 3662-3670.

84. Gutierrez, M.C., et al., *Biocompatible MWCNT scaffolds for immobilization and proliferation of E. coli.* Journal of Materials Chemistry, 2007. **17**(29): p. 2992-2995.

85. Zhang, H. and A.I. Cooper, *Aligned porous structures by directional freezing.* Advanced Materials, 2007. **19**(11): p. 1529-1533.

86. Zhang, H., et al., *Synthesis of porous microparticles with aligned porosity.* Advanced Functional Materials, 2008. **18**(2): p. 222-228.

87. Korber, C., et al., *INTERACTION OF PARTICLES AND A MOVING ICE-LIQUID INTERFACE.* Journal of Crystal Growth, 1985. **72**(3): p. 649-662.

88. Asthana, R. and S.N. Tewari, *THE ENGULFMENT OF FOREIGN PARTICLES BY A FREEZING INTERFACE.* Journal of Materials Science, 1993. **28**(20): p. 5414-5425.

89. Mullins, W.W. and R.F. Sekerka, *STABILITY OF PLANAR INTERFACE DURING SOLIDIFICATION OF DILUTE BINARY ALLOY.* Journal of Applied Physics, 1964. **35**(2): p. 444-&.

90. Barthlott, W. and C. Neinhuis, *Purity of the sacred lotus, or escape from contamination in biological surfaces.* Planta, 1997. **202**(1): p. 1-8.

91. Gao, X.F. and L. Jiang, *Water-repellent legs of water striders.* Nature, 2004. **432**(7013): p. 36-36.

92. Gao, X.F., et al., *The dry-style antifogging properties of mosquito compound eyes and artificial analogues prepared by soft lithography.* Advanced Materials, 2007. **19**(17): p. 2213-+.

93. Parker, A.R. and C.R. Lawrence, *Water capture by a desert beetle.* Nature, 2001. **414**(6859): p. 33-34.

94. Scardino, A., et al., *Microtopography and antifouling properties of the shell surface of the bivalve molluscs Mytilus galloprovincialis and Pinctada imbricata.* Biofouling, 2003. **19**: p. 221-230.

95. Schultz, M.P., C.J. Kavanagh, and G.W. Swain, *Hydrodynamic forces on barnacles: Implications on detachment from fouling-release surfaces.* Biofouling, 1999. **13**(4): p. 323-335.

96. Saito, H., et al., *A study on snow sticking weight to water-repellent coatings.* Materials Science Research International, 1997. **3**(4): p. 216-219.

97. Kako, T., et al., *Adhesion and sliding of wet snow on a super-hydrophobic surface with hydrophilic channels.* Journal of Materials Science, 2004. **39**(2): p. 547-555.

98. Quere, D., *Non-sticking drops.* Reports on Progress in Physics, 2005. **68**(11): p. 2495-2532.

99. Zielecka, M. and E. Bujnowska, *Silicone-containing polymer matrices as protective coatings - Properties and applications.* Progress in Organic Coatings, 2006. **55**(2): p. 160-167.

100. Wenzel, R.N., *Resistance of solid surfaces to wetting by water.* Industrial and Engineering Chemistry, 1936. **28**: p. 988-994.

101. Cassie, A.B.D. and S. Baxter, *Wettability of porous surfaces.* Transactions of the Faraday Society, 1944. **40**: p. 0546-0550.

102. Li, X.M., D. Reinhoudt, and M. Crego-Calama, *What do we need for a superhydrophobic surface? A review on the recent progress in the preparation of superhydrophobic surfaces.* Chemical Society Reviews, 2007. **36**(9): p. 1529-1529.

103. Feng, L., et al., *Super-hydrophobic surfaces: From natural to artificial.* Advanced Materials, 2002. **14**(24): p. 1857-1860.

104. Sun, M.H., et al., *Artificial lotus leaf by nanocasting.* Langmuir, 2005. **21**(19): p. 8978-8981.

105. Lee, W., et al., *Nanostructuring of a polymeric substrate with well-defined nanometer-scale topography and tailored surface wettability.* Langmuir, 2004. **20**(18): p. 7665-7669.

106. Martines, E., et al., *Superhydrophobicity and superhydrophilicity of regular nanopatterns.* Nano Letters, 2005. **5**(10): p. 2097-2103.

107. Furstner, R., et al., *Wetting and self-cleaning properties of artificial superhydrophobic surfaces.* Langmuir, 2005. **21**(3): p. 956-961.

108. Fresnais, J., L. Benyahia, and F. Poncin-Epaillard, *Dynamic (de)wetting properties of superhydrophobic plasma-treated polyethylene surfaces.* Surface and Interface Analysis, 2006. **38**(3): p. 144-149.

109. Minko, S., et al., *Two-level structured self-adaptive surfaces with reversibly tunable properties.* Journal of the American Chemical Society, 2003. **125**(13): p. 3896-3900.

110. Wu, X.D., L.J. Zheng, and D. Wu, *Fabrication of superhydrophobic surfaces from microstructured ZnO-based surfaces via a wet-chemical route.* Langmuir, 2005. **21**(7): p. 2665-2667.

111. Huang, L., et al., *Stable superhydrophobic surface via carbon nanotubes coated with a ZnO thin film.* Journal of Physical Chemistry B, 2005. **109**(16): p. 7746-7748.

112. Shiu, J.Y., et al., *Fabrication of tunable superhydrophobic surfaces by nanosphere lithography.* Chemistry of Materials, 2004. **16**(4): p. 561-564.

113. Zhai, L., et al., *Stable superhydrophobic coatings from polyelectrolyte multilayers.* Nano Letters, 2004. **4**(7): p. 1349-1353.

114. Han, J.T., et al., *Stable superhydrophobic organic-inorganic hybrid films by electrostatic self-assembly.* Journal of Physical Chemistry B, 2005. **109**(44): p. 20773-20778.

115. Jiang, L., Y. Zhao, and J. Zhai, *A lotus-leaf-like superhydrophobic surface: A porous microsphere/nanofiber composite film prepared by electrohydrodynamics.* Angewandte Chemie-International Edition, 2004. **43**(33): p. 4338-4341.

116. Acatay, K., et al., *Tunable, superhydrophobically stable polymeric surfaces by electrospinning.* Angewandte Chemie-International Edition, 2004. **43**(39): p. 5210-5213.

117. Ma, M.L., et al., *Superhydrophobic fabrics produced by electrospinning and chemical vapor deposition.* Macromolecules, 2005. **38**(23): p. 9742-9748.

118. Sommers, A.D. and A.M. Jacobi, *Creating micro-scale surface topology to achieve anisotropic wettability on an aluminum surface.* Journal of Micromechanics and Microengineering, 2006. **16**(8): p. 1571-1578.

119. Zhao, Y., et al., *Anisotropic wetting characteristics on submicrometer-scale periodic grooved surface.* Langmuir, 2007. **23**(11): p. 6212-6217.

120. Xia, D.Y., et al., *Tailoring Anisotropic Wetting Properties on Submicrometer-Scale Periodic Grooved Surfaces.* Langmuir, 2010. **26**(4): p. 2700-2706.

121. Chung, J.Y., J.P. Youngblood, and C.M. Stafford, *Anisotropic wetting on tunable micro-wrinkled surfaces.* Soft Matter, 2007. **3**(9): p. 1163-1169.

122. Bliznyuk, O., et al., *Scaling of anisotropic droplet shapes on chemically stripe-patterned surfaces.* Physical Review E, 2009. **79**(4).

123. Li, W., et al., *Anisotropic wetting behavior arising from superhydrophobic surfaces: Parallel grooved structure.* Journal of Physical Chemistry B, 2008. **112**(24): p. 7234-7243.

124. Semprebon, C., et al., *Anisotropy of Water Droplets on Single Rectangular Posts.* Langmuir, 2009. **25**(10): p. 5619-5625.

125. Yong, X. and L.T. Zhang, *Nanoscale Wetting on Groove-Patterned Surfaces.* Langmuir, 2009. **25**(9): p. 5045-5053.

CHAPTER 3

HIGHLY ALIGNED CELLULOSE NANOWHISKER REINFORCED PVA NANOFIBER WEBS VIA ELECTROSPINNING METHODS

Abstract

Cellulose nanowhisker reinforced poly(vinyl alcohol) (PVA) nanofiber webs are successfully fabricated using an electrospinning technique. The morphology and mechanical properties of aligned and isotropic electrospun fiber webs are investigated. The relative alignment degree of electrospun fiber webs is analyzed using a fast Fourier transform (FFT) method. The standard deviation of aligned and isotropic electrospun webs is 31.3^{o} and 51.9^{o}, respectively. Compared with those of isotropic electrospun fiber webs, the modulus and tensile strength of isotropic webs increase 35% and 45%, respectively. Isotropic electrospun webs, loaded with 15.0wt% of cellulose nanowhiskers, shows an 86% higher tensile strength and 105% higher modulus. For the aligned electrospun webs with same loading ratio, a 95% increase of tensile strength and 117% increase of modulus are observed. The load transfer mechanisms of aligned/isotropic PVA electrospun webs are also investigated.

Keywords: Electrospinning, Fiber alignment, Mechanical properties, FFT image analysis

3.1 Introduction

In recent years, natural fibers have been widely used as reinforcement materials in polymeric nanocomposites due to the environmental concerns. Cellulose nanowhiskers have also attracted much attention as environmentally friendly nanofillers for polymer composite enhancement. It was reported that the modulus of the crystalline region of cellulose was 137GPa measured by X-ray diffraction [1], 143GPa measured by Raman spectroscopic technique [2], and 149GPa ~ 155GPa calculated by computational simulation [3]. It is expected that the modulus of cellulose nanowhiskers is slightly lower than that of the crystalline cellulose. Moreover, cellulose nanowhiskers have a lower density than inorganic filler materials. Cellulose nanowhiskers are also naturally abundant, renewable and non-toxic resources. Cellulose nanowhiskers are bar-type particles. They are considered as a string of cellulose crystals connected by cellulose amorphous domains [4]. The diameters of cellulose nanowhiskers range from 5nm to 20 nm and their lengths are between 150nm and 400nm, depending on the source of cellulose nanowhiskers and their preparation conditions [5].

Cellulose nanowhiskers are stable in aqueous solution and are dispersed well with most of the hydrosoluble polymers. It was also reported that surface modified cellulose nanowhiskers are mixed will with organic solvents. Due to the highly reactive hydroxyl groups on cellulose nanowhiskers, their surfaces can be easily modified with a surfactant [6], chemicals [7-8], and cross-linking agent [9]. It was reported that cellulose nanowhisker reinforced nanocomposites showed significantly improved mechanical properties for both the natural and synthetic polymer matrices such as starch [10], cellulose acetate butyrate [11], poly(vinyl chloride) [12], poly(oxyethylene) [13], and poly(vinyl alcohol) [14].

Electrospinning is a versatile and an effective method to produce nanoscale to microscale fibers from solution. In electrospinning, high charges are applied to the liquid solution. As the intensity of the electric charges on the liquid solution surface increases,

the surface elongates until the electrostatic force overcomes the surface tension and a charged jet of the solution is ejected to the metal collector. During the flight of the jet, the solvent evaporates quickly and the dried electrospun fibers are collected. Various types of nanofibers from polymer [14-15], inorganic materials [16] and hybrid (organic/inorganic) materials [17] were fabricated using the electrospinning technique. These nanofibers can be used for a wide variety of applications such as separation filters, wound dressing materials, tissue scaffold, sensors and so on [18-20]. Cellulose nanowhiskers have been used as reinforcing materials for electrospun fibers such as polystyrene [21], poly(vinylalcohol) [22], poly(lactic acid) [23] and so on.

Many fabrication techniques to control the arrangement and alignment of electrospun fibers have been investigated. These techniques include rotating collector methods [24], parallel electrodes techniques [25], and rotating wire drum methods [26]. It was reported that alignment degrees of electrospun fibers can affect mechanical properties of electrospun fiber webs [27-29] and cell proliferation rates on electrospun fiber templates [28-32]. It was also studied that the linear velocity of the rotating collector can affect the crystallinity, mechanical properties, and alignment degree of electrospun fibers [33].

In this study, the morphology and alignment degree of electrospun fibers was studied and the mechanical properties of cellulose nanowhisker reinforced PVA electrospun fibers have been measured. The alignment effects of electrospun fibers and cellulose nanowhiskers on the bulk properties of electrospun webs have been studied. In these experiments, PVA was used as the matrix material for electrospinning. PVA is a semi-crystalline hydrophilic polymer with good chemical and thermal stability. It was reported that PVA shows positive compatibility with cellulose nanowhiskers [14], and it is highly biocompatible and non-toxic.

3.2 Experimental details

3.2.1 Materials

Poly(vinyl alcohol) (PVA) (Mw=127,000 g/mol, 99+% hydrolyzed) was purchased from Aldrich. The suspensions of cellulose nanowhiskers were prepared from Whatman No. 1 filter paper by sulfuric acid hydrolysis. The concentration of sulfuric acid was fixed at 64%. 20g of filter paper were dispersed in 175ml of sulfuric acid (the ratio of the filter paper to sulfuric acid was fixed at 1:8.75 (g/ml)). The acid hydrolysis conditions were optimized at 45°C and 50mins [34]. After hydrolysis, the suspension was deionized by mixing in 1g of mixed-bed ion exchange resin. The suspension was then washed with DI water and centrifuged (40mins, 3000rpm, Beckman Coulter, GS-6). The suspension was further dispersed by an ultrasound sonicator (15mins at full power, Branson 3510). The length of obtained cellulose nanowhiskers ranges from 180nm to 220nm and the width is between 5nm and 10nm. Water was obtained from a Nanopure ultrapure water system with a resistivity of about 18 MΩ cm.

3.2.2 Electrospinning methods

High voltage power supply (Keltron co., H545A) was used for the electrospinning. The PVA/cellulose nanowhisker solution was put inside a pipette. The end part of insulation rubbers protecting electric cables was removed and a bare copper wire was placed in the pipette. A positive voltage (20kV) was applied to PVA/cellulose nanowhisker solution through a copper wire as shown in Fig 3-1. The distance between the tip of the pipette and a grounded metal sheet was fixed at 20cm. To form isotropic electrospun fiber webs, the PVA/cellulose nanowhisker solution was electrospun onto the stationary aluminum foil. To fabricate oriented fiber webs, a rotating metal drum (diameter=6cm) was used. The rotating rate of metal drum was fixed at 1200 rpm (corresponding to a linear velocity of 3.77m/s). The schematic of the fabrication process

for a) isotropic electrospun webs on a stationary flat metal collector and b) aligned electrospun webs on a rotating metal drum are shown in Fig 3-1.

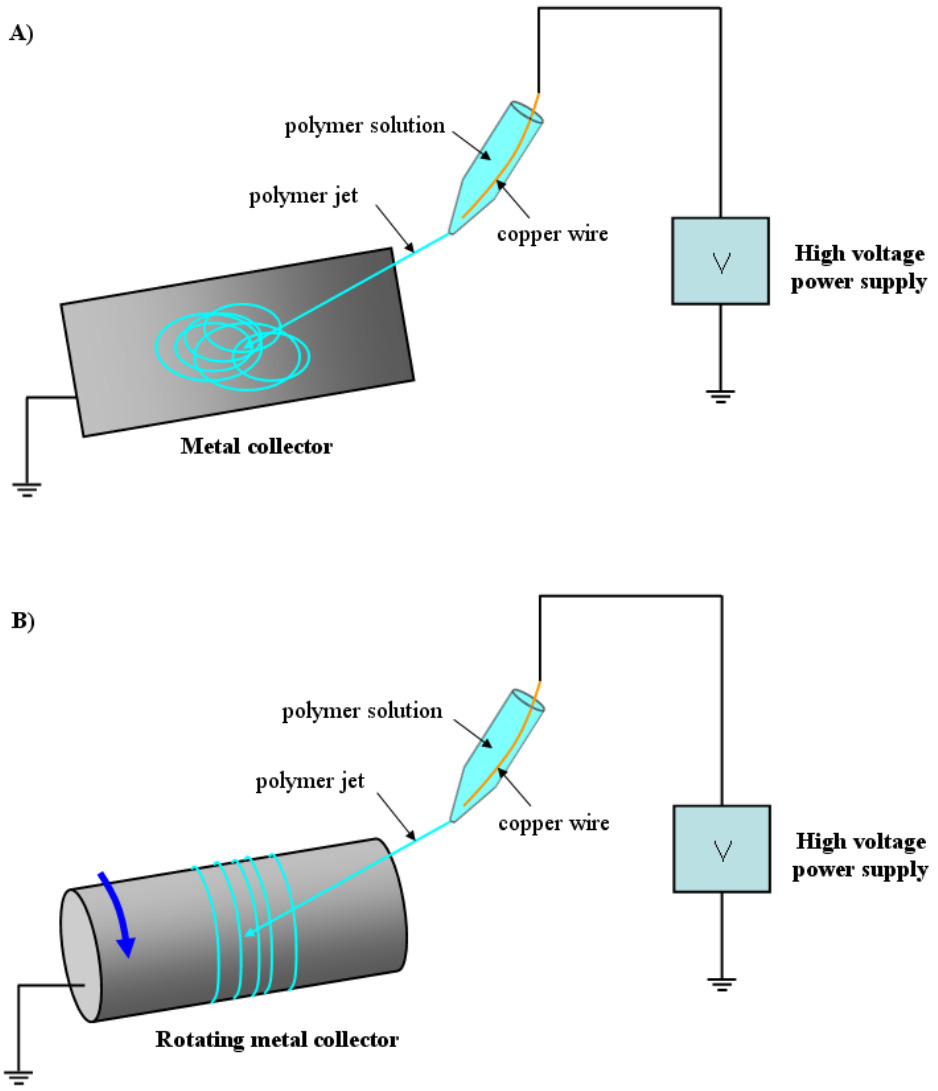

Figure 3-1 (a) Schematic of the fabrication process for isotropic electrospun webs on a stationary flat metal collector (b) Schematic of the fabrication process for aligned electrospun webs on a rotating metal drum.

After electrospinning, the fiber webs were carefully detached from the aluminum foil and metal drum for imaging and mechanical tests. To make it easy to peel off the electrospun fiber webs from the substrates, a thin layer film of poly(propylene) was attached to the aluminum foil and the metal drum before electrospinning. Poly(propylene) coating on the aluminum foil and metal drum doesn't affect the electrospinning process, but it was found that PVA based electrospun fiber webs were peeled off easily.

3.2.3 Image analysis

The relative alignment of electrospun fiber webs was analyzed using a fast Fourier transform (FFT) method [35]. For analysis, grayscale, 8-bit TIF SEM micrograph images were cropped to 2048 × 2048 pixels. FFT analysis was conducted using ImageJ software (NIH, http://rsb.info.nih.gov/ij) supported by an oval profile plug-in (created by William O'Connell).

For FFT analysis, an original data image is first converted to a grayscale data image. The FFT function converts information in the grayscale data image from the real space into the mathematically defined frequency space. This frequency domain maps how fast pixel intensities change in the spatial domain. For example, if the color of pixels arranged to a given direction changes many times between black and white, this direction is considered as a high frequency direction and a bright dot is marked in a frequency space. If there is no change of pixel intensities to a certain direction, a black dot is marked to this direction.

After getting the FFT output image, a radial summation of the pixel intensities of the FFT output image is conducted to convert the FFT frequency distribution to the angular intensity. A circular projection is conducted on the FFT output image for the radial summation. The conversion is done for each angle between 0^o and 359^o (with 1^o increments) using an oval profile plug-in program.

Finally, the angular intensity plot obtained by the radial summation of FFT output image is converted to a normalized % angular distribution plot. The % angular distribution at a certain degree is defined as

$$\frac{\text{the angular intensity at a given degree}}{\text{the summation of angular intensity between } 0^{o} \text{ and } 359^{o}} \times 100 \qquad (3.1)$$

The degree which has the highest intensity is set to 90° and 270° to compare the alignment degree of different samples.

A representative SEM image of the aligned PVA electrospun webs, a FFT output image, a radial summation of the FFT output and its angular distribution plot are all shown in Fig 3-2. A square SEM image was selected and converted to a grayscale image before using the FFT method (Fig 3-2 (a)). As shown in the FFT output image (Fig 3-2 (b)), white dots are found at the direction vertical to the fiber alignment direction. A circular projection was conducted on the FFT output image for the regular radial summation for each degree (Fig 3-2 (c)). The highest angular intensity was found at 143° and 323°. They are converted to 90° and 270° as shown in Fig 3-2 (d).

3.2.4 Characterization

Scanning electron microscopy (SEM) was carried out using a LEO 1530 at 10kV. The samples were sputter coated with Au using EMS 350 sputter (20mA, 2mins) prior to observation. The analysis of SEM images and a measurement of average diameters of electrospun fibers were conducted using ImageTool 3.0 software, which is provided by UTHSCSA. The diameters of electrospun fibers were measured across the image and the average value was determined by taking the average of 60 measurements that were randomly chosen. The tensile strength and modulus were measured using Instron 4400R. The cross head speed was 10mm/min.

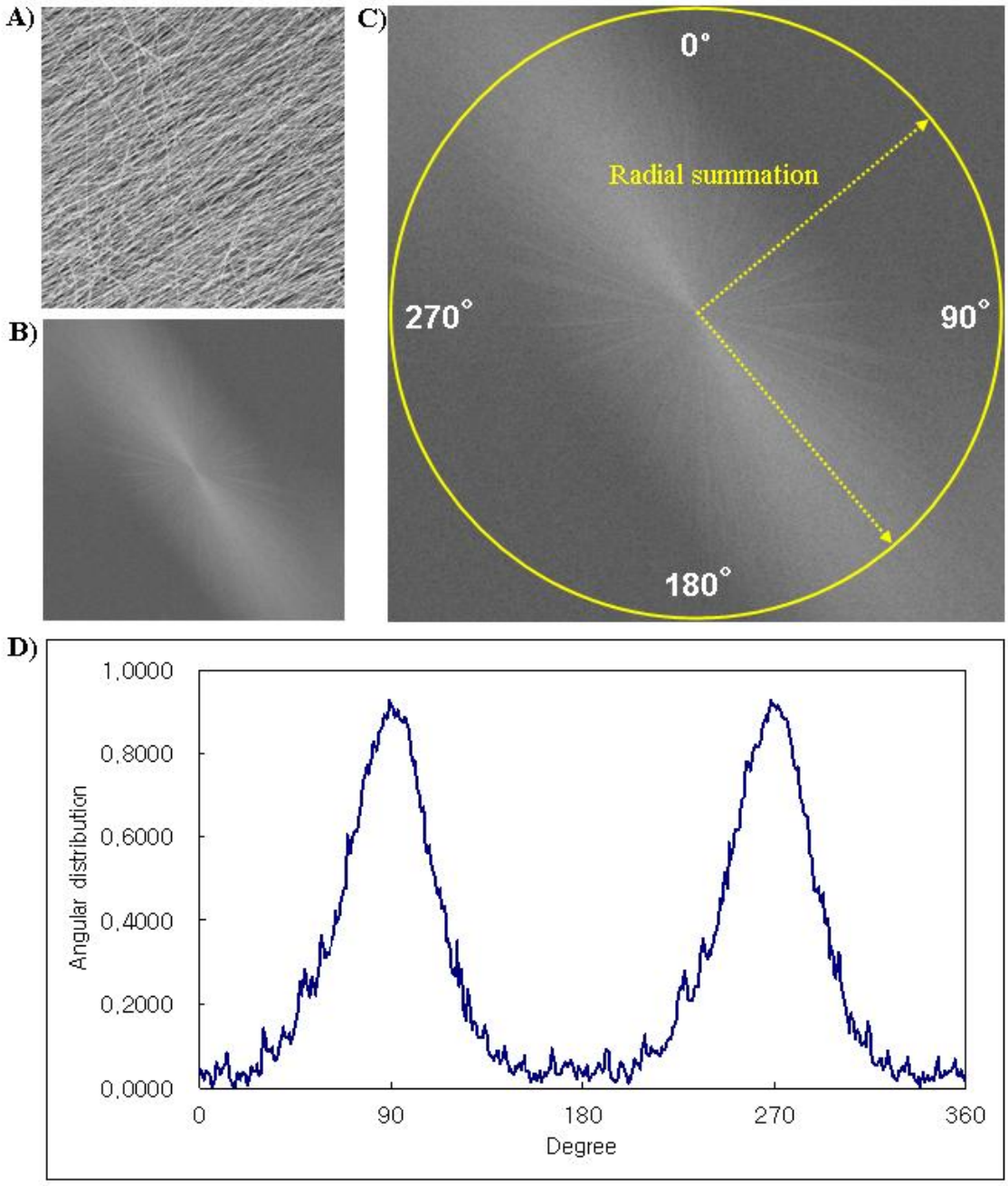

Figure 3-2 (a) A representative SEM image of the aligned electrospun web (b) a fast Fourier transform (FFT) output image (c) a radial summation of the FFT output by the oval projection (d) angular distribution plot.

3.3 Results and discussion

3.3.1 Morphology and alignment of PVA electrospun fibers

The effect of the rotating speed of the metal collector on the morphology of PVA electrospun fibers has been investigated. Various linear velocities ranging from 1.88 m/s to 7.54 m/s have been chosen. Applied voltage and PVA concentration were fixed at 20kV and 8.0wt%, respectively. The distance between the tip of the pipette and the grounded metal sheet was fixed at 25cm.

Table 3-1. The relation between the linear velocity of the rotating collector and fiber alignment.

Sample no.	diameter of metal collector (cm)	rpm	linear velocity (m/s)	alignment of electrospun fibers
1	A stationary metal collector	-	-	no alignment was observed
2	6	600	1.88	no alignment was observed
3	6	1200	3.77	aligned
4	6	1800	7.54	no deposition of fibers
5	7	1200	4.40	aligned
6	8	1200	5.02	aligned

When the rotating speed was fixed at 600 rpm (corresponding to linear velocity of 1.88 m/s), no alignment of electrospun fibers was observed. On the other hand, if the rotating speed is set at 1800 rpm (corresponding to linear velocity of 7.54 m/s), the a very limited number of fibers were deposited on the collector after overnight electrospinning. The results are summarized in Table 3-1.

The mechanism of electrospun fiber alignment via a rotating cylinder has not yet been very clear. A reasonable explanation is given as follows. When the end of fiber is

attached on the cylinder surface and a linear speed of the rotating cylinder surface is the same as the flying speed of the polymer jet, the fibers are tightly taken up on the rotating surface of the cylinder, resulting in the alignment of electrospun fibers. Such a speed can be called an alignment speed. If the surface speed of the cylinder is slower than the alignment speed, randomly deposited fibers will be collected. On the other hand, a rotating speed too high will break the fiber jet resulting in no fiber collection [36].

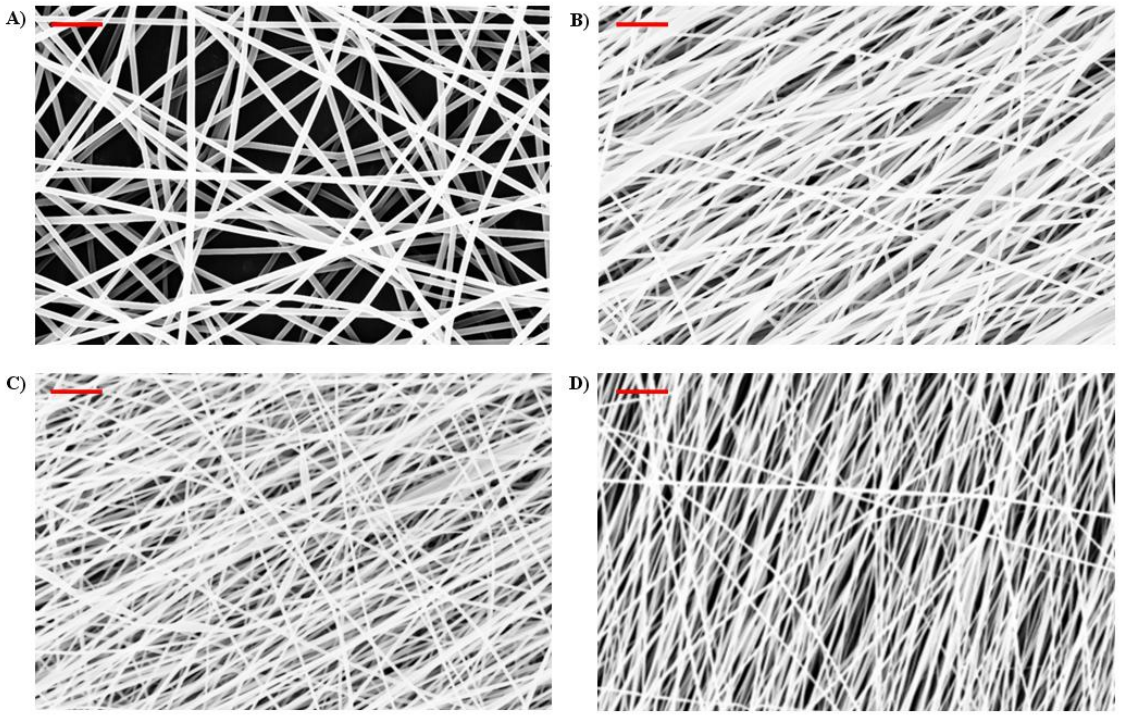

Figure 3-3. SEM images of (a) sample no.1 (a stationary metal collector) (b) sample no.3 (linear velocity: 3.77 m/s) (c) sample no. 5 (linear velocity: 4.40 m/s) (d) sample no. 6 (linear velocity: 5.02 m/s) (scale bar: 4 μm).

The SEM images of each sample are shown in Fig 3-3. The average diameter of sample 1 (a stationary metal collector) was 292nm. When the metal drum starts to rotate, the average diameter of collecting fibers decreases dramatically. When the linear velocity of the metal drum is 3.77 m/s, the diameter is 170 nm. In the case of sample 6 (linear

velocity of 5.02 m/s), the average diameter is 141 nm. The reason for the decrease in diameter is not very clear yet. A possible explanation is the extra stretching of fibers on the rotating metal collector. It is expected that the strong shear force induced by the high speed rotating drum makes the PVA electrospun fibers thinner. The experimental results are summarized in Fig 3-4.

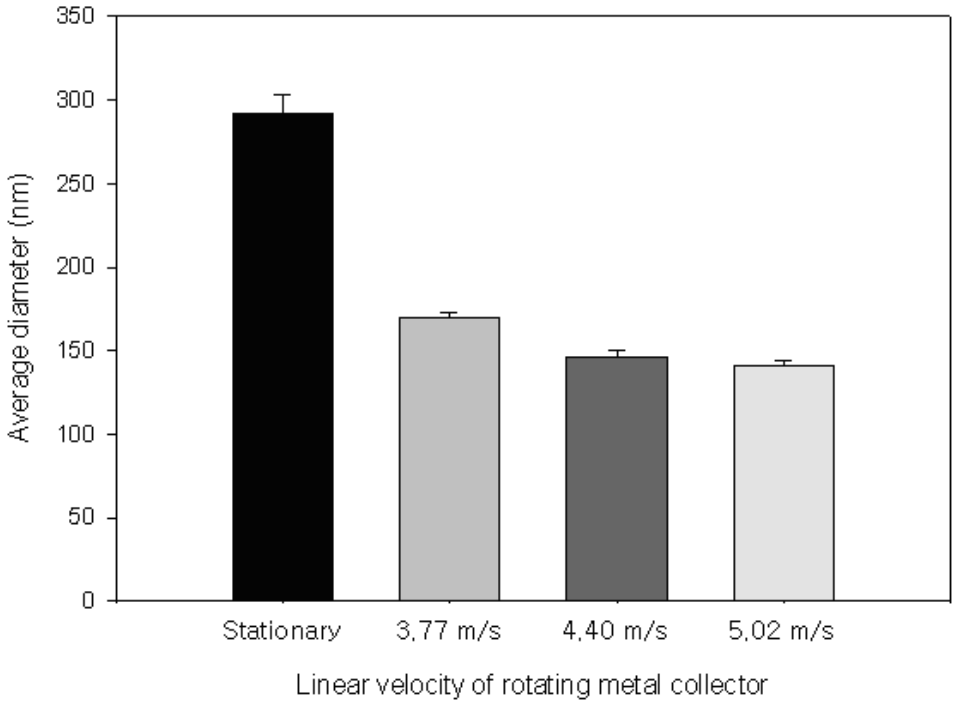

Figure 3-4. Average diameter of PVA electrospun fibers collected with different rotating speeds (0 ~ 5.02 m/s).

3.3.2 Image analysis

The degree of fiber alignment of electrospun webs were analyzed using the FFT method and the oval projection method. Aligned PVA electrospun fiber webs were fabricated using a rotating metal drum with a rotating rate of 1200 rpm (linear velocity of 3.77 m/s), and isotropic electrospun webs were prepared on a stationary flat metal

collector. Applied voltage and PVA concentration were fixed at 20kV and 8.0wt%. 16 samples were used for the image analysis of the aligned and isotropic electrospun webs.

SEM images of the aligned electrospun webs, their fast Fourier transform (FFT) output images, and angular distribution plots of each case are all shown in Fig 3-5. In these cases, most of the Y-axis values (angular distribution, %) were plotted between 0.0 and 1.0. As shown in FFT output images, the brightest peaks were found at 21^o (201^o), 59^o (239^o), 60^o (240^o) and 22^o (202^o), respectively. This suggests that the number of electrospun fibers aligned with those angles is the smallest for each case and the most occupied angles by electrospun fibers are 111^o, 139^o, 150^o and 112^o, respectively. After the oval projection, pixel intensities were converted to % distribution for 360 total degrees using 1^o interval, and then result plots were moved parallel to the x-axis to get the highest peak at 90^o and 270^o as shown in Fig 3-5 (c). The standard deviation of 8 samples was calculated to compare the degree of alignment. The standard deviation of aligned electrospun fiber webs ranges from 27.4 to 33.2, and the average value was 31.3.

The alignment of isotropic webs was investigated in the same manner. SEM images of the isotropic electrospun webs, their fast Fourier transform (FFT) output images, and angular distribution plots of each case are all shown in Fig 3-6. Clearly shown in the FFT output images of aligned electrospun webs, there is no bright peak at a certain angle. Instead, bright dots were found at all of the angles. This suggests that most of the fibers were distributed randomly. FFT results were converted to angular distribution and their % angular distribution ranges from 0.25 to 0.30 as shown in Fig 3-6 (c). A theoretical average value of % angular distribution is 0.278%. The standard deviation of 8 isotropic web samples was also calculated. The standard deviation of each case ranges from 51.7 to 52.0, and the average value is 51.9.

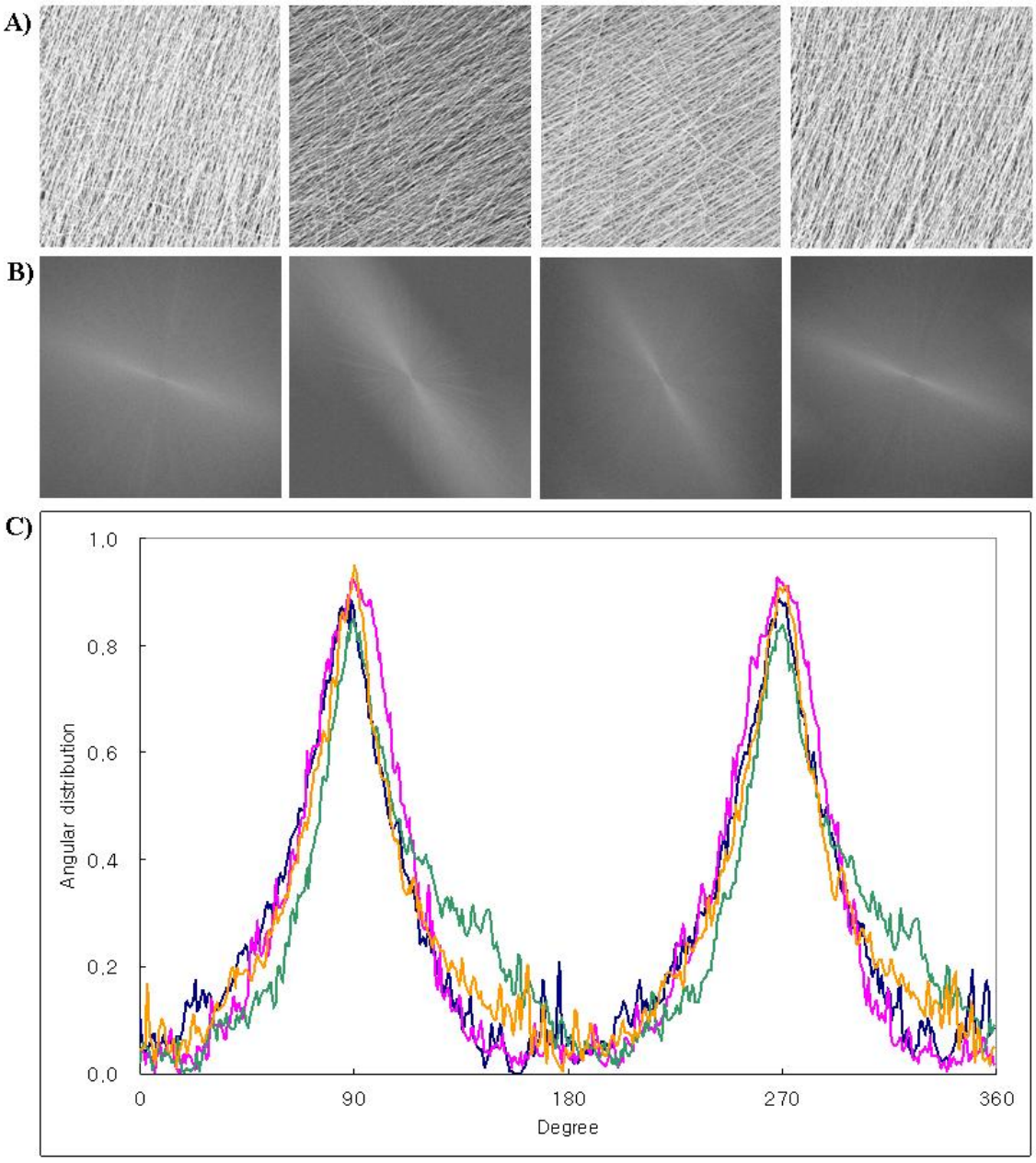

Figure 3-5 (a) SEM images of the aligned electrospun webs (b) fast Fourier transform (FFT) output images (c) angular distribution plots of aligned electrospun webs (angular distribution scale: 0.0 ~ 1.0).

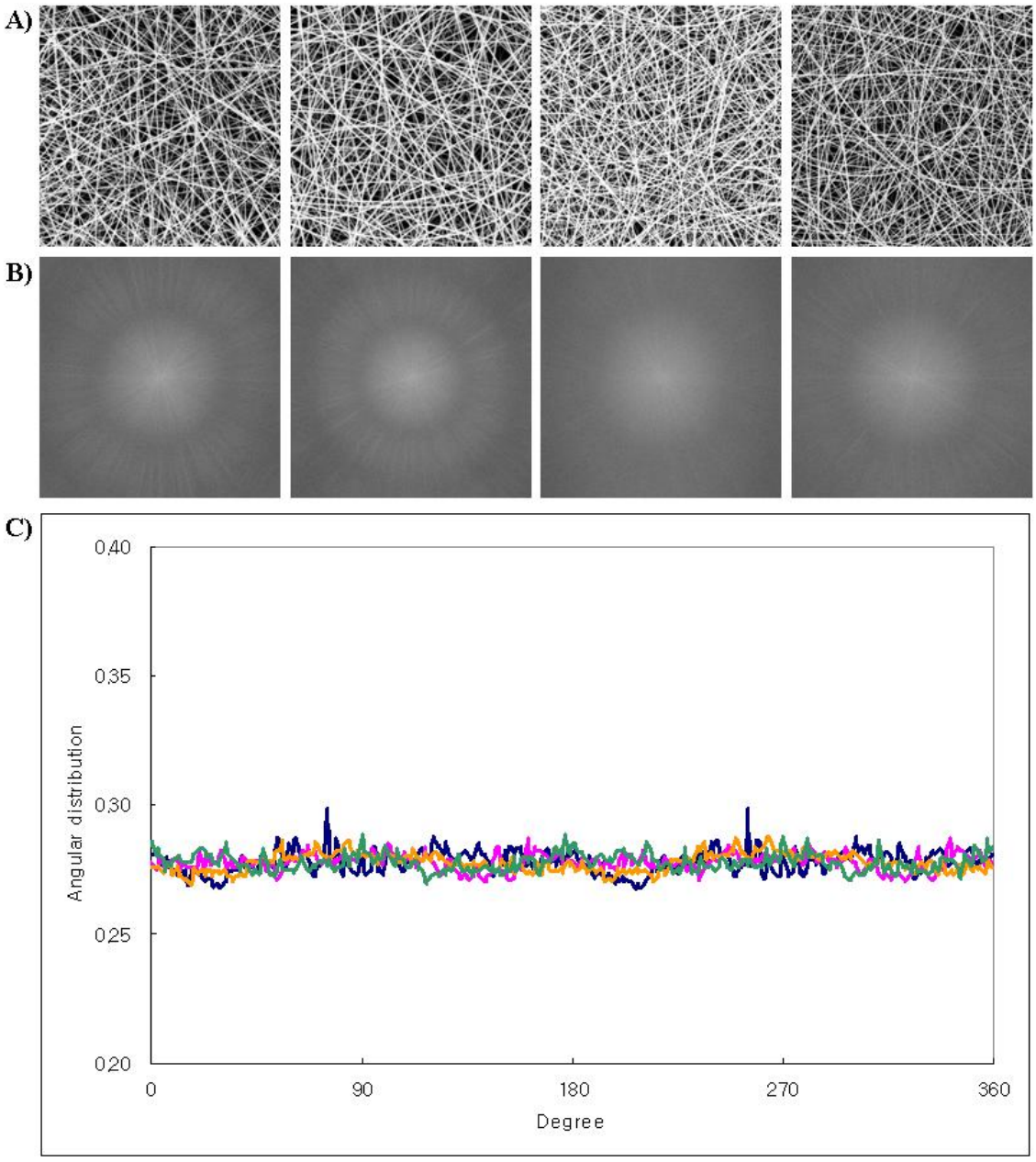

Figure 3-6 (a) SEM images of the isotropic electrospun webs (b) fast Fourier transform (FFT) output images (c) angular distribution plots of isotropic electrospun webs (angular distribution scale: 0.20 ~ 0.40).

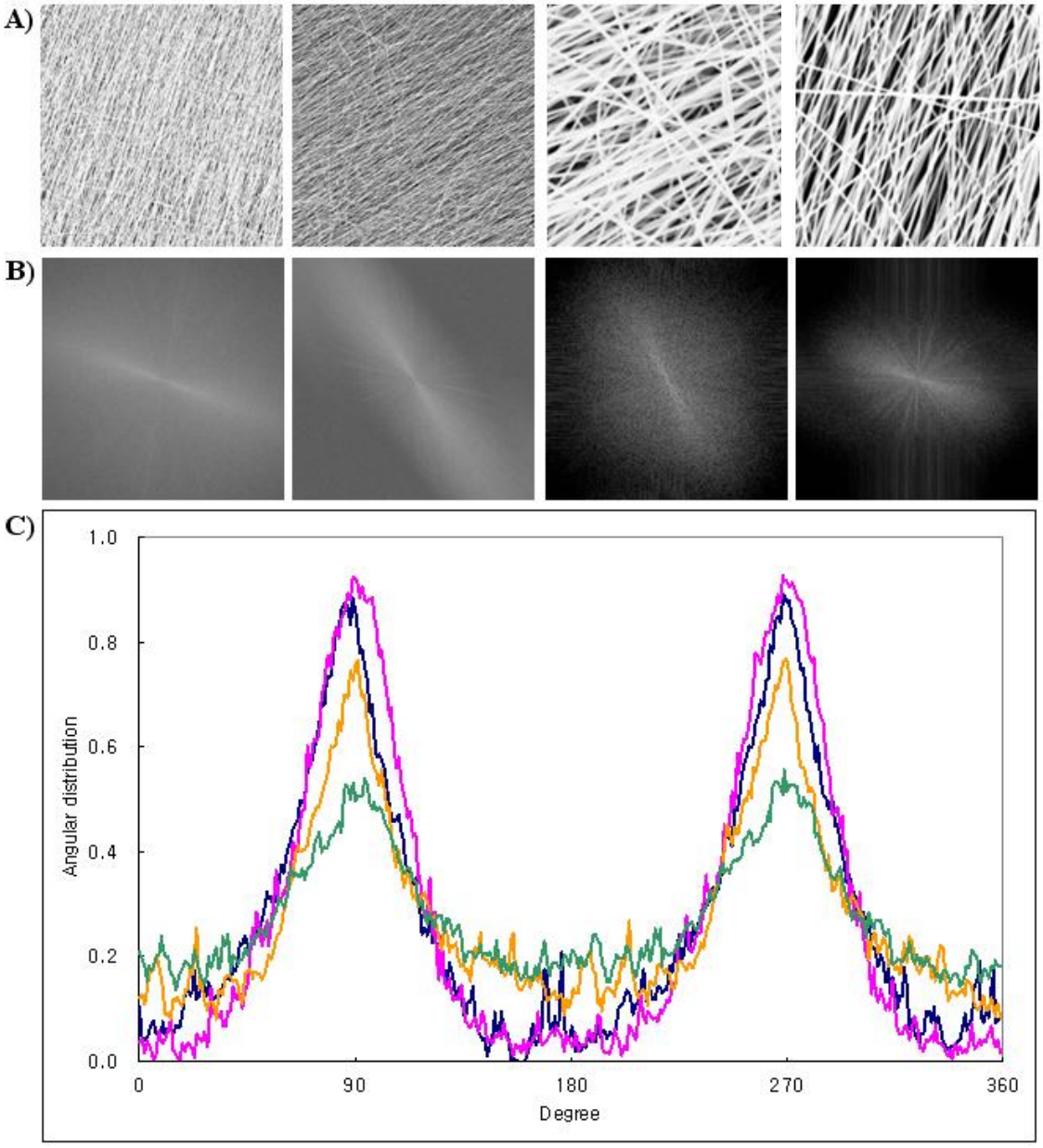

Figure 3-7 (a) SEM images of the aligned electrospun webs prepared using different rotating rates (b) fast Fourier transform (FFT) output images (c) angular distribution plots.

The effect of the linear velocity of the rotating collector on the alignment of electrospun webs was investigated using FFT method. The degree of alignment of electrospun webs prepared by different linear velocities (3.77 m/s, 4.40 m/s and 5.02 m/s) was compared. The FFT output images and their angular distribution plots are shown in Fig 3-7. The standard deviation of aligned webs fabricated using 4.40 m/s ranges from 38.2 to 39.6, and the average value is 38.9. For aligned electrospun webs prepared using 5.02 m/s linear velocity, the standard deviation is between 40.9 and 44.2 with an average of 42.5. As shown in Fig 3-7 (c), the standard deviation of electrospun webs using 3.77 m/s is 31.3. From % angular distribution plots and standard deviation results, it is clear that among all the proposed experimental conditions, using a linear velocity of 3.77m/s will best fabricate the most highly aligned PVA electrospun webs.

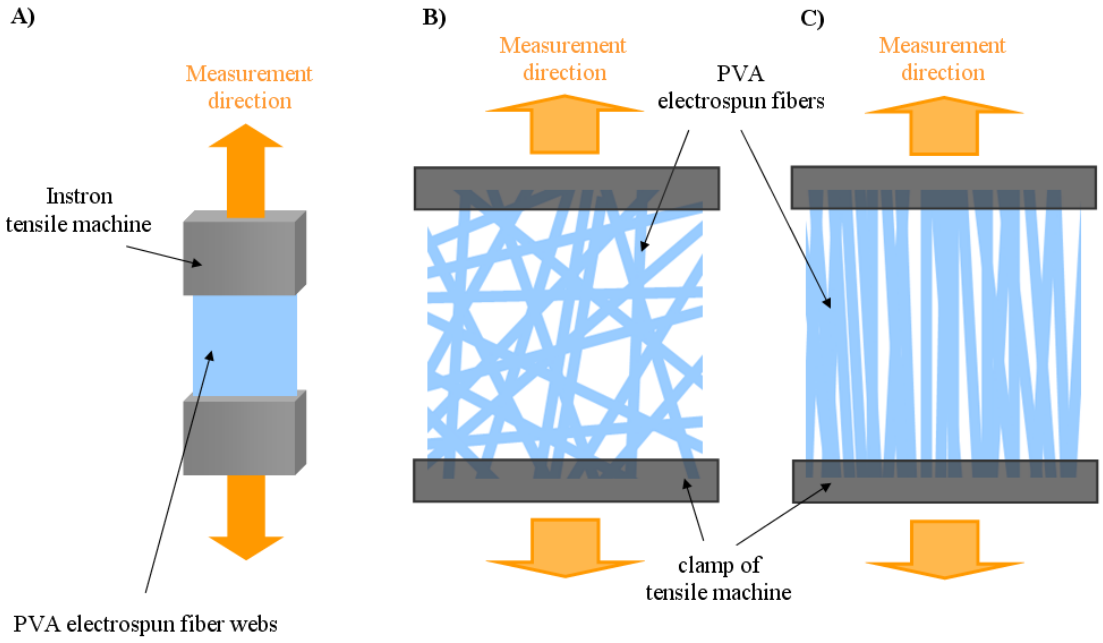

Figure 3-8. Schematics of the mechanical property measurement of the (a) electrospun fiber webs by Instron tensile machine (b) isotropic PVA electrospun webs (c) aligned electrospun webs.

3.3.3 Mechanical properties of aligned/isotropic PVA electrospun fiber webs

The effect of fiber connectivity on the mechanical properties of aligned/isotropic electrospun fiber webs has been studied. The schematic of the electropinning apparatus with a stationary flat metal collector is shown in Fig 3-1 (a). Aligned PVA electrospun fiber webs were fabricated using a rotating metal drum as shown in Fig 3-1 (b). The rotating rate of the metal drum has been fixed at 1200 rpm to get the most oriented electrospun web structure. The direction of a tensile measurement of aligned electrospun fiber webs was along the fiber orientation. From the image analysis results, it was found that the standard deviation of aligned and isotropic electrospun webs is 31.3^{o} and 51.9^{o}, respectively.

The scheme of the mechanical property measurement by Instron tensile machine is shown in Fig 3-8. The measurement direction of aligned electrospun webs is parallel to the fiber alignment direction (Fig 3-8 (c)). The tensile strength of aligned electrospun web and isotropic electrospun webs is shown in Fig 3-9. The tensile strength of pure PVA isotropic electrospun webs is 4.21MPa, and the tensile strength of aligned web is 5.37MPa. For the aligned electrospun web, a 28% increase in tensile strength has been observed, compared to randomly collected electrospun webs. To investigate the fiber density of electrospun webs, the weights of electrospun web membranes were measured. It was found that the density of aligned PVA electrospun fiber webs is 11.2 % higher than the isotropic webs.

As shown in Fig 3-4, the average diameter of randomly deposited PVA fibers is 292 nm, and that of PVA electrospun fibers collected on a rotating drum (with a linear velocity 3.77 m/s) is 170 nm. Based on the assumption that the density of electrospun fibers is the same regardless of the diameter, it is concluded that 336% more number of fibers exist in aligned fiber webs, compared with isotropic electrospun webs. In Fig 3-9, the experimental results were plotted based on both of the thickness (volume) basis and the weight basis. The modulus of aligned electrospun web and isotropic electrospun webs

is shown in Fig 3-10. The modulus of pure PVA isotropic electrospun web is 64.7MPa, and that of aligned webs is 87.4MPa. Aligned electrospun webs showed a 35% increase in modulus, in comparison to unoriented PVA electrospun webs.

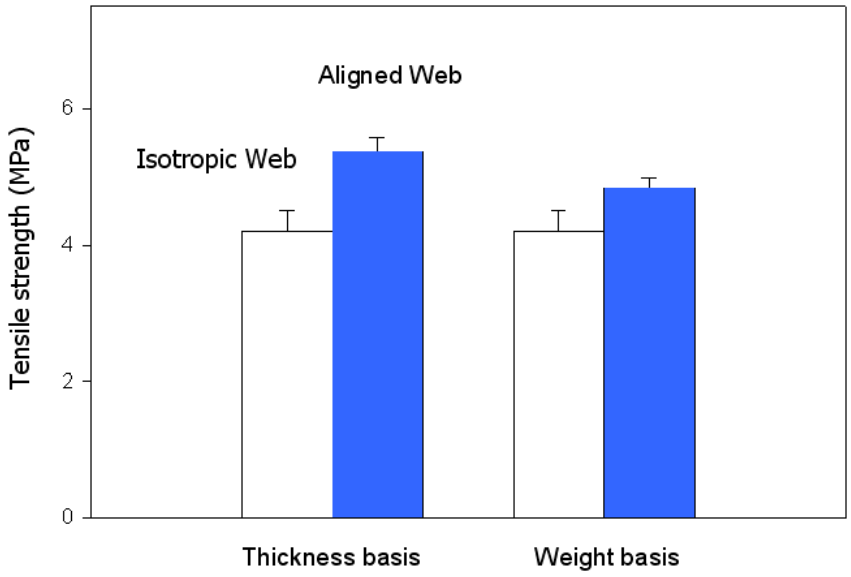

Figure 3-9. Tensile strength of Aligned electrospun web and isotropic electrospun web.

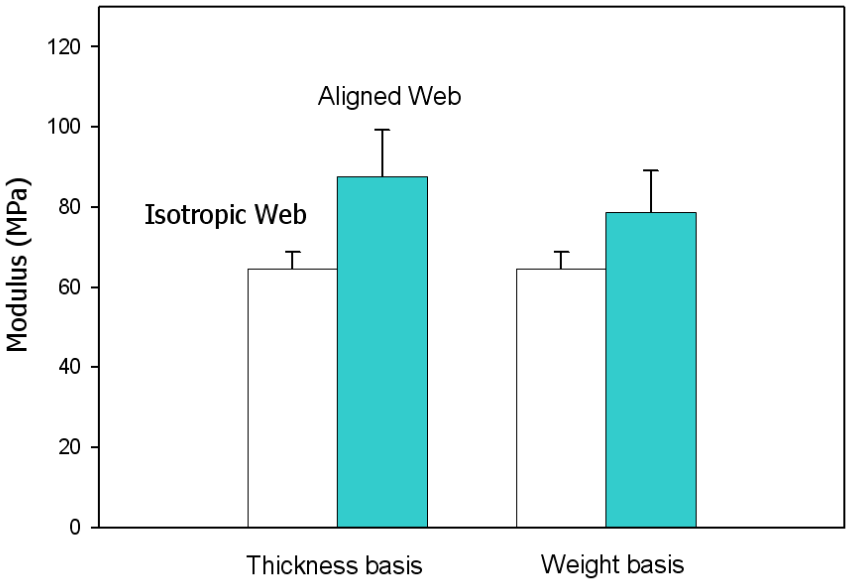

Figure 3-10. Modulus of Aligned electrospun web and isotropic electrospun web.

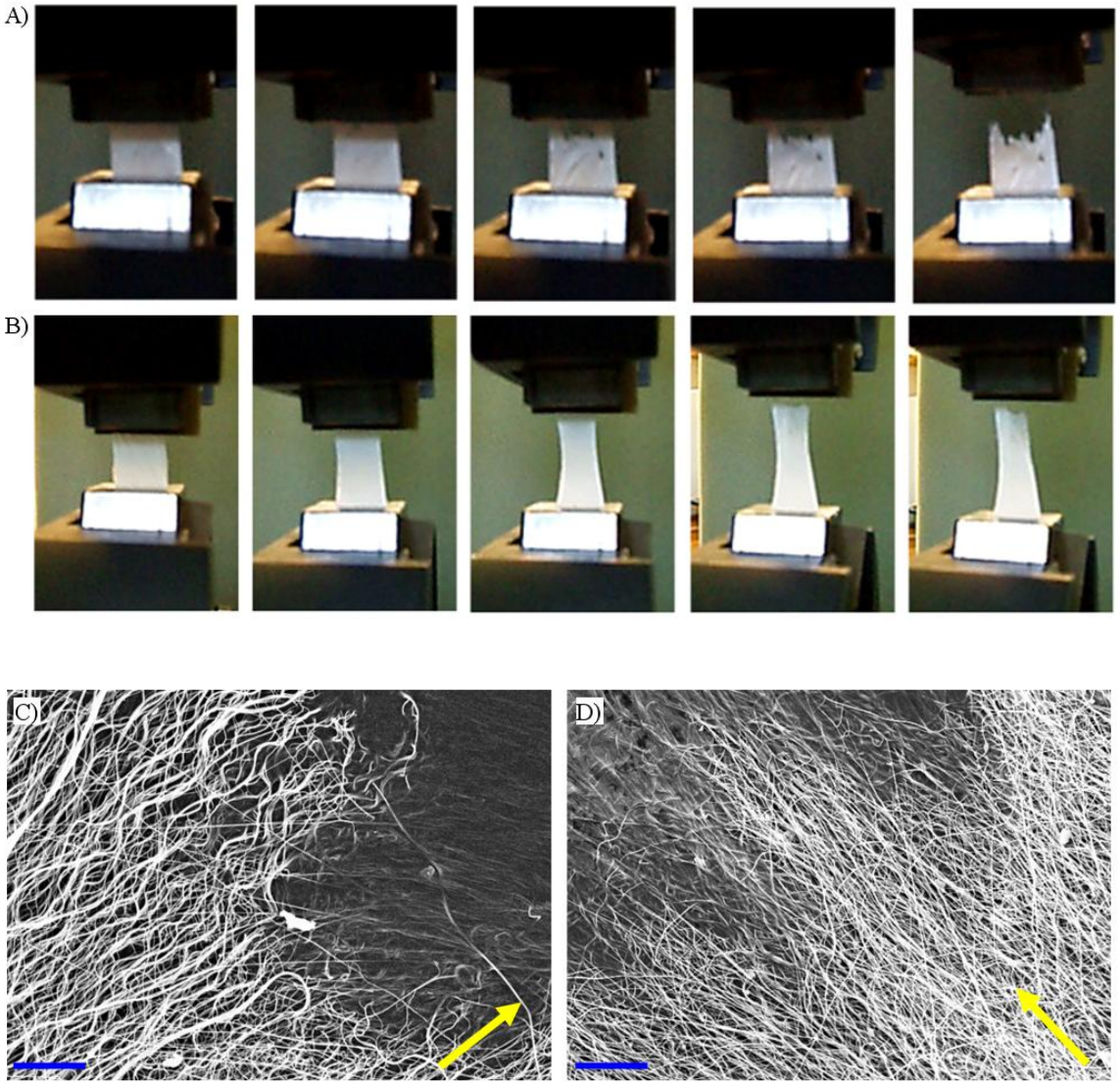

Figure 3-11 (a) snapshot images of tensile tests of aligned PVA electrospun webs (b) snapshot images of tensile tests of isotropic PVA electrospun webs (c) SEM image of a fractured electrospun fibers end of aligned PVA electrospun webs (d) SEM image of a fractured electrospun fibers end of isotropic PVA electrospun webs. Scale bars represent 20 μm. Yellow arrows indicate the direction of tensile test.

To investigate the load transfer mechanisms of aligned/isotropic PVA electrospun webs during the tensile test, snapshots were taken during the tests and SEM images of the fractured sample were also taken. Figure 3-11 (a) shows the snapshots of the tensile tests

of aligned PVA electrospun webs. Each of the images was taken after 0sec, 3.0sec, 4.5sec, 7.2sec and after finishing the tensile test. The cross head speed was fixed at 10mm/min. The aligned PVA electrospun fiber web sample starts to break at 3.0sec. And then, the sample was totally separated into two pieces after 7.2sec. In this case, the width of the aligned PVA electrospun fiber webs didn't change during the tensile test and the fractured end of the electrospun webs is irregular. Figure 3-11 (b) gives the snapshots of tensile tests of isotropic PVA electrospun webs. Each of the images was taken after 0sec, 37sec, 67sec, 85sec, and after finishing the tensile test. The isotropic PVA electrospun fiber web sample starts to rupture at 67sec, and the sample was totally broken into two pieces after 85sec. Before the rupture, the electrospun web sample was elongated during the test and the width of the sample became narrower. The fractured end of the webs was relatively flat, compared to the aligned PVA electrospun webs. As shown in Fig 3-11 (a) and (b), the shape change of aligned/isotropic PVA electrospun webs during the tensile test and the final fractured ends of each case after the test are totally different. It seems that the difference is due to the different load transfer mechanism of the aligned/isotropic PVA electrospun webs. For the aligned webs, two clamps of the tensile machine may grab both ends of individual electrospun fibers as shown in Fig 3-8 (c). Therefore, the stress by the tensile machine is exerted on each individual fiber during the test and then weaker fibers start to break one by one. On the other hand, for the isotropic webs, the clamp of the tensile machine may grab only one end of the fibers and these fibers are connected with other fibers. Therefore, when the machine stretches the electron web sample, the stress is exerted on the fiber networks, rather than individual fibers. During the test, it seems that rearrangement of the fiber networks occurs, resulting in the elongation of electrospun fiber webs. As shown in Fig 3-11 (d), electrospun fibers of the isotropic web sample are partially oriented along the measurement direction after the tensile test. In conclusion, for the aligned PVA electrospun webs, individual fiber strength is a more important parameter to the mechanical properties, compared with the

isotropic webs. On the other hand, for the isotropic PVA electrospun webs, fiber-fiber interaction force is a more critical parameter, compared with aligned webs.

3.3.4 Mechanical properties of cellulose nanowhisker/PVA electrospun fiber web

The tensile strength of PVA electrospun fiber webs with different cellulose nanowhisker loading ratio have been measured. The applied voltage and PVA concentration were fixed at 20kV and 8.0wt% for all of the cases. The tensile strength of isotropic PVA electrospun fiber webs with 0, 5.0 and 15.0wt% cellulose nanowhisker loading are 4.21MPa, 5.48MP and 7.84MPa, respectively. On the other hand, the tensile strength of 0, 5.0 and 15.0wt% cellulose nanowhisker reinforced oriented PVA electrospun fiber webs are 5.37MPa, 7.26MP and 10.5MPa, respectively. The results are summarized in Table 3-2 and Fig 3-12.

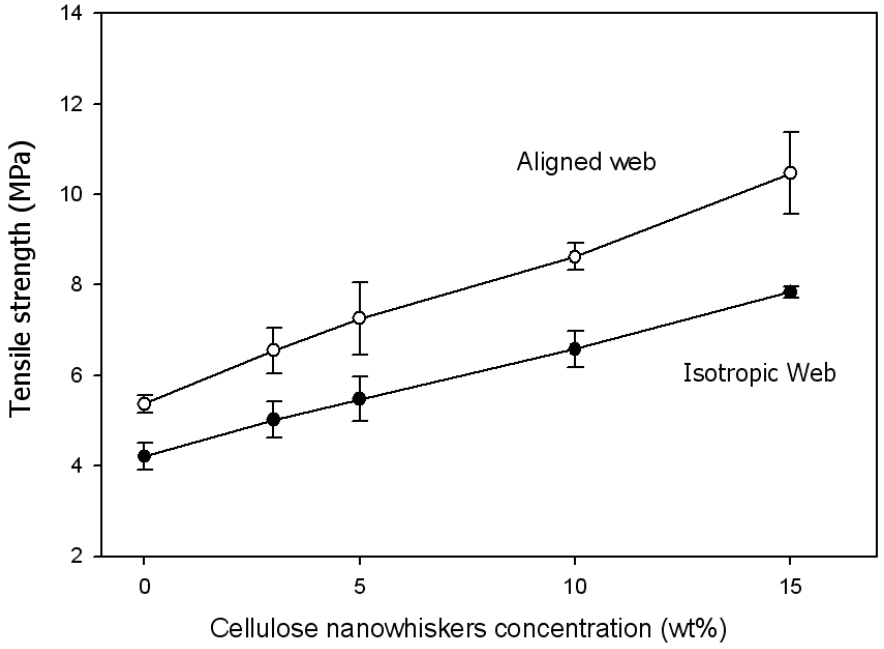

Figure 3-12. Tensile strength of aligned and isotropic PVA electrospun fiber webs with different cellulose nanowhiskers loading ratio (0wt% ~ 15.0wt%).

For both the isotropic web and aligned web, tensile strength increases linearly with increasing cellulose nanowhisker loading ratio up to 15.0wt%. In case of isotropic PVA webs with 15.0wt% cellulose nanowhisker, an 86% increase in tensile strength has been observed, compared with pure PVA electrospun web. The aligned PVA electrospun web with 15.0wt% loading showed a 95% increase in tensile strength, compared with that of aligned pure PVA electrospun web as shown in Fig 3-12.

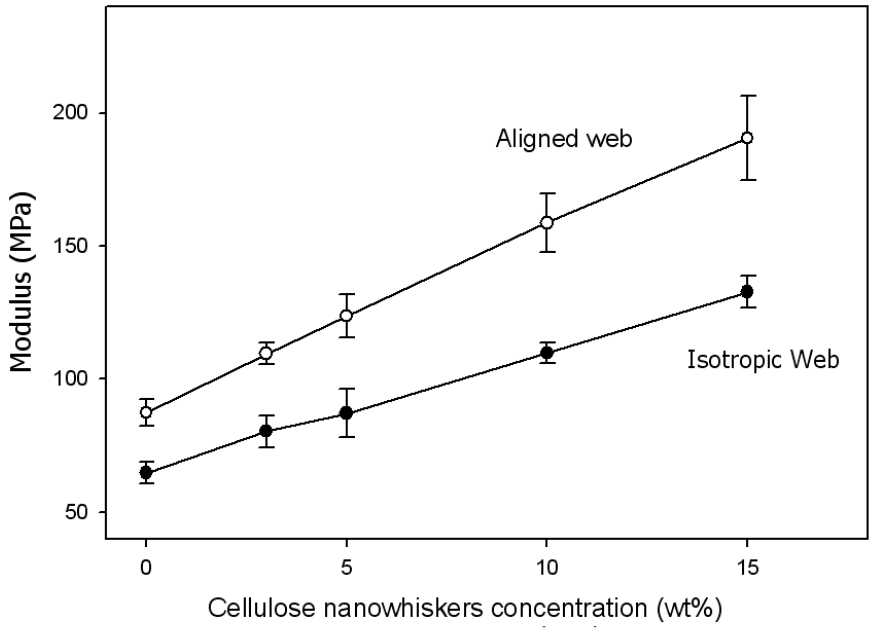

Figure 3-13. Modulus of aligned and isotropic PVA electrospun fiber webs with different cellulose nanowhiskers loading ratio (0wt% ~ 15.0wt%).

The modulus of PVA electrospun fiber webs with different cellulose nanowhisker loading ratio have also been measured. Fig 3-13 shows the modulus of isotropic webs and aligned webs with different loading ratio of cellulose nanowhiskers (0wt% ~ 15.0wt%). For both cases, the modulus also increases linearly with increasing cellulose nanowhisker

loading ratio up to 15.0wt%. The modulus of isotropic PVA electrospun web with 3.0wt% cellulose nanowhiskers is 80.3MPa, and in the case of 15.0wt%, the modulus is 132.8MPa. For the aligned PVA web with 0, 3.0wt% and 15.0wt% loading, the results are 87.7MPa, 109.6MPa and 190.5MPa, respectively. Generally speaking, oriented electrospun webs always show 30% ~ 45% higher tensile strength and modulus than isotropic electrospun webs, regardless of the cellulose nanowhisker contents. Experimental results are summarized in Table 3-2.

Table 3-2. Mechanical properties of isotropic webs and aligned webs.

Cellulose nanowhiskers loading ratio (wt%)	Tensile strength				Modulus			
	Isotropic webs (MPa)	Aligned webs (MPa)	Increase (MPa)	Extra Increase (MPa)	Isotropic webs (MPa)	Aligned webs (MPa)	Increase (MPa)	Extra Increase (MPa)
0	4.21	5.37	1.16	_	64.7	87.4	22.6	_
3	5.02	6.55	1.53	0.37	80.3	109.6	29.3	6.7
5	5.48	7.26	1.78	0.62	87.2	123.7	36.5	13.9
10	6.58	8.62	2.04	0.88	109.7	158.7	49.0	26.4
15	7.84	10.47	2.63	1.47	132.8	190.5	57.7	35.1

The load transfer mechanism of aligned/isotropic PVA electrospun webs also agrees well with the experimental results shown in Table 3-2. The mechanical properties of aligned webs are more sensitive to the change of cellulose nanowhisker contents. There are extra increases of mechanical properties between aligned webs and isotropic webs, and this extra increases become larger with increasing loading ratio of cellulose nanowhiskers. It is expected that the loading ratio change of cellulose nanowhiskers affects the individual fiber strength more than the fiber-fiber bonding strength. As discussed before, the contribution of the individual fiber strength is larger in the case of aligned electrospun webs. Therefore, it is concluded that the increment of the cellulose

nanowhisker loading ratio affects the mechanical properties of aligned electrospun webs more than it does with isotropic electrospun webs.

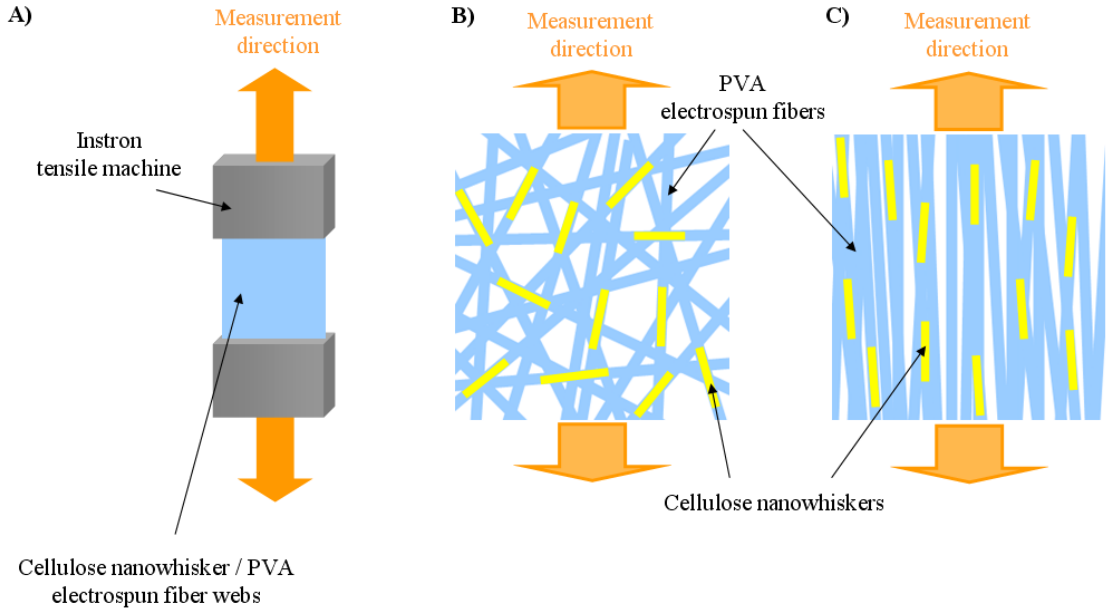

Figure 3-14 (a) Schematic of the tensile measurement of electrospun fiber webs (b) Schematic of unoriented cellulose nanowhiskers in isotropic electrospun webs (b) Schematic of oriented cellulose nanowhiskers in aligned electrospun webs. (note: Average diameter of PVA electrospun fiber is 280nm and average diameter of cellulose nanowhiskers is 10nm).

It is also expected that the alignment of cellulose nanowhiskers in the PVA fiber matrix affects the mechanical properties of aligned electrospun webs to a certain extent. It is well known that nanoparticles are aligned inside of the matrix materials during electrospinning due to the high shear force of the polymer jet [37-40]. It is also expected that cellulose nanowhiskers are aligned inside PVA fibers automatically during electrospinning. Fig 3-14 shows the orientation of cellulose nanowhiskers in isotropic and aligned electrospun webs. Because the orientation of cellulose nanowhiskers follows the orientation of electrospun fibers, cellulose nanowhiskers are also unoriented in isotropic

PVA electrospun webs (Fig 3-14 (b)). On the other hand, cellulose nanowhiskers are oriented in aligned electrospun webs as shown in Fig 3-14 (c). It was reported that CNT aligned with the same direction as the tensile test can improve the physical properties of nanocomposites thin film [41-42]. It is also expected that cellulose nanowhisker alignment can affect the physical properties of aligned web in a similar manner.

It is very difficult to predict the mechanical properties of aligned/isotropic electrospun webs quantitatively by mathematical models because there are too many factors to consider such as individual fiber strength, fiber connectivity, fiber alignment degree, and so on. In this study, a simple model to quantitatively predict the mechanical properties is introduced. Mechanical properties (M) of PVA/cellulose nanowhisker electrospun fiber webs can be simply expressed as the function of fiber strength related parameters (S_E) and the function of fiber-fiber bonding strength related parameters (B_E). Fiber properties are affected by several factors such as cellulose nanowhisker loading ratio (s_1), crystallinity of PVA (s_2), average diameter of electrospun fibers (s_3) and so on. Fiber-fiber bonding characters are also affected by fiber alignment degree (b_1), fiber connectivity (b_2), bonding area between fibers (b_3) and so on. In this case, M, S_E and B_E are given by,

$$M = f(S_E, B_E) \tag{3.2}$$

$$S_E = f_s(s_1, s_2, s_3 ...) \tag{3.3}$$

$$B_E = f_b(b_1, b_2, b_3 ...) \tag{3.4}$$

If it is assumed that fiber strength related parameters and fiber-fiber bonding strength related parameters do not affect each other, the mechanical properties of aligned PVA electrospun webs ($M_{aligned}$) and isotropic PVA electrospun webs ($M_{isotropic}$) are simply expressed as follows,

$$M_{aligned} = a\,S_E + b\,B_E$$
$$M_{isotropic} = a'\,S_E + b'\,B_E \qquad (a > a' \text{ and } b < b') \tag{3.5}$$

where a, b, a’ and b’ are constants. Based on the load transfer mechanisms of aligned/isotropic electrospun webs, a is larger than a’ and b’ is larger than b. Although they are very simple equations, they are useful to predict the effect of a certain parameter. If the crystallinity of PVA is increased and the crytallinity change affects the fiber strength more than the fiber-fiber bonding strength, it is predicted that the increase of $M_{aligned}$ is larger than that of $M_{isotropic}$.

3.4 Conclusions

Cellulose nanowhisker reinforced poly(vinyl alcohol) (PVA) nanofiber webs were successfully fabricated using an electrospinning technique. The morphology and mechanical properties of electrospun fiber webs are significantly affected by the linear velocity of a rotating collector. The modulus and tensile strength of aligned webs increased 35% and 45%, respectively, compared to those of isotropic electrospun fiber webs. 15.0wt% cellulose nanowhiskers loaded electrospun webs showed an 86% higher tensile strength and 105% higher modulus. It is expected that the different mechanical properties of aligned and isotropic PVA electrospun webs is due to the different load transfer mechanism. The mechanical properties of aligned webs are more sensitive to the change of cellulose nanowhisker contents. It is also expected that cellulose nanowhisker alignment can increase the mechanical properties of aligned PVA electrospun webs.

References

1. Sakurada, I., Y. Nukushina, and T. Ito, *EXPERIMENTAL DETERMINATION OF ELASTIC MODULUS OF CRYSTALLINE REGIONS IN ORIENTED POLYMERS.* JOURNAL OF POLYMER SCIENCE, 1962. **57**(165): p. 651-&.

2. Sturcova, A., G.R. Davies, and S.J. Eichhorn, *Elastic modulus and stress-transfer properties of tunicate cellulose whiskers.* Biomacromolecules, 2005. **6**(2): p. 1055-1061.

3. Eichhorn, S.J. and G.R. Davies, *Modelling the crystalline deformation of native and regenerated cellulose.* Cellulose, 2006. **13**(3): p. 291-307.

4. Samir, M., F. Alloin, and A. Dufresne, *Review of recent research into cellulosic whiskers, their properties and their application in nanocomposite field.* Biomacromolecules, 2005. **6**(2): p. 612-626.

5. Czaja, W.K., et al., *The future prospects of microbial cellulose in biomedical applications.* Biomacromolecules, 2007. **8**(1): p. 1-12.

6. Bonini C, H.L., *French patent FR 99.07493.*

7. Gousse, C., et al., *Stable suspensions of partially silylated cellulose whiskers dispersed in organic solvents.* Polymer, 2002. **43**(9): p. 2645-2651.

8. Grunert, M. and W.T. Winter, *Cellulose nanocrystal reinforced cellulose acetate butyrate nanocomposites.* Abstracts of Papers of the American Chemical Society, 2002. **223**: p. 240-PMSE.

9. Samir, M., et al., *Cross-linked nanocomposite polymer electrolytes reinforced with cellulose whiskers.* Macromolecules, 2004. **37**(13): p. 4839-4844.

10. Angles, M.N. and A. Dufresne, *Plasticized starch/tunicin whiskers nanocomposites. 1. Structural analysis.* Macromolecules, 2000. **33**(22): p. 8344-8353.

11. Grunert, M. and W.T. Winter, *Nanocomposites of cellulose acetate butyrate reinforced with cellulose nanocrystals.* Journal of Polymers and the Environment, 2002. **10**(1-2): p. 27-30.

12. Chazeau, L., et al., *Viscoelastic properties of plasticized PVC reinforced with cellulose whiskers.* Journal of Applied Polymer Science, 1999. **71**(11): p. 1797-1808.

13. Samir, M., et al., *Cellulose nanocrystals reinforced poly(oxyethylene).* Polymer, 2004. **45**(12): p. 4149-4157.

14. Lu, J., T. Wang, and L.T. Drzal, *Preparation and properties of microfibrillated cellulose polyvinyl alcohol composite materials.* Composites Part a-Applied Science and Manufacturing, 2008. **39**(5): p. 738-746.

15. Yeo, I.S., et al., *Collagen-based biomimetic nanofibrous scaffolds: Preparation and characterization of collagen/silk fibroin bicomponent nanofibrous structures.* Biomacromolecules, 2008. **9**(4): p. 1106-1116.

16. Ko, F., et al., *Electrospinning of continuons carbon nanotube-filled nanofiber yarns.* Advanced Materials, 2003. **15**(14): p. 1161-+.

17. Fong, H., et al., *Generation of electrospun fibers of nylon 6 and nylon 6-montmorillonite nanocomposite.* Polymer, 2002. **43**(3): p. 775-780.

18. Wang, X.F., et al., *Formation of water-resistant hyaluronic acid nanofibers by blowing-assisted electro-spinning and non-toxic post treatments.* Polymer, 2005. **46**: p. 4853-4867.

19. Teo, W.E., et al., *Porous tubular structures with controlled fibre orientation using a modified electrospinning method.* Nanotechnology, 2005. **16**(6): p. 918-924.

20. Li, D., Y.L. Wang, and Y.N. Xia, *Electrospinning nanofibers as uniaxially aligned arrays and layer-by-layer stacked films.* Advanced Materials, 2004. **16**(4): p. 361-366.

21. Rojas, O.J., G.A. Montero, and Y. Habibi, *Electrospun Nanocomposites from Polystyrene Loaded with Cellulose Nanowhiskers.* Journal of Applied Polymer Science, 2009. **113**(2): p. 927-935.

22. Junkasem, J., R. Rujiravanit, and P. Supaphol, *Fabrication of alpha-chitin whisker-reinforced poly(vinyl alcohol) nanocomposite nanofibres by electrospinning.* Nanotechnology, 2006. **17**(17): p. 4519-4528.

23. Xiang, C.H., Y.L. Joo, and M.W. Frey, *Nanocomposite Fibers Electrospun from Poly(lactic acid)/Cellulose Nanocrystals.* Journal of Biobased Materials and Bioenergy, 2009. **3**(2): p. 147-155.

24. Matthews, J.A., et al., *Electrospinning of collagen nanofibers.* Biomacromolecules, 2002. **3**(2): p. 232-238.

25. Li, D., Y.L. Wang, and Y.N. Xia, *Electrospinning of polymeric and ceramic nanofibers as uniaxially aligned arrays.* Nano Letters, 2003. **3**(8): p. 1167-1171.

26. Katta, P., et al., *Continuous electrospinning of aligned polymer nanofibers onto a wire drum collector.* Nano Letters, 2004. **4**(11): p. 2215-2218.

27. Mathew, G., et al., *Preparation and anisotropic mechanical behavior of highly-oriented electrospun poly(butylene terephthalate) fibers.* Journal of Applied Polymer Science, 2006. **101**(3): p. 2017-2021.

28. Stylianopoulos, T., et al., *Computational predictions of the tensile properties of electrospun fibre meshes: Effect of fibre diameter and fibre orientation.* Journal of the Mechanical Behavior of Biomedical Materials, 2008. **1**(4): p. 326-335.

29. Shields, K.J., et al., *Mechanical properties and cellular proliferation of electrospun collagen type II.* Tissue Engineering, 2004. **10**(9-10): p. 1510-1517.

30. Bashur, C.A., et al., *Effect of Fiber Diameter and Alignment of Electrospun Polyurethane Meshes on Mesenchymal Progenitor Cells.* Tissue Engineering Part A, 2009. **15**(9): p. 2435-2445.

31. Courtney, T., et al., *Design and analysis of tissue engineering scaffolds that mimic soft tissue mechanical anisotropy.* Biomaterials, 2006. **27**(19): p. 3631-3638.

32. Zong, X.H., et al., *Electrospun fine-textured scaffolds for heart tissue constructs.* Biomaterials, 2005. **26**(26): p. 5330-5338.

33. Kim, G., Y.S. Cho, and W.D. Kim, *Stability analysis for multi jets electrospinning process modified with a cylindrical electrode.* European Polymer Journal, 2006. **42**(9): p. 2031-2038.

34. Dong, X.M., J.F. Revol, and D.G. Gray, *Effect of microcrystallite preparation conditions on the formation of colloid crystals of cellulose.* Cellulose, 1998. **5**(1): p. 19-32.

35. Ayres, C., et al., *Modulation of anisotropy in electrospun tissue-engineering scaffolds: Analysis of fiber alignment by the fast Fourier transform.* Biomaterials, 2006. **27**(32): p. 5524-5534.

36. Huang, Z.M., et al., *A review on polymer nanofibers by electrospinning and their applications in nanocomposites.* Composites Science and Technology, 2003. **63**(15): p. 2223-2253.

37. Liu, L.Q., et al., *Tensile mechanics of electrospun multiwalled nanotube/poly(methyl methacrylate) nanofibers.* Advanced Materials, 2007. **19**(9): p. 1228-+.

38. Li, L., et al., *Formation and properties of nylon-6 and nylon-6/montmorillonite composite nanofibers.* Polymer, 2006. **47**(17): p. 6208-6217.

39. Dror, Y., et al., *Carbon nanotubes embedded in oriented polymer nanofibers by electrospinning.* Langmuir, 2003. **19**(17): p. 7012-7020.

40. Ge, J.J., et al., *Assembly of well-aligned multiwalled carbon nanotubes in confined polyacrylonitrile environments: Electrospun composite nanofiber sheets.* Journal of the American Chemical Society, 2004. **126**(48): p. 15754-15761.

41. Thostenson, E.T. and T.W. Chou, *Aligned multi-walled carbon nanotube-reinforced composites: processing and mechanical characterization.* Journal of Physics D-Applied Physics, 2002. **35**(16): p. L77-L80.

42. Qian, D., et al., *Load transfer and deformation mechanisms in carbon nanotube-polystyrene composites.* Applied Physics Letters, 2000. **76**(20): p. 2868-2870.

CHAPTER 4

NANOINDENTATION OF A CELLULOSE NANOWHISKER REINFORCED PVA ELECTROSPUN FIBER

Abstract

The mechanical properties of cellulose nanowhisker reinforced poly(vinyl alcohol) (PVA) electrospun fibers rather than fiber webs, have been measured using a nanoindentation method. Due to the small size of electrospun fibers (average diameter = ~250nm), measurement errors occur during the nanoindentation measurement. The reasons for the measurement errors, solutions, and data analysis methods have all been discussed. In this chapter, the modulus of PVA/cellulose nanowhisker electrospun fibers increases linearly with increasing loading ratio of cellulose nanowhiskers up to 20.0wt%. The modulus of a pure PVA electrospun fiber and a 20.0wt% cellulose nanowhisker reinforced PVA electrospun fiber is 2.1GPa and 7.6GPa, respectively. Experimental results were compared using a longitudinal Halpin-Tsai model. The nanoindentation results are 20~30% smaller than the longitudinal model predictions. The reasons for the difference between measurement results and model predictions have been discussed.

Keywords: Electrospinning, Cellulose nanowhisker, Nanoindentation

4.1. Introduction

In recent years, natural fibers have been widely used as reinforcement materials in polymeric nanocomposites due to the environmental concerns. Cellulose nanowhiskers have also attracted much attention as environmentally friendly nanofillers for polymer composite enhancement. It was reported that the modulus of the crystalline region of cellulose was 137GPa measured by X-ray diffraction [1], 143GPa measured by Raman spectroscopic technique [2], and 149GPa ~ 155GPa calculated by computational simulation [3]. The modulus of cellulose nanowhiskers has not yet been measured but it is expected that the modulus of cellulose nanowhiskers is slightly lower than that of the crystalline cellulose. Moreover, cellulose nanowhiskers have a lower density than inorganic filler materials. Cellulose nanowhiskers are also naturally abundant, renewable and non-toxic resources. Cellulose nanowhiskers are bar-type particles. They are considered as a string of cellulose crystals connected by cellulose amorphous domains [4]. The diameters of cellulose nanowhiskers range from 5nm to 20 nm and their lengths are between 150nm and 400nm, depending on the source of cellulose nanowhiskers and their preparation conditions [5]. It was reported that cellulose nanowhisker reinforced nanocomposites showed significantly improved mechanical properties for both the natural and synthetic polymer matrices such as starch [6], cellulose acetate butyrate [7], poly(vinyl chloride) [8], and poly(vinyl alcohol) [9].

Electrospinning is a versatile and an effective method to produce nanoscale to microscale fibers from solution. In electrospinning, high charges are applied to the liquid solution. As the intensity of the electric charges on the liquid solution surface increases, the surface elongates until the electrostatic force overcomes the surface tension and a charged jet of the solution is ejected to the metal collector. During the flight of the jet, the solvent evaporates quickly and the dried electrospun fibers are collected. Various types of nanofibers from polymer [9-10], inorganic materials [11] and hybrid (organic/inorganic) materials [12] were fabricated using the electrospinning technique. These nanofibers can

be used for a wide variety of applications such as separation filters, wound dressing materials, tissue scaffold, sensors and so on [13-15].

An understanding of the mechanical properties of electrospun fibers is very important for investigating the bulk properties of electrospun webs. However, direct measurement of the physical properties of electrospun fibers is difficult because isolating and controlling the nanosize electrospun fiber is not easy. It has been reported that the mechanical properties of electrospun fibers could be measured using the Atomic force microscope (AFM) cantilever [16], nano tensile test method [17], AFM three-point bend test method [18] and nanoindentation method [11, 19]. Among all of the nanomechanical characterization techniques, nanoindentation is perhaps the most convenient method [20]. The samples for nanoindentation can be simply prepared by depositing the electrospun fibers on a hard and flat substrate with sufficient adhesion between the substrate and the nanosize electrospun fibers.

In this study, PVA was used as the matrix material for electrospinning. PVA is a semi-crystalline polymer and shows positive compatibility with cellulose nanowhiskers [9]. The mechanical properties of cellulose nanowhisker reinforced PVA electrospun fibers have been measured using the nanoindentation method. The mechanical properties of electrospun webs and individual fibers are quite different. For electrospun webs, both the properties of individual fibers and the fiber-fiber bonding force along with the connectivity between fibers affect the properties of electrospun webs. Therefore, the isolation of the electrospun fiber and its property measurements are key factor in understanding the reinforcement effects of cellulose nanowhiskers on PVA electrospun fibers. Experimental results were theoretically investigated using a longitudinal Halpin-Tsai model.

4.2. Experimental

4.2.1. Materials

Poly(vinyl alcohol) (PVA) (Mw=127,000 g/mol, 99+% hydrolyzed) was purchased from Aldrich. The suspensions of cellulose nanowhiskers were prepared from Whatman No. 1 filter paper by sulfuric acid hydrolysis. The concentration of sulfuric acid was fixed at 64%. 20g of filter paper were dispersed in 175ml of sulfuric acid (the ratio of the filter paper to sulfuric acid was fixed at 1:8.75 (g/ml)). The acid hydrolysis conditions were optimized at 45°C and 50mins [21]. After hydrolysis, the suspension was deionized by mixing in 1g of mixed-bed ion exchange resin. The solution was then washed with DI water and centrifuged (40mins, 3000rpm, Beckman Coulter, GS-6). The suspension was further dispersed by an ultrasound sonicator (15mins at full power, Branson 3510). The length of obtained cellulose nanowhiskers ranges from 180nm to 220nm and the width is between 5nm and 10nm. Water was obtained from a Nanopure ultrapure water system with a resistivity of about 18 MΩ cm.

4.2.2. Sample preparation

High voltage power supply (Keltron co., H545A) was used for the electrospinning. The PVA/cellulose nanowhisker solution was put inside a pipette. The end part of insulation rubbers protecting electric cables was removed and a bare copper wire was inserted to the pipette. A positive voltage (10kV ~ 25kV) was applied to the PVA/cellulose nanowhisker solution through a copper wire as shown in Fig 4-1 (a). For the morphology study, electrospun fibers were deposited on a stationary flat metal collector (Fig 3-1 (a)) and electrospun fibers for nanoindentation measurements were collected on a glass substrate having two parallel electrodes (Fig 4-1 (b)). Using a sputter coater, Au was coated onto the glass substrate that had a string (diameter = 0.5mm)

attached onto its surface. After removing the string, the gold coating was separated by a 0.5mm distance gap, resulting in two parallel electrodes attached glass substrate.

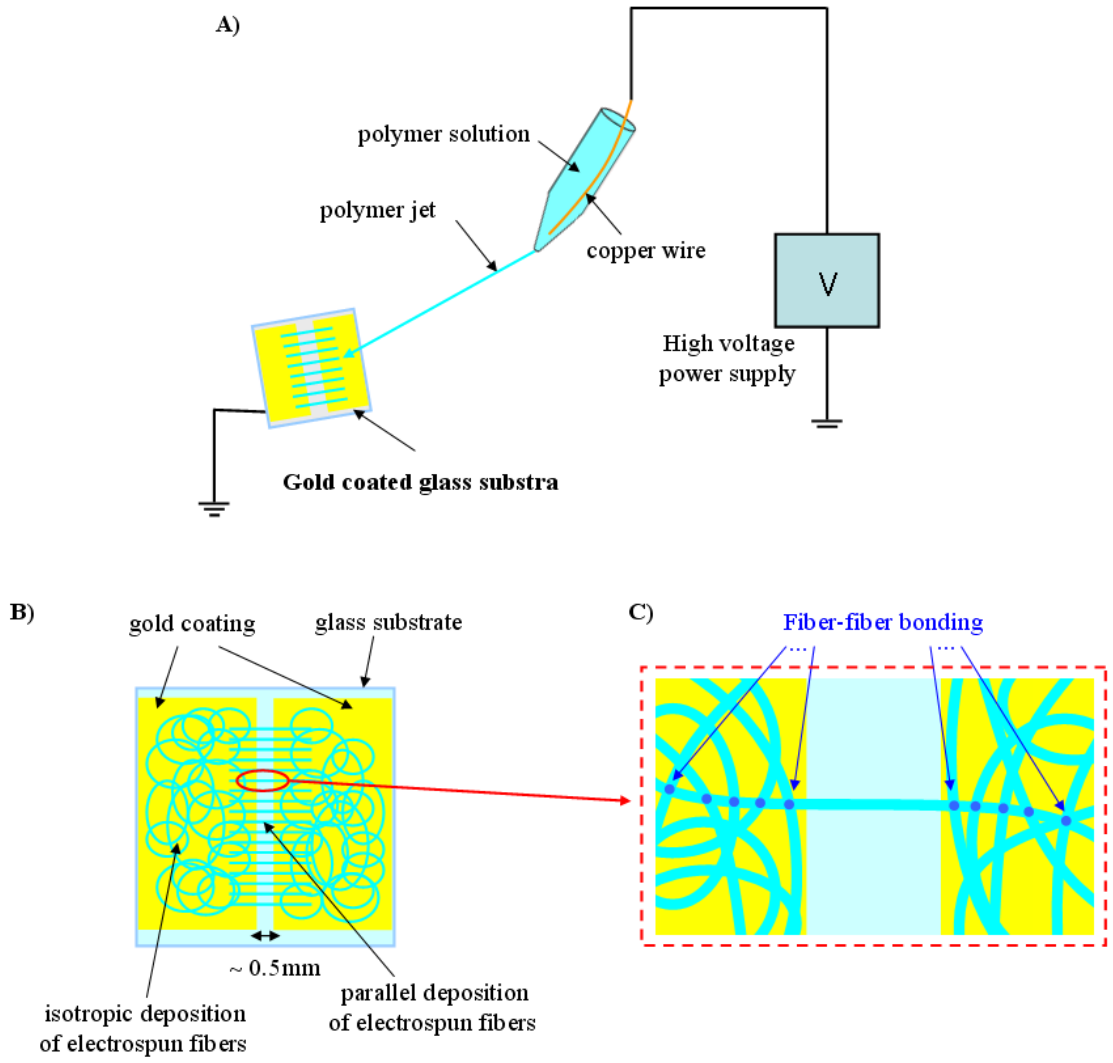

Fig 4-1 (a) Schematic of the fabrication process for parallel deposited electrospun fibers (b) Schematic of electrospun fiber deposition on gold coated glass substrate (c) Schematic of fiber-fiber bonding between the fibers on parallel deposition region and fibers on isotropic deposition region.

A sample preparation for the nanoindentation measurement using a two parallel electrode collector has two advantages. First, highly aligned electrospun fibers are deposited between two electrodes [22], making it possible to deposit electrospun fibers without the overlapping of fibers. Second, isotropically deposited electrospun fibers on electrodes may function as anchors for the fibers between electrodes. As shown in Fig 4-1 (b) and (c), fiber-fiber bonding exists between the fibers on parallel deposition region and fibers on isotropic deposition region. It helps to prevent the slippage of fibers during nanoindentation. The distance between the tip of the pipette and the grounded substrate was fixed at 20cm. The SEM image of electrospun fibers deposited on two parallel electrodes is shown in Fig 4-2.

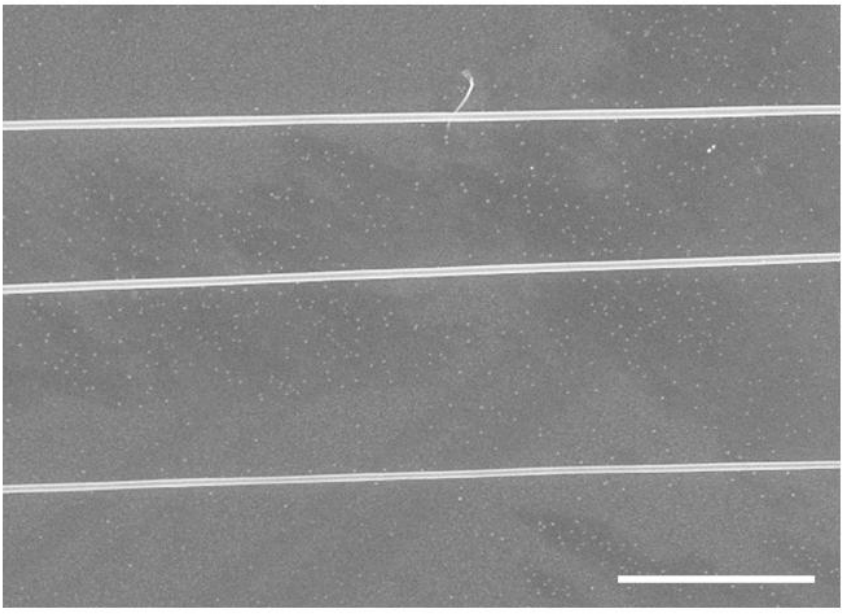

Figure 4-2. SEM image of electrospun fibers deposited on two parallel electrodes. (Scale bar: 10 μm).

4.2.3. Nanoindentation

The modulus of the electrospun fiber was measured using MTS Nanoindenter XP with a cube-corner three-sided pyramidal diamond tip. A schematic illustration of the nanoindentation experiment is shown in Fig 4-3. Among the electrospun fibers deposited between two electrodes, an isolated fiber was selected carefully. At this time, electrospun fibers overlapping with other fibers within a parallel deposition region were excluded. Next, the exact x and y coordinates where the nanoindenter tip should be loaded were found using an optical microscope equipped in MTS Nanoindenter XP and were inputted into the machine. Using MTS Nanoindenter XP, 25 pairs of x and y coordinates can be inputted at a time. Each indentation was carried out on the different fiber because deformation of the electrospun fiber caused by a previous indentation can change the mechanical properties of that fiber. After the indenter tip started to contact the fiber surface, it was approaching into the fiber at a constant strain rate (0.05 s^{-1}) until it reached a 30nm depth. At maximum load, the load was held for 10 seconds and then the indenter was withdrawn from the sample. The unloading rate was set to be same as the loading rate. Constant strain rate was employed to avoid strain hardening effects [23].

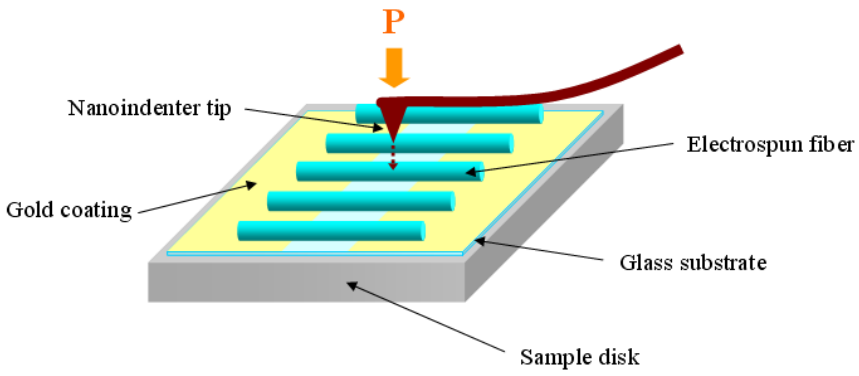

Figure 4-3. Schematic of the nanoindentation test.

The elastic modulus (E) is obtained from maximum loads on the tip (P_{max}) and indentation depth (h_{max}). The relationship among elastic modulus (E), maximum load on the tip (P_{max}) and indentation depth (h_{max}) is given by,

$$S = \frac{P_{\max}}{h_{\max}} - (K_s - 4m\pi^2 f^2) \tag{4.1}$$

$$\frac{E}{1-\nu^2} = \left(\frac{\pi}{4A_C}\right)^{0.5} \times S \tag{4.2}$$

where K_s is spring constant, m is mass of the indenter column, f is the frequency of the AC signal, ν is the Poisson's ratio of the tip and A_C is the projected area of the indenter [24]. For MTS Nanoindenter XP, the spring constant is $1.2 Nm^{-1}$, the frequency of the AC signal is 45Hz. For the diamond cube-corner tip used in this measurement, the Poisson's ratio is 0.04 and the projected area is expressed as $A=2.60h_{max}^2$ [25].

4.2.4. Characterization

The modulus was measured using MTS Nanoindenter XP (MTS Co., Nano Instruments Innovation Center, TN, USA). Scanning electron microscopy (SEM) was carried out using a LEO 1530 at 10kV. The samples were sputter coated with Au using EMS 350 sputter (20mA, 2mins) prior to observation. A measurement of average diameters of electrospun fibers were conducted using ImageTool 3.0 software which is provided by UTHSCSA. The diameters of electrospun fibers were measured across the image and the average value was determined by taking the average of 60 measurements that were randomly chosen.

4.3. Results and discussion

4.3.1. Morphology of cellulose nanowhisker/PVA electrospun fiber

The effect of applied voltage on the morphology of PVA electrospun fibers has been investigated. Different voltages ranging from 10kV to 25kV were applied to the PVA solution. The distance between the tip of the pipette and a grounded metal sheet was fixed at 25cm, and 8.0wt% PVA solution was used in this study. SEM photos of PVA electrospun fiber applying different voltages are shown in Fig 4-4.

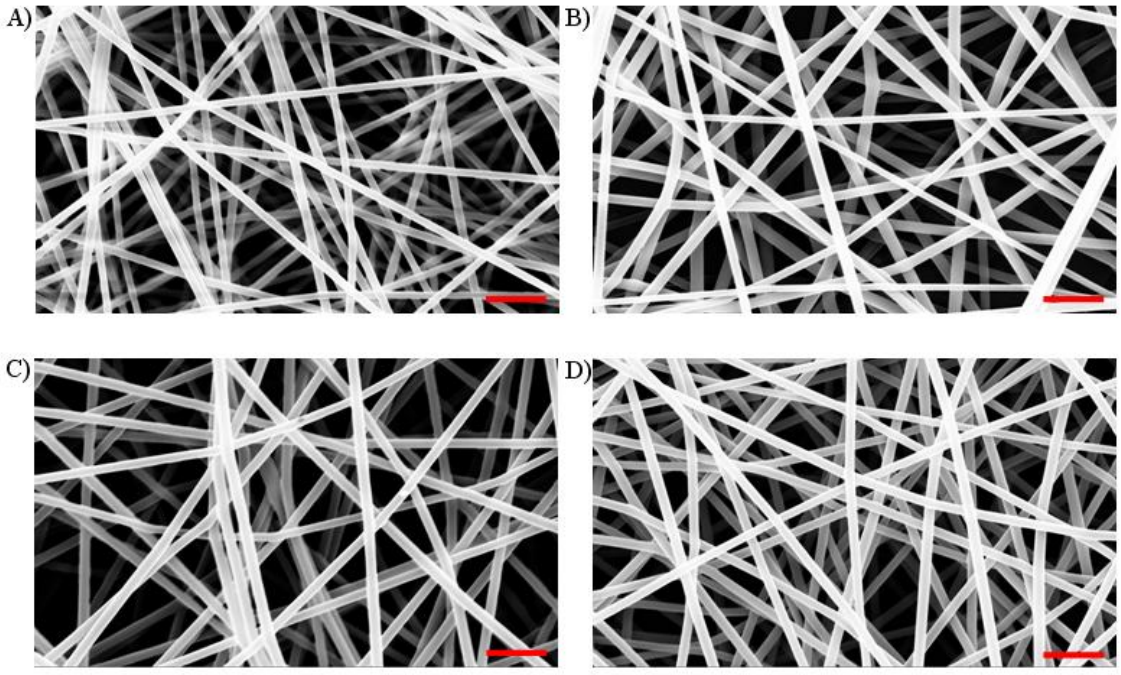

Figure 4-4. SEM images of PVA electrospun fibers prepared using different applying voltage a) 10kV, b) 15kV, c) 20kV and d) 25kV. Scale bars represent 2 μm.

The average diameters of each case have been measured based on the SEM images. The average diameter of fibers using 10kV is 260nm, while the average diameter of fibers using 25kV is around 310nm. The experimental results are summarized at Fig 4-5. As shown in Fig 4-5, it is observed that average diameter of PVA electrospun fibers

increases with increasing applied voltage. For all of the cases, the surfaces of the fibers were very smooth.

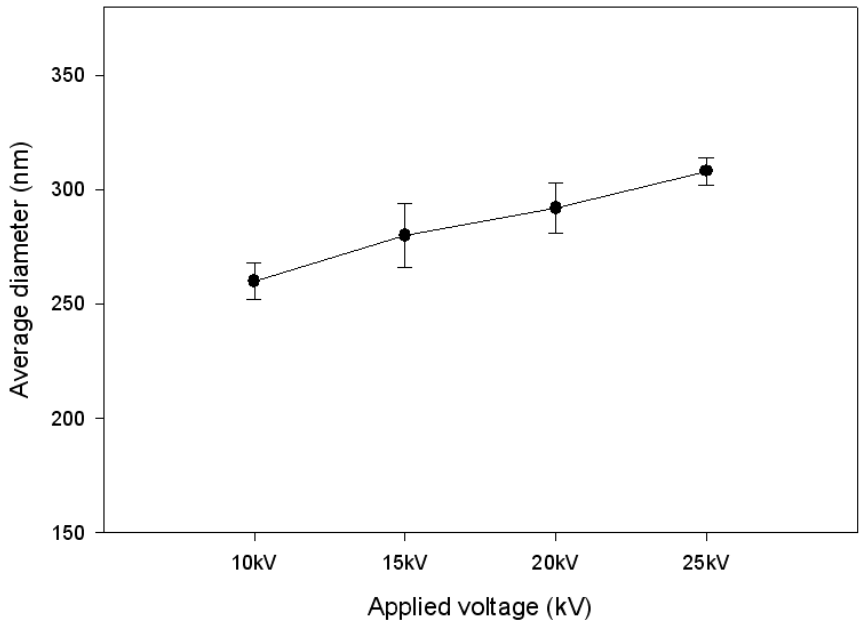

Figure 4-5. Average diameter of PVA electrospun fibers prepared using different applying voltage (10kV~25kV).

The effect of cellulose nanowhisker content on the morphology of cellulose nanowhisker/PVA electrospun fibers has also been studied. The applied voltage and PVA concentration were fixed at 20kV and 8.0wt%. SEM images of cellulose nanowhisker/PVA electrospun fibers with different loading ratio of cellulose nanowhiskers are shown in Fig 4-6, and the results are summarized in Fig 4-7. The average diameter of pure PVA fiber is measured as 290nm, with an 11nm deviation. On the other hand, the average diameter of PVA fibers with 15.0wt% cellulose nanowhiskers loading is 220nm, and the deviation is 28nm. In conclusion, it is observed that the fiber diameter of cellulose nanowhisker/PVA electrospun fibers decreases and the deviation

increases with increasing cellulose nanowhiskers content. For all of the cases, the surfaces of the fibers were also very smooth.

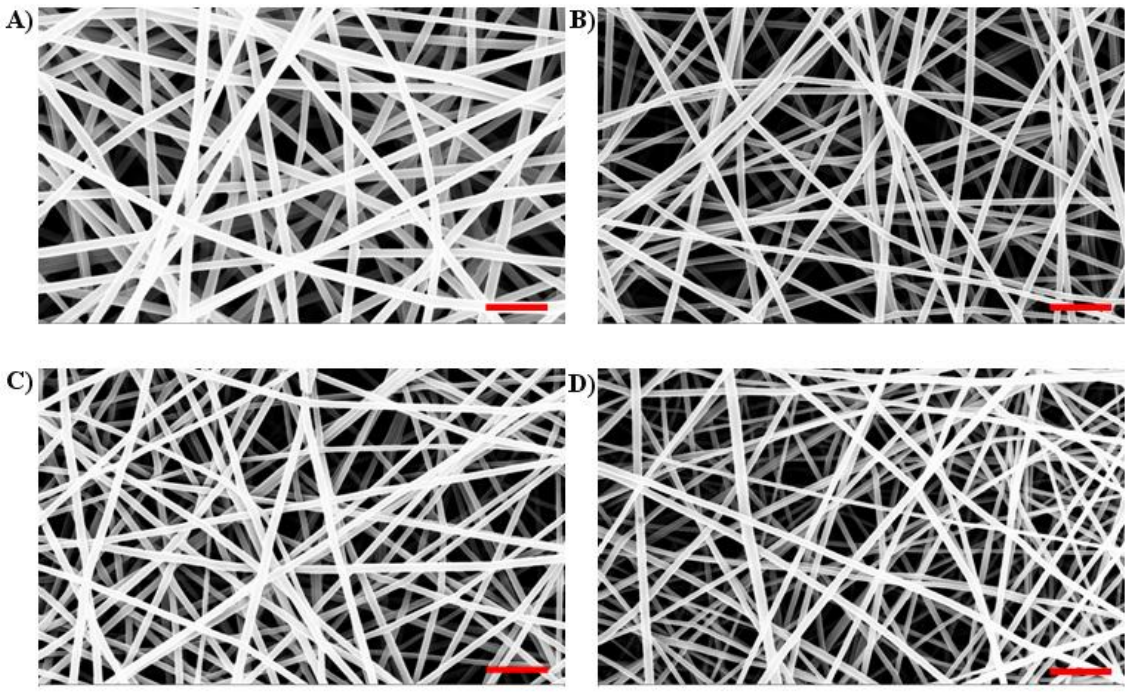

Figure 4-6. SEM images of PVA/cellulose nanowhiskers electrospun fibers with different loading ratio a) 0wt%, b) 5.0wt%, c) 10.0wt% and d) 15.0wt%. Scale bars represent 2 μm.

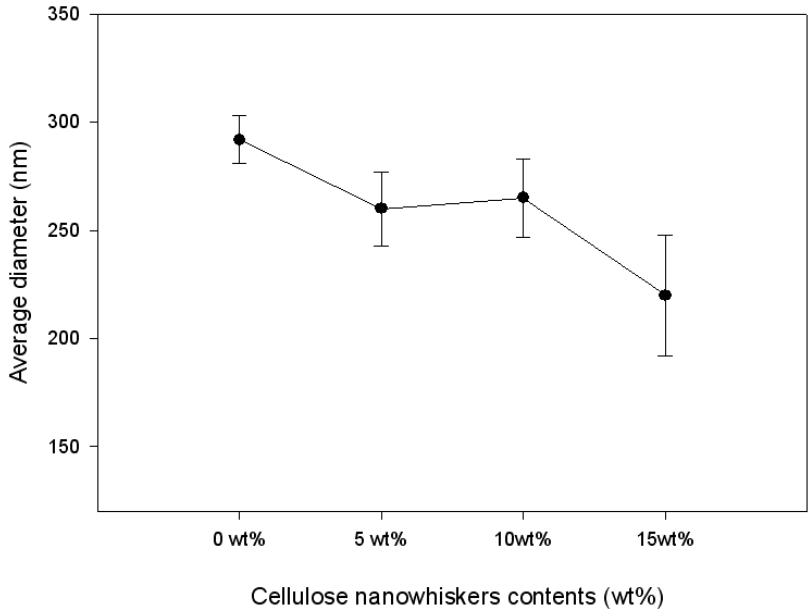

Figure 4-7. Average diameter of PVA/cellulose nanowhiskers electrospun fibers with different loading ratio (0wt% ~ 15.0wt%).

4.3.2. Nanoindentation of the cellulose nanowhiskers / PVA electrospun fiber

To analyze the reinforcement effect of cellulose nanowhiskers on PVA electrospun fibers intensively, a modulus of the electrospun fiber has been measured using a nanoindenter. Cellulose nanowhisker/PVA electrospun fibers were fabricated on a glass substrate as shown in Fig 4-1. The PVA solution concentration was fixed as 8.0wt% and the cellulose nanowhisker loading ratio varied from 0wt% to 20.0wt%. The indenting depth (h) was set up as 10% ~ 15% of the average thickness of the samples. As shown in Fig 4-7, the average diameters of electrospun fibers ranged from 290nm to 220nm, and the indenting depth was fixed at 30nm.

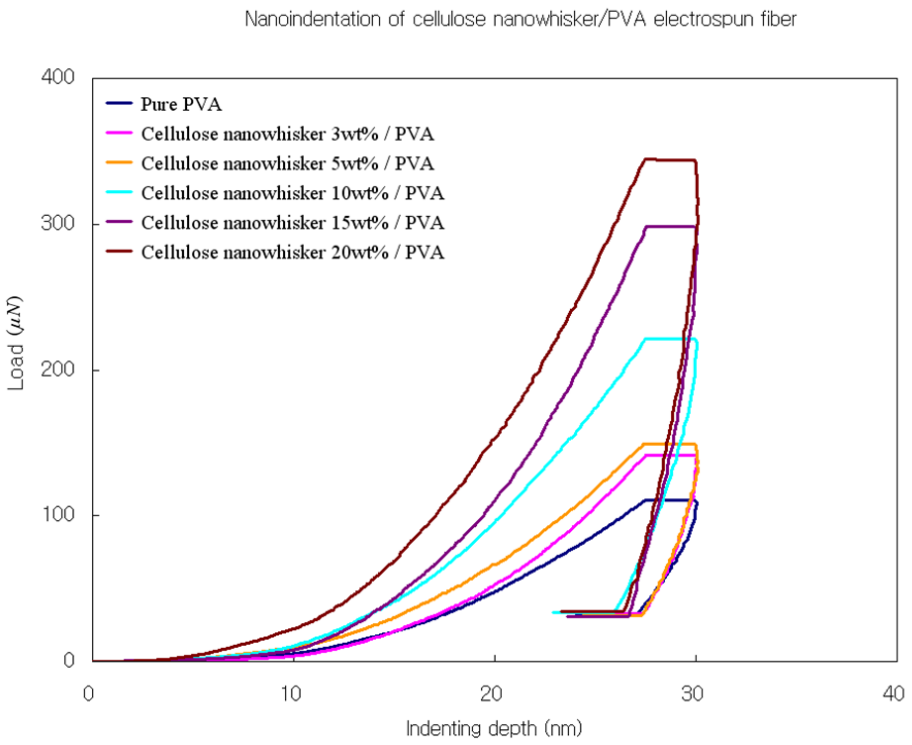

Figure 4-8. Representative load-hold-unload plots of indentation on the pure PVA electrospun fiber and cellulose nanowhisker/PVA electrospun fiber with different loading ratio (3.0wt% ~ 20.0wt%).

Fig 4-8 shows the representative load-hold-unload plots of nanoindentation on the pure PVA and cellulose nanowhisker/PVA electrospun fibers with different loading ratios of cellulose nanowhiskers (3.0wt% ~ 20.0wt%) as a function of the indenting depth. When the indenter tip was loaded on the electrospun fiber with a constant strain rate (0.05 s^{-1}), the load measured by the tip increased with increasing contact area between the tip and the fiber sample. After the tip penetrated into the fiber until 30nm depth, the load was held for 10 seconds and then the indenter tip was withdrawn from the sample. The unloading rate was set equal to the loading rate. The curves shifted upwards with increasing cellulose nanowhiskers concentration. This suggests that the load employed on the tip increased gradually with increasing cellulose nanowhisker content.

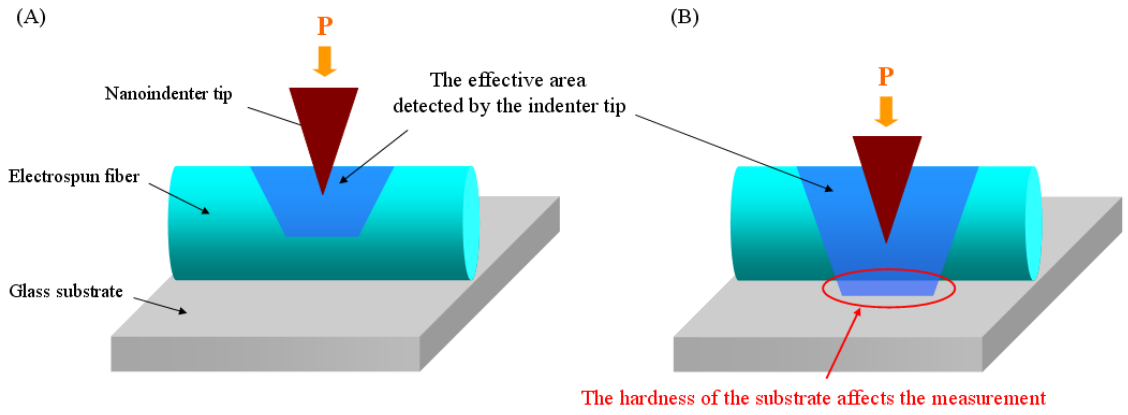

Figure 4-9. Schematic of nanoindentation and the effective area detected by the indenter tip (a) when the indenting depth is 15% of the electrospun fiber diameter (b) when the indenting depth is 60% of the electrospun fiber diameter.

When a modulus of electrospun fibers is measured using the nanoindenter, several factors may cause errors and should be considered carefully. The first factor is the effect of the substrate. Because the average diameter of the electrospun fibers is very small (220nm ~ 290nm), the indenting depth should be selected carefully. If the indenting tip penetrates too close to the underlying hard substrate, the tip can detect the hardness of the substrate in spite of there being no contact with the substrate. In conclusion, measured modulus values can be overestimated [27]. To prevent this problem, the indenting depth was fixed at 30nm and the remaining distance between the penetrated tip and substrate was larger than 180nm. The schematic of nanoindentation and the effective area detected by the indenter tip are shown in Fig 4-9. The effective area detected by the indenter tip is marked with a blue color. As shown in Fig 4-9 (b), the effective area is overlapped with the substrate and the hardness of the substrate can affect the measurement. A fiber surface morphology can also affect the measurement results. A rough fiber surface changes the contact pressure on the tip [28] and it causes a larger deviation of measured values. In this experiment, the PVA solution concentration was fixed at 8.0wt% to fabricate a smooth electrospun fiber without any beads. To confirm the smoothness of

fiber surfaces, the surface morphology of each sample was also observed using SEM before the nanoindentation measurement. The third possible problem is the slippage of the tip. If the nanoindenter tip is not perpendicular to the fiber surface, it may cause the slip and then friction between the tip and fiber surface [29]. The slippage caused untypical load-displacement curves, and they were excluded before the data analysis was performed. Finally, a fiber may move during indentation due to the pressure of the tip. Movement of the fiber also caused untypical load-displacement curves and its corresponding data were deleted as well.

Table 4-1. The nanoindentation results of 20.0wt% cellulose nanowhiskers reinforced PVA electrospun fibers and the measurement errors.

Sample no.	Modulus (GPa)	Note	Sample no.	Modulus (GPa)	Note
1	7.56		26	7.96	
2	7.32		27	0.45	deleted
3	7.90		28	7.25	
4	8.27		29	error	deleted
5	7.93		30	7.68	
6	error	deleted	31	0.66	deleted
7	8.06		32	8.21	
8	0.85	deleted	33	8.16	
9	7.96		34	8.32	
10	7.83		35	7.32	
11	8.04		36	error	deleted
12	8.21		37	7.04	
13	error	deleted	38	7.32	
14	7.59		39	7.69	
15	8.31		40	0.23	deleted
16	error	deleted	41	8.41	
17	6.32		42	7.84	
18	1.34	deleted	43	7.38	
19	7.42		44	error	deleted
20	6.84		45	8.49	
21	error	deleted	46	8.22	
22	7.56		47	error	deleted
23	8.34		48	7.89	
24	7.90		49	6.89	
25	7.66		50	7.95	

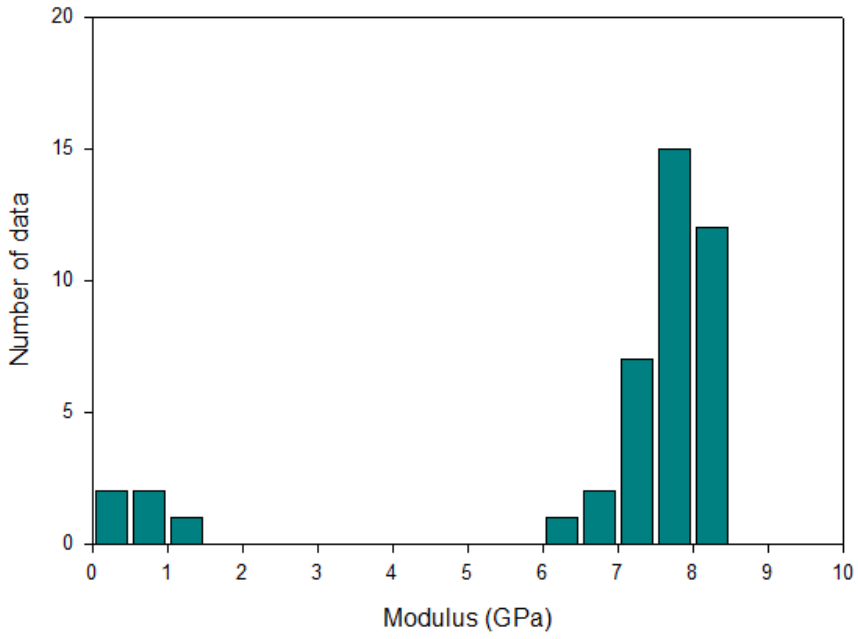

Figure 4-10. The data distribution of nanoindentation measurement results of 20.0wt% cellulose nanowhiskers reinforced PVA electrospun fibers.

During the nanoindentation, measurement errors are unavoidable due to the nano-size of cellulose nanowhisker/PVA electrospun fibers. To obtain an accurate data analysis, nanoindentation measurements were repeated 50 times. The entire set of data points from the nanoindentation measurements of 20.0wt% cellulose nanowhisker reinforced PVA electrospun fibers are summarized in Table 4-1. When the indenter tip slips on the electrospun fiber or the fiber moves due to the pressure of the tip, the error messages are shown on the nanoindentation instrument. If the tip is loaded on the edge of the fiber, the measured modulus is much smaller than the normal value. If the measured data is 50% smaller than the average of other data points, the data was considered as a measurement error. Fig 4-10 is the data distribution of nanoindentation measurement results of 20.0wt% cellulose nanowhiskers reinforced PVA electrospun fibers. As shown in Fig 4-10, it looks very reasonable that data ranged between 0.0GPa and 2.0GPa were considered as measurement errors.

For pure PVA and cellulose nanowhisker (1.0wt% ~ 20.0wt%) / PVA electrospun fibers, the nanoindentation was conducted 50 times. Among 50 measurements, 10 ~ 15 data points were measurement errors, therefore 35 ~ 40 data points were used to get the average modulus value and the standard deviation. Fig 4-11 shows the average modulus and the standard deviation of pure PVA and cellulose nanowhisker (1.0wt% ~ 20.0wt%) / PVA electrospun fibers as a function of cellulose nanowhisker content (wt%). The modulus of electrospun fibers increased linearly with increasing cellulose nanowhisker loading ratio up to 20.0wt%. In the case of PVA electrospun fibers with 5.0wt% cellulose nanowhisker, a 55% increase has been observed compared to pure PVA electrospun fiber. The PVA electrospun fiber with 15.0wt% and 20.0wt% loading of cellulose nanowhiskers showed an 180% and 261% increase of modulus, respectively.

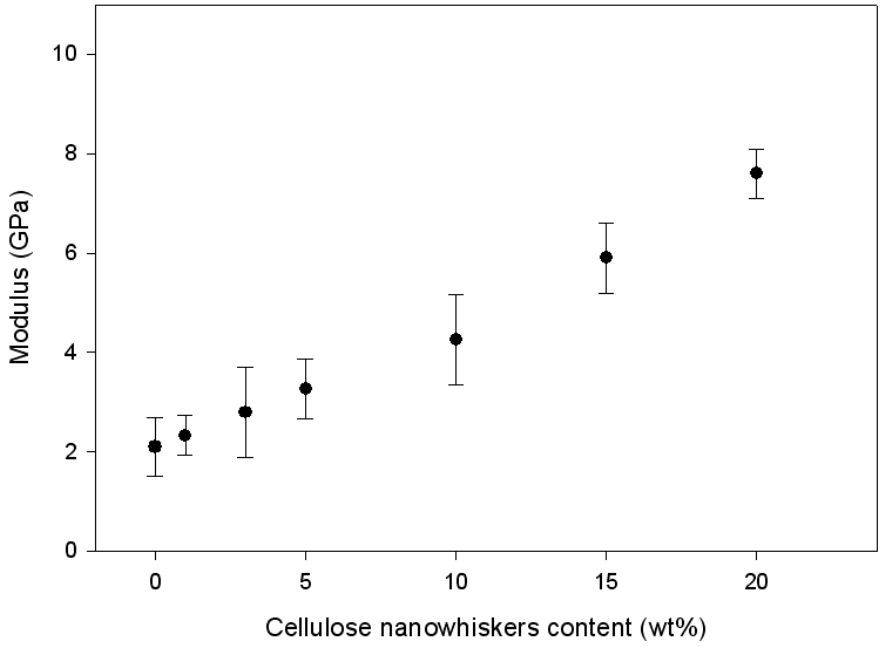

Figure 4-11. Average modulus of pure PVA and cellulose nanowhiskers (1.0wt% ~ 20.0wt%) / PVA electrospun fibers as a function of cellulose nanowhiskers contents (wt%).

4.3.3. Model study

Halpin-Tsai equation is the most widely used model for the analysis of mechanical properties of nanocomposites [30]. Halpin-Tsai model has been successfully applied to predict the modulus of bar-type filler reinforced nanocomposites. The schematics of longitudinal, transverse and isotropic arrangement of bar-type fillers are shown in Fig 4-12. When fillers are aligned parallel to the tensile test direction, the longitudinal Halpin-Tsai model can be used to predict the modulus of nanocomposites. If the orientation of fillers is vertical to the test direction, the transverse Halpin-Tsai model can be applied [31-32].

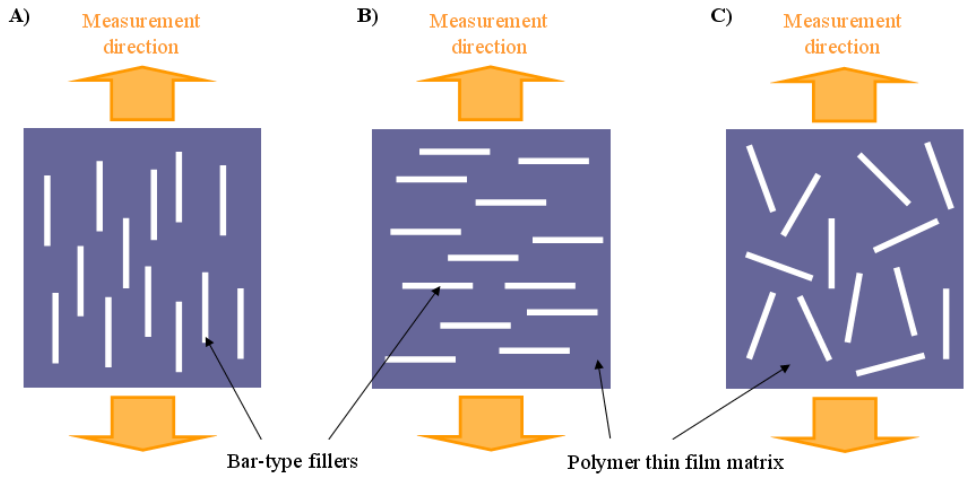

Figure 4-12. Schematics of the arrangement of bar-type fillers in polymer thin film nanocomposites (a) longitudinal arrangement (b) transverse arrangement (c) isotropic arrangement of bar-type fillers.

The longitudinal Halpin-Tsai model (E_L) is given by

$$E_L = \frac{1+\zeta\eta_L V_f}{1-\eta_L V_f} E_m \quad , \tag{4.3}$$

where E_m and E_f are the modulus of the matrix and bar-type fillers, respectively and V_f is the volume fraction of fillers in the matrix. ζ (shape factor) and η_L are defined as,

$$\eta_L = \frac{(E_f / E_m) - 1}{(E_f / E_m) + \zeta} \tag{4.4}$$

$$\zeta = 2\frac{L}{d} \quad , \tag{4.5}$$

where L and d is the average length and diameter of fillers. On the other hand, the transverse Halpin-Tsai model (E_T) is given by

$$E_T = \frac{1 + 2\eta_T V_f}{1 - \eta_T V_f} E_m \quad , \tag{4.6}$$

where ζ (shape factor) is 2 and η_T is defined as,

$$\eta_T = \frac{(E_f / E_m) - 1}{(E_f / E_m) + 2} \quad . \tag{4.7}$$

The modulus of nanocomposites reinforced by isotropically oriented fillers can be predicted by the isotropic Halpin-Tsai model (E), which is expressed as the fractional summation of E_L and E_T.

$$E = \frac{3}{8}E_L + \frac{5}{8}E_T \tag{4.8}$$

It was reported that the modulus of the crystalline region of cellulose was 137GPa measured by X-ray diffraction [1], 143GPa measured by Raman spectroscopic technique [2], and149GPa ~ 155GPa calculated by computational simulation [3]. The modulus of an isolated cellulose microfibril was measured directly using an atomic force microscope (AFM) 3-point bend test and was evaluated to be 93GPa [33]. It is very difficult to measure the mechanical properties of cellulose nanowhiskers directly. The diameter and the length of cellulose nanowhiskers are nano-size and much smaller than those of cellulose microfibrils, therefore isolating, gripping and holding the isolated cellulose nanowhisker is not technically feasible. Therefore, the modulus of a cellulose nanowhisker should be based on the modulus of the crystalline cellulose and cellulose microfibrils. It seems reasonable for the modulus of cellulose nanowhiskers to be between that of crystalline cellulose (137GPa ~ 155GPa) and that of cellulose microfibrils (~93GPa) because the ratio of crystalline domain in cellulose nanowhiskers is between that of crystalline cellulose and cellulose microfibrils.

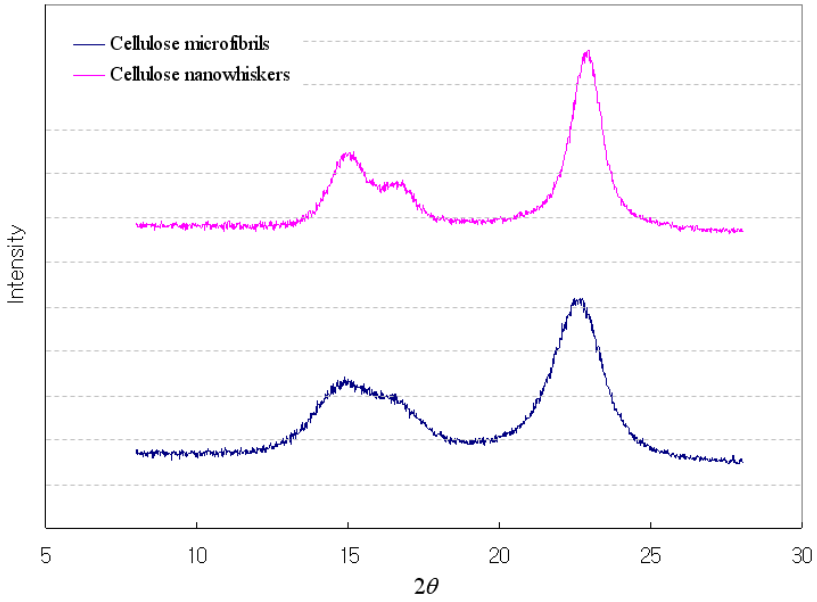

Figure 4-13. Wide-angle X-ray diffraction (WXRD) results of cellulose microfibrils and cellulose nanowhiskers.

Fig 4-13 provides the Wide-angle X-ray diffraction (WXRD) results of cellulose microfibrils and cellulose nanowhiskers. Both of the plots show 2θ peaks at approximately 14.8°, 16.5° and 22.8°, which can be assigned to cellulose I crystal planes $(1\bar{1}0)$, (110) and (200), respectively [34]. However, the intensities of the peaks are quite different. The 2θ peaks of cellulose nanowhiskers are narrower and shaper than those of cellulose microfibrils. Crystallinity of cellulose microfibrils and cellulose nanowhiskers are calculated according to Martin and Segal method [35]. It uses the height of (200) peak and the minimum between (200) and (110) peaks, assuming that intensity of (200) represents both crystalline and amorphous part while the minimum intensity between (200) and (110) peaks indicates the amorphous part only.

$$CrI = (I_{(200)}-I_{am})/I_{(200)} \quad (4.9)$$

Where, CrI is the crystallinity index, $I_{(200)}$ is the intensity at (200) peak (2θ=22.8°) and I_{am} is the intensity at the minimum between (110) peak and (200) peak. Calculated crytallinity of cellulose microfibrils and cellulose nanowhiskers are 84.7% and 91.6%, respectively. From the WXRD results, it is confirmed that cellulose nanowhiskers have a higher crystalline ratio than cellulose microfibrils.

In the model study, the modulus of cellulose nanowhiskers is assumed to be 110GPa. The average length and diameter of cellulose nanowhiskers are 200nm and 10nm, respectively. The density of cellulose nanowhiskers was reported as $1.5\ g/cm^3$ [36]. The modulus and the density of the PVA matrix are 2.1GPa and $1.25\ g/cm^3$, respectively. The modulus of cellulose nanowhiskers/PVA electrospun fibers predicted by the longitudinal Halpin-Tsai model, the transverse Halpin-Tsai model, and the isotropic Halpin-Tsai model are shown in Fig 4-14. The longitudinal Halpin-Tsai model shows the highest modulus value and the modulus predicted by the transverse

Halpin-Tsai model is the smallest among the three models. If bar-type fillers are aligned in the same direction as the tensile test, the physical properties of nanocomposite thin films are improved due to the significant load transfer across the filler-matrix interface [37-38].

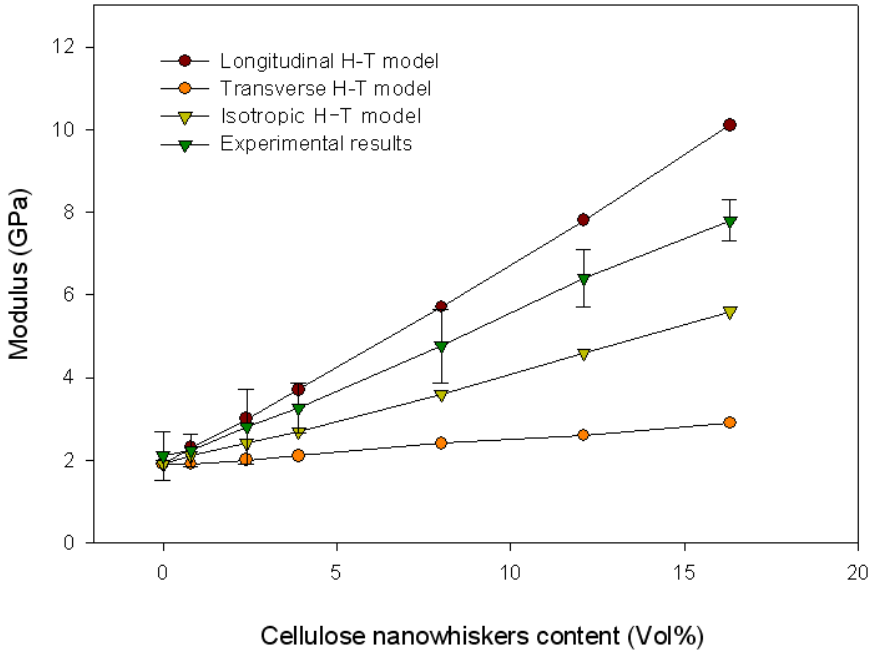

Figure 4-14. The modulus of cellulose nanowhiskers/PVA electrospun fiber predicted by Halpin-Tsai models and the experimental results.

At Fig 4-14, experimental results are plotted together to compare with the model prediction. Experimental results are larger than the predication by the isotropic and transverse Halpin-Tsai model. It suggests that cellulose nanowhiskers are aligned in PVA electrospun fibers. This agrees with the well-known fact that nanoparticles are aligned automatically inside of the electrospun fiber during the electrospinning process due to the high shear force of the polymer jet [39-42]. However, the experimental results are 20~30% smaller than the longitudinal model predictions. For example, the calculated

modulus of PVA electrospun fibers with 20.0wt% cellulose nanowhisker loading (V_f = 16.3%) is 10.1GPa, whereas the actual modulus is 7.8GPa.

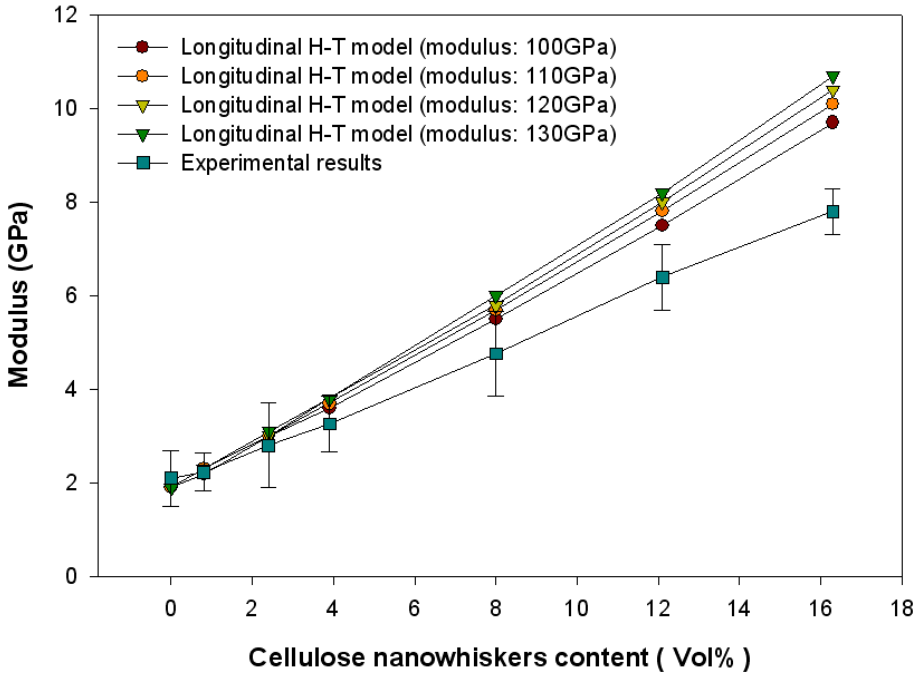

Figure 4-15. The modulus of cellulose nanowhiskers/PVA electrospun fiber predicted by Halpin-Tsai models with various assumed modulus of cellulose nanowhiskers (100GPa ~ 130GPa) and the experimental results.

There are several possible explanations for the difference between the longitudinal modulus and the experimental results. First, the actual modulus of cellulose nanowhiskers could be different from the assumed value (110GPa). Fig 4-15 shows the longitudinal model prediction plots and experimental results when the assumed modulus of cellulose nanowhiskers is 100GPa, 110GPa, 120GPa and 130GPa, respectively. Second, there could be a deviation of the orientation of cellulose nanowhiskers in PVA electrospun fibers. From the TEM images of references [39-42], it seems that the orientation of bar-type fillers has a deviation (~5°). The deviation of cellulose

nanowhisker orientation in the PVA fiber matrix can decrease the experimental results. It is difficult to take TEM images of cellulose nanowhiskers without staining the sample [4, 36, 43], therefore the actual alignment of cellulose nanowhiskers in PVA matrix could not be confirmed by TEM images. The indenter tip used in the measurement is a cube-corner three-sided pyramidal diamond tip. The centerline to face angle of the cube-corner tip is 35.3° [25] and the actual angle between the tip and aligned cellulose nanowhisker is 54.7°, not the 90.0°. Therefore, it is expected that the measured modulus is between the longitudinal model and the isotropic model prediction. The load transfer mechanism of aligned bar-type particles in a polymer matrix during the nanoindentation has not been studied. In future studies, the load transfer mechanism and the effect of aligned cellulose nanowhiskers in the PVA matrix on the nanoindentation measurement will be investigated.

4.4. Conclusions

The mechanical properties of cellulose nanowhiskers reinforced poly(vinyl alcohol) (PVA) electrospun fibers have been measured using the nanoindentation method. Due to the small size of PVA electrospun fibers, ~ 10 - 15 measurement errors occurred during the total of 50 measurements. The modulus of PVA/cellulose nanowhisker electrospun fibers increases linearly with increasing loading ratio of cellulose nanowhiskers up to 20.0wt%. The modulus of a pure PVA electrospun fiber is 2.10GPa. The modulus of 5.0wt%, 10.0wt% and 20.0wt% cellulose nanowhisker reinforced PVA electrospun fibers were 3.26GPa, 4.26GPa and 7.80GPa, respectively. Cellulose nanowhisker/PVA electrospun fibers with 20.0wt% loading shows a 260% increase of modulus compared to that of a pure PVA electrospun fiber. Experimental results were compared with Halpin-Tsai models. The experimental results were larger than the predicted values by the isotropic Halpin-Tsai model and the transverse Halpin-Tsai

model, however, the experimental results were 20~30% smaller than the longitudinal Halpin-Tsai model predictions.

References

1. Sakurada, I., Y. Nukushina, and T. Ito, *EXPERIMENTAL DETERMINATION OF ELASTIC MODULUS OF CRYSTALLINE REGIONS IN ORIENTED POLYMERS.* JOURNAL OF POLYMER SCIENCE, 1962. **57**(165): p. 651-&.

2. Sturcova, A., G.R. Davies, and S.J. Eichhorn, *Elastic modulus and stress-transfer properties of tunicate cellulose whiskers.* Biomacromolecules, 2005. **6**(2): p. 1055-1061.

3. Eichhorn, S.J. and G.R. Davies, *Modelling the crystalline deformation of native and regenerated cellulose.* Cellulose, 2006. **13**(3): p. 291-307.

4. Samir, M., F. Alloin, and A. Dufresne, *Review of recent research into cellulosic whiskers, their properties and their application in nanocomposite field.* Biomacromolecules, 2005. **6**(2): p. 612-626.

5. Czaja, W.K., et al., *The future prospects of microbial cellulose in biomedical applications.* Biomacromolecules, 2007. **8**(1): p. 1-12.

6. Angles, M.N. and A. Dufresne, *Plasticized starch/tunicin whiskers nanocomposites. 1. Structural analysis.* Macromolecules, 2000. **33**(22): p. 8344-8353.

7. Grunert, M. and W.T. Winter, *Nanocomposites of cellulose acetate butyrate reinforced with cellulose nanocrystals.* Journal of Polymers and the Environment, 2002. **10**(1-2): p. 27-30.

8. Chazeau, L., et al., *Viscoelastic properties of plasticized PVC reinforced with cellulose whiskers.* Journal of Applied Polymer Science, 1999. **71**(11): p. 1797-1808.

9. Lu, J., T. Wang, and L.T. Drzal, *Preparation and properties of microfibrillated cellulose polyvinyl alcohol composite materials.* Composites Part a-Applied Science and Manufacturing, 2008. **39**(5): p. 738-746.

10. Yeo, I.S., et al., *Collagen-based biomimetic nanofibrous scaffolds: Preparation and characterization of collagen/silk fibroin bicomponent nanofibrous structures.* Biomacromolecules, 2008. **9**(4): p. 1106-1116.

11. Ko, F., et al., *Electrospinning of continuons carbon nanotube-filled nanofiber yarns.* Advanced Materials, 2003. **15**(14): p. 1161-+.

12. Fong, H., et al., *Generation of electrospun fibers of nylon 6 and nylon 6-montmorillonite nanocomposite.* Polymer, 2002. **43**(3): p. 775-780.

13. Wang, X.F., et al., *Formation of water-resistant hyaluronic acid nanofibers by blowing-assisted electro-spinning and non-toxic post treatments.* Polymer, 2005. **46**: p. 4853-4867.

14. Teo, W.E., et al., *Porous tubular structures with controlled fibre orientation using a modified electrospinning method.* Nanotechnology, 2005. **16**(6): p. 918-924.

15. Li, D., Y.L. Wang, and Y.N. Xia, *Electrospinning nanofibers as uniaxially aligned arrays and layer-by-layer stacked films.* Advanced Materials, 2004. **16**(4): p. 361-366.

16. Tan, E.P.S., et al., *Tensile test of a single nanofiber using an atomic force microscope tip.* Applied Physics Letters, 2005. **86**(7).

17. Inai, R., M. Kotaki, and S. Ramakrishna, *Structure and properties of electrospun PLLA single nanofibres.* Nanotechnology, 2005. **16**(2): p. 208-213.

18. Duvail, J.L., et al., *Physical properties of conducting polymer nanofibers.* Synthetic Metals, 2003. **135**(1-3): p. 329-330.

19. Mack, J.J., et al., *Graphite nanoplatelet reinforcement of electrospun polyacrylonitrile nanofibers.* Advanced Materials, 2005. **17**(1): p. 77-+.

20. Tan, E.P.S. and C.T. Lim, *Mechanical characterization of nanofibers - A review.* Composites Science and Technology, 2006. **66**(9): p. 1102-1111.

21. Dong, X.M., J.F. Revol, and D.G. Gray, *Effect of microcrystallite preparation conditions on the formation of colloid crystals of cellulose.* Cellulose, 1998. **5**(1): p. 19-32.

22. Li, D., Y.L. Wang, and Y.N. Xia, *Electrospinning of polymeric and ceramic nanofibers as uniaxially aligned arrays.* Nano Letters, 2003. **3**(8): p. 1167-1171.

23. Beake, B.D., et al., *Nanoindentation behavior of clay/poly(ethylene oxide) nanocomposites.* Journal of Nanoscience and Nanotechnology, 2002. **2**(1): p. 73-79.

24. Shen, L., et al., *Nanoindentation and morphological studies on nylon 66 nanocomposites. I. Effect of clay loading.* Polymer, 2004. **45**(10): p. 3341-3349.

25. Strader, J.H., et al., *An experimental evaluation of the constant ss relating the contact stiffness to the contact area in nanoindentation.* Philosophical Magazine, 2006. **86**(33-35): p. 5285-5298.

26. Oliver, W.C. and G.M. Pharr, *AN IMPROVED TECHNIQUE FOR DETERMINING HARDNESS AND ELASTIC-MODULUS USING LOAD AND DISPLACEMENT SENSING INDENTATION EXPERIMENTS.* Journal of Materials Research, 1992. **7**(6): p. 1564-1583.

27. Chizhik, S.A., et al., *Surface force spectroscopy of elastomeric nanoscale films.* Macromolecular Symposia, 2001. **167**: p. 167-175.

28. Johnson, K.L., *Contact mechanics and the wear of metals.* Wear, 1995. **190**(2): p. 162-170.

29. Li, X.D., et al., *Nanoindentation of silver nanowires.* Nano Letters, 2003. **3**(11): p. 1495-1498.

30. Lee, J., Q.H. Sun, and Y.L. Deng, *Nanocomposites from regenerated cellulose and nanoclay.* Journal of Biobased Materials and Bioenergy, 2008. **2**(2): p. 162-168.

31. Liu, L.Q., et al., *Mechanical properties of functionalized single-walled carbon-nanotube/poly(vinyl alcohol) nanocomposites.* Advanced Functional Materials, 2005. **15**(6): p. 975-980.

32. Cadek, M., et al., *Morphological and mechanical properties of carbon-nanotube-reinforced semicrystalline and amorphous polymer composites.* Applied Physics Letters, 2002. **81**(27): p. 5123-5125.

33. Cheng, Q.Z. and S.Q. Wang, *A method for testing the elastic modulus of single cellulose fibrils via atomic force microscopy.* Composites Part a-Applied Science and Manufacturing, 2008. **39**(12): p. 1838-1843.

34. French AD, R.W., Miller DP, *X-ray diffraction studies of ramie cellulose I.* ACS Symp. Series, 1987. **340**: p. 15-37.

35. Segal L, Creely JJ, Martin AE and Conrad CM, *An empirical mothod for estimating the degree of crystallinity of native cellulose using the X-ray diffractometer.* Textile Research Journal, 1959, 29(10), 786-794.

36. Eichhorn, S.J., et al., *Review: current international research into cellulose nanofibres and nanocomposites.* Journal of Materials Science, 2010. **45**(1): p. 1-33.

37. Thostenson, E.T. and T.W. Chou, *Aligned multi-walled carbon nanotube-reinforced composites: processing and mechanical characterization.* Journal of Physics D-Applied Physics, 2002. **35**(16): p. L77-L80.

38. Qian, D., et al., *Load transfer and deformation mechanisms in carbon nanotube-polystyrene composites.* Applied Physics Letters, 2000. **76**(20): p. 2868-2870.

39. Liu, L.Q., et al., *Tensile mechanics of electrospun multiwalled nanotube/poly(methyl methacrylate) nanofibers.* Advanced Materials, 2007. **19**(9): p. 1228-+.

40. Li, L., et al., *Formation and properties of nylon-6 and nylon-6/montmorillonite composite nanofibers.* Polymer, 2006. **47**(17): p. 6208-6217.

41. Dror, Y., et al., *Carbon nanotubes embedded in oriented polymer nanofibers by electrospinning.* Langmuir, 2003. **19**(17): p. 7012-7020.

42. Ge, J.J., et al., *Assembly of well-aligned multiwalled carbon nanotubes in confined polyacrylonitrile environments: Electrospun composite nanofiber sheets.* Journal of the American Chemical Society, 2004. **126**(48): p. 15754-15761.

43. Lima, M.M.D. and R. Borsali, *Rodlike cellulose microcrystals: Structure, properties, and applications.* Macromolecular Rapid Communications, 2004. **25**(7): p. 771-787.

CHAPTER 5

THE MORPHOLOGY AND MECHANICAL PROPERTIES OF ICE-TEMPLATED CELLULOSE MICROFIBRIL POROUS FOAMS

Abstract

Ice-templated (IT) cellulose microfibril porous foams are successfully fabricated via unidirectional freezing methods. IT cellulose microfibril foam prepared from 1.0wt% suspension shows a cross-linked network structure. Increasing the concentration of the cellulose microfibril suspension up to 2.75wt% leads to a gradual transition from a crosslinked network structure to a lamellar channel structure. Increasing the concentration of the suspension from 3.0wt% up to 8.0wt% will cause both the formation of highly aligned channel structures that are parallel to the freezing direction and an increase in the structure's wall thickness. It was found that cellulose microfibrils are partially aligned along the freezing direction. During IT methods, cellulose bridge structures are fabricated, instead of dendrite structures. The wavelength of IT channel structures can be controlled from 2.8 μm to 11.2 μm by changing the temperature gradient between the ice front and the cellulose microfibril suspension. It was found that the compressive stress of IT cellulose microfibril foams increases linearly from 30.7KPa to 360.2KPa with increasing concentrations of cellulose microfibril suspension from 2.0wt% up to 8.0wt%.

Keywords: Cellulose microfibril, Ice-templated method, Multichannel porous foam, Compressive stress

5.1. Introduction

Porous foam materials have attracted a great attention in both of academia and industry due to a wide range of applications such as artificial bone materials, drug delivery carriers, filter materials, and the parts of a motor vehicle. Porous foam materials demonstrate strong mechanical performance in spite of their light weights. They also have a large porosity to store or carry other materials. Porous foams posses various properties according to their architecture. Therefore, it is very important to control their architectural properties such as pore size, pore morphology, and porous space arrangement. So far, the most common processing methods are template replica methods [1-5], sacrificial template techniques [6-9], and direct foaming methods [10-13].

Of the many techniques reported to prepare porous foams, ice-templated (IT) methods are relatively new [14]. IT techniques are very simple but can produce highly ordered porous structures. The unidirectional freezing of the aqueous suspension, followed by the unidirectional growth of ice crystals and sublimation of ice crystal templates result in highly ordered porous foams with unidirectional channels. Moreover, IT methods can be applied to a wide variety of material systems such as inorganic particles [15], polymers [16], and inorganic-polymer hybrids [17]. In conventional foaming methods, the chemical interactions between component materials and templates are critical. On the other hand, IT foaming process is simply dependent on the physical entrapment of particles or polymers between ice crystals. Therefore, the IT method is more simple and versatile than other methods.

Recently, cellulose microfibrils have been widely used as reinforcement materials in polymeric nanocomposites due to the environmental concerns. Cellulose microfibrils show environmentally friendly characteristics and good mechanical properties. It was reported that the modulus of cellulose microfibrils was in the range of 78 ~ 114GPa [18-19]. Cellulose microfibrils are high aspect ratio string particles. Their diameters range from 10nm to 30nm and the length of cellulose microfibrils is between 1 μm and 30 μm,

depending on the preparation method and the source of cellulose microfibrils [20-21]. So far, it was reported that cellulose microfibrils were used as reinforcement materials for the nanocomposites with various matrix materials such as polyurethane [22], poly(lactic acid) [23], starch [24], cellulose acetate butyrate [25], poly(vinyl chloride) [26], and poly(vinyl alcohol) [27].

Porous foams prepared from cellulose microfibrils and amylopectin were reported [28]. IT porous foams prepared from rigid sphere particles such as alumina particles [29], rigid pallet type particles such as MMT [30], rigid belt type particles such as SWNT [15], and polymers such as PVA [16] have also been investigated. Cellulose microfibrils are high aspect ratio string-like particles with much flexibility. In this report, the growth mechanism of multichannel porous foams of pure cellulose microfibrils prepared via IT methods was investigated. The characteristic features of IT foams prepared from flexible string particles were also shown.

The compressive stress of IT cellulose microfibril foams has been measured. To compare the effects of characteristics of cellulose microfibrils on the mechanical properties of IT foams, the compressive stresses of IT foams prepared from MMT Na+ and cellulose nanowhiskers were also measured. Cellulose microfibrils show higher particle-particle interactions than MMT Na+ due to the strong hydrogen bonds. Although both the cellulose microfibrils and cellulose nanowhiskers have hydroxyl groups on the particle surfaces, cellulose microfibrils show higher aspect ratios than cellulose nanowhiskers.

5.2. Experimental

5.2.1. Materials

Montmorillonite Na+ (MMT Na+) clays were supplied by the Southern Clay Products. Cellulose microfibrils were prepared through acid hydrolysis of filter paper

with 50% sulfuric acid (VWR, USA). Briefly, 602 ml concentrated sulfuric acid was added drop-wise to a chilled mixture of 120 g Whatman No. 1 filter paper and 598 ml deionized water. This slurry was then placed into a 30°C hot water bath for 130 min and stirred. The resulting material underwent centrifuging and dialysis with deionized water to remove excess acid. After dialysis, the solution pH was raised to pH 6 using Amberlite (VWR, USA) resin beads. The cellulose suspension was sonicated in an ice bath for 20 minutes, centrifuged for 5 min at 14,000 rpm, and the cloudy supernatant was collected (this is the collected fibrils). This step was repeated until cloudy supernatant was no longer formed. The collected cloudy supernatant (the fibrils) were concentrated by placing into dialysis tubing in a PEG-water solution. A SEM image of prepared cellulose microfibrils is shown in Fig 5-1. The diameters of the microfibrils range from 10nm to 30nm, and their lengths are between 1 μm and 30 μm.

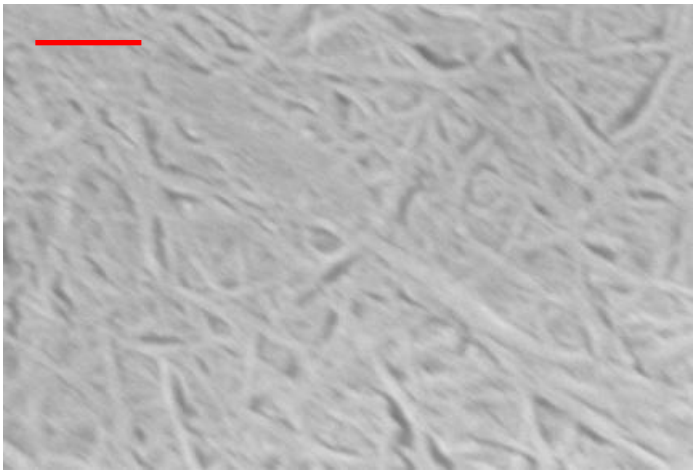

Figure 5-1. SEM image of cellulose microfibrils. Scale bars are of length 200nm.

Cellulose nanowhiskers were prepared using the method described by Dong et al. [31]. The suspensions of cellulose nanowhiskers were prepared from Whatman No. 1 filter paper by sulfuric acid hydrolysis. The concentration of sulfuric acid was fixed at 64%. The acid hydrolysis conditions were optimized at 45°C and 50mins. After

hydrolysis, the suspension was deionized by mixing in 1g of mixed-bed ion exchange resin and filtered. And then the suspension was washed with DI water and centrifuged (40mins, 3000rpm, Beckman Coulter, GS-6). The suspension was further dispersed by an ultrasound sonicator (15mins at full power, Branson 3510). The diameters of the nanowhisker range from 5nm to 10nm and their average length is ~ 200 nm.

5.2.2. Ice-templated method

Cellulose microfibrils suspension was freezed using liquid N_2 as shown in Fig 5-2 (a). A suspension sample was attached to a syringe pump and immersed into an insulated liquid N_2 bath. The immersing depth of the sample was maintained at 1mm during the whole freezing process using a syringe pump.

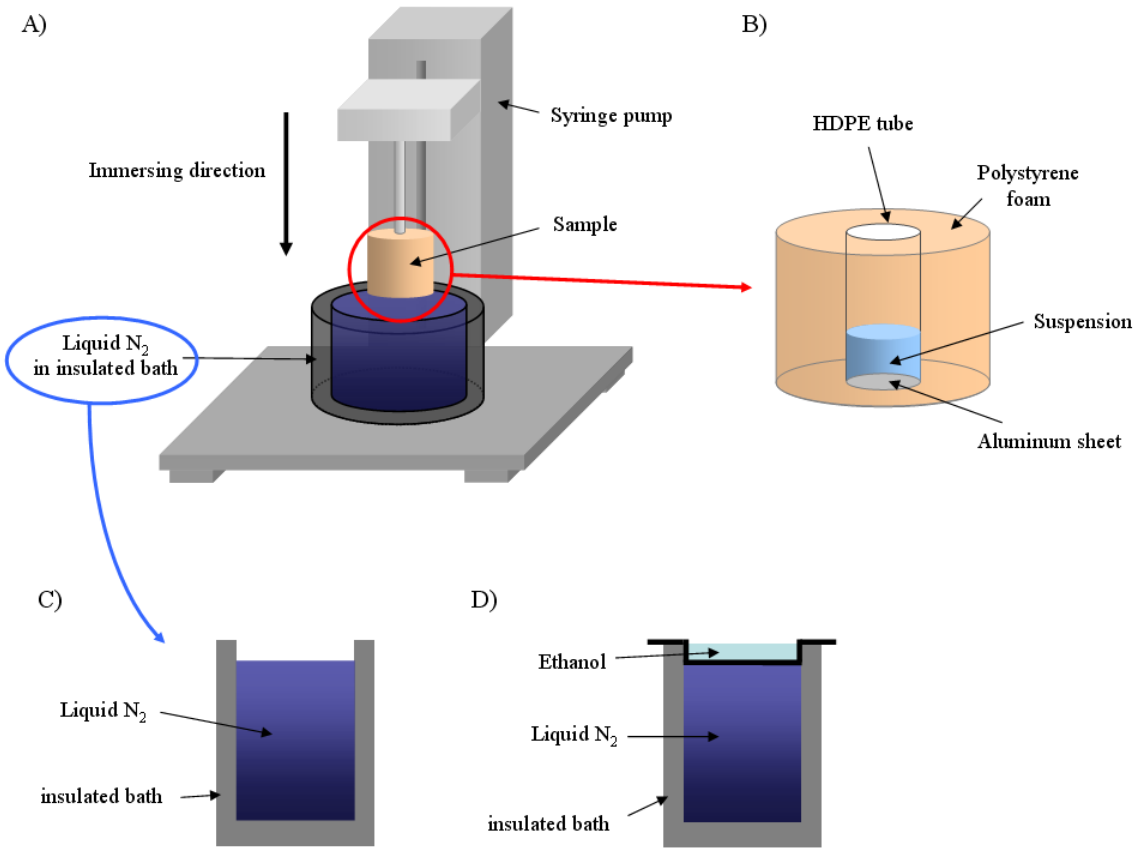

Figure 5-2 (a) Scheme of a freezing apparatus (b) scheme of a sample preparation (c) scheme of an insulated liquid N_2 bath (d) Scheme of an insulated liquid N_2 bath with a secondary freezing source (ethanol).

As shown in Fig 5-2 (b), a suspension was put inside a high density polyethylene (HDPE) tube. The inner diameter of the HDPE tube was 10 mm. To prevent vertical heat transfer as the temperature gradient orientation, the HDPE tube was insulated using polystyrene foam. An aluminum sheet was attached to the bottom of the HDPE tube. For the preparation of low freezing rate samples by a small temperature gradient, ethanol was used as a secondary freezing source (Fig 5-2 (d)). The m.p. of ethanol and b.p. of N_2 are -114°C and -196°C, respectively. Freezed samples were immediately put in a freeze-dryer to remove ice crystal templates by sublimation. After 48 hours, freeze-dried samples were taken out from the freeze-dryer. After that, polystyrene foams, HDPE tubes, and aluminum sheets were removed carefully. The image of prepared samples is shown in Fig 5-3. The diameter of the sample is 10 mm and the height is also 10 mm.

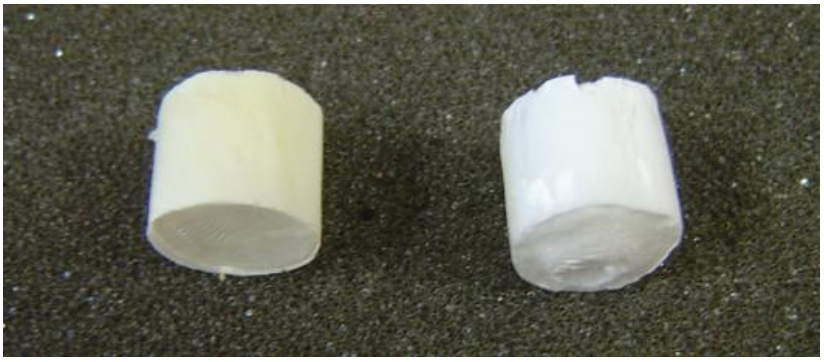

Figure 5-3. Cellulose microfibril porous foams (right side) and MMT Na+ porous foams (left side) prepared by ice-template method.

5.2.3. Characterization

Scanning electron microscopy (SEM) was carried out using a LEO 1530 at 10kV. The samples were sputter coated with Au using EMS 350 sputter (20mA, 2mins) prior to observation. A measurement of the average channel size of cellulose microfibril IT foams was conducted using ImageTool 3.0 software, which is provided by UTHSCSA. The compressive strength and modulus were measured using Instron 5566 (Instron Co., Canton, MA, USA). The compression head speed was 1mm/min.

5.3. Results and discussion

5.3.1 A growth mechanism of IT cellulose microfibril foams (1.0wt% ~ 2.75wt%)

In ice-templated methods, the particle concentration in suspension is an important factor when deciding the morphology of the IT porous foam [29]. In this study, IT cellulose microfibril porous foams were prepared from the various concentrations of cellulose microfibrils suspensions to investigate the detailed morphology and growth mechanism. IT foam samples were prepared as described in Fig 5-2 (b) and (c). Freeze-dried samples were cut off parallel to the orientation of the freezing direction and the center areas, which were fully developed during the freezing process, were examined using SEM (Fig 5-4).

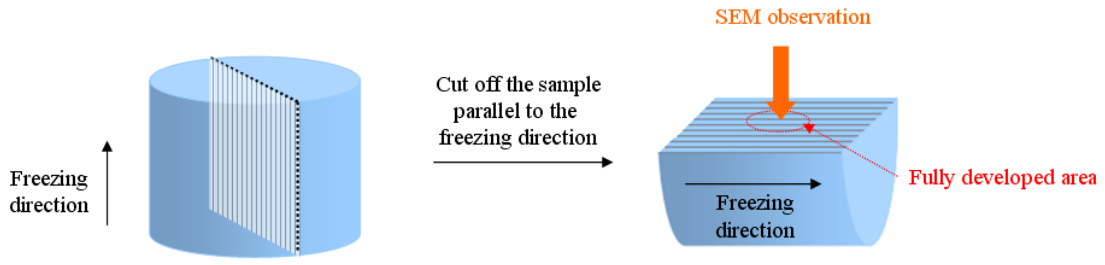

Figure 5-4. Schematic of the prepared sample and SEM observation.

The SEM images of IT cellulose microfibril porous foams prepared from 1.0wt% ~ 2.75wt% cellulose microfibril suspensions are shown in Fig 5-5, and their high resolution SEM images are shown in Fig 5-6. As shown in Fig 5-5 (a) and 5-6 (a), cellulose microfibrils foams prepared from 1.0wt% suspension shows a cross-linked network structure. The characteristic channel structure of IT porous foams can not be observed. The unique morphology of the crosslinked network structure is due to the distinctive characteristics of cellulose microfibrils. First, cellulose microfibrils are high aspect ratio string particles. The diameters of cellulose microfibrils range from 10nm to 30nm, and the lengths of cellulose microfibrils ranges from 1 micron and 30 micron. In addition, cellulose microfibrils exhibit strong hydrogen bonding with adjacent cellulose microfibril particles. Cellulose microfibrils are also relatively flexible nanoparticles, compared to other inorganic nanoparticles. Due to the alternating arrangement of crystalline and amorphous domains, cellulose microfibrils possesses enough flexibility to bend as shown in Fig 5-1. In conclusion, cellulose microfibrils bend and rotate to form tight bonds with adjacent microfibrils during the freezing process, resulting in the unique network structure of IT porous foams. As shown in Fig 5-6 (a), some parts of the strings constituting the network structure show a larger diameter than that of cellulose microfibrils. This suggests that several cellulose microfibrils are piled up together, resulting in the formation of a framework of IT network foams.

A transition from a crosslinked network structure to a lamellar channel structure occurs gradually as the concentration of cellulose microfibril suspensions are increased up to 2.75wt% (Fig 5-5 (b) ~ (f)). Contrary to the isotropic arrangement of cellulose microfibrils shown in Fig 5-5 (a), IT cellulose microfibril foams prepared with 1.5wt% and 2.0wt% suspension start to show the oriented porous structures (Fig 5-5 (b) and (c)). Cellulose microfibril walls parallel to the freezing direction start to emerge and the empty space between cellulose microfibrils become smaller. For IT cellulose microfibril foams made with 2.25wt% and 2.5wt% suspension (Fig 5-5 (d) and (e)), the wall structures are observed clearly and the size of the pores on the cellulose microfibril walls decreases with increasing concentration of microfibril suspension. For 2.75wt% cellulose microfibril foams, the formation of individual wall structures and lamellar channel structures are almost completed as shown in Fig 5-5 (f). Only a small number of defects on the wall structure are observed and their sizes are all less than 100nm. Detailed structures, pores and defects on IT cellulose microfibril foams are shown in high resolution SEM images (Fig 5-6).

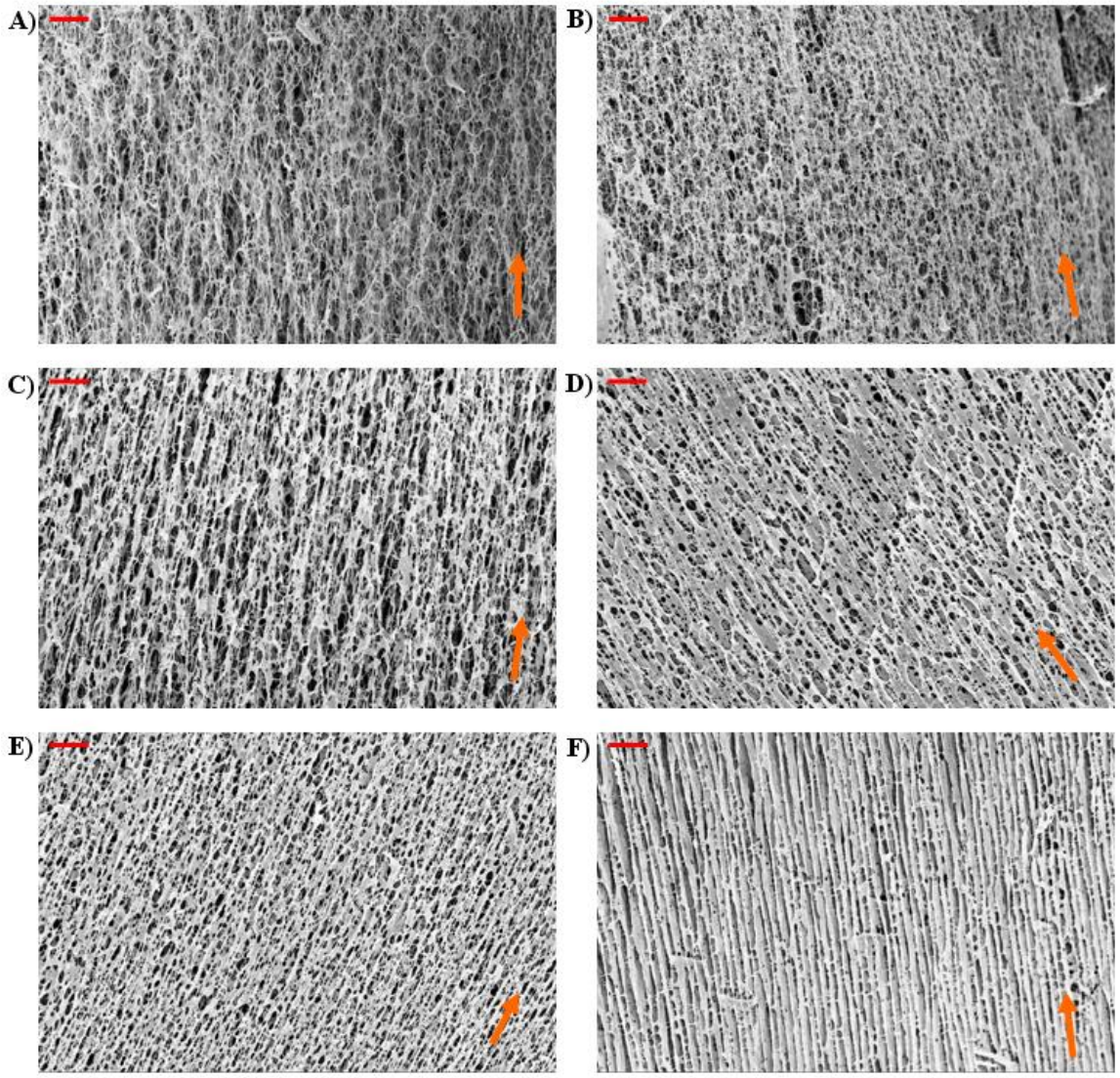

Figure 5-5. The SEM images of IT cellulose microfibril porous foams made with the various cellulose microfibrils suspension. Scale bars are of length 10 μm. Orange color arrows indicate the freezing direction. The suspension concentrations are (a) 1.0wt% (b) 1.5wt% (c) 2.0wt% (d) 2.25wt% (e) 2.5wt% (f) 2.75wt%, respectively.

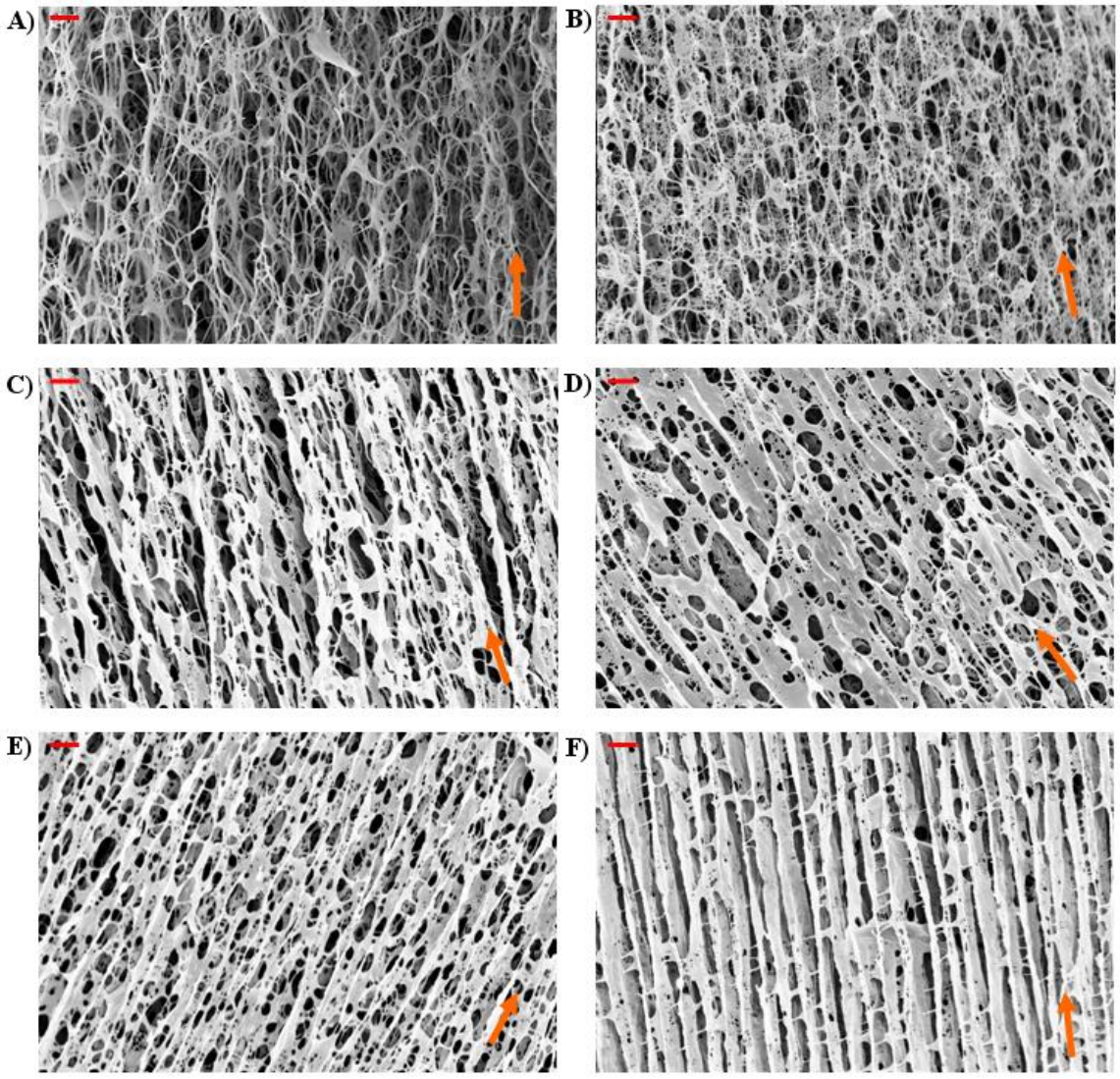

Figure 5-6. The high resolution SEM images of IT cellulose microfibril porous foams made with the various cellulose microfibrils suspension. Scale bars are of length 3 μm. Orange color arrows indicate the freezing direction. The suspension concentrations are (a) 1.0wt% (b) 1.5wt% (c) 2.0wt% (d) 2.25wt% (e) 2.5wt% (f) 2.75wt%, respectively.

In ice-templated methods, the unidirectional freezing of the cellulose microfibrils suspension, followed by the unidirectional growth of ice crystals, could result in highly ordered porous foams with unidirectional channels (Fig 5-5 (f) and Fig 5-6 (f)). During the freezing process, ice crystals grow in the same direction as the temperature gradient and cellulose microfibrils are entrapped between ice crystals as shown in Fig 5-7. After removing ice crystal templates by sublimation, the lamellar channel structures, which are a replica of the original ice-template, are obtained.

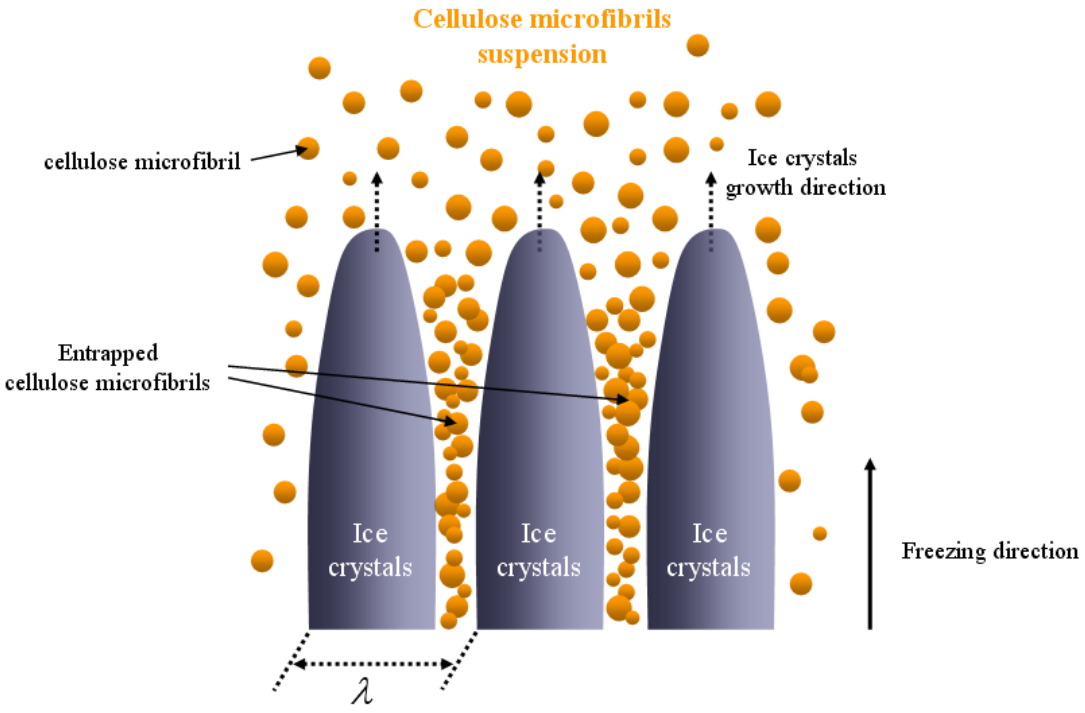

Fig 5-7. A schematic of the growth of ice crystals and the cellulose microfibril entrapment. Orange color spheres represents cellulose microfibrils. The wavelength of the structure is defined by λ.

Contrary to polymer based IT foams, the minimum wall thickness of IT cellulose microfibril foams is confined to the diameter of cellulose microfibrils. If it is assumed

that cellulose microfibrils in the individual walls are closely packed as a single layer, the critical concentration to form a fully developed IT channel structure can be calculated by

$$C = \frac{d\rho}{\lambda} \tag{5.1}$$

where λ is the wavelength of the structure, d is the average diameter of cellulose microfibrils, and ρ is the density of cellulose microfibrils. For IT cellulose microfibril foams, a typical value of λ is 3 μm, d = 20 nm and ρ = 1.5 g/cm^3 [32]. In this case, the theoretical critical concentration is 1 wt%. However, the cellulose microfibril wall obtained by IT methods is not an ideal single layer. Therefore, the experimental critical concentration is higher than the calculated value. As shown in Fig 5-5 and 5-6, the critical concentration is ~ 2.75 wt%.

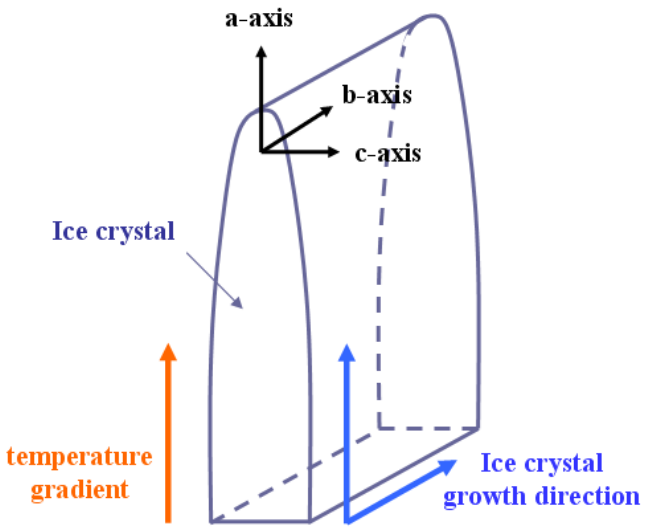

Figure 5-8. A scheme of ice crystal growth at the lamellar region.

The morphology of the individual wall structure of lamellar channels is significantly affected by the amount of entrapped cellulose microfibrils. If the suspension

concentration is 2.75wt%, the amount of cellulose microfibrils is enough to form smooth walls without defects, allowing fully developed channel structures to be obtained. If the suspension concentration is lower than 2.75wt%, partially developed channel structures are observed. In the case of a very low concentration of cellulose microfibrils suspension (1.0wt%) crosslinked network structures are fabricated.

Ice crystals grow anisotropically. The ice front velocity parallel to the temperature gradient orientation, crystallographic a-axis, is $10^2 \sim 10^3$ times faster than that of the c-axis, which is perpendicular to the temperature gradient [29]. If the growth of ice crystals is mature, ice crystals will grow to the a-axis and b-axis direction. On the other hand, the ice crystal growth to c-axis direction is still very slow. Therefore, the thickness of ice crystals along c-axis is very small and ice crystal grows as a flat platelet form, shown in Fig 5-8. The growth pattern of ice crystals affect the morphology of IT cellulose microfibril foams directly. As shown in Fig 5-5 (f), cellulose microfibril walls are formed along the a-axis and b-axis.

Another interesting feature in Fig 5-6 is the shape of the pores on cellulose microfibril walls. Most of the pores have an elliptical shape, rather than the circular form. To observe the shape of pores more clearly, negative images of Fig 5-6 are shown in Fig 5-9. Ellipse-shaped pores are especially prominent in the porous structure prepared from 2.0wt% ~ 2.5wt% cellulose microfibrils suspension (Fig 5-9 (c) ~ (e)). This suggests that cellulose microfibrils constituting the outer boundary of ellipses are anisotropically arranged. If cellulose microfibrils are randomly oriented without any preferred direction, the pore shape should be a circle, not an ellipse. It is also interesting that most of the major axes of elliptical pores (the white color shown in the images) are aligned parallel to the orientation of freezing direction. This indicates that microfibrils are also partially oriented to the direction of freezing. It is very difficult to measure the direction of each cellulose microfibrils in IT porous foams directly. Aligned elliptical pores are indirect evidences of the microfibril alignment along the freezing direction.

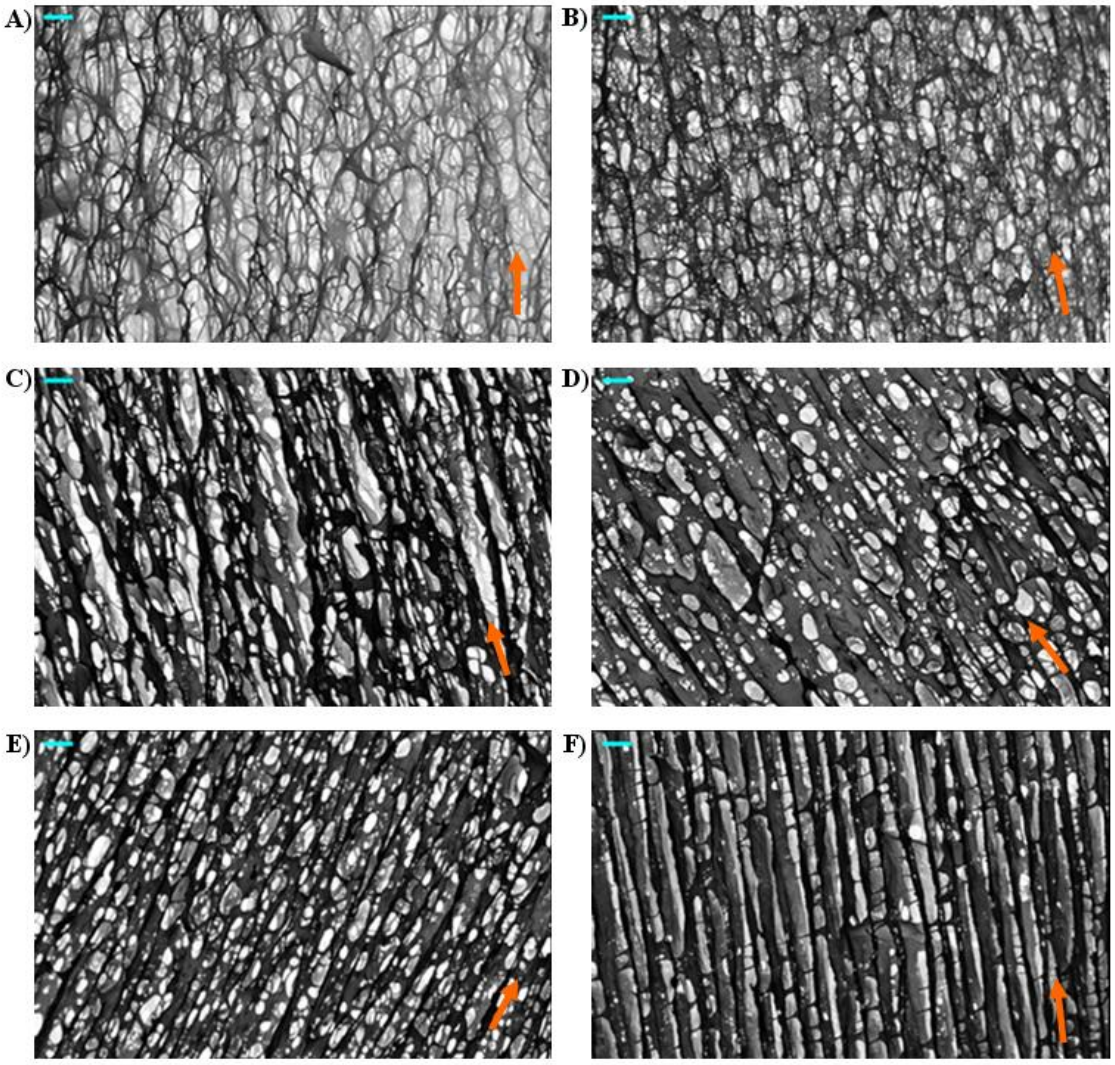

Figure 5-9. The negative images of SEM photos of IT cellulose microfibril porous foams made with the various cellulose microfibrils suspension. Scale bars are of length 3 μm. Orange color arrows indicate the freezing direction. The concentrations of the cellulose microfibril suspension are (a) 1.0wt% (b) 1.5wt% (c) 2.0wt% (d) 2.25wt% (e) 2.5wt% (f) 2.75wt%, respectively.

A possible explanation of cellulose microfibril alignment is the momentum exerted by growing ice crystals. A scheme of the cellulose microfibril alignment is shown in Fig 5-10. To simplify the system, a single microfibril and ice crystal model was suggested. As shown in Fig 5-10 (a), one end of cellulose microfibril was entrapped between two ice crystals and the other end has free movement at the unfreezed suspension. The free part of a microfibril is located across the ABC - space (Fig 5-10 (b)).

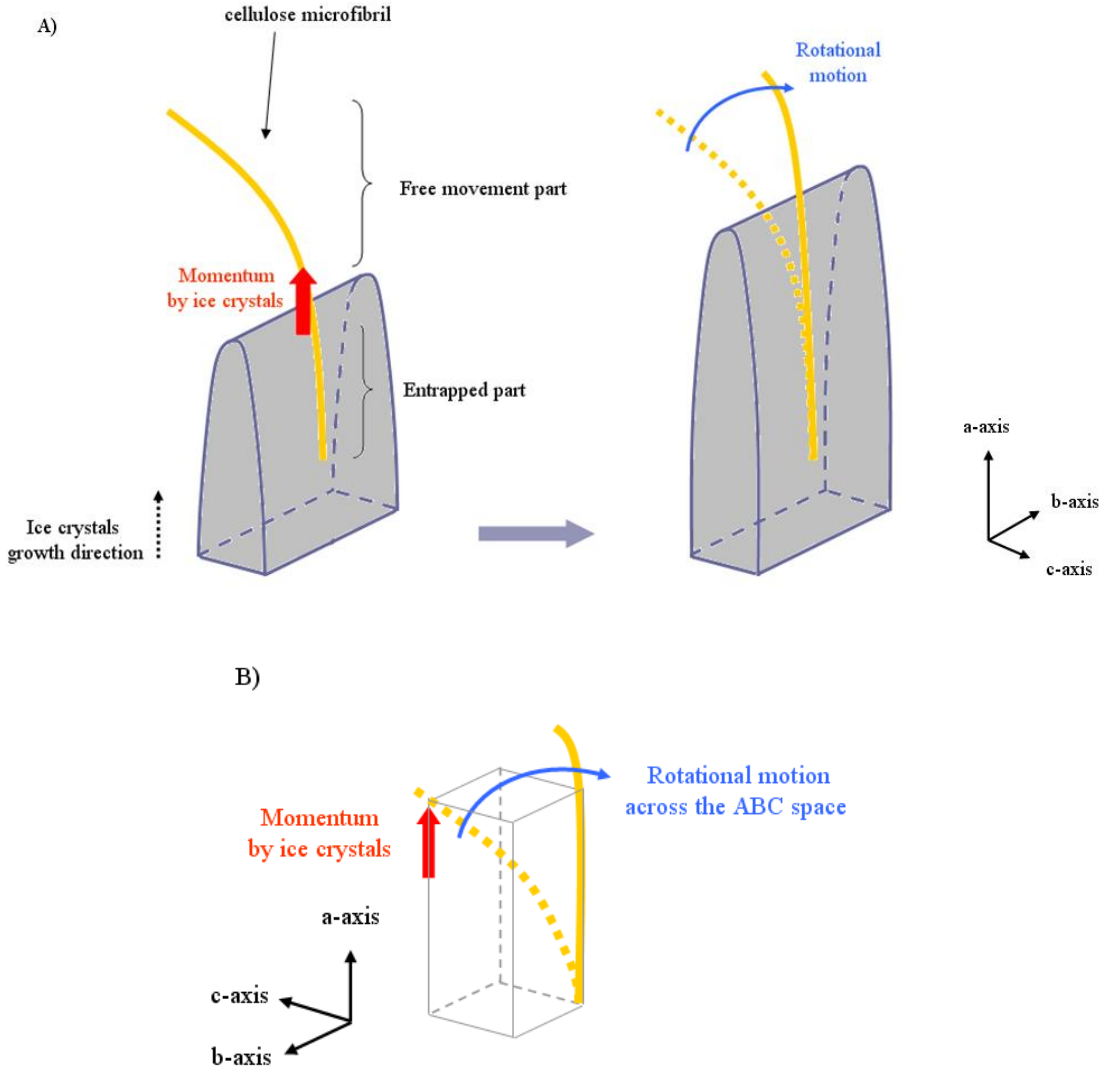

Figure 5-10 (a) A scheme of the cellulose microfibril alignment (b) A scheme of rotational motion of cellulose microfibril.

When the ice crystal grows along the a-axis, momentum exerted by the ice crystal is applied to the cellulose microfibril along the a-axis. Because one end of cellulose microfibril is fixed, the other end of the fibril shows a rotational motion across the ABC space, instead of a translational motion along the a-axis. Consequently, cellulose microfibrils are aligned along the a-axis, the freezing direction. The movement of cellulose microfibrils in a real system is more complicated than the suggested model because fibril-fibril interactions are also important. Therefore, all of the fibrils cannot be aligned as in the suggested model. However, as shown in Fig 5-9, it looks very clear that cellulose microfibrils are partially aligned along the freezing direction.

5.3.2 Morphology of IT cellulose microfibril foams (3.0wt% ~ 8.0wt%)

To investigate the morphology of fully developed channel structures of IT cellulose microfibril foams, various concentrations of cellulose microfibril suspension (3.0wt% ~ 8.0wt%) were used to prepare the IT foams. As shown in Fig 5-11 (a) ~ (f), all of the IT foams show the highly aligned channel structures parallel to the freezing direction. No defects and pores are observed on the cellulose microfibril walls. As the concentration of suspension increases up to 8.0wt%, the thickness of the individual walls increases.

It is well known that ice crystals grow anisotropically and make ice dendrites on one side of the ice crystals [17, 29]. Therefore, small dendrite structures are observed frequently on one side of the IT wall structures. In this case, the other side of the wall is relatively smooth (Fig 5-12 (c) ~ (f)). On the other hand, bridge structures are found within IT cellulose microfibril foams, instead of the typical dendrite structures. It was reported that a ceramic bridge was seldom observed only within IT foams prepared from very high concentrated suspensions [29]. However, highly ordered bridge structures have not been reported yet. As shown in Fig 5-12 (a), most of fibril bridges connect two

adjacent walls vertically. It is also found that some bridges stand vertically but cannot reach the next wall. It seems that each bridge is composed of one or more cellulose microfibril (Fig 5-12 (b)). To compare the dendrite structures and bridge structures, IT cellulose nanowhisker foams were prepared from the same concentration (3.0wt%). The average diameter of cellulose nanowhiskers is ~ 10nm and their lengths range from 180 nm to 220 nm. Fig 5-12 (d) shows the dendrite structures of cellulose nanowhisker foams. The blue arrow indicates the dendrite structure. Fig 5-12 (c) is the smooth side of the cellulose nanowhisker wall, which doesn't have a dendrite. Cellulose microfibrils and cellulose nanowhiskers are very similar, except for their dimensions. This suggests that the difference of architecture between these two structures is attributed to the particle size. IT PVA foams were also prepared from the same concentration (3.0wt%). The smooth sides and dendrite sides of their walls are shown in Fig 5-12 (e) and (f).

The formation mechanism of cellulose microfibril bridges is not yet clear. A possible mechanism is based on the splitting and subsequent healing of the ice crystal tip [29]. In the case that the ice front pushes and transports the particles, a liquid film of sufficient thickness is needed between the ice front and the particles. If the ice front velocity is too high or the movement speed of the particles is too slow, the liquid film disappears and the particles are embedded inside the ice crystals (tip splitting) instead of being entrapped between ice crystals [33]. After that, subsequent tip healing occurs and forms the bridge structure (Fig 5-13). Cellulose microfibrils are larger and heavier than cellulose nanowhiskers. Therefore, the movement speed of microfibrils during the freezing process is slower than that of nanowhiskers, creating more possibilities to make bridge structures. It is also not yet clear why bridge structures are vertical to the wall structure. It is expected that it is more difficult to move or rotate cellulose microfibrils if they are arranged vertically to the ice crystals.

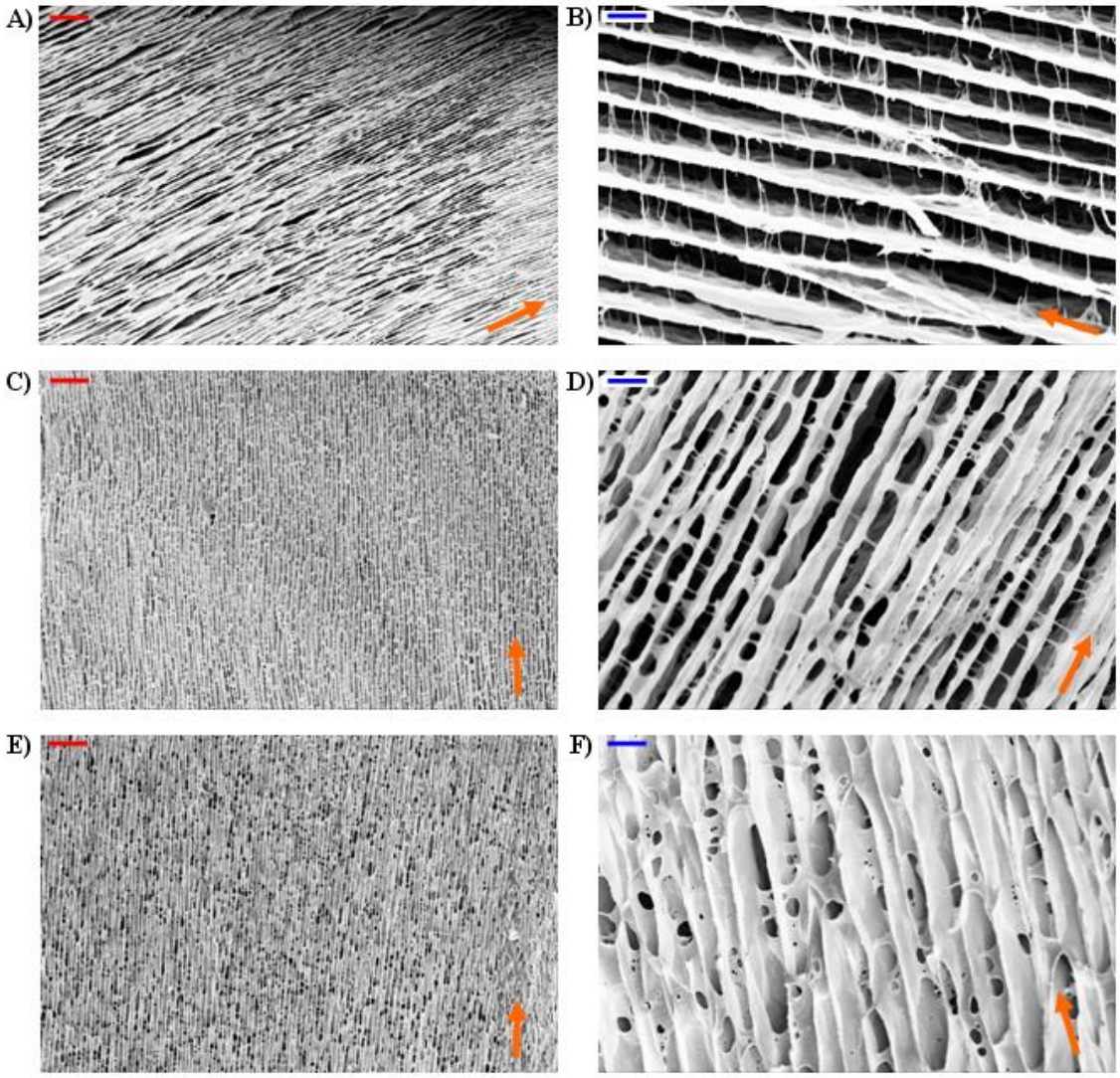

Figure 5-11. The SEM images of IT cellulose microfibril porous foams made with the various cellulose microfibrils suspension. Red scale bars are of length 20 μm and blue scale bars are of length 3 μm. Orange color arrows indicate the freezing direction. The suspension concentrations are (a) 3.0wt% (b) 3.0wt% (c) 4.0wt% (d) 4.0wt% (e) 8.0wt% (f) 8.0wt%, respectively.

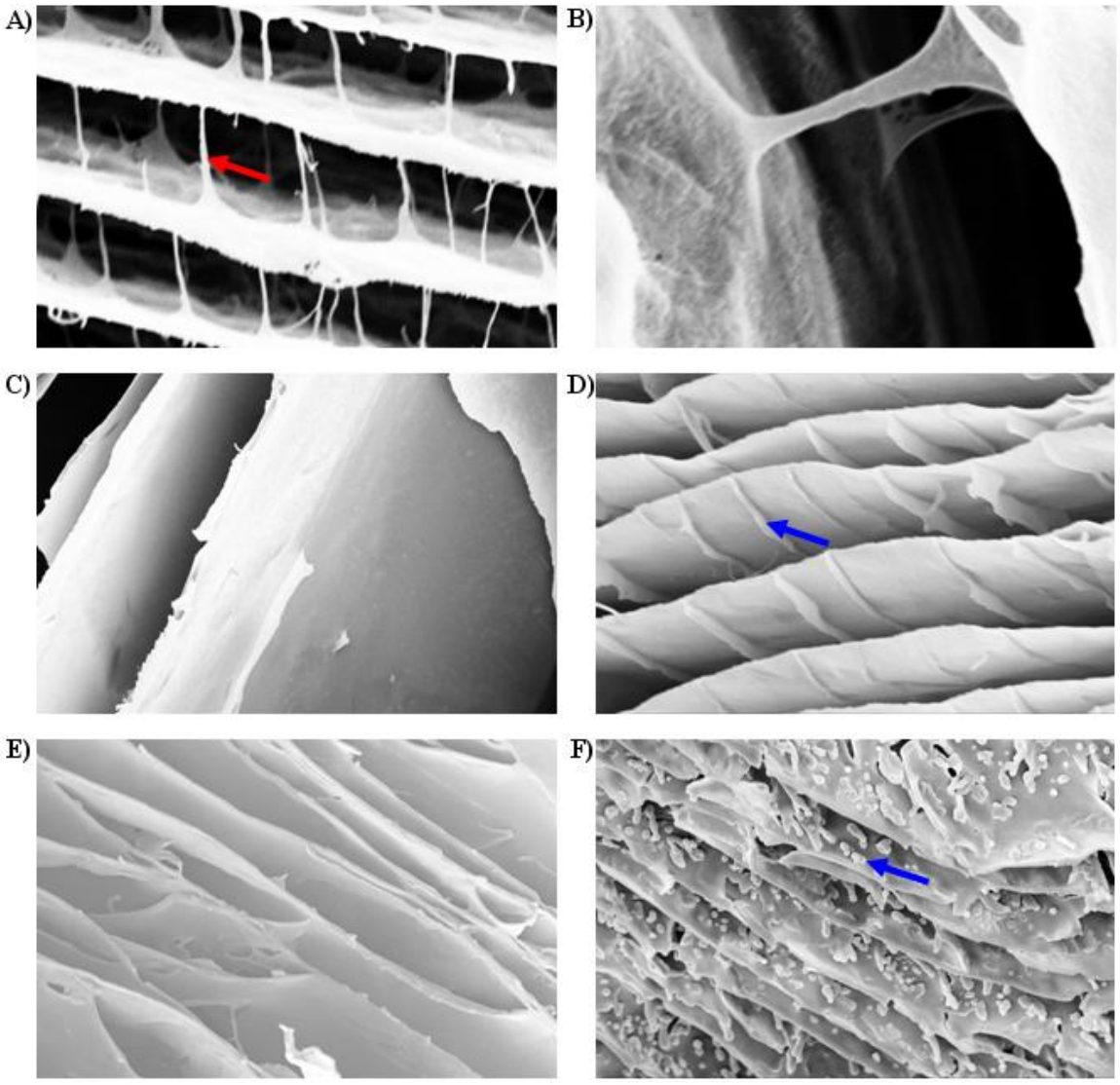

Figure 5-12 (a) Bridge structures of IT cellulose microfibril foams (3.0wt%) (b) High resolution SEM image of the bridge structure (3.0 wt%) (c) Smooth surfaces of IT cellulose nanowhisker foams (3.0wt%) (d) Dendrites structures of IT cellulose nanowhisker foams (3.0wt%) (e) Smooth surfaces of IT PVA foams (3.0wt%) (f) Dendrites structures of IT PVA foams (3.0wt%). Red arrow indicates a bridge structure and blue arrows indicate dendrite structures.

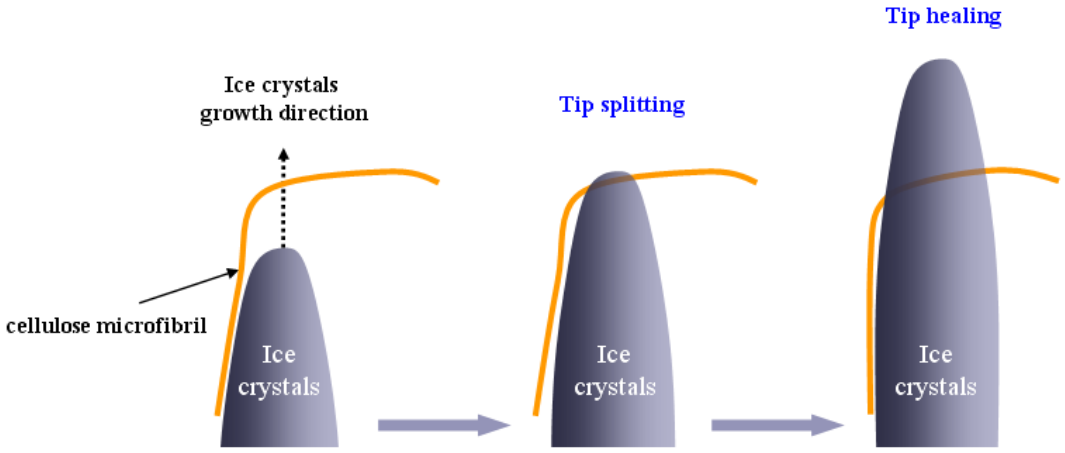

Figure 5-13. A schematic of the formation mechanism of cellulose microfibril bridges.

5.3.3 Control of the structure of IT cellulose microfibril foams

The formation mechanism of IT cellulose microfibril foams is very complicated, therefore it is difficult to analyze the structures theoretically. Instead, a model equation about cellular array growth of the metal alloy at a solid-liquid interface during the unidirectional freezing was used to correlate the simplified IT structure and experimental conditions [34]. The wavelength of the channel structure λ can be expressed as a function of ΔT by the following equation [35],

$$\lambda = \alpha \left(\frac{m_L D_c \Delta C}{v_{front} \Delta T} \right)^{0.5} \tag{5.2}$$

where α, m_L, D_c, ΔC, v_{front} and ΔT are constant, the slope of the liquid line, diffusion coefficient of solute, the concentration difference between the solid-liquid interface and the center of the two rods, the cell front velocity and the temperature difference between

the liquid phase and solid phase, respectively. Because m_L, D_c and ΔC can be assumed as a constant, λ is given by

$$\lambda = k\left(v_{front}\Delta T\right)^{-0.5} \tag{5.3}$$

Although the model equation is simplified, it is still difficult to apply it to IT porous foam structures. It is not easy to measure the temperature of the ice front and the freezing velocity exactly. Therefore, the model equation was simply used to find the tendency between λ and the temperature gradient. IT cellulose microfibril foams were prepared under different temperature gradient as described in Fig 5-2 (c) and (d). The concentration of cellulose microfibril suspension was fixed at 3.0wt%. The experimental results are summarized in Fig 5-14. Blue triangle data points are IT foams prepared using ethanol (m.p.= -114°C) as the freezing source (Fig 5-2 (c)). Black triangles indicate the experimental results of IT foams using liquid nitrogen (b.p.= -196°C) directly (Fig 5-2 (a)). Prepared IT foams were cut off parallel to the orientation of the freezing direction and the center areas were examined as shown in Fig 5-4. The morphology of IT foam structures is sensitive to the growth length of the ice crystals. Therefore, SEM examination areas should be selected carefully.

As shown in Fig 5-14, λ of IT structure prepared using 60°C cellulose microfibril suspension and liquid nitrogen is 2.8 μm. For IT foams prepared from 0°C suspension under liquid nitrogen freezing, λ is 8.7 μm. In cases where ethanol was used, λ's of IT samples prepared from 0°C and 20°C suspension were 10.0 μm and 11.2 μm, respectively. As the temperature gradient between the ice front and cellulose microfibril suspension increases, the growth speed along the a-axis increases, while the growth speed along the c-axis is still very slow (Fig 5-8). The growth speed ratio is expressed as,

$$\left(\frac{G_{a-axis}}{G_{c-axis}}\right)_{\Delta T} > \left(\frac{G_{a-axis}}{G_{c-axis}}\right)_{\Delta T'} \quad ,(\Delta T > \Delta T') \tag{5.4}$$

where G is the growth speed of ice crystals. In conclusion, as the temperature gradient increases, the width (c-axis direction) of ice crystals decreases and the wavelength of the channel structure decreases. In this case, the total number of wall structures also increases.

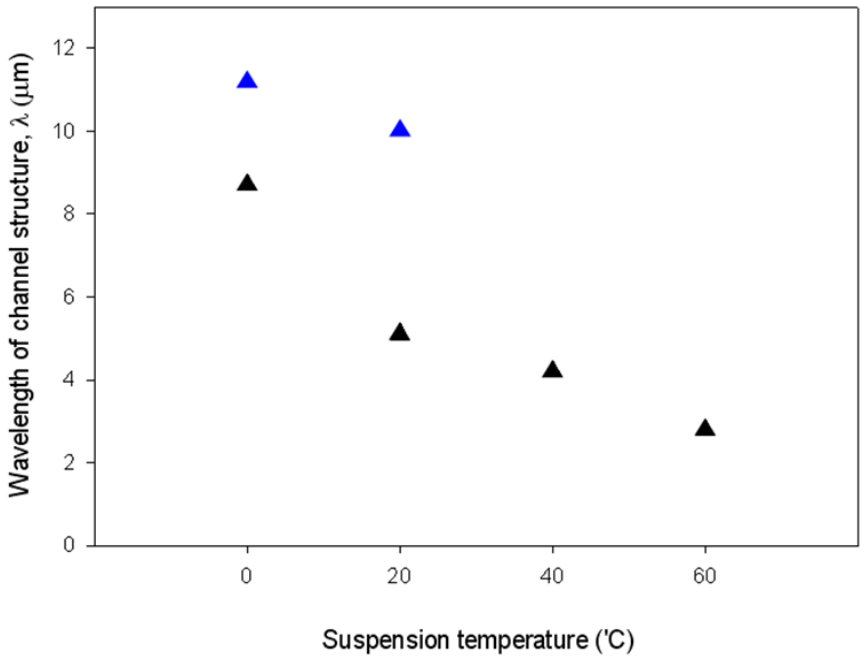

Figure 5-14. Wavelength of IT channel structures under various temperature gradients.

5.3.4 Mechanical properties of IT cellulose microfibril foams

The compressive stress of IT cellulose microfibril foams has been measured using Instron 5566 with the compression head speed set at 1mm/min. Samples were prepared as

described in Fig 5-2. The diameter of the prepared samples was 10 mm and the height was also 10 mm. IT foam samples were also prepared using cellulose nanowhiskers and montmorillonite Na+ (MMT Na+) to compare their mechanical properties with IT cellulose microfibril foams. IT porous foams were prepared from various concentrations of suspension (2.0wt% up to 8.0wt%).

The porosities of IT foams were calculated from the mass and the volume of the porous foams [36]. The porosity of the foam φ_F is given by

$$\varphi_F = 1 - \frac{\rho_F}{\rho_P} \tag{5.5}$$

where ρ_F is the density of a porous foam and ρ_P is the density of the foam materials. The density of cellulose nanowhiskers is 1.5 g / cm^3 [37] and the density of MMT Na+ is 2.8 g / cm^3 [38]. The density of cellulose microfibrils is assumed to be the same value with cellulose nanowhiskers. The results are summarized in Table 5-1.

Table 5-1. Porosity of IT porous foams.

Suspension concentration (wt%)	Porosity (%)		
	Cellulose microfibril	Cellulose nanowhisker	MMT Na+
2	98.7	98.7	99.3
3	98.0	98.0	98.9
4	97.3	97.3	98.6
6	96.0	96.0	97.9
8	94.7	94.7	97.1

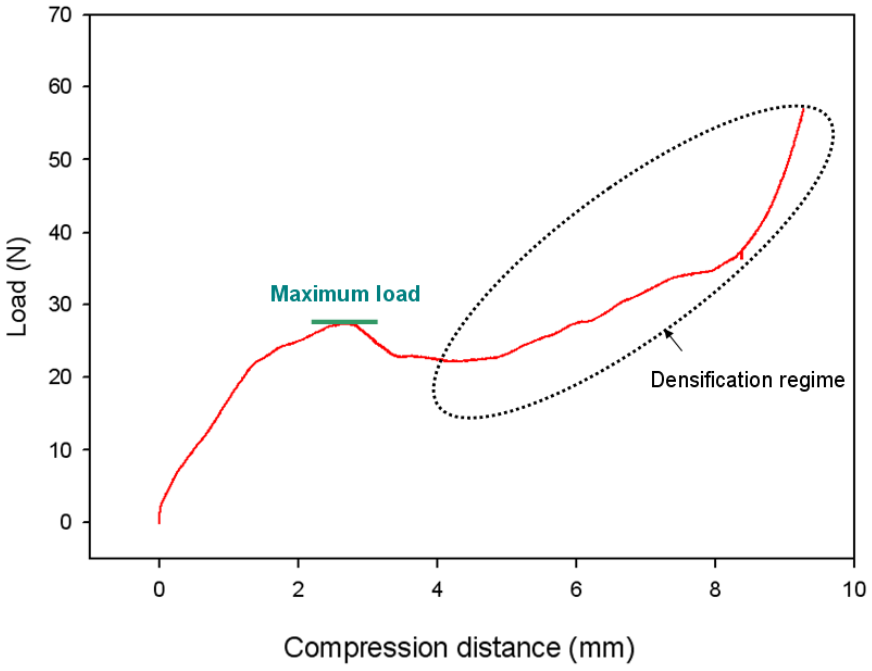

Figure 5-15. A representative compression distance-load plot of IT cellulose microfibrils porous foams.

Fig 5-15 gives the representative compression distance-load plot of IT cellulose microfibril foams prepared from 8.0wt% cellulose microfibril suspension. As shown in Fig 5-15, the plot increases linearly at low strains. This indicates that the elasticity of the foams is constant within that region. At a local maximum (compression distance: 2.6mm), cell walls of IT cellulose microfibril foams start to collapse. If the collapse of cell walls proceeds further, opposing cell walls will be contacted, resulting in the increase of wall thickness. The area in which this occurs is called the densification regime [39]. Within the densification regime, the load on the sample increases dramatically as the compression distance increases, due to the increasing thickness of the cell walls. In this

case, the local maximum (compression distance = 2.6mm) is the maximum load of the IT cellulose microfibril foams.

The compressive stress S_C of IT foams is calculated by

$$S_C = \frac{F_C}{A} \tag{5.6}$$

where F_C is the maximum load of the compression distance-load plot and A is the area of the samples. The compressive stress of IT cellulose microfibril foams is shown in Fig 5-16. The compressive stresses of IT cellulose microfibril porous foams increase linearly with increasing suspension concentration up to 8.0wt%. As shown in Fig 5-5 (c), the cell wall structures are not fully developed and lots of pores are observed at the wall structures. Therefore, the compressive stress of 2.0wt% cellulose microfibril foams (porosity: 98.7%) is as low as 30.7KPa. When the concentration of cellulose microfibril suspension changes from 3.0wt% up to 8.0wt%, the porosity of IT foams changes from 98.0 % to 94.7%, and the compressive stress increases from 117.5KPa to 360.2KPa.

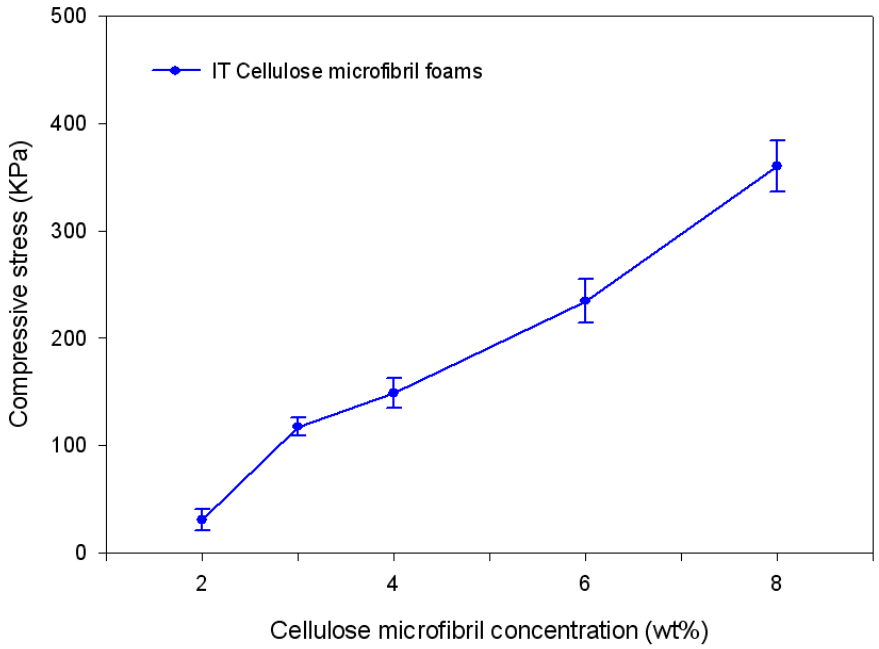

Figure 5-16. Compressive stresses of IT cellulose microfibril porous foams at various concentrations.

Meanwhile, the thickness of cellulose microfibril bridges increases as shown in Fig 5-11 (a) ~ (f). This suggests that the channel structures of IT porous foams are changing from open-cell structures to closed-cell structures, even though a 8.0wt% cellulose microfibrils IT foam is not a perfectly closed-cell structure. Closed-cell foams usually show a higher compressive stress than open-cell foams [40]. In this case, it is expected that the increase of the compressive stress of 8.0wt% cellulose microfibrils IT foam attributes to the increasing thickness of cellulose microfibril bridges.

The compressive stresses of IT foams prepared from cellulose microfibrils and MMT Na+ are shown together in Fig 5-17. IT MMT Na+ foams prepared from 2.0wt% and 3.0wt% MMT suspensions are too soft to handle them and measure their properties. Therefore, only the results prepared from 4.0wt% ~ 8.0wt% suspensions are shown. The compressive stress of IT foams prepared from 8.0wt% MMT and cellulose microfibril

suspensions are 35.2KPa and 360.2KPa, respectively. The measured compressive stress of IT MMT Na+ foams with 97.1% porosity (prepared from 8.0wt% suspension) and IT cellulose microfibril foams with 97.3% porosity (prepared from 4.0wt% suspension) are 35.2KPa and 148.6KPa, respectively. The modulus of cellulose microfibril particles and MMT Na+ particles are 93GPa [41] and 178GPa [42], respectively. However, cellulose microfibrils have a lot of hydroxyl groups on their surfaces. Therefore, there are strong particle-particle interactions between cellulose microfibrils due to the hydrogen bonds. It was reported that the modulus of pure cellulose microfibril thin films with 20% porosity is as high as 13.7GPa due to the strong hydrogen bonding [43]. It is also expected that one factor contributing to the high compressive stress of IT cellulose microfibrils is the strong particle-particle interaction force.

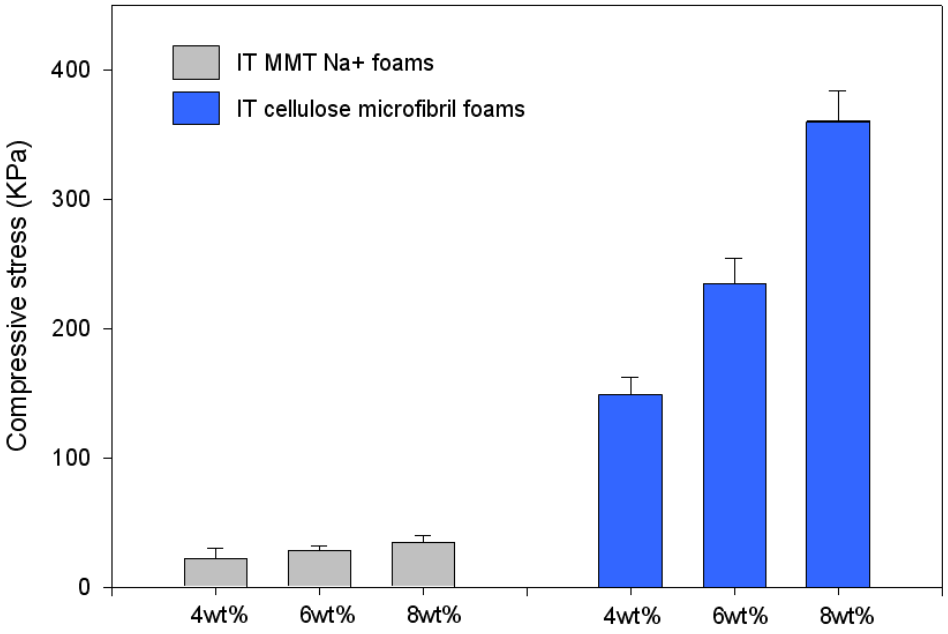

Figure 5-17. Compressive stresses of IT MMT Na+ and cellulose microfibril porous foams at various suspension concentrations.

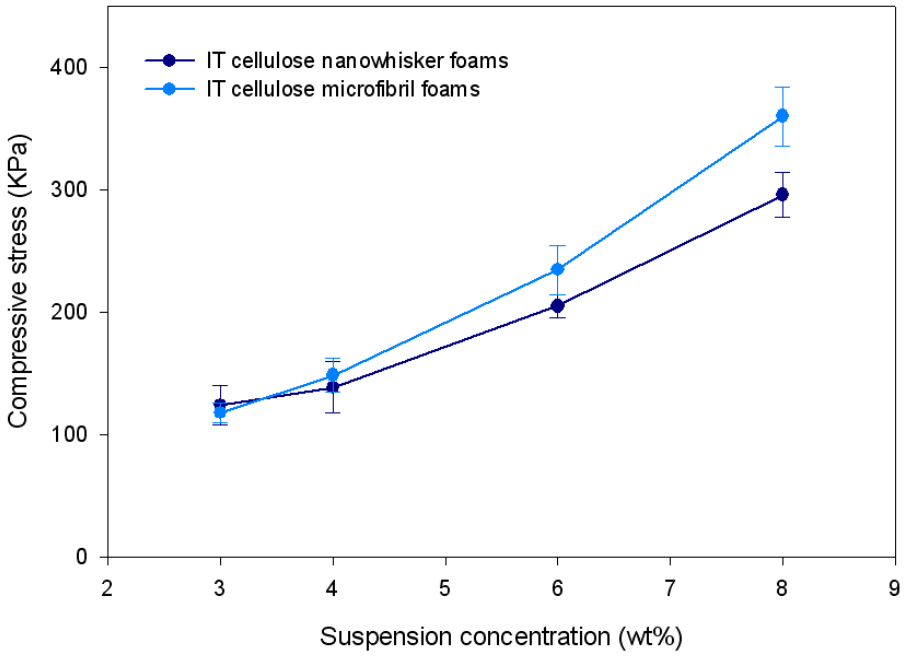

Figure 5-18. Compressive stresses of IT cellulose nanowhisker and cellulose microfibril porous foams at various suspension concentrations.

The compressive stresses of IT foams prepared from cellulose microfibrils and cellulose nanowhiskers are plotted together in Fig 5-18. Cellulose microfibrils and cellulose nanowhiskers have very similar physical and chemical properties. Both of the particles have hydroxyl groups on their surfaces. A distinctive feature of both of the particles is the length of the particles. The length of cellulose nanowhiskers is between 180nm and 220nm [31]. On the other hand, the length of cellulose microfibrils ranges from 1 μm to 30 μm [20-21]. As shown in Fig 5-12, IT cellulose microfibril foams and IT cellulose nanowhisker foams show different morphologies due to the different lengths of the particles. IT cellulose microfibril foams show bridge structures, while IT cellulose nanowhisker foams have dendrite structures. Due to the large deviation of the measured data, it is difficult to conclude that IT cellulose microfibril foams show a higher

mechanical performance than IT cellulose nanowhisker foams. However, the compressive stress of IT cellulose microfibril foams prepared from 8.0wt% suspension is clearly larger than that of 8.0wt% cellulose nanowhisker foams. Therefore, it seems that the cellulose microfibril bridges contribute to the increase of the compressive stress at some point.

5.4. Conclusions

The growth mechanism of IT cellulose microfibril porous foams was investigated successfully. Cellulose microfibrils foam prepared from 1.0wt% suspension showed a cross-linked network structure. Increasing the concentration of cellulose microfibrils suspension up to 2.75wt% led to a gradual transition from a crosslinked network structure to a lamellar channel structure. As the concentration of suspension was increased up to 8.0wt%, highly aligned channel structures parallel to the freezing direction were obtained. It was also observed that the thickness of individual walls and bridge structure increased with increasing suspension concentration. It was found that cellulose microfibrils were partially aligned along the freezing direction through the observation of aligned ellipse-shaped pores. Due to the unique characteristic of cellulose microfibrils, cellulose bridge structures were fabricated during the IT process, instead of dendrite structures. It was confirmed that the wavelength of IT channel structures could be controlled by changing the temperature gradient between the ice front and cellulose microfibril suspension. It was found that the compressive stresses of IT cellulose microfibril foams increased linearly from 30.7KPa to 360.2KPa with increasing suspension concentrations (2.0wt% - 8.0wt%).

References

1. Sun, B.H., et al., *The synthesis and microstructure of morph-genetic TiC/C ceramics.* Carbon, 2004. **42**(1): p. 177-182.

2. Saggiowoyansky, J., C.E. Scott, and W.P. Minnear, *PROCESSING OF POROUS CERAMICS.* American Ceramic Society Bulletin, 1992. **71**(11): p. 1674-1682.

3. White, R.A., E.W. White, and J.N. Weber, *REPLAMINEFORM - NEW PROCESS FOR PREPARING POROUS CERAMIC, METAL, AND POLYMER PROSTHETIC MATERIALS.* Science, 1972. **176**(4037): p. 922-&.

4. Liu, Z.T., et al., *The synthesis of hierarchical porous iron oxide with wood templates.* Microporous and Mesoporous Materials, 2005. **85**(1-2): p. 82-88.

5. Vogt, U., et al., *Porous ceramics derived from wood*, in *Euro Ceramics Vii, Pt 1-3*. 2002. p. 1941-1944.

6. Luyten, J., et al., *New processing techniques of ceramic foams.* Advanced Engineering Materials, 2003. **5**(10): p. 715-718.

7. Kuang, D.B., et al., *Fabrication of ordered macroporous rutile titania at low temperature.* New Journal of Chemistry, 2002. **26**(7): p. 819-821.

8. Lyckfeldt, O. and J.M.F. Ferreira, *Processing of porous ceramics by 'starch consolidation'.* Journal of the European Ceramic Society, 1998. **18**(2): p. 131-140.

9. Androff, N.W., L.F. Francis, and B.V. Velamakanni, *Macroporous ceramics from ceramic-polymer dispersion methods.* Aiche Journal, 1997. **43**(11): p. 2878-2888.

10. Bao, X., M.R. Nangrejo, and M.J. Edirisinghe, *Synthesis of silicon carbide foams from polymeric precursors and their blends.* Journal of Materials Science, 1999. **34**(11): p. 2495-2505.

11. Colombo, P. and M. Modesti, *Silicon oxycarbide ceramic foams from a preceramic polymer.* Journal of the American Ceramic Society, 1999. **82**(3): p. 573-578.

12. Kim, Y.W., et al., *Fabrication of porous preceramic polymers using carbon dioxide.* Journal of Materials Science Letters, 2002. **21**(21): p. 1667-1669.

13. Grader, G.S., G.E. Shter, and Y. de Hazan, *Novel ceramic foams from crystals of AlCl3((Pr2O)-O-i) complex.* Journal of Materials Research, 1999. **14**(4): p. 1485-1494.

14. Araki, K. and J.W. Halloran, *Porous ceramic bodies with interconnected pore channels by a novel freeze casting technique.* Journal of the American Ceramic Society, 2005. **88**(5): p. 1108-1114.

15. Gutierrez, M.C., et al., *Biocompatible MWCNT scaffolds for immobilization and proliferation of E. coli.* Journal of Materials Chemistry, 2007. **17**(29): p. 2992-2995.

16. Zhang, H. and A.I. Cooper, *Aligned porous structures by directional freezing.* Advanced Materials, 2007. **19**(11): p. 1529-1533.

17. Deville, S., et al., *Freezing as a path to build complex composites.* Science, 2006. **311**(5760): p. 515-518.

18. Guhados, G., W.K. Wan, and J.L. Hutter, *Measurement of the elastic modulus of single bacterial cellulose fibers using atomic force microscopy.* Langmuir, 2005. **21**(14): p. 6642-6646.

19. Hsieh, Y.C., et al., *An estimation of the Young's modulus of bacterial cellulose filaments.* Cellulose, 2008. **15**(4): p. 507-513.

20. Nogi, M., et al., *Optically Transparent Nanofiber Paper.* Advanced Materials, 2009. **21**(16): p. 1595-+.

21. Henriksson, M., et al., *An environmentally friendly method for enzyme-assisted preparation of microfibrillated cellulose (MFC) nanofibers.* European Polymer Journal, 2007. **43**(8): p. 3434-3441.

22. Wu, Q.J., et al., *A high strength nanocomposite based on microcrystalline cellulose and polyurethane.* Biomacromolecules, 2007. **8**(12): p. 3687-3692.

23. Kim, Y., et al., *Transparent nanocomposites prepared by incorporating microbial nanofibrils into poly(L-lactic acid).* Current Applied Physics, 2009. **9**: p. S69-S71.

24. Angles, M.N. and A. Dufresne, *Plasticized starch/tunicin whiskers nanocomposites. 1. Structural analysis.* Macromolecules, 2000. **33**(22): p. 8344-8353.

25. Grunert, M. and W.T. Winter, *Nanocomposites of cellulose acetate butyrate reinforced with cellulose nanocrystals.* Journal of Polymers and the Environment, 2002. **10**(1-2): p. 27-30.

26. Chazeau, L., et al., *Viscoelastic properties of plasticized PVC reinforced with cellulose whiskers.* Journal of Applied Polymer Science, 1999. **71**(11): p. 1797-1808.

27. Lu, J., T. Wang, and L.T. Drzal, *Preparation and properties of microfibrillated cellulose polyvinyl alcohol composite materials.* Composites Part a-Applied Science and Manufacturing, 2008. **39**(5): p. 738-746.

28. Svagan, A.J., M. Samir, and L.A. Berglund, *Biomimetic foams of high mechanical performance based on nanostructured cell walls reinforced by native cellulose nanofibrils.* Advanced Materials, 2008. **20**(7): p. 1263-+.

29. Deville, S., E. Saiz, and A.P. Tomsia, *Ice-templated porous alumina structures.* Acta Materialia, 2007. **55**(6): p. 1965-1974.

30. Hostler, S.R., et al., *Thermal conductivity of a clay-based aerogel.* International Journal of Heat and Mass Transfer, 2009. **52**(3-4): p. 665-669.

31. Dong, X.M., J.F. Revol, and D.G. Gray, *Effect of microcrystallite preparation conditions on the formation of colloid crystals of cellulose.* Cellulose, 1998. **5**(1): p. 19-32.

32. Sakurada, I., Y. Nukushina, and T. Ito, *EXPERIMENTAL DETERMINATION OF ELASTIC MODULUS OF CRYSTALLINE REGIONS IN ORIENTED POLYMERS.* Journal of Polymer Science, 1962. **57**(165): p. 651-&.

33. Korber, C., et al., *INTERACTION OF PARTICLES AND A MOVING ICE-LIQUID INTERFACE.* Journal of Crystal Growth, 1985. **72**(3): p. 649-662.

34. Nishihara, H., S. Iwamura, and T. Kyotani, *Synthesis of silica-based porous monoliths with straight nanochannels using an ice-rod nanoarray as a template.* Journal of Materials Chemistry, 2008. **18**(31): p. 3662-3670.

35. Flemings, M.C., *Solidification processing*. 1974, New York: McGraw-Hill.

36. Thomson, R.C., et al., *FABRICATION OF BIODEGRADABLE POLYMER SCAFFOLDS TO ENGINEER TRABECULAR BONE.* Journal of Biomaterials Science-Polymer Edition, 1995. **7**(1): p. 23-38.

37. Eichhorn, S.J., et al., *Review: current international research into cellulose nanofibres and nanocomposites.* Journal of Materials Science, 2010. **45**(1): p. 1-33.

38. Southern Clay Products, I., *Cloisite Na+ Typical physical properties bulletin.* Product Bulletin.

39. Gibson LJ, A.M., *Cellular solids, Structure and Properties, 2nd Ed.* 1997, Cambridge: Cambridge University Press.

40. Studart, A.R., et al., *Processing routes to macroporous ceramics: A review.* Journal of the American Ceramic Society, 2006. **89**(6): p. 1771-1789.

41. Cheng, Q.Z. and S.Q. Wang, *A method for testing the elastic modulus of single cellulose fibrils via atomic force microscopy.* Composites Part a-Applied Science and Manufacturing, 2008. **39**(12): p. 1838-1843.

42. Fornes, T.D. and D.R. Paul, *Modeling properties of nylon 6/clay nanocomposites using composite theories.* Polymer, 2003. **44**(17): p. 4993-5013.

43. Henriksson, M., et al., *Cellulose nanopaper structures of high toughness.* Biomacromolecules, 2008. **9**(6): p. 1579-1585.

CHAPTER 6

THE MORPHOLOGY AND WETTING PROPERTIES OF PATTERNED SURFACES OF ICE-TEMPLATED CELLULOSE MICROFIBRIL FOAMS

Abstract

The morphology and growth mechanism of Ice-Templated (IT) foam surfaces are investigated successfully. When the height of the IT cellulose microfibril foam surface is 50 μm, the surface shows honey-comb like structures. When the height of the IT foam surface is between 100 μm and 200 μm, a transition from a honey-comb like structure to a multilayer structure occurs. In these cases, ellipse-shaped channels are observed. If the height of the IT surface is larger than 300 μm, then a fully developed multichannel foam surface is obtained. By controlling the temperature gradient between cellulose microfibril suspensions and freezing mediums, various surface structures including honey-comb like structures, ellipse-shape channel structures, and fully developed multichannel structures are obtained successfully. The average contact angle of honeycomb-like IT cellulose microfibril foam surfaces is ~143°. Multichannel IT cellulose microfibril foam surfaces show anisotropic wetting properties at a low suspension concentration.

Keyword: Cellulose microfibril, Ice-templated method, Wetting properties

6.1. Introduction

Wetting properties on patterned solid surfaces are important to both academia and many industrial processes such as cleaning, drying, painting, coating, and adhesion. Specially, superhydrophobic surfaces have attracted great attention due to its wide range of potential applications such as antibiofouling boats [1-2], antisticking antennas [3], antisticking windows [4], self-cleaning windshields [5], and stain resistant textiles [6]. Superhydrophobic surfaces form very high contact angles with water (greater than 150°) and low contact angle hysteresis. The design of superhydrophobic surfaces have been biologically inspired by lotus leafs [7], legs of the water strider [8], eyes of mosquito [9], beetles [10], and so on. During the last 10 years, a lot of techniques for the fabrication of surperhydrophobic surfaces have been reported, including templation methods [11-12], lithographic approaches [13-14], plasma etching methods [15-16], chemical deposition techniques [17-18], layer by layer (LbL) methods [19-20], electrospinning techniques [21-23], and so on. The various geometries of superhydrophobic surfaces include asperities [11, 14], aligned nanotubes [18], multiple fractal structures [24], isotropic fibers [21-23], and honey comb like structures [19].

Recently, interests in the anisotropic wetting properties have been increased. Understanding anisotropic wetting properties is important in that it is possible to control the wettability of the target surface by controlling the architecture of the surface. Potential applications include self-cleaning, biosensing, lab-on-a chip systems, intelligent membranes, microfluid devices, and microreactor systems [25]. There have been many efforts to investigate the anisotropic wetting phenomenon through theoretical [26-28] and experimental studies via photolithography [29], interferometric lithography [25, 30], and micro-wrinkling techniques [31]. In spite of several theoretical studies, the quantitative explanation of anisotropic wetting phenomenon is not yet clear.

Ice-templated (IT) methods have been used to prepare seashell mimetic nanocomposites [32] and multichannel porous foams [33-36]. In IT methods, the

unidirectional freezing of the aqueous suspension, followed by the unidirectional growth of ice crystals and subsequent sublimation of ice templates, results in highly ordered porous foams that have unidirectional channels. Due to the unique structure of IT nanocomposites and IT porous foams, there have been many reports about its possible applications such as artificial bones [32, 37], drug delivery channels [38], cell culture templates [36], and anodes for direct methanol fuel cells [39].

In this report, new surface fabrication techniques via IT methods are introduced for the first time. IT methods are very versatile and can be applied to a wide variety of material systems such as inorganic particles [34], polymers [35], and inorganic-polymer hybrids [32]. The morphology and growth mechanism of IT foam surfaces are investigated using cellulose microfibrils. The wetting properties of IT foam surfaces prepared from cellulose microfibrils and cellulose nanowhiskers are also measured.

6.2. Experimental

6.2.1. Materials

1H,1H,2H,2H-perfluorooctyltriethoxysilane (POTS) was supplied by Alfa Aesar. Octadecyltrichlorosilane (OTS) was purchased from Sigma-Aldrich. Cellulose microfibrils were prepared through acid hydrolysis of filter paper with 50% sulfuric acid (VWR, USA). Briefly, 602 ml concentrated sulfuric acid was added drop-wise to a chilled mixture of 120 g Whatman No. 1 filter paper and 598 ml deionized water. This slurry was then placed into a 30°C hot water bath for 130 min and stirred. The resulting material underwent centrifuging and dialysis with deionized water to remove excess acid. After dialysis, the solution pH was raised to pH 6 using Amberlite (VWR, USA) resin beads. The cellulose suspension was sonicated in an ice bath for 20 minutes, centrifuged for 5 min at 14,000 rpm, and the cloudy supernatant was collected (this is the

collected fibrils). This step was repeated until cloudy supernatant was no longer formed. The collected cloudy supernatant (the fibrils) were concentrated by placing into dialysis tubing in a PEG-water solution. The diameter of microfibrils ranged from 10nm to 30nm and their lengths were between 1 μm and 30 μm. Cellulose nanowhiskers were prepared using the method described by Dong et al. [41]. The suspensions of cellulose nanowhiskers were prepared from Whatman No. 1 filter paper by sulfuric acid hydrolysis. The concentration of sulfuric acid was fixed at 64%. The acid hydrolysis conditions were optimized at 45°C and 50mins. After hydrolysis, the suspension was deionized by mixing 1g of mixed-bed ion exchange resin and filtered. The suspension was then washed with DI water and centrifuged (40mins, 3000rpm, Beckman Coulter, GS-6). The suspension was further dispersed by an ultrasound sonicator (15mins at full power, Branson 3510). The diameter of nanowhiskers ranged from 5nm to 10nm and their average length was ~ 200 nm.

6.2.2. Sample preparation

IT cellulose microfibril foam surface samples were prepared using IT methods as shown in Fig 6-1. The cellulose microfibril suspension was dropped on a template attached to a glass substrate as shown in Fig 6-1 (b). The size of the template was $1\times1cm^2$ and the height of the template was changed from 50 μm to 300 μm. The amount of the suspension was varied between 5 μl to 30 μl, according to the height of the templates. Prepared samples were covered with surface treated glasses or silicon wafers and then placed on the aluminum tray. Prepared samples were freezed unidirectionally using liquid N_2 as shown in Fig 6-1 (a). The aluminum tray was attached to the syringe pump and immersed into the insulated liquid N_2 bath. The immersing depth of the tray was maintained as 1mm during the whole freezing process using a syringe pump. To change the temperature gradient between a sample and a freezing source, secondary

freezing mediums were inserted between the sample and liquid N_2 as shown in Fig 6-1 (d). Ethanol, methanol, n-octane, and water were used as secondary freezing mediums. Freezed samples were immediately put in a freeze-dryer (VirTis, Freezemobile 25EL) to remove ice crystal templates by sublimation. After 48 hours, freeze-dried samples were taken out from the freeze-dryer. After that, the aluminum tray, surface treated glasses/silicon wafers, and templates were all removed carefully.

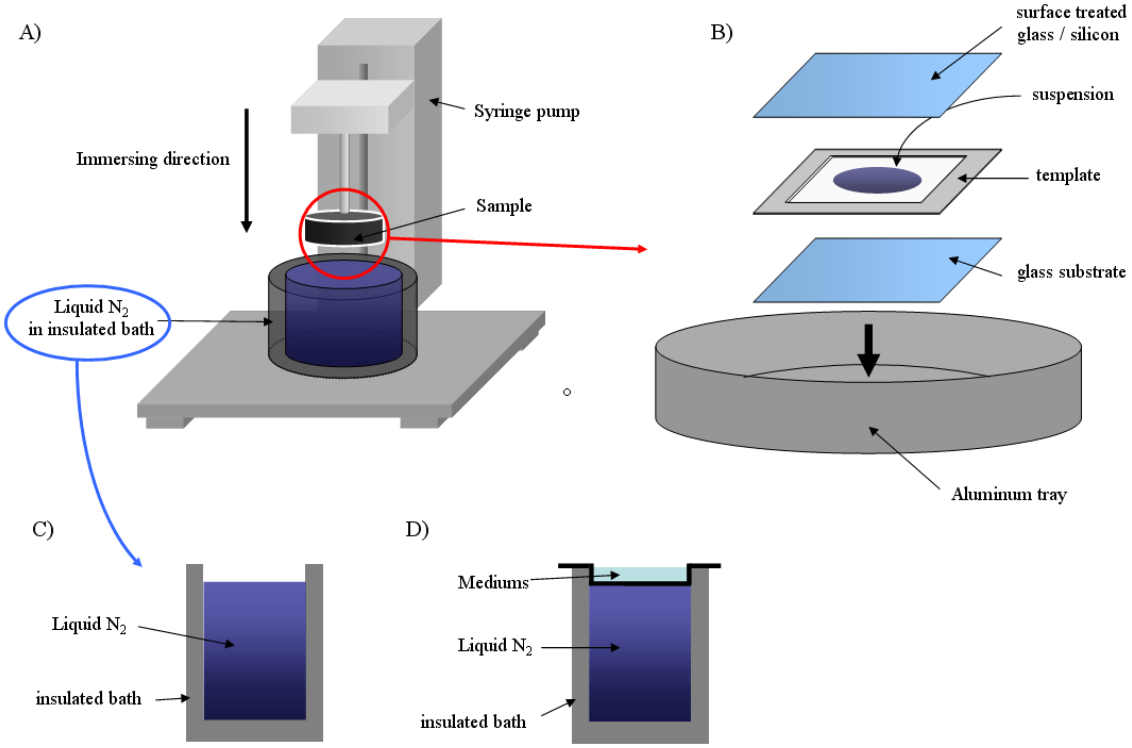

Figure 6-1. Scheme of (a) a freezing apparatus (b) a sample preparation (c) an insulated liquid N_2 bath (d) an insulated liquid N_2 bath with a secondary freezing source.

6.2.3. Characterization

Scanning electron microscopy (SEM) was carried out using a LEO 1530 at 10kV. The samples were sputter coated with Au using EMS 350 sputter (20mA, 2mins) prior to

observation. Contact angle measurements were performed on a FTA 200 Dynamic contact angle analyzer. Image analysis was conducted using ImageJ software, which is provided by NIH and ImageTool 3.0 software that is provided by UTHSCSA.

6.3. Results and discussion

6.3.1 Opening and closing the channels of IT foam structures

IT foam surfaces were prepared using hydrophobic and hydrophilic substrates. To make hydrophilic substrates, SiO_2 glasses were exposed to piranha solution (H_2SO_4 : H_2O_2 = 7:3). Piranha solution reacts with organic contaminates on the SiO_2 glasses and removes them. Additionally, piranha solution also hydroxylates many surfaces, resulting in hydrophilic surface properties [42]. The average contact angle of piranha solution-treated SiO_2 glasses is 9.41°. To prepare hydrophobic substrates, silicon wafers were treated with octadecyltrichlorosilane (OTS, $CH_3(CH_2)_{17}SiCl_3$). The average contact angle of OTS-treated silicon substrates is 100.73°. The contact angle measurement results of piranha solution-treated SiO_2 and OTS-treated silicon wafers are shown in Fig 6-2.

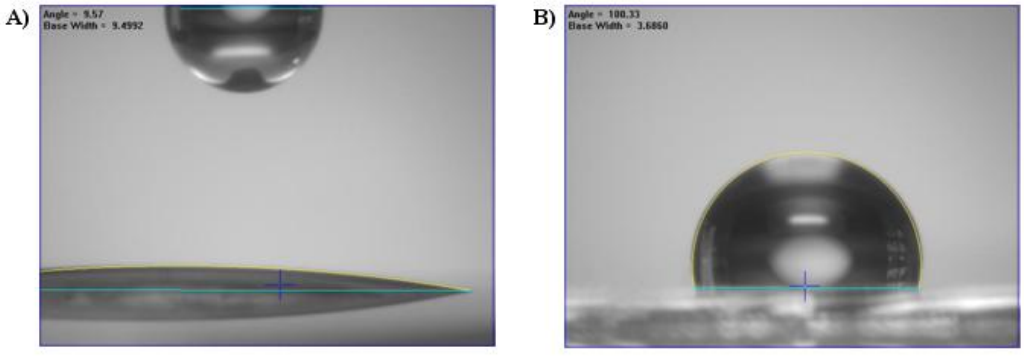

Figure 6-2 (a) A contact angle of the piranha solution treated SiO_2 glass (b) A contact angle of the OTS-treated silicon wafer.

The morphology of cellulose microfibril IT foam surface structures was investigated by SEM observation while parallel to the freezing direction (Fig 6-3). After sublimation of the ice templates, SEM observation was performed directly without any physical or chemical treatments, which may change the morphology of surface structures.

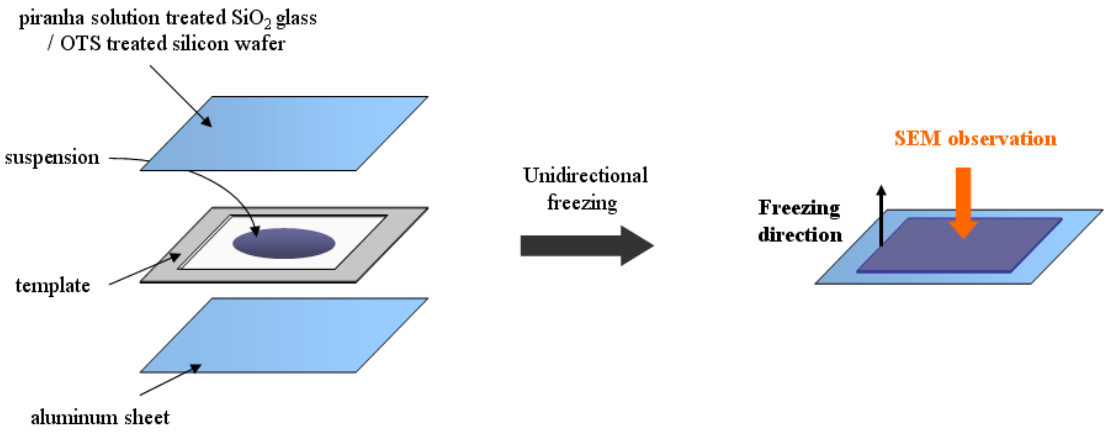

Figure 6-3. Scheme of SEM observation of IT foam surface structures.

As shown in Fig 6-4 (a), IT cellulose microfibril foam surfaces prepared using piranha solution-treated SiO_2 substrates show open channel structures. Porous channels are aligned in the same direction as the freezing direction and the end of each channel is exposed to the air. The diameters of the channels range from 3 μm to 10 μm. Fig 6-4 (b) is the high resolution image of open channel structures. Fig 6-4 (c) is the SEM image of IT cellulose microfibril foam surfaces prepared using OTS-treated silicon substrates. Contrary to IT foam surfaces prepared using a hydrophilic substrate, IT cellulose microfibril foam surfaces fabricated with a hydrophobic substrate show closed channel structures. From the image analysis using ImageJ and ImageTool 3.0 software, it was found that 94.6% of the channels are closed and only 5.4% are the pores. The diameters

of the pores range from 10nm to 400nm. Except a small portion of pores, IT foam surfaces are covered with smooth cellulose microfibril layers as shown in Fig 6-4 (c).

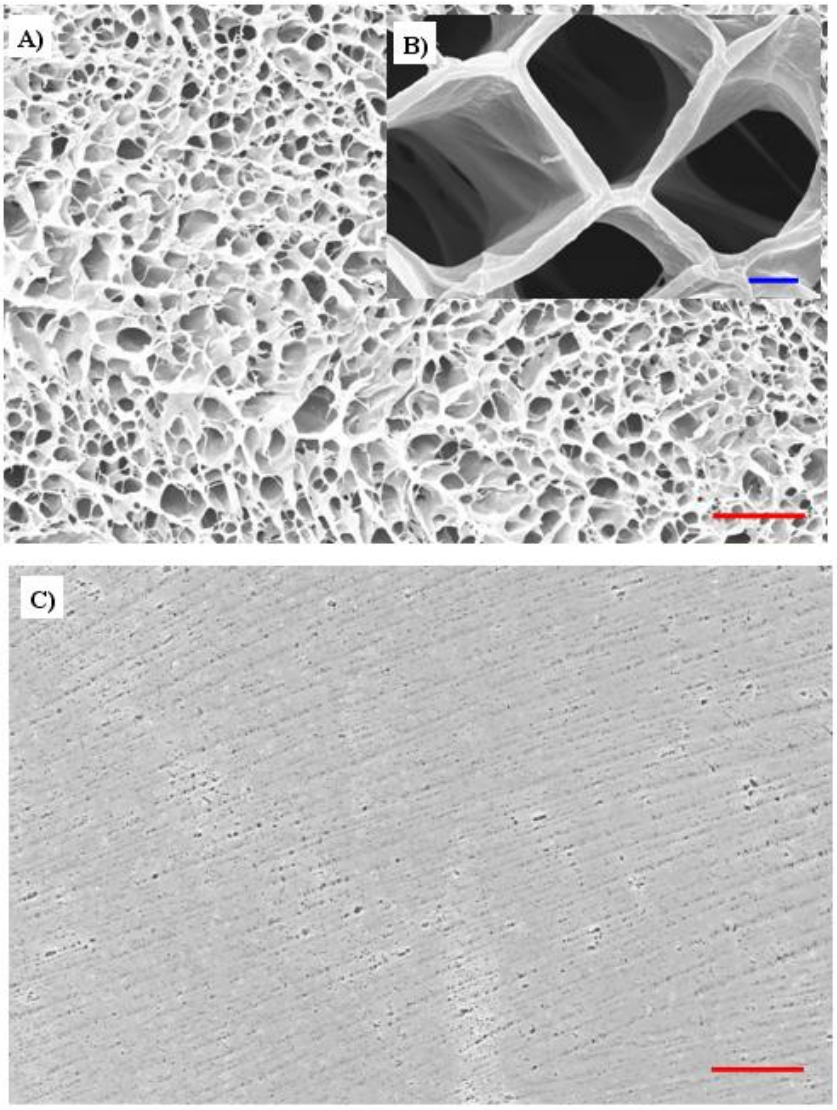

Figure 6-4 (a) SEM image of cellulose microfibrils IT foam surface structures prepared using piranha solution treated SiO_2 substrates (b) high resolution image of open channel structures (c) SEM image of cellulose microfibrils IT foam surface structures prepared using OTS-treated silicon substrates. Red and blue scale bars represent 20 μm and 2 μm, respectively.

It is expected that the difference in the IT foam surface morphology prepared using hydrophilic and hydrophobic substrates is due to the hydrophobic/hydrophilic

interaction between cellulose microfibrils and the substrates in water. The hydrophobic interaction is the strong attraction between hydrophobic molecules and surfaces in water [43]. The hydrophobic interaction force is an order of magnitude stronger than van der waals interaction force [44]. The hydrophobic interaction force is effective within the distance range of 30nm ~ 50nm [44-46]. The hydrophilic interaction is the repulsive interaction between hydrophilic molecules and surfaces in water [43]. Directly measuring of the hydrophobic/hydrophilic interaction forces between the cellulose microfibrils and the substrates in water is very difficult. Instead, a qualitative explanation and comparison of the two systems, cellulose microfibrils - hydrophilic substrate - water molecules / cellulose microfibrils - hydrophobic substrate - water molecules, is performed. First, contact angles of cellulose microfibrils and two substrates were measured and summarized in Table 6-1. Cellulose microfibrils thin film was made on a silicon wafer substrate using a spin coater. From the contact angle measurement results, it is confirmed that the hydrophobicity of the system's component is as follows: water < Piranha solution-treated SiO_2 glass < cellulose microfibril < OTS-treated silicon wafer.

Table 6-1. Contact angles and hydrophobicity of components of the two systems.

Component	Contact angle	hydrophobicity
Water	-	Increase ↓
Piranha solution treated SiO_2 glass	9.41	
Cellulose microfibril thin film	45.7	
OTS treated silicon wafer	100.73	

Fig 6-5 shows the scheme of the hydrophobic/hydrophilic interaction between cellulose microfibrils and the two substrates in water. To simplify, one cellulose

microfibril and one water molecule are presented for each system. C and W denote the cellulose microfibril and water molecule, respectively.

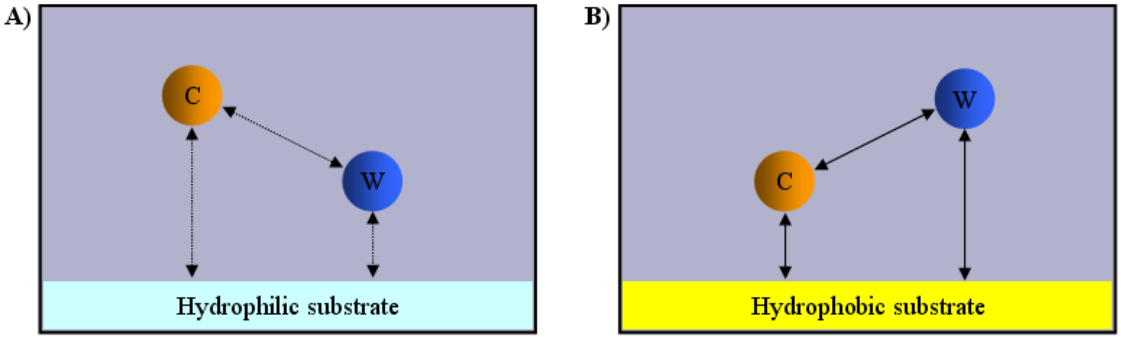

Figure 6-5. Scheme of hydrophobic/hydrophilic interactions among a cellulose microfibril, a water molecule and two substrates.

For cellulose microfibril – water – hydrophilic substrate system, it is preferred thermodynamically that a cellulose microfibril is located further from the hydrophilic substrate than a water molecule. The contact angles of Piranha solution-treated SiO_2 glass and the cellulose microfibril thin film are 9.41° and 45.7°, respectively. Therefore, Piranha solution-treated hydrophilic SiO_2 glass prefers to be in contact with water rather than the cellulose microfibril [43]. On the other hand, for cellulose microfibril – water – hydrophobic substrate system, it is preferred thermodynamically that a cellulose microfibril is located closer to the hydrophobic substrate than a water molecule. The contact angles of the OTS-treated hydrophobic silicon wafer substrate and cellulose microfibril thin film are 100.73° and 45.7°, respectively. In this case, the substrate prefers to be in contact with cellulose microfibril rather than the water molecule. If the models are extended to the real systems, the arrangement of cellulose microfibrils and water molecules are explained in the same manner.

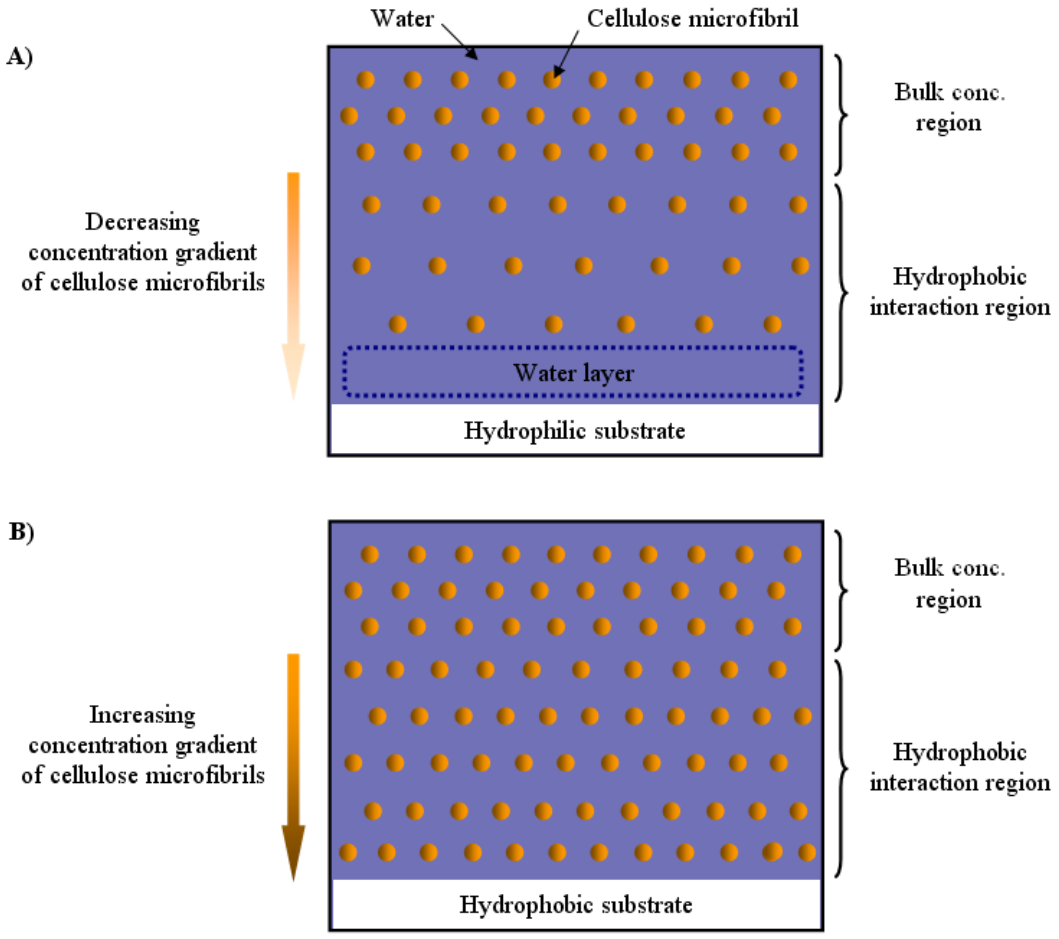

Figure 6-6 Schemes of arrangement of cellulose microfibrils and water (a) with a hydrophilic substrate (b) with a hydrophobic substrate.

As shown in Fig 6-6 (a), the concentration of cellulose microfibrils decreases as the hydrophobic/hydrophilic interaction among cellulose microfibrils, water molecules and the substrates increases. The range of hydrophobic/hydrophilic interaction is known to be between 30nm ~ 50nm [44-46]. Therefore, it is expected that the concentration of cellulose microfibrils decreases gradually in the hydrophobic/hydrophilic interaction region (30nm ~ 50nm). It also is expected that a thin water layer without cellulose

microfibrils can exist in the region which is contacted with the hydrophilic substrate. For the hydrophobic substrates, it is expected that the concentration of cellulose microfibrils increases at the hydrophobic/hydrophilic region. It is also expected that the concentration is the highest at the substrate contacting region.

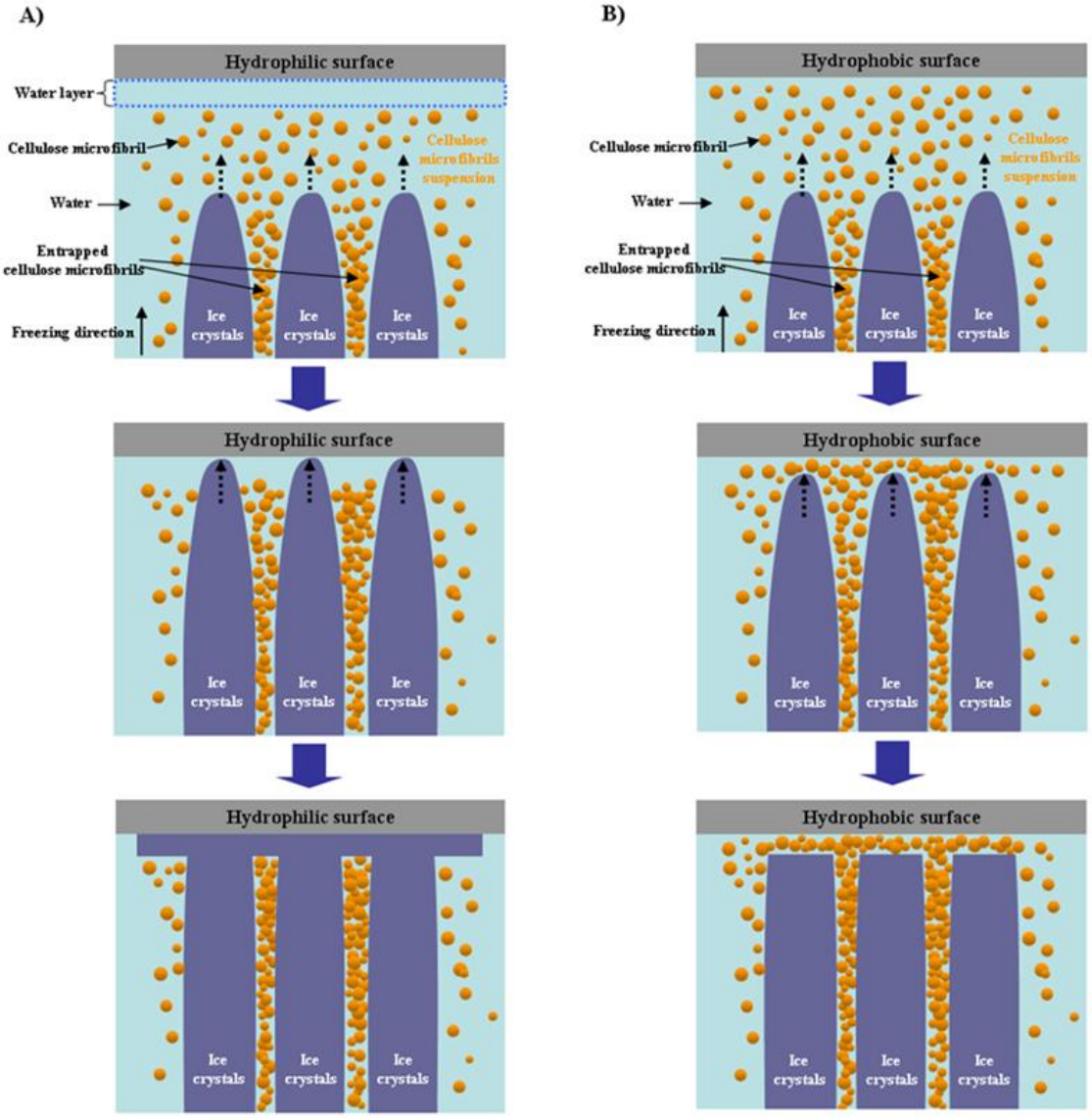

Figure 6-7. Schemes of unidirectional growth of ice crystals of the cellulose microfibrils suspension with (a) piranha solution-treated hydrophilic SiO_2 glass substrates (b) OTS-treated hydrophobic silicon substrates.

When the cellulose microfibril suspension is freezed, a concentration gradient within the hydrophobic interaction region affects the final morphology of the cellulose microfibrils IT surfaces. For the IT structures prepared using hydrophilic substrates, there is no available cellulose microfibril particle in the region close to the substrate. Therefore, ice crystals grow up to the substrates directly and cellulose microfibril channels are covered with ice crystals as shown in Fig 6-7 (a). After the sublimation of ice crystals, IT surfaces show open channel structures as shown 6-4 (a). When cellulose microfibril IT surface structures are prepared using hydrophobic substrates, there are enough cellulose microfibrils in the region close to the substrate. Therefore, cellulose microfibrils are entrapped between the ends of ice crystals and substrates. After the sublimation of ice-templates, IT surfaces show closed channel structures as shown in Fig 6-4 (c).

6.3.2 Mechanism study of developing IT foam structures

The morphology of cellulose microfibril IT foams in the structure-developing region was investigated using piranha solution-treated hydrophilic SiO_2 substrates. When hydrophilic substrates are used, it requires the same effort to "quench" the freezing procedures. The thickness of the templates (Fig 6-3) was changed from 50 μm to 300 μm. The morphology was observed parallel to the freezing direction using SEM. The thicknesses of IT structures were 50 μm, 100 μm, 200 μm and 300 μm.

In case that the ice crystals grow and push cellulose microfibrils, an aqueous film of sufficient thickness is needed between the ice front and cellulose microfibrils [47]. When the velocity of the ice front increases, the thickness of the aqueous film decreases. If the ice front velocity is too high ($v_{ice-front} > v_c$), the cellulose microfibrils are embedded inside the ice crystals instead of being entrapped between ice crystals [47]. The critical velocity, v_c is given by [48]

$$v_c = \frac{\Delta\sigma d}{3\eta R}\left(\frac{a_0}{d}\right)^z \tag{6.1}$$

where a_0 is the average intermolecular distance in the film, d is the overall thickness, η is the solution viscosity, R is the particles radius and z is an exponent that can vary from 1 to 5 depending on the specific model. For micron size particles, typical critical velocity ranges from 1 to 10 $\mu m\, s^{-1}$ and for nanometer size particles, the typical values is around 0.1 ~ 1 $m\, s^{-1}$, which is reversely proportional to the particle radius [48].

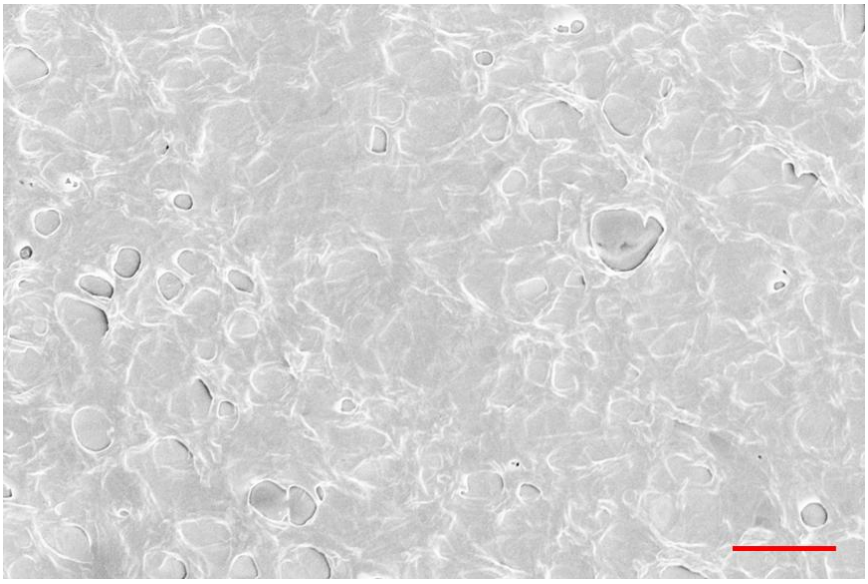

Figure 6-8 SEM image of the bottom of the cellulose microfibril IT structures (4.0wt%). Scale bar represents 40 μm.

Fig 6-8 is an SEM image of the bottom structure of the cellulose microfibril IT surface. When a cellulose microfibril suspension is freezed unidirectionally, the ice crystals start to grow at the bottom, which is contacted to liquid N_2. At that moment, the

ice-front velocity, denoted by $v_{ice-front}$, usually is larger than v_c; therefore, the ice front is planar and cellulose microfibrils are encapsulated in the ice front, instead of entrapped between ice crystals. Therefore, the morphology of the bottom of the cellulose microfibrils IT surface is a dense planar layer structure as shown in Fig 6-8.

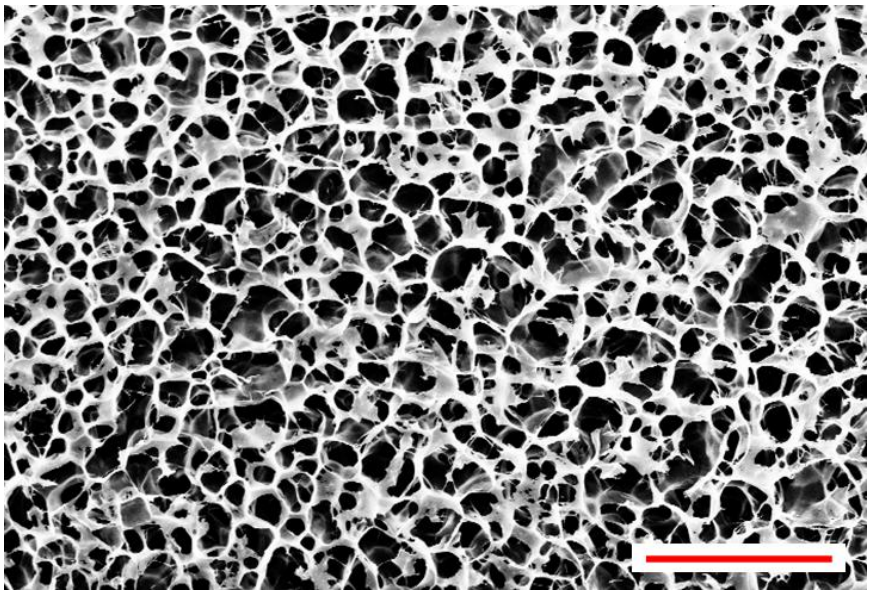

Figure 6-9 SEM image of the 50 μm high cellulose microfibril IT surfaces (4.0wt%). Scale bar represents 20 μm.

Fig 6-9 is the SEM image of the 50 μm high cellulose microfibril IT surface. As shown in the image, IT structures show a honeycomb-like architecture. When the ice crystals grow further, a transition from planar structure to columnar structure occurs. The transition phenomenon can be explained by the decrease of the freezing velocity [49]. Because this cooling process is unidirectional, a temperature gradient exists along the suspension. After a formation of planar ice crystals in the $v_{ice-front} > v_c$ zone, $v_{ice-front}$

decreases gradually below v_c, and ice crystals start to grow like ice-columns. At this moment, cellulose microfibrils start to become separated from the ice-front, resulting in the entrapment of cellulose microfibrils between ice-columns. Finally, honeycomb-like cellulose microfibrils IT structures are obtained after the sublimation of ice columns.

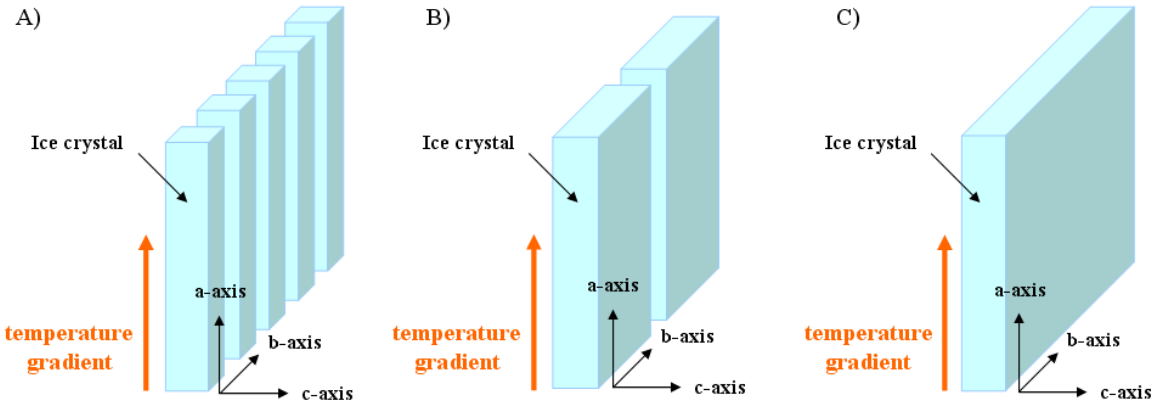

Figure 6-10. Schemes of anisotropical growth of ice crystals (a) at circular columnar region (50 μm) (b) at ellipse shape columnar region (100 μm and 200 μm) (c) at lamellar region (300 μm).

SEM images of the 100 μm high cellulose microfibril IT surfaces are shown in Fig 6-11 (a). Contrary to circular channels of 50 μm high surfaces, ellipse-shaped channels are observed. The transition from circular channels to elliptical channels attributes to the anisotropical growth of ice crystals. When the temperature gradient is high and $v_{ice-front}$ is fast, the ice front velocity, which is parallel to the temperature gradient orientation (crystallographic a-axis), is $10^2 \sim 10^3$ times faster than that of the b-axis and c-axis, which is perpendicular to the temperature gradient. At this time, ice crystals grow like columns (Fig 6-10 (a)). After the temperature gradient decreases, v_{a-axis} decreases and the difference between v_{a-axis} and v_{b-axis} becomes smaller than the columnar ice crystal region. v_{a-axis}, v_{b-axis} and v_{c-axis} represent the ice-front velocity

parallel to the crystallographic a, b and c axis, respectively. Therefore, ice crystals grow like ellipse-shaped columns as shown in Fig 6-10 (b), and entrapped cellulose microfibrils also form the ellipse-shaped channels. When the ice crystals keep growing (200 μm high) and $v_{ice-front}$ decreases further, high aspect ratio elliptical channels can be obtained (Fig 6-11 (b)).

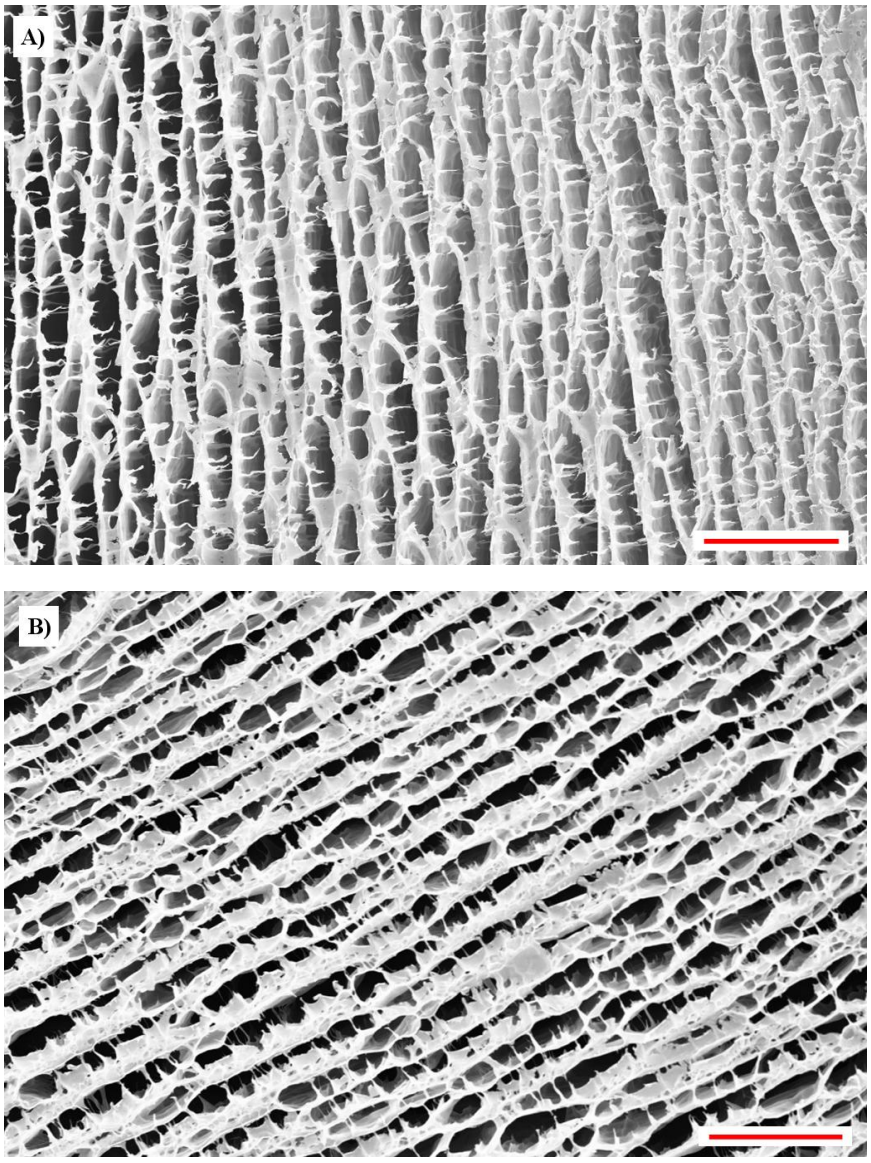

Figure 6-11 (a) SEM image of the 100 μm high cellulose microfibril IT surfaces (4.0wt%). (b) SEM image of the 200 μm high cellulose microfibril IT surfaces. (4.0wt%). Scale bar represents 20 μm.

When the height of ice crystals is larger than 300 μm, fully developed multichannel structures are obtained. As shown in Fig 6-12, there is a transition from ellipse-shaped channels to flat multichannel structures. At this region, the temperature gradient and v_{a-axis} decreases further. v_{a-axis} and v_{b-axis} become similar, but v_{c-axis} is still very slow. Therefore, ice crystals grow like a flat plank (Fig 6-10 (c)) and multichannel structures can be obtained after the sublimation of ice templates. A scheme of the growth mechanism of IT cellulose microfibril foams, as well as SEM images of IT cellulose microfibril foam surfaces and the schemes of ice crystal growth are all summarized in Fig 6-13.

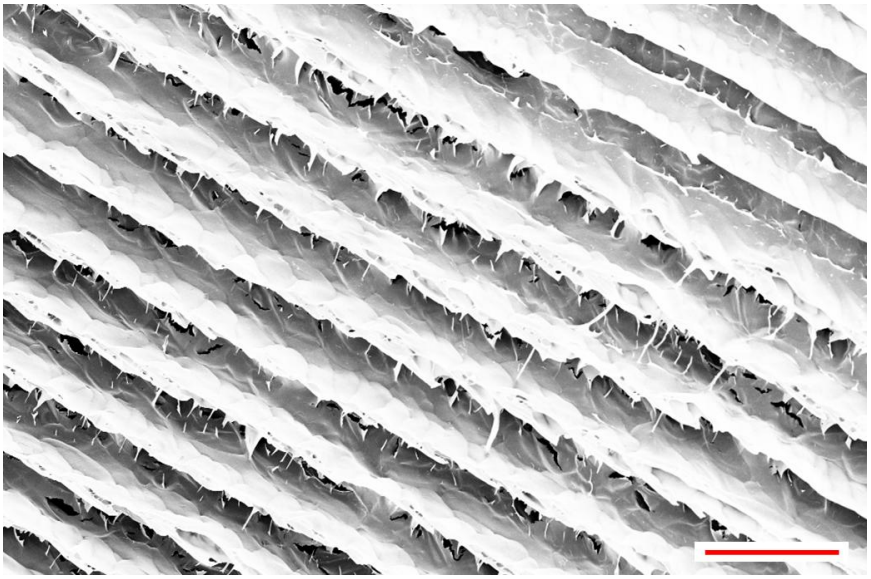

Figure 6-12 SEM image of the 300 μm high cellulose microfibril IT surfaces. (4.0wt%). Scale bar represents 10 μm.

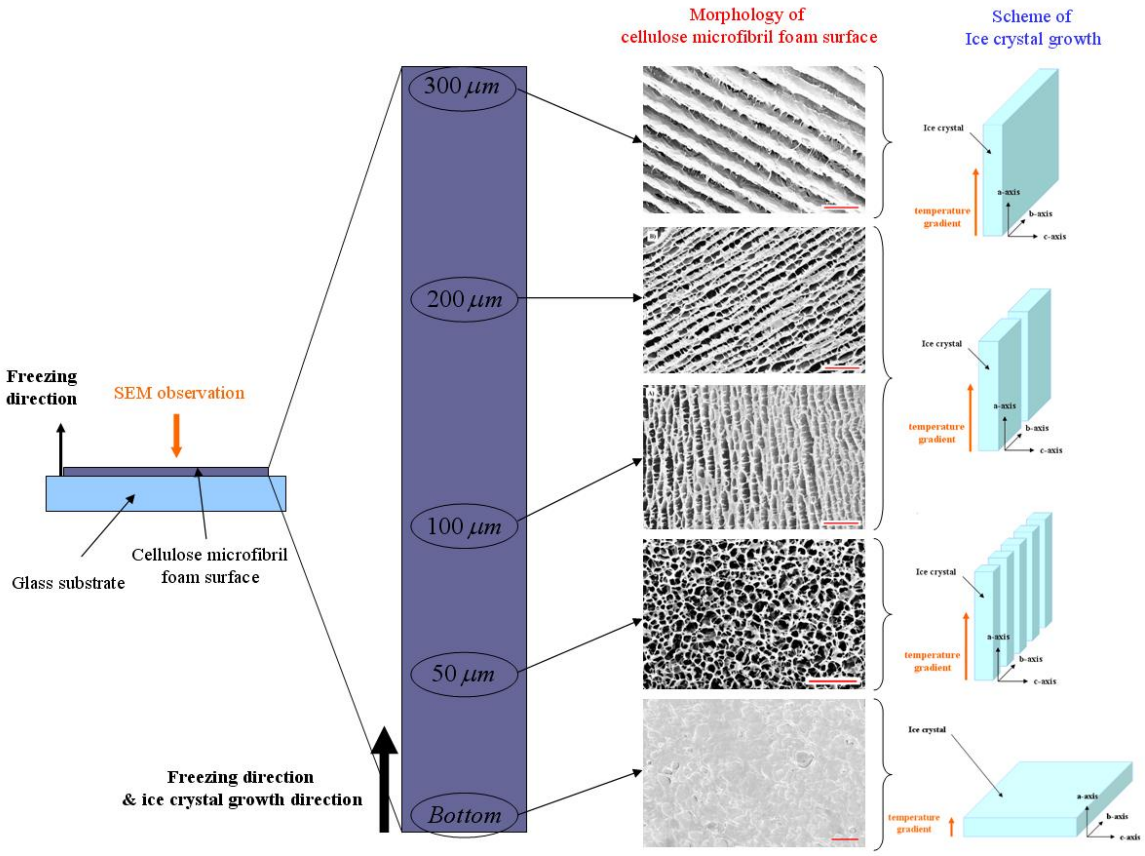

Figure 6-13. Scheme of the growth mechanism of IT cellulose microfibril foams.

6.3.3 Control of the surface structures via IT methods

From the mechanism studies of cellulose microfibril IT surface structures, it is confirmed that the morphology of cellulose microfibrils IT surfaces is significantly affected by the temperature gradient. During the freezing the cellulose microfibril suspension, the temperature gradient decreases automatically with increasing sample thickness and it causes a change in the surface morphology. For the fabrication of functional surfaces, morphology control is needed when the height of surface structures is fixed. In this study, the fabrication methods of honeycomb-like surfaces and anisotropic groove patterned surfaces are introduced using IT techniques. For all of the cases, the height of cellulose microfibrils IT surface structures is fixed at 50 μm.

Even though there is not a mathematical model to correlate the temperature gradient with the transition of ice crystal growth states, circular columns, ellipse shape columns, and lamellar structures, it is still possible to find appropriate conditions experimentally. As shown in Fig 6-1 (c), medium materials were inserted between liquid nitrogen and a suspension sample to retard the heat transfer and reduce the temperature gradient. Ethanol, methanol, n-octane, and water were used as medium materials. Their melting points are -114°C, -97°C, -57°C and 0°C, respectively. The height of the mediums was fixed at 5mm.

The experimental conditions and results are summarized in Table 6-2. Without a medium, the surface morphology is the honeycomb-like structure as shown in Fig 6-9. With an ethanol medium, the surface shows an ellipse-shaped channel structure. Upon changing the medium from low melting point materials to high melting point materials, the transition from ellipse-shaped channel structures to multichannel structures occurs. When methanol and n-octane are used as medium materials, the surface structures are the mixed form of ellipse-shaped channels and multichannel structures. When water was used as a medium, fully developed multichannel structures were obtained. The SEM images of IT surface structures with various mediums are shown in Fig 6-14.

Table 6-2. Experimental conditions and surface structures of IT foam surfaces.

Medium	m.p. (°C)	Surface structure
No medium	-	Honeycomb-like structure
Ethanol	-114	Ellipse-shape channel structure [A]
Methanol	-97	Mixed structure of A and B
n-Ocatane	-57	Mixed structure of A and B
Water	0	Multichannel strucuture [B]

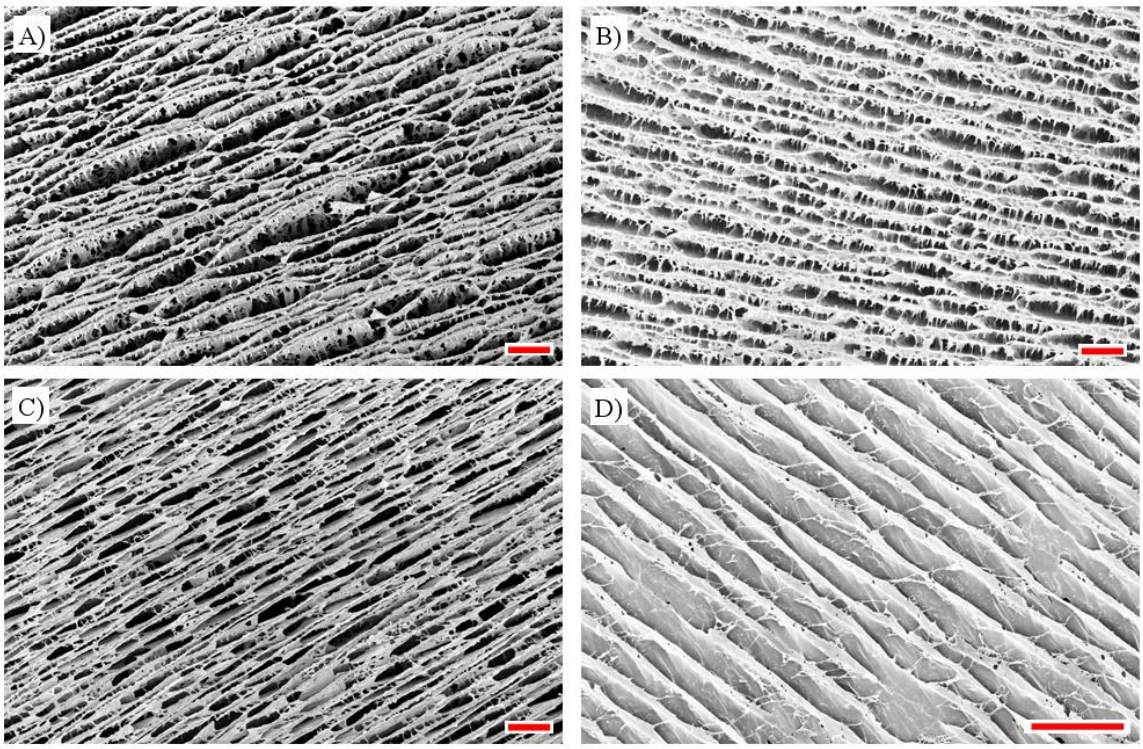

Figure 6-14. SEM images of cellulose microfibrils IT foam surface structures with various mediums, such as (a) ethanol (b) methanol (c) n-octane (d) water. Scale bars represent 10 μm.

6.3.4 Wetting properties of IT foam surfaces

The contact angles of IT cellulose microfibril foam surfaces were measured using a FTA 200 Dynamic contact angle analyzer. Two different types of IT foam surfaces, honeycomb-like structure and aligned multichannel structure, were prepared as described in Table 6-2 and Fig 6-13, and their contact angles were measured. Before the measurements were taken, surface modification carried out by chemical vapor deposition of 1H,1H,2H,2H-perfluorooctyltriethoxysilane (POTS) was performed as shown in Fig 6-15. Prepared IT foam surface samples and a small amount of POTS were placed in a sealed vessel. The sealed vessel was put in an oven at 125°C for 3 h. Then, samples were

heated to 150°C for 3 h to remove the unreacted POTS molecules from the IT foam surfaces. For comparative purposes, the contact angles of IT cellulose nanowhisker foam surfaces were also measured.

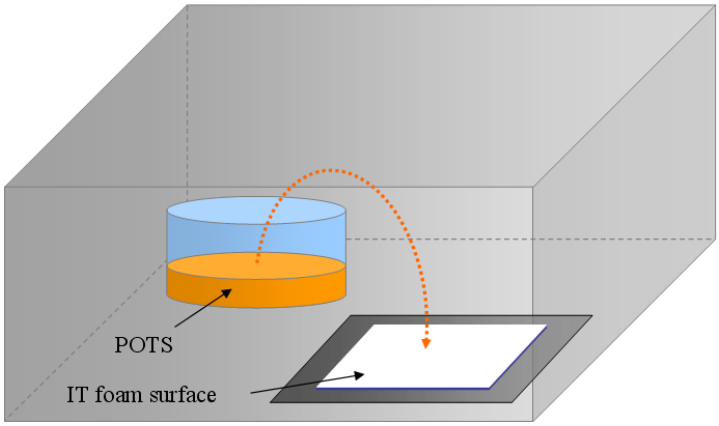

Figure 6-15. Scheme of POTS vapor deposition on the IT foam surface.

Fig 6-16 provides the contact angle measurement results of IT cellulose microfibril foam surfaces and IT cellulose nanowhisker foam surfaces that both have honeycomb-like structures. The average contact angle of IT cellulose microfibril foam surfaces are ~144°, regardless of the suspension concentration (4.0wt% ~ 8.0wt%). Although the wall thickness of IT structures increases with increasing cellulose microfibril suspension concentration, it seems that the thickness change of honeycomb-like structures does not affect the contact angle of IT foam surfaces significantly. Due to the roughness of the honeycomb-like structure surface [19, 50], IT cellulose microfibril foam surfaces show high contact angles, compared with POTS-treated cellulose microfibril thin films (contact angle: 75.6°). The average contact angle of IT cellulose nanowhisker foam surfaces (4.0wt% ~ 8.0wt%) are similar with those of IT cellulose

microfibril foam surfaces and ranges from 141.6° to 143.7°. The shape of water droplet on POTS-treated cellulose microfibril foam surfaces is shown in Fig 6-17.

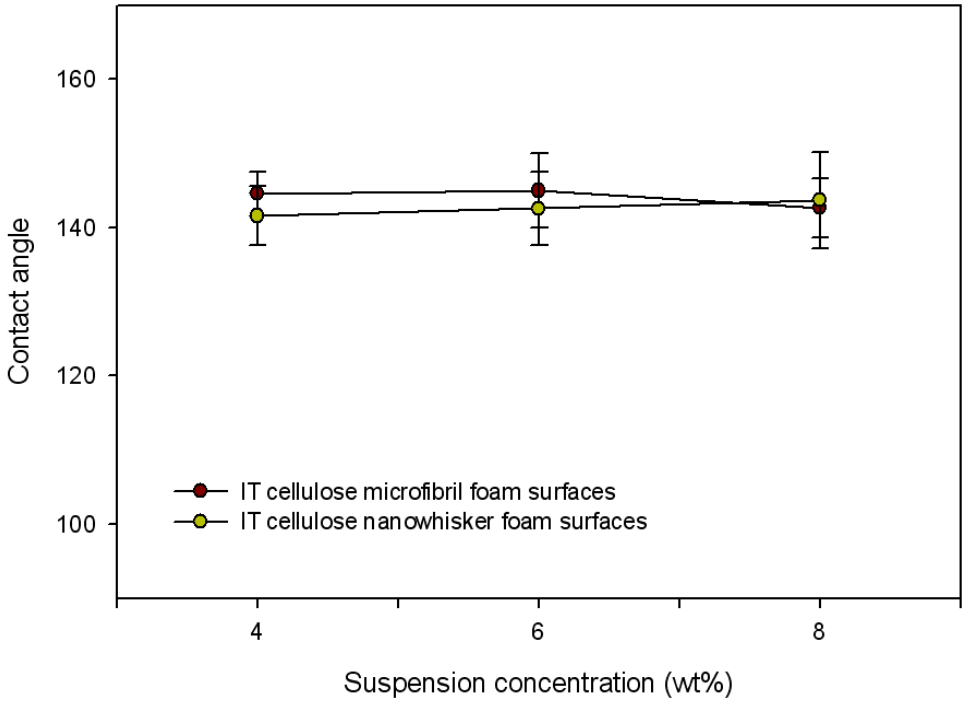

Figure 6-16. Contact angle measurement results of honeycomb-like IT cellulose microfibril foam surfaces and IT cellulose nanowhisker foam surfaces.

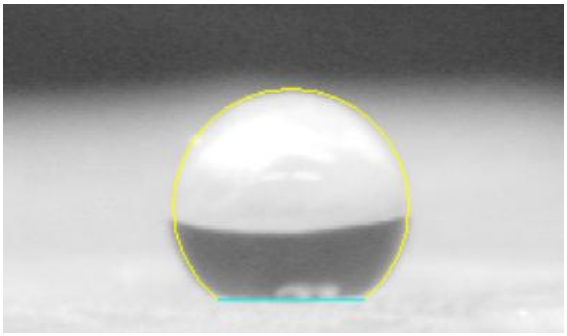

Figure 6-17. The shape of water droplets on POTS-treated honeycomb-like IT cellulose microfibril foam surfaces (contact angle: 142.1°).

The contact angles of highly aligned multichannel IT foam surfaces were measured perpendicular ($\phi_{\perp}$) and parallel ($\phi_{\parallel}$) to the direction of grooves as shown in Fig 6-19. It was reported that the aligned groove surfaces show anisotropic wetting properties [25, 29-31]. Fig 6-18 contains the contact angle ($\phi_{\perp}$ and $\phi_{\parallel}$) measurement results of IT cellulose microfibril foam surfaces and IT cellulose nanowhisker foam surfaces. For the IT cellulose microfibril foam surfaces prepared from the low concentration suspension (4.0wt%), anisotropic wetting properties are evident. In this case, $\phi_{\perp}$ is ~122.6° and $\phi_{\parallel}$ is ~103.4°. However, if the suspension concentration is higher than 6.0wt%, the anisotropic wetting properties are not observed. In this case, the contact angles range from 131.6° to 135.2°, for both of the $\phi_{\perp}$ and $\phi_{\parallel}$. By increasing the suspension concentration, the thickness of cellulose microfibril bridges also increases (Fig 5-11). It is expected that cellulose microfibril bridges prevent the water droplet from spreading anisotropically on the multichannel structure IT foam surface. On the other hand, IT cellulose nanowhisker foam surfaces show anisotropic wetting properties up to 8.0wt%. For 4.0wt% samples, $\phi_{\perp}$ and $\phi_{\parallel}$ are ~112.5° and ~85.4°, respectively. IT cellulose nanowhisker foams have dendrite structures, instead of bridge structures (Fig 5-12). The anisotropic shapes of water droplets on cellulose microfibril/cellulose nanowhisker foam surfaces are shown in Fig 6-19.

Even though IT cellulose microfibril foam surfaces (4.0wt%) and IT cellulose nanowhisker foam surfaces (4.0wt% ~ 8.0wt%) show anisotropic wetting properties, the difference between $\phi_{\perp}$ and $\phi_{\parallel}$ is small, compared with the references [25, 29-31]. The contact angle (~143°) of honeycomb-like IT foam surfaces is also smaller than that of superhydrophobic surfaces (> 150°). In addition, the wetting phenomenon of honeycomb-like surfaces and anisotropic surfaces has not been investigated theoretically. In future studies, the methods used to enhance wetting properties of IT foam surfaces will be

investigated. Also, a theoretical study concerning the wetting properties of honeycomb-like surfaces and anisotropic surfaces will be done.

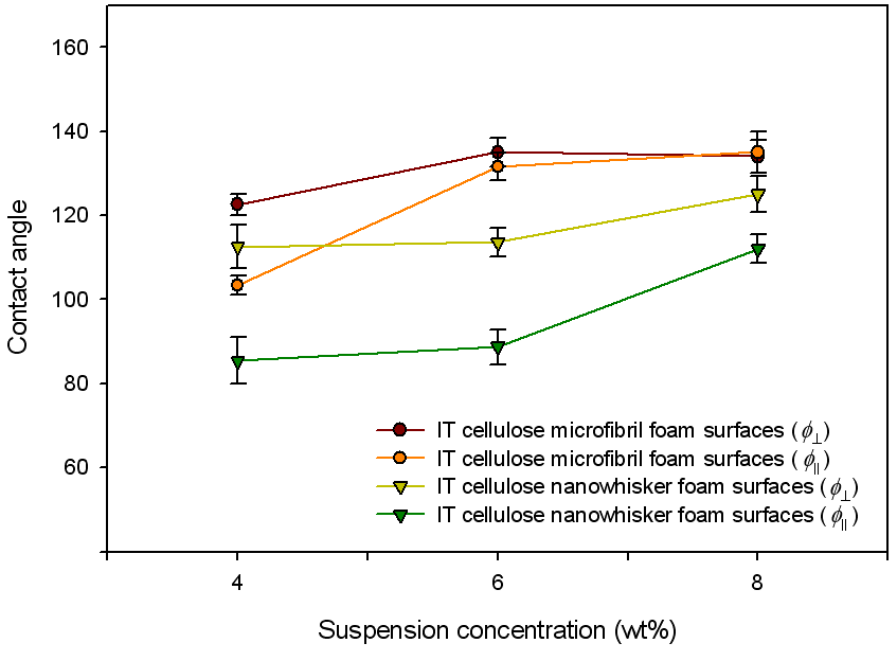

Figure 6-18. Contact angle measurement results of highly aligned multichannel IT foam surfaces measured perpendicular ($\phi_\perp$) and parallel ($\phi_\parallel$) to the direction of grooves.

\

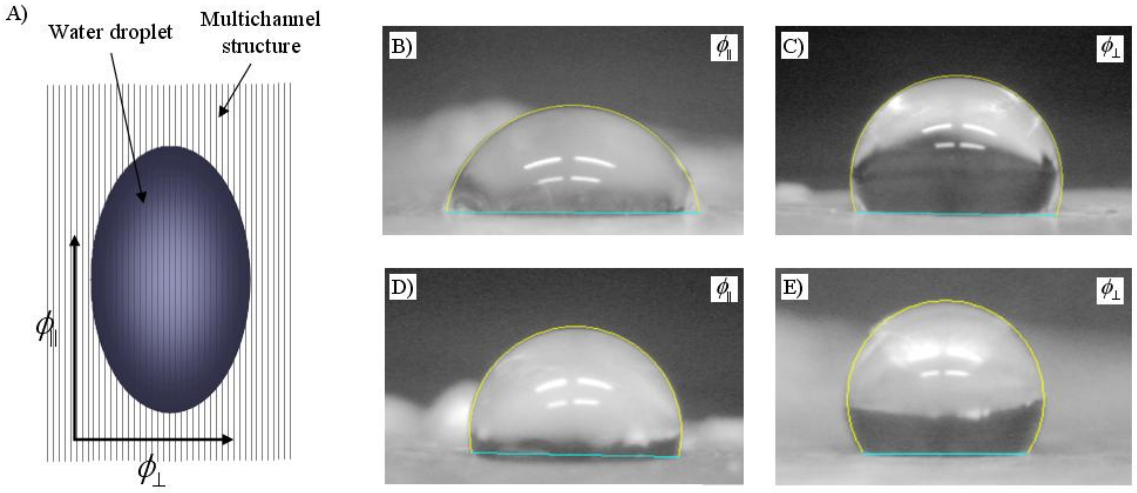

Figure 6-19 (a) Scheme of anisotropic spreading of water droplet; (b) and (c) shapes of water droplet on multichannel IT cellulose microfibril foam surface (4.0wt%) ($\phi_{\parallel}$ = 82.6° and $\phi_{\perp}$ = 108.5°); (d) and (e) shapes of water droplet on multichannel IT cellulose nanowhisker foam surface (4.0wt%) ($\phi_{\parallel}$ = 101.3° and $\phi_{\perp}$ = 123.9°).

6.4. Conclusions

The morphology and growth mechanism of IT cellulose microfibril foam surfaces were investigated successfully. When the height of IT surfaces was 50 μm, the surface showed honey-comb like structures. When the height of IT surfaces was between 100 μm and 200 μm, a transition from honey-comb like structures to multilayer structures occurs. In these cases, ellipse-shaped channels were observed. If the height of IT surfaces was larger than 300 μm, fully developed multichannel structures were obtained. By controlling the temperature gradient between cellulose microfibril suspensions and secondary freezing mediums, various surface structures including honey-comb like structures, ellipse-shape channel structures, and fully developed multichannel structures were obtained successfully. The average contact angles of honeycomb-like IT cellulose microfibril and cellulose nanowhisker foam surfaces are ~143°, regardless of the suspension concentration (4.0wt% ~ 8.0wt%). Multichannel IT cellulose microfibril foam surfaces showed anisotropic wetting properties at a low suspension concentration (4.0wt%). On the other hand, multichannel IT cellulose nanowhisker foam surfaces showed anisotropic wetting properties up to 8.0wt%.

References

1. Scardino, A., et al., *Microtopography and antifouling properties of the shell surface of the bivalve molluscs Mytilus galloprovincialis and Pinctada imbricata.* Biofouling, 2003. **19**: p. 221-230.

2. Schultz, M.P., C.J. Kavanagh, and G.W. Swain, *Hydrodynamic forces on barnacles: Implications on detachment from fouling-release surfaces.* Biofouling, 1999. **13**(4): p. 323-335.

3. Saito, H., et al., *A study on snow sticking weight to water-repellent coatings.* Materials Science Research International, 1997. **3**(4): p. 216-219.

4. Kako, T., et al., *Adhesion and sliding of wet snow on a super-hydrophobic surface with hydrophilic channels.* Journal of Materials Science, 2004. **39**(2): p. 547-555.

5. Quere, D., *Non-sticking drops.* Reports on Progress in Physics, 2005. **68**(11): p. 2495-2532.

6. Zielecka, M. and E. Bujnowska, *Silicone-containing polymer matrices as protective coatings - Properties and applications.* Progress in Organic Coatings, 2006. **55**(2): p. 160-167.

7. Barthlott, W. and C. Neinhuis, *Purity of the sacred lotus, or escape from contamination in biological surfaces.* Planta, 1997. **202**(1): p. 1-8.

8. Gao, X.F. and L. Jiang, *Water-repellent legs of water striders.* Nature, 2004. **432**(7013): p. 36-36.

9. Gao, X.F., et al., *The dry-style antifogging properties of mosquito compound eyes and artificial analogues prepared by soft lithography.* Advanced Materials, 2007. **19**(17): p. 2213-+.

10. Parker, A.R. and C.R. Lawrence, *Water capture by a desert beetle.* Nature, 2001. **414**(6859): p. 33-34.

11. Sun, M.H., et al., *Artificial lotus leaf by nanocasting.* Langmuir, 2005. **21**(19): p. 8978-8981.

12. Lee, W., et al., *Nanostructuring of a polymeric substrate with well-defined nanometer-scale topography and tailored surface wettability.* Langmuir, 2004. **20**(18): p. 7665-7669.

13. Furstner, R., et al., *Wetting and self-cleaning properties of artificial superhydrophobic surfaces.* Langmuir, 2005. **21**(3): p. 956-961.

14. Martines, E., et al., *Superhydrophobicity and superhydrophilicity of regular nanopatterns.* Nano Letters, 2005. **5**(10): p. 2097-2103.

15. Fresnais, J., L. Benyahia, and F. Poncin-Epaillard, *Dynamic (de)wetting properties of superhydrophobic plasma-treated polyethylene surfaces.* Surface and Interface Analysis, 2006. **38**(3): p. 144-149.

16. Minko, S., et al., *Two-level structured self-adaptive surfaces with reversibly tunable properties.* Journal of the American Chemical Society, 2003. **125**(13): p. 3896-3900.

17. Wu, X.D., L.J. Zheng, and D. Wu, *Fabrication of superhydrophobic surfaces from microstructured ZnO-based surfaces via a wet-chemical route.* Langmuir, 2005. **21**(7): p. 2665-2667.

18. Huang, L., et al., *Stable superhydrophobic surface via carbon nanotubes coated with a ZnO thin film.* Journal of Physical Chemistry B, 2005. **109**(16): p. 7746-7748.

19. Zhai, L., et al., *Stable superhydrophobic coatings from polyelectrolyte multilayers.* Nano Letters, 2004. **4**(7): p. 1349-1353.

20. Han, J.T., et al., *Stable superhydrophobic organic-inorganic hybrid films by electrostatic self-assembly.* Journal of Physical Chemistry B, 2005. **109**(44): p. 20773-20778.

21. Jiang, L., Y. Zhao, and J. Zhai, *A lotus-leaf-like superhydrophobic surface: A porous microsphere/nanofiber composite film prepared by electrohydrodynamics.* Angewandte Chemie-International Edition, 2004. **43**(33): p. 4338-4341.

22. Acatay, K., et al., *Tunable, superhydrophobically stable polymeric surfaces by electrospinning.* Angewandte Chemie-International Edition, 2004. **43**(39): p. 5210-5213.

23. Ma, M.L., et al., *Superhydrophobic fabrics produced by electrospinning and chemical vapor deposition.* Macromolecules, 2005. **38**(23): p. 9742-9748.

24. Feng, L., et al., *Super-hydrophobic surfaces: From natural to artificial.* Advanced Materials, 2002. **14**(24): p. 1857-1860.

25. Xia, D.Y., et al., *Tailoring Anisotropic Wetting Properties on Submicrometer-Scale Periodic Grooved Surfaces.* Langmuir, 2010. **26**(4): p. 2700-2706.

26. Bliznyuk, O., et al., *Scaling of anisotropic droplet shapes on chemically stripe-patterned surfaces.* Physical Review E, 2009. **79**(4).

27. Li, W., et al., *Anisotropic wetting behavior arising from superhydrophobic surfaces: Parallel grooved structure.* Journal of Physical Chemistry B, 2008. **112**(24): p. 7234-7243.

28. Semprebon, C., et al., *Anisotropy of Water Droplets on Single Rectangular Posts.* Langmuir, 2009. **25**(10): p. 5619-5625.

29. Sommers, A.D. and A.M. Jacobi, *Creating micro-scale surface topology to achieve anisotropic wettability on an aluminum surface.* Journal of Micromechanics and Microengineering, 2006. **16**(8): p. 1571-1578.

30. Zhao, Y., et al., *Anisotropic wetting characteristics on submicrometer-scale periodic grooved surface.* Langmuir, 2007. **23**(11): p. 6212-6217.

31. Chung, J.Y., J.P. Youngblood, and C.M. Stafford, *Anisotropic wetting on tunable micro-wrinkled surfaces.* Soft Matter, 2007. **3**(9): p. 1163-1169.

32. Deville, S., et al., *Freezing as a path to build complex composites.* Science, 2006. **311**(5760): p. 515-518.

33. Nishihara, H., S. Iwamura, and T. Kyotani, *Synthesis of silica-based porous monoliths with straight nanochannels using an ice-rod nanoarray as a template.* Journal of Materials Chemistry, 2008. **18**(31): p. 3662-3670.

34. Gutierrez, M.C., et al., *Biocompatible MWCNT scaffolds for immobilization and proliferation of E. coli.* Journal of Materials Chemistry, 2007. **17**(29): p. 2992-2995.

35. Zhang, H. and A.I. Cooper, *Aligned porous structures by directional freezing.* Advanced Materials, 2007. **19**(11): p. 1529-1533.

36. Zhang, H., et al., *Synthesis of porous microparticles with aligned porosity.* Advanced Functional Materials, 2008. **18**(2): p. 222-228.

37. Deville, S., E. Saiz, and A.P. Tomsia, *Freeze casting of hydroxyapatite scaffolds for bone tissue engineering.* Biomaterials, 2006. **27**(32): p. 5480-5489.

38. Gutierrez, M.C., et al., *Poly(vinyl alcohol) scaffolds with tailored morphologies for drug delivery and controlled release.* Advanced Functional Materials, 2007. **17**(17): p. 3505-3513.

39. Gutierrez, M.C., et al., *Macroporous 3D architectures of self-assembled MWCNT surface decorated with Pt nanoparticles as anodes for a direct methanol fuel cell.* Journal of Physical Chemistry C, 2007. **111**(15): p. 5557-5560.

40. Nogi, M., et al., *Optically Transparent Nanofiber Paper.* Advanced Materials, 2009. **21**(16): p. 1595-+.

41. Dong, X.M., J.F. Revol, and D.G. Gray, *Effect of microcrystallite preparation conditions on the formation of colloid crystals of cellulose.* Cellulose, 1998. **5**(1): p. 19-32.

42. Ashley, K.M., et al., *Combinatorial investigation of dewetting: polystyrene thin films on gradient hydrophilic surfaces.* Polymer, 2003. **44**(3): p. 769-772.

43. Israelachvili, J., *Intermolecular and surface forces*. 2nd Edition ed. 1991, San Diego: Academic Press.

44. Israelachvili, J. and R. Pashley, *THE HYDROPHOBIC INTERACTION IS LONG-RANGE, DECAYING EXPONENTIALLY WITH DISTANCE.* Nature, 1982. **300**(5890): p. 341-342.

45. Israelachvili, J.N. and R.M. Pashley, *MOLECULAR LAYERING OF WATER AT SURFACES AND ORIGIN OF REPULSIVE HYDRATION FORCES.* Nature, 1983. **306**(5940): p. 249-250.

46. Israelachvili, J.N. and R.M. Pashley, *MEASUREMENT OF THE HYDROPHOBIC INTERACTION BETWEEN 2 HYDROPHOBIC SURFACES IN AQUEOUS-ELECTROLYTE SOLUTIONS.* Journal of Colloid and Interface Science, 1984. **98**(2): p. 500-514.

47. Korber, C., et al., *INTERACTION OF PARTICLES AND A MOVING ICE-LIQUID INTERFACE.* Journal of Crystal Growth, 1985. **72**(3): p. 649-662.

48. Asthana, R. and S.N. Tewari, *THE ENGULFMENT OF FOREIGN PARTICLES BY A FREEZING INTERFACE.* Journal of Materials Science, 1993. **28**(20): p. 5414-5425.

49. Deville, S., E. Saiz, and A.P. Tomsia, *Ice-templated porous alumina structures.* Acta Materialia, 2007. **55**(6): p. 1965-1974.

50. Li, S.H., et al., *Super-hydrophobicity of large-area honeycomb-like aligned carbon nanotubes.* Journal of Physical Chemistry B, 2002. **106**(36): p. 9274-9276.

CHAPTER 7

CONCLUSIONS AND FUTURE WORKS

7.1. Conclusions

In this thesis, we primarily focused on our attention on investigating the relationship between structures, surface chemistry and properties of cellulosic nanocomposites. Chapter 2 was intended to give a general background related with this thesis, such as cellulose, cellulose nanowhiskers, cellulose microfibrils, electrospinning, nanoindentation, properties of porous foams and wetting properties of patterned surfaces.

In Chapter 3, cellulose nanowhiskers reinforced PVA nanofiber webs were successfully fabricated using electrospinning technique. The morphology and mechanical properties of electrospun fiber webs are significantly affected by the alignment of electrospun fibers. It was confirmed from the experimental results that aligned electrospun webs showed enhanced mechanical properties, compared with isotropic electrospun fiber webs. It is expected that the different mechanical properties of aligned and isotropic PVA electrospun webs is due to the different load transfer mechanism.

In Chapter 4, the mechanical properties of cellulose nanowhiskers reinforced PVA electrospun fiber were measured using nanoindentation method. It was confirmed that the modulus of PVA/cellulose nanowhiskers electrospun fiber increases linearly with increasing loading ratio of cellulose nanowhiskers up to 20.0wt%. From the model studies, nanoindentation measurement results are larger than the predicted values by the isotropic Halpin-Tsai model and the transverse Halpin-Tsai model, however the experimental results are 20~30% smaller than the longitudinal Halpin-Tsai model predictions.

In Chapter 5, the growth mechanism of IT cellulose microfibril porous foams was investigated successfully. It was found that the morphology of IT cellulose microfibril foams is significantly affected by the suspension concentration, the morphology of cellulose microfibrils and the temperature gradient. From the compressive load measurement experiments, it was found that the compressive stresses of IT cellulose microfibril foams increase linearly as increasing concentrations of cellulose microfibril suspension.

In Chapter 6, the morphology and growth mechanism of IT cellulose microfibril foam surfaces were investigated successfully. It was found that IT cellulose microfibril foam surfaces show honey-comb like structures, ellipse-shape channels and multichannel structures according to the growth length. The structure of IT cellulose microfibril foam surfaces can be controlled by varying the temperature gradient. From the contact angle measurement results, it was found that IT cellulose microfibril foam surfaces show high contact angles and anisotropic wetting properties.

7.2. Future works

In Chapter 3, the quantitative analysis of aligned/isotropic electrospun webs has not been done. In future works, model study of aligned/isotropic electrospun webs and cellulose nanowhiskers reinforce aligned/isotropic electrospun webs will be done. In addition, it was found that the crystallinity of PVA electrospun fiber webs is relatively low, compared with blade casted PVA thin film (not shown in this thesis). It was also found that the crystallinity of aligned PVA electrospun fiber webs is lower than that of isotropic PVA electrospun webs. In future study, the relationship between the crystallinity change and electrospinning parameters will be investigated.

In Chapter 4, the load transfer mechanism during the nanoindentation of cellulose nanowhiskers reinforced electrospun fiber has not been studied. It will be very

meaningful to investigate the detailed load transfer mechanism between the nanoindenter tip and nanocomposites reinforced with aligned nanoparticles.

In Chapter 5, the mechanical properties of IT cellulose microfibril foams prepared from 2.0wt% ~ 8.0wt%. In future studies, IT cellulose microfibril foams will be prepared from high concentration suspensions, such as 40.0wt%, 50.0wt% and 60.0wt%. Also, the channel orientation effects on the mechanical properties of IT cellulose microfibril foams will be studied.

In Chapter 6, the wetting phenomenon of honeycomb-like surfaces and anisotropic surfaces has not been investigated theoretically. In the future studies, the theoretical study about the wetting properties of honeycomb-like surfaces and anisotropic surfaces will be done. Also, methods to enhance wetting properties of IT foam surfaces will be investigated.

APPENDIX A

NANOCOMPOSITES FROM

REGENERATED CELLULOSE AND NANOCLAY

Abstract

A new and environmental benign method for preparing cellulose and montmorillonite (MMT) biodegradable nanocomposites via a cellulose regeneration approach using 4-methylmorpholine N-oxide (NMMO) as the solvent was developed. Results showed that for hydrophilic MMT, the tensile strength in the cellulose / nanoclay composite increases with increase of clay loading up to 6%, and then decreases. In contrary, the modulus of the nanocomposites increases linearly at the MMT loading range of 1–10%.An interaction force measurement between the cellulose and MMT was conducted. Using Wide Angle X-ray Diffraction (WXRD) analysis, scanning electron microscopy (SEM) and transmission electron microscopy (TEM) observation, it was found for the first time that the MMT was intercalated and exfoliated in the pure cellulose matrix. The relationship between the degree of intercalation or exfoliation of MMT clays and the modulus of the nanocomposite was studied.

Keywords: Cellulose, Nanocomposites, Hydrophobicity, Nanoclay.

A.1. Introduction

A dramatic increase in the usage of non-biodegradable wastes made from petroleum based polymers such as polypropylene (PP), polyethylene (PE) and poly(vinyl chloride) (PVC) have raised serious environmental concerns. As oil resources declines and costs of petroleum and petrochemical products increase, requirements for sustainable materials to replace petrochemical-based materials have been growing steadily [1]. Cellulose is one of the most prospective biomaterials. It is environmentally friendly, biocompatible, renewable and an abundant natural polymer which exhibits outstanding properties. Regenerated cellulose can be manufactured as fibers, films, food casings, membranes and sponges. It can also be converted into cellulose derivatives like cellulose esters and ethers that have been widely used for coatings, optical films, sorption materials and additives in building materials and pharmaceuticals. However, only 2% (3.2 million tons in 2003) of annual consumption of wood fibers is used for regenerated cellulose products and cellulose derivatives, and most of them, almost 98%, are used as papers and cardboards [2]. The main reason for the low utilization rate of cellulose fibers, except paper products, is because of its poor processibility due to the strong hydrogen bonding between cellulose molecules [3]. Therefore development of more effective manufacturing methods and application are important, which could make cellulose as more valuable raw materials instead of ordinary consumptions.

In general, cellulose is insoluble in common solvents due to its strong hydrogen bonding and partial crystalline structure. For more than one century, the regeneration of cellulose has depended on a viscose technique that produces environmental hazardous byproducts such as CS_2, H_2S, and heavy metals [3]. Recently, a new cellulose solvent N-methylmorpholine-N-oxide (NMMO) has been developed [4]. The strong N-O dipoles of NMMO can substitute the hydrogen bonding between cellulose molecules [5], making cellulose molecules soluble in NMMO. The most outstanding advantage of this process is that the NMMO was environmentally friendly and 100% recyclable in comparison with

the viscose technique. The cellulose–NMMO–water system has been widely investigated [6-7] and the regenerated cellulose fibers using NMMO method is called Lyocell [8-11].

It has been well known that polymer/layered silicate (PLS) nanocomposites have many advantages than polymer alone. For example, some PLS nanocomposites exhibit remarkable improvement of properties such as high modulus [12], improved tensile strength [13-14], reduced gas permeability [15-16], decreased flammability [17-18], increased biodegradability [19] and enhanced ionic conductivity [20-21]. Many polymeric composites using nanostructured clay as reinforcement fillers have been developed, and it was found that nanoclay is one of the best nanofillers in terms of its low cost and unique structure. However, the nanocomposites made by regenerated cellulose matrix and nanoclay have not been reported. It is expected that by adding layered silicate into regenerated cellulose matrix under optimized conditions, the physical properties of cellulose will be significantly improved. It has also been reported in literature that nanoclay is an effective fire retardant and anti-electric agent when it is incorporated into a polymeric matrix. Therefore, it is also expected that the nanocomposites made from regenerated cellulose and nanoclay will also enhance both the physical and fire retardant of cellulosic properties for textile fibers and films. A successful synthesis of regenerated cellulose based nanocomposites may also lead to some novel applications in the biomedical engineering related area because cellulose is nontoxic and biodegradable.

In this study, we report a new and facile approach to prepare nanocomposites comprising of natural cellulose and layered silicate nanoclays via a cellulose regeneration approach using NMMO as the solvent. The interactive force between the cellulose and the nanoclay was measured, and the mechanical properties of the nanocomposites were correlated with the hydrophobicity of the clay.

A.2. Experimental details

A.2.1. Materials

Cellulose powder was supplied by Fisher Science Education. 4-Methylmorpholine N-oxide (50% w/w aqueous solution) (NMMO) was supplied by Alfa Aesar. Montmorillonite (MMT) clays were supplied by the Southern Clay Products, Inc. USA, with properties shown in Table A-1. N-propyl gallate was purchased from Aldrich and used as an antioxidant. Water was obtained from a Nanopure water system with a resistivity of ca. 18 MΩ cm.

Table A-1. Properties of montmorillonites (MMT).

Sample	2θ (°)	*d*-spacing (Å)	Particle size (nm)	Organic modifier	Modifier concentration meq/100g clay
MMT Na^+	7.66	11.5	75~150	N/A	N/A
MMT 10A	4.58	19.2	75~150	Dimethyl benzyl dehydrogenated tallow quaternary ammonium	125
MMT 30B	4.77	18.5	75~150	Methyl tallow bis-2-hydroxyethyl quaternary ammonium	90
MMT 25A	4.75	18.6	75~150	Dimethyl dehydrogenated tallow 2-ethylhexyl quaternary ammonium	95
MMT 93A	3.74	23.6	75~150	Methyl dehydrogenated tallow ammonium	90
MMT 20A	3.67	24.2	75~150	Dimethyl dehydrogenated tallow quaternary ammonium	95
MMT 15A	2.80	31.5	75~150	Dimethyl dehydrogenated tallow quaternary ammonium	125

A.2.2. Sample Preparation

According to the phase diagram of cellulose-NMMO-water system [3], the ratio of cellulose and NMMO was fixed to 0.10 by weight for the effective dissolution. MMT clay contents varied from 1.0wt% and 10.0wt% to cellulose. The cellulose/MMT clay nanocomposites were prepared according to the following procedures, taking cellulose/2.0wt% MMT Na^+ system as an example. In a 200mL beaker with 100mL NMMO (50.0wt%), 0.114g of MMT Na^+ was added. The suspension was ultrasonicated for 5 minutes and slowly agitated for 24 hrs using a mechanical stirrer at ca. 100 rpm.

After the complete swelling of MMT clay, 5.7g of cellulose powder was added to the MMT Na^+-NMMO suspension and mixed for 1hr with 100 rpm. 0.005 g of N-propyl gallate was then added to the mixture as an antioxidant. This mixture was placed in a round-bottom flask and rotatory evaporator at 70 °C under vacuum for 20 min. After that, the temperature of the evaporator was raised to 95°C to evaporate the water and dissolve the cellulose powders. A high viscous cellulose/MMT Na^+ mixture was formed with an amber color, which was then cast onto a glass plate as showed in Fig A-1, using a razor blade. Paper frame template was attached on the glass plate with glue. The thickness of paper template was 20μm. The cast film was immediately immersed into a 20 L DI water bath for more than 48 hrs. During this process, the water bath had kept stirring at a very slow speed to facilitate the removal of NMMO from the composite. The DI water in the bath was changed every 12 hrs. The obtained milky cellulose/MMT Na^+ film was washed for another 3 hrs to remove the residue of NMMO. The thin cellulose was peeled off from the glass and then dried at room temperature for 48 hrs.

Because of the strong hydrogen bonding force between cellulose molecules, the film shrunk during the drying process, resulting in many defects and cracks on the film. Average size of shrunk cellulose films was less than 60% compared to the original one and the surface of shrunk cellulose film was very irregular. Because a wet cellulose film was very soft and squashed easily, it is difficult to fix the film on the glass template with a mechanical method such as clampers or pins. To solve this problem, as shown in Fig A-1, the wet cellulose film was attached to a paper frame before drying. During the drying, the hydrogen bond between paper template and cellulose film increased gradually with increasing hydrogen bonds between cellulose molecules. After the complete drying of the film, the interaction force between the template and film was maximized. Therefore, paper frame can prevent the shrinkage of the cellulose film without squashing of the film.

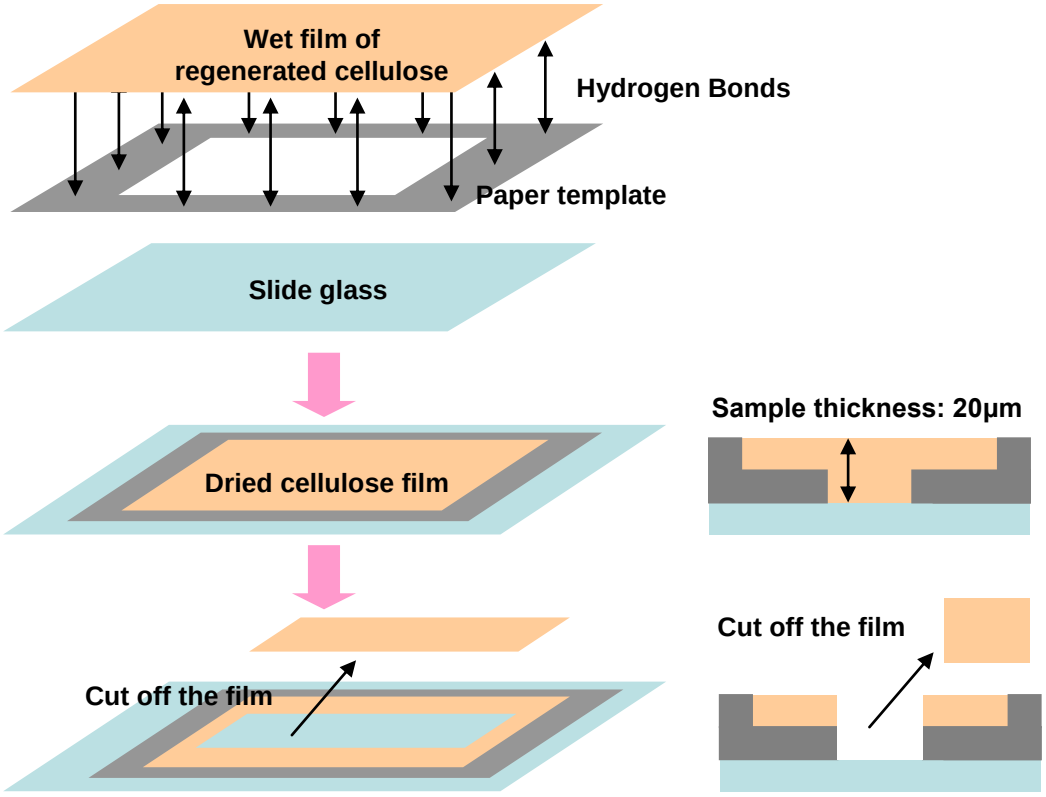

Figure A-1. Regenerated cellulose film preparation.

A.2.3.Characterization

X-ray diffractometry (XRD) was performed on a X'pert pro Alpha-1 diffractometer with Cu-Kα radiation, in a 2θ range between 0.5-40°. A step size of 0.01° and a scan step time of 0.5 sec. The wave length of X-ray beam is 0.154056 nm. Scanning electron microscopy (SEM) was carried out on a LEO 1530 SEM machine with an accelerating potential of 10kV. The samples were sputter coated with a thin layer of Au/Pd (ca. 10 nm thick) prior to the testing. The Transmission electron microscopy (TEM) analysis was conducted on a JEOL 100C type TEM machine with an accelerating voltage of 100 kV. The samples ultratoming was conducted on a Leica Ultracut R machine with samples embedded within an epoxy resin matrix. The ultrathin cut films

with thickness about 50-70 nm were directly transferred onto the TEM grid for TEM observation. Tensile strength and modulus were measured using an Instron 4400R machine, with a cross head speed set at 10 mm/min. Contact angle measurement was performed on a FTA 200 Dynamic contact angle analyzer. The MMT clay disks were prepared for the measurement on a hydraulic press at 30,000 lb/in.^{2}. The images were taken at 0.1 and 10 seconds respectively after the water was dropped onto the clay pellet surface. The data obtained were the average of 10 measurements. We also measured the interaction force between a MMT pellet and a pure cellulose film, as illustrated in Fig A-2. The samples were prepared by attaching a wet cellulose film onto a MMT pellet, and then dried for 48 hrs.

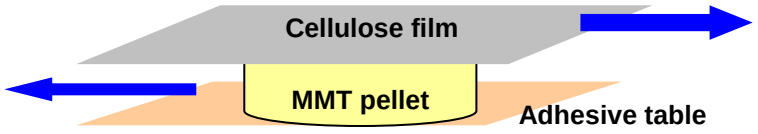

Figure A-2. Schematic illustration of interaction force measurement between a cellulose film and a clay pellet.

A.3 Results and Discussions

A.3.1 Characterization of Nanoclays and Cellulose/MMT nanocomposites

The XRD results (WAXD) of cellulose/clay nanocomposite, as shown in Fig A-3 and Table A-2, revealed that the diffraction pattern (2θ) of MMT Na^+ in the nanocomposites has shifted from 2θ of 7.72 ° (corresponding to *d*-spacing of 11.5 Å) to 6.03° (*d*-spacing 14.6 Å), about 3.1Å change in the d-space calculated from the Bragg

formula $\lambda_B=2d\sin\theta$, where λ is the wave length of the X-ray beam and θ is the scattering angle.

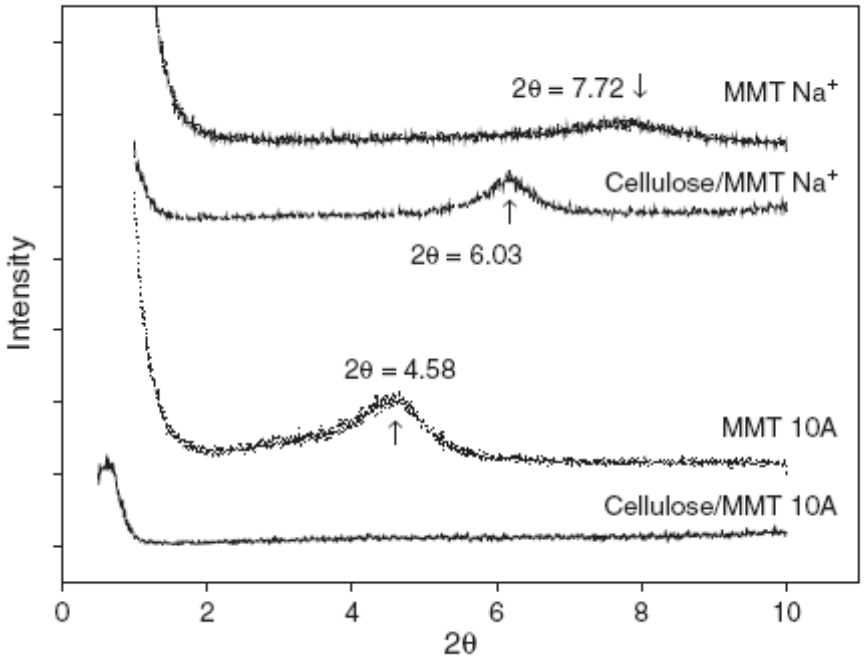

Figure A-3. WXRD patterns of cellulose/MMT Na^+ (A) and cellulose/MMT 10A (B) nanocomposites, in comparison with the pristine clays.

The large shift in the nanoclay d-space suggests that MMT Na^+ layers were intercalated in the cellulose matrix [22]. The d-spacing peak of MMT 10A in cellulose matrix disappeared. It indicates interlayer distance between MMT 10A single layers was infinite and MMT 10A was totally exfoliated in cellulose nanocomposites. It should be noted, however, that no diffraction peak shift in the composites was observed when other clay samples (30B, 25A, 93A, 20A and 15A) were used.

A closer examination of the detailed structure of the cellulose/clay nanocomposite revealed that a fully intercalated structure in the system comprising of cellulose/MMT NA^+ did occur, as shown in Fig A-4. As indicated in the circles, the width and length of the layered structure was about 20 and 200 nanometers, respectively, encompassing ca. 10 layers, in agreement with the WXRD results discussed above.

Table A-2. XRD results of the cellulose/MMT nanocomposites.

	Nanocomposite				
Sample	2θ (°)	d-spacing (Å)	Interlayer spacing (Å)	Notes	Instron interaction force measurement (lbf/mm^2)
MMT Na^+	6.03	14.6	4.6	Intercalated	2.475
MMT 10A	—	∞	∞	Exfoliated	1.056
MMT 30B	4.77	18.5	8.5	Neither intercalated nor exfoliated	0.530
MMT 25A	4.75	18.6	8.6	Neither intercalated nor exfoliated	N/A
MMT 93A	3.74	23.6	13.6	Neither intercalated nor exfoliated	N/A
MMT 20A	3.67	24.2	14.2	Neither intercalated nor exfoliated	N/A
MMT 15A	2.80	31.5	21.5	Neither intercalated nor exfoliated	N/A

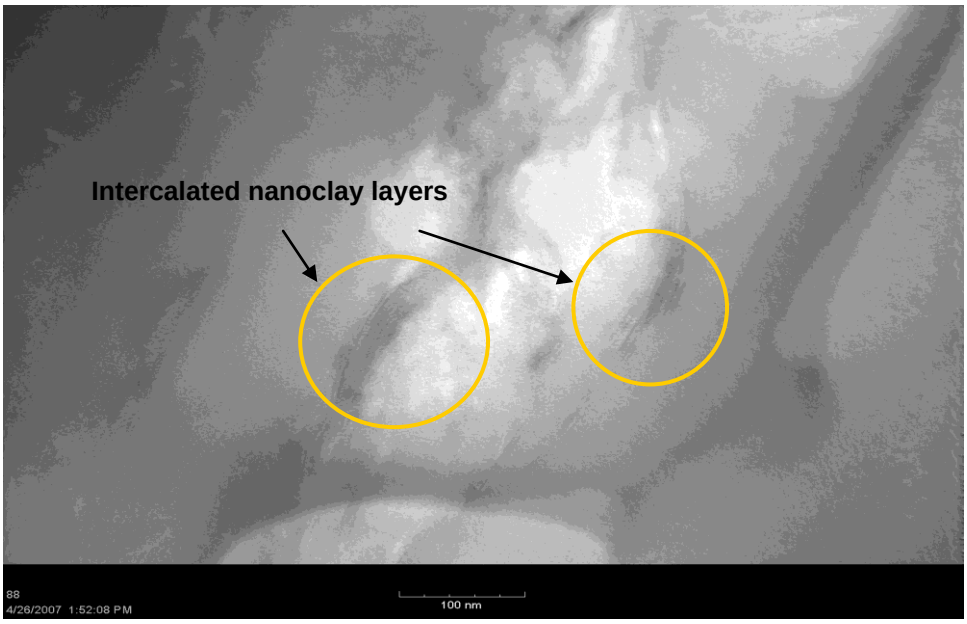

Figure A-4. TEM image of MMT Na^+/cellulose nanocomposites (2.0wt% of MMT loading) after ultratoming of the sample indicating a fully intercalated structure.

A.3.2 Hydrophobicity and interaction force measurements

According to clay supplier, the MMT Na^+ was hydrophilic and MMT 10A and 30B have been surface modified into less hydrophilic than MMT Na^+. The results of the interaction force between the cellulose clay, as shown in Table A-3, did prove this. MMT clay pellets were made under 30,000lb pressure. Diameter of each pellet was 13mm. Regenerated cellulose film was attached on MMT pellet just before the drying procedure. Cellulose film/MMT pellet was dried for 48hrs and then tensile strength of this sample was measured using Instron 4400R with 10mm/min cross head speed as shown in Fig A-2. Tensile strength of cellulose/MMT Na+, 10A and 30B pellet was measured as 2.475 lbf/mm^2, 1.056 lbf/mm^2 and 0.530 lbf/mm^2 respectively. MMT 20A, 93A, 20A and 15A pellets were separated automatically from cellulose film during drying process. A sequential decrease in the bonding force between cellulose and clay

pellets from MMT Na^+, 10A, and 30B were observed in accordance with the sequential decrease of the hydrophilicity of the clay [23-24]. The interaction force measurement results between cellulose film and hydrophobic clays of MMT 25A, 93A, 20A, and 15A suggested the incompatible interaction between clay pellet and cellulose film due to the high hydrophobicity of clay particles.

The contact angle of water on the clay surface was interesting. As shown in Fig A-5 and Table A-3, with the increase of the hydrophobicity of the clays, the contact angles increase steadily. MMT Na+ had the smallest contact angle (28°) and contact angle of water on the MMT 10A was the second largest (53.3°). Cellulose has four –OHs per each single molecule so it has a large hydrophilic character. Therefore, hydrophobicity of MMT clays can be critical index to represent the interaction force between cellulose and MMT particles. As hydrophobicity of MMT molecules increases, interaction force between cellulose and the MMT particle decreases. MMT Na+ was intercalated and MMT 10A was exfoliated in cellulose matrix.

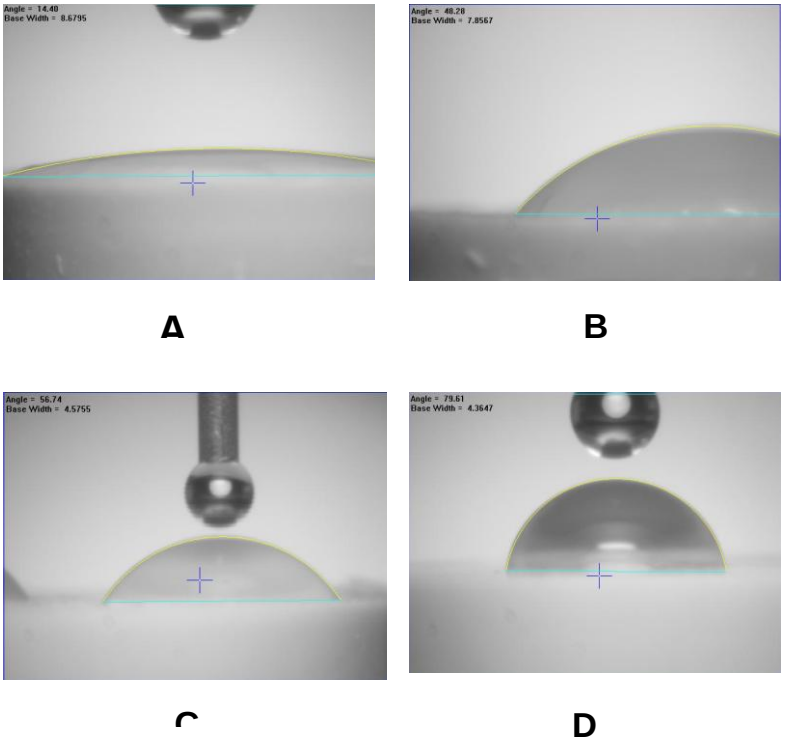

Figure A-5. Images of the contact angle of water on different clay pellet surfaces: (A) MMT Na^{+}; (B) MMT 30B; (C) MMT 10A; and (D) MMT 15A, respectively.

Table A-3. Contact angles measurement of cellulose/clay nanocomposites.

Nanocomposites comprised of cellulose	Contact angle		
	(0.1 sec/°)	(10 sec/°)	Deviation (%)
MMT Na^{+}	28.4	—	—
MMT 10A	53.3	51.2	3.9
MMT 30B	66.0	65.5	0.8
MMT 25A	65.2	64.7	0.8
MMT 93A	68.2	68.4	−0.3
MMT 20A	72.7	72.5	0.3
MMT 15A	75.6	75.3	0.4
Pure cellulose	45.7	40.0	12.5

Based on the contact angle measurement results and structural analysis, it is concluded that MMT clays which have the small hydrophobicity and the large interaction force were intercalated or exfoliated respectively. It should be noted that the contact angles of water on other clays, including MMT 25A, 93A, 20A, and 15A, were higher than that on sample MMT Na^+ and there was no structural change of those clays.

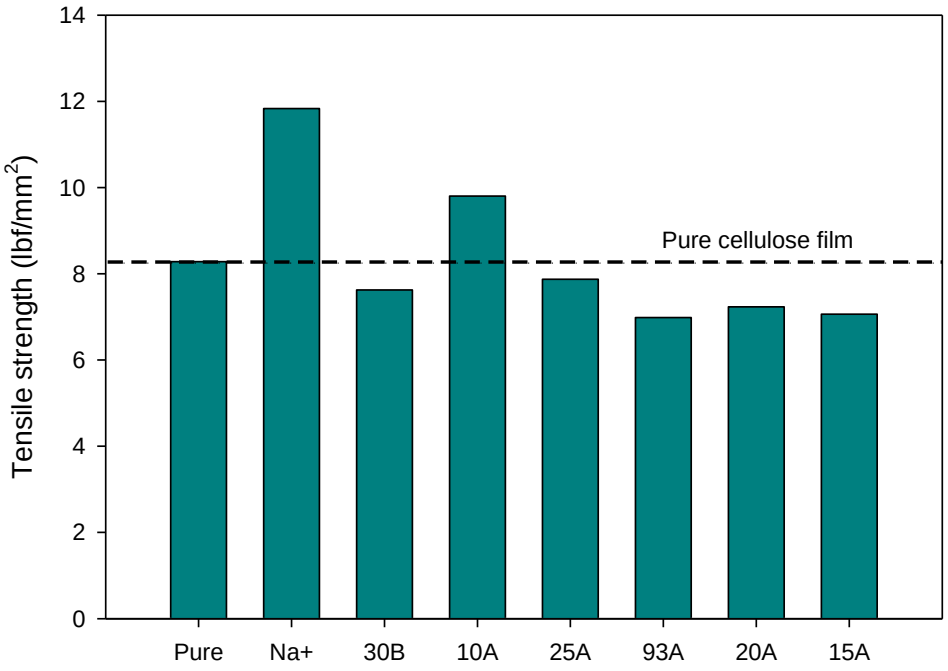

Figure A-6. Tensile strengths of pure cellulose and cellulose/MMT nanocomposites at 2 % clay loading.

A.3.3 Physical properties

Tensile strength and Young's modulus obtained from cellulose composites with several nanoclays are shown in Fig A-6. It was interesting to note that for the composites composed of cellulose/MMT Na^+ and cellulose/MMT 10A, a 43 % and 18 % increase in the tensile strength were observed respectively. However, the tensile strengths in all

other systems exhibited a decrease. This decrease may be attributed to the poor compatibility between cellulose and the aggregation formation of hydrophobic MMT particles in the composite matrixes.

It was reported that the modulus of composite is not the function of particle size but proportional to the volume fraction of particle when the thickness of the particle is more than 30 nm [25]. In this study, it was found that the modulus of the clay with 2.0wt% MMT loading increased for all cases.

It was also found that modulus increased 10%~20% respectively regardless of the aggregation of MMT particles. Theoretical analysis indicated that modulus is not the function of particle size but proportional to the volume fraction of particle if the thickness of particle is more than 30nm [25]. It was reported through theoretical calculations that the nanocomposites could result in 12% increase of modulus with 2.0wt% filler loading, and it increases remarkably when the particle size is less than 3nm [25].

Further study on the tensile strength and Young's modulus with different loading ratio (1.0wt%~10.0wt%) of MMT Na^+ and MMT 10A samples are shown in Fig A-7. The tensile strength of MMT Na^+/cellulose increases remarkably with the increasing MMT contents and reached the maximum value with 6.0wt% loading, and then decreases rapidly due to the agglomeration of MMT particles. The tensile of MMT 10A-cellulose is significantly lower than that of the composite made from cellulose and MMT Na^+. Although XRD (Fig A-3) and TEM (Fig A-4) indicated that MMT 10A was fully exfoliated and MMT Na^+ was only intercalated in the cellulose matrix, the poor tensile strength of the former may be the results of larger aggregates in the cellulose matrix. The SEM pictures (not shown) indicate that for the sample made from MMT 10A, some aggregates were presented in this sample although XRD shows the particles are intercalated by cellulose molecules.

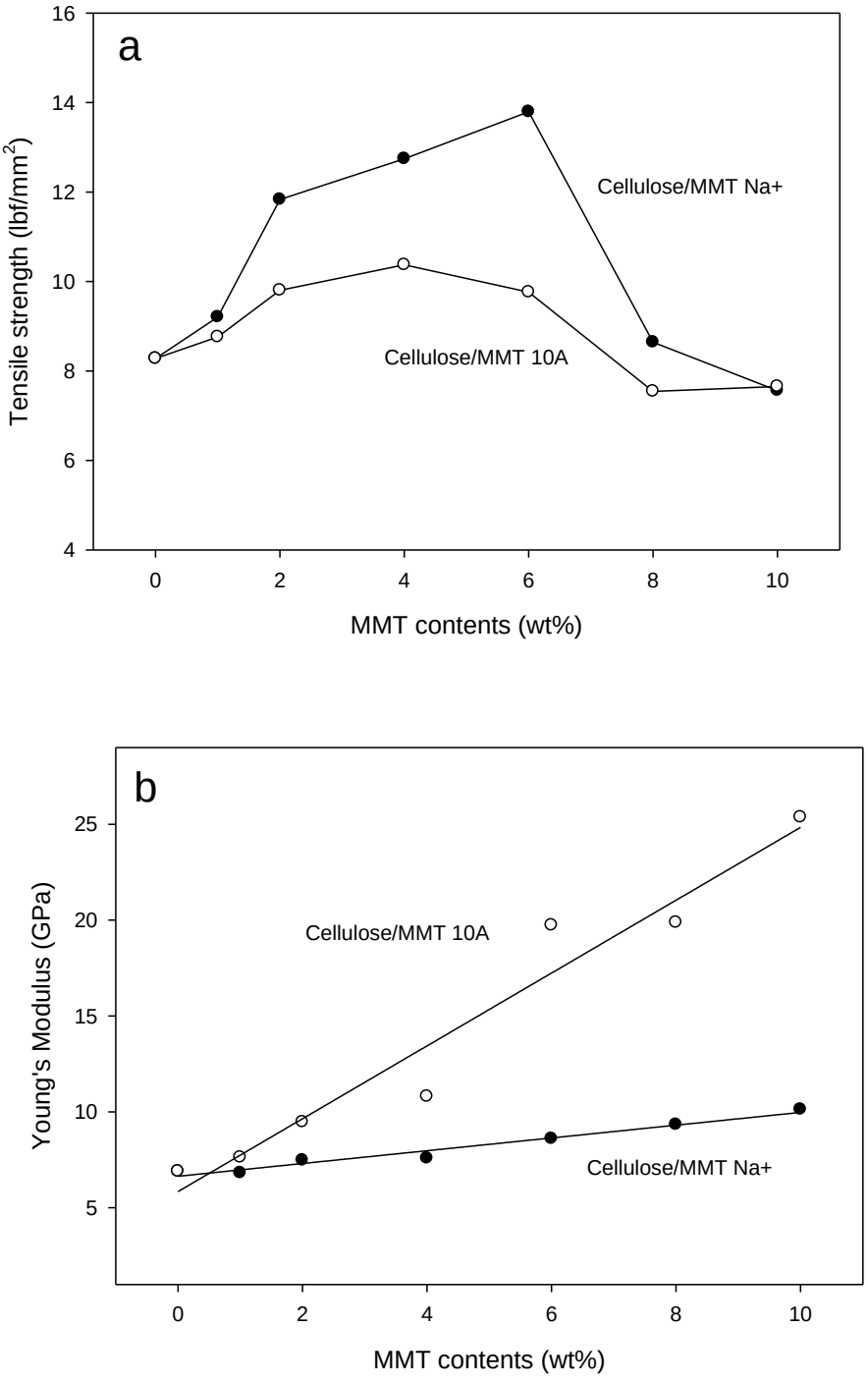

Figure A-7 (a) Tensile strength with different loading levels (1-10 wt %), and (b) Young's modulus of the composites comprised of cellulose/MMT 10A and cellulose/MMT Na^+ at different clay loadings.

A.3.4 Model study

Modulus with different contents was shown in Fig A-7 (b). Modulus of MMT 10A/cellulose increased linearly with increasing MMT 10A contents up to 10.0wt%. Modulus of 10.0wt% MMT 10A and Na+ loading showed 260% and 50% increase respectively. Several previous studies used the traditional composite theory such as Halpin-Tsai and Mori-Tanaka theories to the examination of physical properties of nanocomposites [26]. Geometric assumption in the Halpin-Tsai theory is that reinforcement materials have constant thickness. Model equation is given by the following,

$$\frac{E}{E_m} = \frac{1+\zeta\eta\phi_f}{1-\eta\phi_f} \tag{A.1}$$

Where E is modulus of composite, E_m is modulus of matrix, E_f is modulus of filler, ζ is shape factor 2*(diameter/thickness), Φ is volume fraction and η is defined as,

$$\eta = \frac{E_f / E_m - 1}{E_f / E_m + \zeta} \tag{A.2}$$

Comparison between theoretical value and experimental data was shown in Fig A-8. It was reported that the modulus of MMT clays is 178GPa [27]. Aspect ratio of the single layer of MMT was reported as 70 ~ 150. Therefore shape factor of MMT 10A is around 140-300 and shape factor of MMT Na+ is expected as 10-20 based on the assumption that average number of MMT Na+ layers is 10. Halpin-Tsai theoretical value of each shape factor increases linearly like experimental data. Even though there are small deviation between theoretical values and Halpin-Tsai model values, it predicts the

experimental values very well.

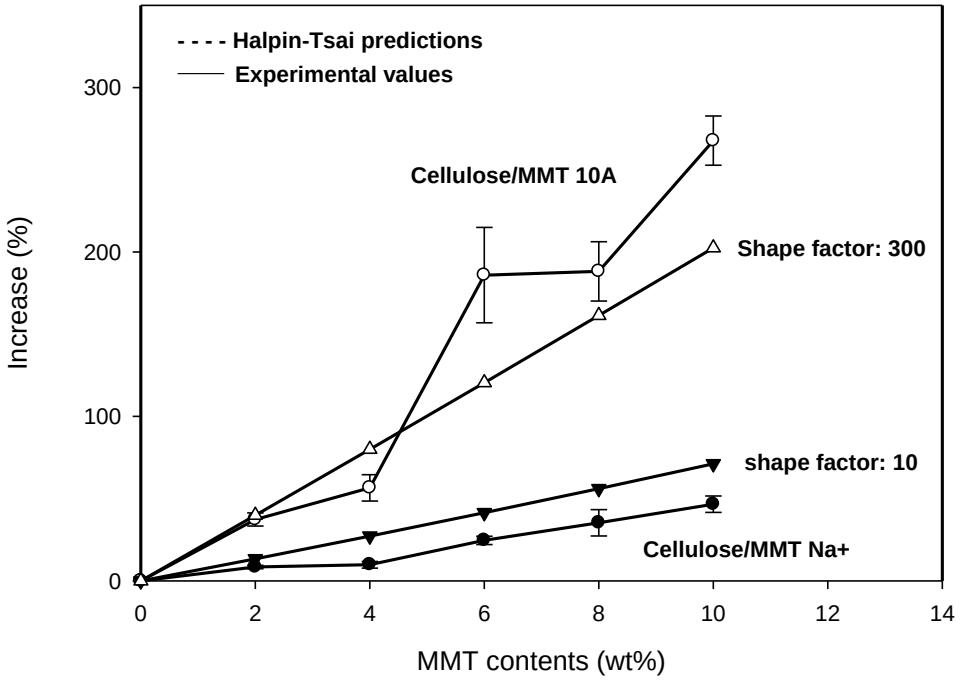

Figure A-8. Comparison of experimental Young's modulus for Cellulose/MMT 10A and Cellulose/MMT Na+ nanocomposites with Halpin-Tsai predictions.

A.4 Conclusions

In this study, we successfully demonstrated that biodegradable nanocomposites can be manufactured from regenerated cellulose and MMT clays using NMMO as the solvent. Results showed that the tensile strength and modulus of the composites were strongly dependent on the compatibility between cellulose molecules and nanoclay surface. The surface hydrophobicity of the nanoclay played a dominant role in nanoclay intercalation and exfoliation within the cellulose matrix. The tensile strength of cellulose/MMT 10A system exhibited an increase at 1%~4% clay loading. In contrary, the Young's modulus continually increased up to10% MMT 10A loading, allowing a 260% increase compared to that when no nanoclay was added.

References

1. Ray, S.S. and M. Bousmina, *Biodegradable polymers and their layered silicate nano composites: In greening the 21st century materials world.* Progress in Materials Science, 2005. **50**(8): p. 962-1079.

2. Klemm, D., et al., *Cellulose: Fascinating biopolymer and sustainable raw material.* Angewandte Chemie-International Edition, 2005. **44**(22): p. 3358-3393.

3. Fink, H.P., et al., *Structure formation of regenerated cellulose materials from NMMO-solutions.* Progress in Polymer Science, 2001. **26**(9): p. 1473-1524.

4. Johnson, D., *US Patent 3,447,939, Compounds dissolved in cyclic amine oxides.* assigned to Eastman Kodak, 1969.

5. CC Mccorsely, J.V., *US Patent 4,142,913, Process for making a precursor of a solution of cellulose,.* assigned to Akzona Inc, March 6 (1979).

6. NE Franks, J.V., *US Patent 4,196,282, Process for making a shapeable cellulose and shaped cellulose products.* assigned to Akzona Inc, April 1 (1980).

7. Chanzy, H., et al., *Phase-Behavior of the Quasi-Ternary System N-Methylmorpholine-N-Oxide, Water, and Cellulose.* Journal of Polymer Science Part B-Polymer Physics, 1982. **20**(10): p. 1909-1924.

8. Blachot, J.F., et al., *Rheological behavior of cellulose/monohydrate of n-methylmorpholine n-oxide solutions - Part 1: Liquid state.* Rheologica Acta, 1998. **37**(2): p. 107-114.

9. Loubinoux, D. and S. Chaunis, *An Experimental Approach to Spinning New Cellulose Fibers with N-Methylmorpholine-Oxide as a Solvent.* Textile Research Journal, 1987. **57**(2): p. 61-65.

10. Lenz, J., J. Schurz, and E. Wrentschur, *Properties and Structure of Solvent-Spun and Viscose-Type Fibers in the Swollen State.* Colloid and Polymer Science, 1993. **271**(5): p. 460-468.

11. Ganster, J., et al., *Relation between Structure and Elastic-Constants of Man-Made Cellulosic Fibers .1. A 2-Phase Anisotropic Model with Contiguity Parameter.* Acta Polymerica, 1994. **45**(4): p. 312-318.

12. Giannelis, E.P., *Polymer layered silicate nanocomposites.* Advanced Materials, 1996. **8**(1): p. 29-&.

13. Giannelis, E.P., *Polymer-layered silicate nanocomposites: Synthesis, properties and applications.* Applied Organometallic Chemistry, 1998. **12**(10-11): p. 675-680.

14. Vaia, R.A., et al., *Polymer/layered silicate nanocomposites as high performance ablative materials.* Applied Clay Science, 1999. **15**(1-2): p. 67-92.

15. Messersmith, P.B. and E.P. Giannelis, *Synthesis and Barrier Properties of Poly(Epsilon-Caprolactone)-Layered Silicate Nanocomposites.* Journal of Polymer Science Part a-Polymer Chemistry, 1995. **33**(7): p. 1047-1057.

16. Kojima, Y., et al., *Mechanical-Properties of Nylon 6-Clay Hybrid.* Journal of Materials Research, 1993. **8**(5): p. 1185-1189.

17. Gilman, J.W., *Flammability and thermal stability studies of polymer layered-silicate (clay) nanocomposites.* Applied Clay Science, 1999. **15**(1-2): p. 31-49.

18. Gilman, J.W., et al., *Flammability properties of polymer - Layered-silicate nanocomposites. Polypropylene and polystyrene nanocomposites.* Chemistry of Materials, 2000. **12**(7): p. 1866-1873.

19. Ray, S.S. and M. Okamoto, *New polylactide/layered silicate nanocomposite: a novel biodegradable material.* Nano Letters, 2002: p. 1093-1096.

20. Vaia, R.A., et al., *New Polymer Electrolyte Nanocomposites - Melt Intercalation of Poly(Ethylene Oxide) in Mica-Type Silicates.* Advanced Materials, 1995. **7**(2): p. 154-156.

21. Aranda, P. and E. Ruizhitzky, *Poly(Ethylene Oxide)-Silicate Intercalation Materials.* Chemistry of Materials, 1992. **4**(6): p. 1395-1403.

22. Ray, S.S. and M. Okamoto, *Polymer/layered silicate nanocomposites: a review from preparation to processing.* Progress in Polymer Science, 2003. **28**: p. 1539-1641.

23. Cappella, B. and G. Dietler, *Force-distance curves by atomic force microscopy.* Surface Science Reports, 1999. **34**(1-3): p. 1-+.

24. Tormoen, G.W., J. Drelich, and E.R. Beach, *Analysis of atomic force microscope pull-off forces for gold surfaces portraying nanoscale roughness and specific chemical functionality.* Journal of Adhesion Science and Technology, 2004. **18**(1): p. 1-17.

25. Ji, X.L., et al., *Tensile modulus of polymer nanocomposites.* Polymer Engineering and Science, 2002. **42**(5): p. 983-993.

26. Stretz, H.A., et al., *Intercalation and exfoliation relationships in melt-processed poly(styrene-co-acrylonitrile)/montmorillonite nanocomposites.* Polymer, 2005. **46**(8): p. 2621-2637.

27. Fornes, T.D. and D.R. Paul, *Modeling properties of nylon 6/clay nanocomposites using composite theories.* Polymer, 2003. **44**(17): p. 4993-5013.